Effects of Sink Strength and Irradiation Parameters on Defect Evolution in Additively Manufactured HT9

by

Pengyuan Xiu

A dissertation submitted in partial fulfillment
of the requirements for the degree of
Doctor of Philosophy
(Nuclear Engineering and Radiological Sciences)
in the University of Michigan
2022

Doctoral Committee:

Associate Professor Kevin G. Field, Co-Chair
Professor Lumin Wang, Co-Chair
Professor Todd R. Allen
Professor Fei Gao
Professor Amit Misra

Pengyuan Xiu

xiupy@umich.edu

ORCID iD: 0000-0002-5267-6278

Dedication

To my family, friends and those supporting me

Acknowledgements

First, I would like to thank my current advisor, Dr. Kevin G. Field, for providing his insights, suggestions, and guidance throughout my thesis work. I would also like to thank my previous advisor, Dr. Lumin Wang, for providing guidance and experience on materials characterization as well as foundation for conducting research on irradiation effects with other projects prior to my thesis work. Without their help, I would not be the scientist that I am today. I would also like to thank the members of my committee, Dr. Todd R. Allen, Dr. Fei Gao, and Dr. Amit Misra for their valuable input which greatly improved this thesis.

I am very grateful to the past and present members of the Nuclear Oriented Materials & Examination (NOME) research group led by Dr. Kevin G. Field as well as the research group led by Dr. Lumin Wang: Dr. Chenyang Lu, Dr. Tai-Ni Yang, Dr. Li Jiang, Dr. Chao Ye, Dr. Priyam Patki, T.M. Kelsy Green, Gabriella Bruno, Matthew Lynch, Mackenzie Warwick, and Ethan Polselli. Their mentorship, as well as technical and moral support in the laboratory and office have been one of the highlights of my graduate studies.

Thank you to the past and present staff members at the Michigan Ion Beam Laboratory (MIBL), Dr. Ovidiu Toader, Dr. Zhijie Jiao, Thomas Kubley, Robert Hensley, Dr. Prashanta Niraula, and Dr. Fabian Naab, for their great efforts of running the accelerator laboratory, without which these experiments would not have been possible. I can remember the times when I call one or some of you at midnight and have you come to MIBL to fix issues with the on-going irradiation experiments. In addition, I would like to thank some in the research group led by Dr. Gary S. Was

for the great help, training, and suggestions on performing irradiation experiments: Dr. David Woodley, Logan Clowers, Valentin Pauly, Dr. Miao Song, Dr. Peng Wang, Dr. Stephen Taller, Dr. Drew Johnson, and Katey Thomas.

I also want to thank the staff at the Michigan Center for Materials Characterization (MC^2) for the training and maintenance of the state-of-art materials characterization equipment. Dr. Kai Sun and Dr. Tao Ma provided a lot of guidance on equipment operation and diagnosis of various models of S/TEMs that made me skillful on this powerful material characterization tool. Dr. Allen Hunter, Dr. Bobby Kerns, and Dr. Haiping Sun helped me with the training on the operation of SEM, EBSD, FIB, and nano-indentation.

To my parents, Binglin Xiu and Zhonghuan Wang who supported me throughout the years, thank you for always listening to me, helping me focus on what is important, and encouraging me to pursuit my dreams and possibilities during difficult times. I would not have been able to complete this without your love.

Finally, to my girlfriend, Siyin Zheng. Thank you for all the warmth and encouragement during the darkest days. Thank you for your companion during my whole PhD study process. You made me become a better person and made me realize how much more potential I can achieve without a limit. I am forever grateful that you are always there.

Table of Contents

List of Tables

List of Figures

List of Equations

List of Appendices

Abstract

A ferritic-martensitic (FM) steel, HT9, has been studied for use in advanced nuclear reactors for its excellent swelling resistance and high-temperature strength. However, the effects of sink strength (SS) on tailoring the radiation responses in HT9 have not yet been fully studied. The advancement of the mechanistic understanding of how SS affects microstructural evolution is of great importance to the development of new radiation-tolerant materials in the future.

Additive-manufacturing (AM) has been drawing attention due to the advantage of its ability to control the complex geometry and composition of the structural components. The SS effects on radiation responses are studied within by using the as-built (ASB) and the post-built heat-treated (called ACO3 and FCRD) AM-HT9, with their starting SSs significantly differ from each other. Heat A of AM-HT9 in this study demonstrated a SS of $12.2\times10^{15}/m^2$ in the ASB and a nearly 5-time reduction in SS to $2.4\times10^{15}/m^2$ and $2.7\times10^{15}/m^2$ for the ACO3 and FCRD specimens, respectively. Ion-irradiations focusing on irradiation dose and temperature are conducted to systematically study the radiation responses and defect evolutions in AM-HT9 alloys.

Experimental results showed that the high SS in the ASB drastically suppresses all microstructural evolution with damage levels up to 250 dpa. A higher normalization temperature used in the ACO3 results in a reduction of SS compared to the FCRD, leading to a ten-time-higher swelling rate in ACO3 after irradiation to 250 dpa. The complicated microstructural evolution including all features contribute to evolving defect sinks that collectively tailor the swelling behavior in the AM-HT9, which is verified using a simplified rate-theory model that considers the

ratio of biased to neutral SS, Q. It was found that the analytical model does highlight both the overall SS and the balance between biased and neutral sinks are strong indicating factors for increased swelling resistance in AM-HT9. In addition, the Ni/Si/Mn-rich precipitate and dislocation loop coarsening processes are captured with increasing damage levels, whereas these processes are either observed to complete at much lower damage levels, or even not observed indicating an early saturation occurring in the ACO3/FCRD that contain about 5-time lower SS in the starting microstructures.

Irradiation temperatures also greatly affected the radiation responses of AM-HT9. The density of $a\langle 100\rangle$ type dislocation loops dropped from $3.2\times10^{21}/m^3$ to $3.0\times10^{20}/m^3$ in the ASB specimen and dropped from $(5.9\text{-}6.4)\times10^{21}/m^3$ to $(0.3–0.4)\times10^{21}/m^3$ in the ACO3/FCRD heat-treated specimens. In addition, the higher irradiation temperatures stabilize the $a\langle 100\rangle$ loops and enables higher coarsening rates than lower irradiation temperatures. The precipitate evolution is greatly accelerated by the available kinetic energy at higher temperatures to overcome the pinning effects imposed by high SS, while cavity swelling exhibits the typical bell-shaped curve in the heat-treated ACO3/FCRD specimens with varying peak swelling temperatures by 30°C tailored by SSs.

The overall result of this work is a wide range of microstructural responses under irradiation that can be obtained by AM fabrication with post-build heat-treatments, through the tuning of SS in the starting and the irradiated microstructures. The radiation response then needs to balance with other factors that are tied to the sink strength of AM-HT9 alloys including the mechanical properties such as tensile strength and fracture toughness. These insights obtained will stimulate further the optimization of using AM to fabricate materials that are highly radiation tolerant for advanced nuclear reactor applications.

Chapter 1 Introduction

Nuclear energy, as a clean and sustainable energy form, contributes about 20% and 10% of the electricity generation in America and around the globe, respectively [1,2]. It is a critical alternative energy form to replace fossil fuels for energy production with reduced carbon emissions. However, one challenge for the safe operation of the current fission reactors and the advanced Generation IV (Gen IV) nuclear reactor concepts is the high demand placed on the materials performance. In these nuclear reactors, the in-core materials are expected to sustain extremely harsh environments that involve elevated temperature and high radiation levels. Designing, fabricating, and evaluating the performance of resilient structural materials are essential to the safety, high energy yield and reduced waste production of current and future nuclear reactors.

Within the core and surrounding structures in nuclear reactors, energetic neutrons bombard the structural materials. These neutrons can strike an atom contained within the material, and if sufficient energy is transferred to displace that atom, it is called a primary knock-on atom (PKA). PKAs get displaced from their lattice sites and can keep displacing more atoms in the target material. These secondary displaced atoms or second knock-atoms can also keep displacing more atoms. This process is known as a damage cascade event. The event stops when the kinetic energy carried by all atoms and/or ions are lower than the threshold displacement energy of atoms in the lattice of the material. During the process, point defects called interstitials and vacancies are generated – vacancies refer to the vacant lattice sites previously occupied by an atom, and interstitials refer to the atoms displaced and come to rest in positions other than their perfect lattice

sites. There are a few fates for these generated point defects. An interstitial and a vacancy can recombine in the matrix, resulting in the local restoration of the perfect lattice. Another way to eliminate point defects are through (i) the absorption of point defects at defect sinks, such as line dislocations, grain boundaries, and interfaces between matrix and precipitates that are incoherent or semi-coherent; and (ii) enhanced point defect recombination at the interfaces between matrix and coherent precipitates. The point defects surviving from the recombination and defect absorption for a given amount of time can agglomerate to form larger features such as dislocation loops, line dislocations, cavities, and precipitates. Additional elemental segregation can occur at defect sinks and defects due to mobility imbalances in between solutes and solvents under irradiation. These irradiation-induced microstructural and microchemical changes result in various macroscopic mechanical property evolutions such as hardening and embrittlement, swelling, increase of corrosion susceptibility, and reduction of fraction toughness [3–7].

To suppress the radiation damage in nuclear structural materials, one of the strategies is to enhance the defect absorption by defect sinks. Zinkle et al. [8] in a review showed that with higher initial sink strength, (i) the radiation hardening in several ferritic-based steels under low-dose fission-neutron irradiation at 250–300°C is strongly suppressed, and (ii) the void swelling resistance in ion or fission-neutron irradiated austenitic stainless steels is significantly improved. In addition, at high temperatures, high densities of defect sinks such as precipitates can efficiently trap He and thereby suppress high-temperature He embrittlement [8]. Therefore, high-sink-strength modifications have the potential to beneficially suppress low-temperature radiation hardening and/or high-temperature He embrittlement and thereby expand the operating temperature window for structural materials in nuclear energy systems [8].

Ferritic-martensitic (FM) steels are considered candidate materials for Gen IV nuclear reactors with a range of applications due to their excellent swelling resistance [9–11], corrosion/oxidation resistance [12,13], and high temperature strength [14,15]. FM steels, such as HT9 [16–18], Grade 91 (also known as T91 or P91 in literature) [19–22], F82H [6,23,24], Eurofer97 [25–27], and HCM12A [28,29], have increased radiation tolerance due to their increased sink strength because of their hierarchical microstructure consisting of prior austenite grain boundaries (PAGBs), blocks, packets, laths (e.g., low-angle grain boundaries), sub-grain boundaries, precipitates, and line dislocations.

In particular, HT9 – a 12Cr-1MoVW (in wt. %) FM steel – is considered for fuel cladding [30,31] and duct materials [32–34] in fast-fission reactors, as well as use in the first wall and blanket structures [35,36] in fusion reactor systems [37]. Various studies show the formation of the above-mentioned microstructural features induced by irradiation in HT9 – dislocation loops, line dislocations, cavities, Ni/Si/Mn-rich and Cr-rich precipitates, and radiation-induced segregation that may lead to degradation in mechanical properties [38][3].

Traditionally, wrought HT9 (W-HT9) is fabricated using casting followed by forging. However, the lack of flexibility with respect to complex geometry control [39] is a challenge with this fabrication route. Traditional welding techniques have successfully ensured structural integrity in fabricating components that have more complex geometries, but it still requires the production of shaped feedstock (e.g., plates, rods, sheets) welded together to form the final product [37]. Additionally, if the welding procedures are not carefully controlled, the heat input from welding can form fusion zones and heat-affected zones that are considerably different from the base material in terms of microstructures and properties [37,40–42]. Such heterogeneities between the

base metal, fusion zone, and heat-affected zone may further affect radiation-induced microstructures [43–45].

Recently, fusion-based additive manufacturing (AM), a 3D printing technique where a structure is fabricated in a layer-wise manner, is gaining more attention in the materials science community due to its capability of accurate control over geometries and compositions of the printed structural components [37]. AM-based techniques give end-users greater computer-aided control over process parameters and thus enable systematic tailoring of the material's localized microstructures. The desired result is a potential for reducing the cost of fabricating components with geometrical complexity or reducing or eliminating tooling costs of low-volume or custom components [37]. AM-based techniques overcome the feedstock/retooling requirements and have thus become attractive considerations for the nuclear materials community [37,46,47].

However, challenges related to localized fusion-based processes as is the case for welding still exist in process control when it comes to fabricating HT9 alloys via fusion-based AM techniques [39,48]. Vendors have recently begun to explore a method of process control during AM called *laser-blown powder directed-energy-deposition (DED)* to fabricate HT9 alloys (AM-HT9) for nuclear applications. At the time of writing, process parameters for the DED process (e.g., cross-hatch spacing, laser power) have been established for AM-HT9, and the mechanical properties have been characterized and shown to be satisfactory [48,49]. Mechanical properties, particularly the room and high-temperature tensile properties in the unirradiated state, showed an increase (>100–200 MPa) of yield strength and ultimate tensile strength in the as-built (ASB) AM-HT9 compared with those measured for W-HT9 [49]. The mechanical response of the AM-HT9 in the ASB condition can be partially attributed to the anisotropy of the layered structure from the DED process and the formation of un-tempered martensite as a result of the high cooling rates in

the AM-DED process. The reheating passes led to the formation of the unwanted δ-ferrite phases that could affect the mechanical properties, such as fracture toughness [49], necessitating post-build heat-treatments. Post-build heat-treatments at typical normalization and tempering temperatures successfully eliminated the δ-ferrite phases and resulted in a tempered martensite microstructure, even though the heat-treatments could increase the final cost of the product.

Characterizing the ASB condition of the AM-HT9 microstructure showed a high density of refined carbides and carbon-nitrides, a refined lath structure, and a high density of line dislocations [49]. The high sink density could greatly enhance the swelling resistance. However, as mentioned previously, heat-treatments are necessary for tempering the martensitic structure and eliminating the δ-ferrite. Further characterization of the heat-treated AM-HT9 showed that the normalizing and tempering treatments coarsened the microstructure and led to the recovery of the dislocations [49]. These microstructural changes would lead to a reduction in sink density from the ASB AM-HT9. These preliminary results provide prima facie evidence that points to the possibility of unique microchemical evolution and mechanisms operating in AM-fabricated FM steels compared with those of their wrought variants under irradiation [49].

The objective of this thesis is to understand the role of starting microstructures and irradiation parameters on the defect evolution in AM-HT9 using ion irradiation techniques. A combination of ion irradiation experiments, post-irradiation examination and rate-theory calculation were used to achieve this objective. Chapter 2 provides a background on ferritic-martensitic steels and the radiation effects on the microstructural evolution. Chapter 3 summarizes the objective of the thesis and the approach taken to achieve the objective. Chapter 4 describes the experimental procedures for the ion irradiation experiments and the post-irradiation examination techniques used to characterize the microstructures. Chapter 5 summarizes the results gathered

from the experiments and analytical techniques. Chapter 6 offers an interpretation and discussion of the experimental results and addresses the objective. Chapter 7 provides the conclusions drawn from this thesis and Chapter 8 suggests future work.

Chapter 2 Background

W-HT9 alloys and their radiation effects have been extensively studied owing to their exceptional high damage level performance for Gen IV reactor applications. Chen et al. [50] provided a review of radiation responses in W-HT9. The radiation responses of recently developed AM-HT9 alloys, fabricated by laser-blown powder DED coupled with post-build heat-treatments, however, was not evaluated. This chapter will summarize the metallurgy and microstructures of the W-HT9 alloy and AM-HT9 alloys, and the changes induced by irradiation in W-HT9 to provide the foundational understanding needed to evaluate the influence of microstructure on the sink strength and irradiation performance between the two variants of HT9 Generalized theoretical work regarding swelling will be outlined in addition, as this lays the foundations for evaluating the central hypothesis of this work.

2.1 Microstructures of FM Steels

As mentioned before, FM steels are a carbon-bearing Fe-based body-centered cubic (bcc) material with a complex hierarchical microstructure. A combination of martensite, retained austenite, and δ-ferrite may exist due to incomplete phase transformations during the cooling process. The 12 wt. % Cr class of FM steels were developed to provide a substitute for low Cr steels by permitting manufacturing of components that could be used at temperatures at or above 600˚C in power generation plants [51–53]. The metallurgical basis and development of high-chromium wrought FM steels, as well as the fusion-based welding and additive manufacturing

processes applied on FM steels are briefly reviewed here with similarity to [49,54,55]. Factors determining the constitution, transformation, and tempering characteristics are summarized within.

2.1.1 Wrought FM Steel Processing

The primary elements in FM steels are Fe with varying Cr and C. A phase diagram for the Fe-Cr-C ternary system with varying Cr content and 0.1 wt. % C is shown in Figure 2.1 [54]. As can be seen, for HT9 alloy which contains 12 wt. % Cr, the austenitic phase is stable at the normalization temperatures between 900 to 1050°C, though the γ-Fe phase boundary is tailored by other minor elements existing in HT9 alloys. For example, the austenite-stabilizing elements – such as C, N, Ni, Mn, Cu, and Co [54] – push the γ-Fe phase boundary to the right and expand the stable formation region. On the other hand, the ferrite-forming elements like Cr, Mo, Nb, V, W, Si, Ti, and A1 act in contract to this effect [54]. The tempering resistance of the steels is increased by the addition of the ferrite-forming elements and, consequently, highly alloyed commercial steels may contain some δ-ferrite [54]. The ferrite phase inhibits austenite grain growth, but it adversely influences the strength and, directly or indirectly, the fracture toughness [54].

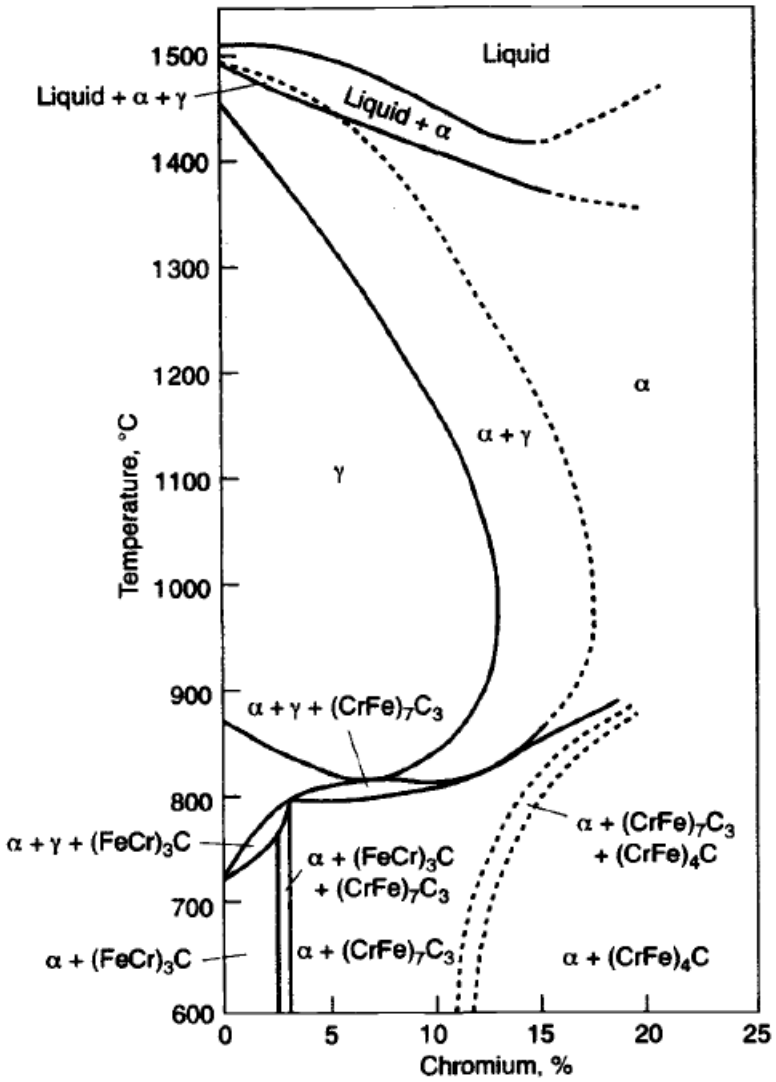

Figure 2.1. Effect of chromium (in wt. %) on Fe-Cr-C steels containing 0.1 wt. % C from [54].

The formation of δ-ferrite can be avoided by the addition of the austenite-forming elements; thus, the balancing of the constitution to ensure 100% austenite at the austenitizing temperature may be effected [54]. Carbon is the cheapest austenite former, but is not always favored, as it decreases the toughness and impairs the weldability and corrosion resistance. Furthermore, higher austenitizing temperatures are required to dissolve carbides of the MX type (where M is V, Nb, Ti, or Ta, and X is C and N for carbonitrides), resulting in coarser prior austenite grain sizes and reductions in toughness and creep ductility. Nitrogen can also be utilized

as an austenite stabilizer, but the amount required is generally high compared to those available in the FM steels. Nickel, although less effective than carbon and nitrogen, is usually not used in steels for nuclear applications due to the adverse effect of extensive transmutation reaction with high thermal neutron fluences, resulting in the production of H and He that promote cavity swelling. Manganese has been considered as an alternative; however, it is inferior to nickel as an austenite stabilizer, and 0.1% C, 12% Cr steels contain some δ-ferrite even with an addition of 6% manganese [54,56]. The high-manganese steels are also prone to embrittlement during thermal aging and/or irradiation, possibly because of χ-phase formation [56]. Cobalt may also be employed, but it is expensive and, in common with nickel, must be minimized in steels for component applications in fusion reactor systems because of the high residual radioactivity induced by neutron irradiation. The difficulty in eliminating δ-ferrite in the 12% Cr martensitic steels is one of the factors contributing to the lower (7 to 10%) chromium steels being favored for nuclear fusion applications. The ferrite-forming elements V, Nb, Ta, Ti, and A1 are also effective in removing the austenite formers carbon and/or nitrogen from solution as insoluble carbides and nitrides, thereby indirectly affecting the constitution of the steels [54,57].

The austenite present at the austenitizing temperature should transform fully to martensite during air cooling or rapid quenching to ambient temperature [58]. In the normalized condition, the microstructure consists of martensite laths with the width in the range of 250–500 nm and dislocation density greater than $1\times10^{13}/m^2$ [51,52]. The alloying additions made to balance the constitution or improve the tempering resistance of the steels also lower the martensite start (M_s) and finish (M_f) temperatures, resulting in a tendency for retained austenite to be present if the M_s temperature is close to or below room temperature [54]. The retained austenite increases the toughness of high chromium transformable steels but, in other respects, it is undesirable as

distortion occurs during its transformation and it decreases the strength. It follows that the composition of the steel must be adjusted not only to control the constitution but also to maintain the M_s-M_f temperature range above ambient [54].

Martensite forms in thick sections known as laths due to inhibition of pearlite transformation and absence of bainite [59]. A continuous cooling transformation (CCT) diagram is shown in Figure 2.2.

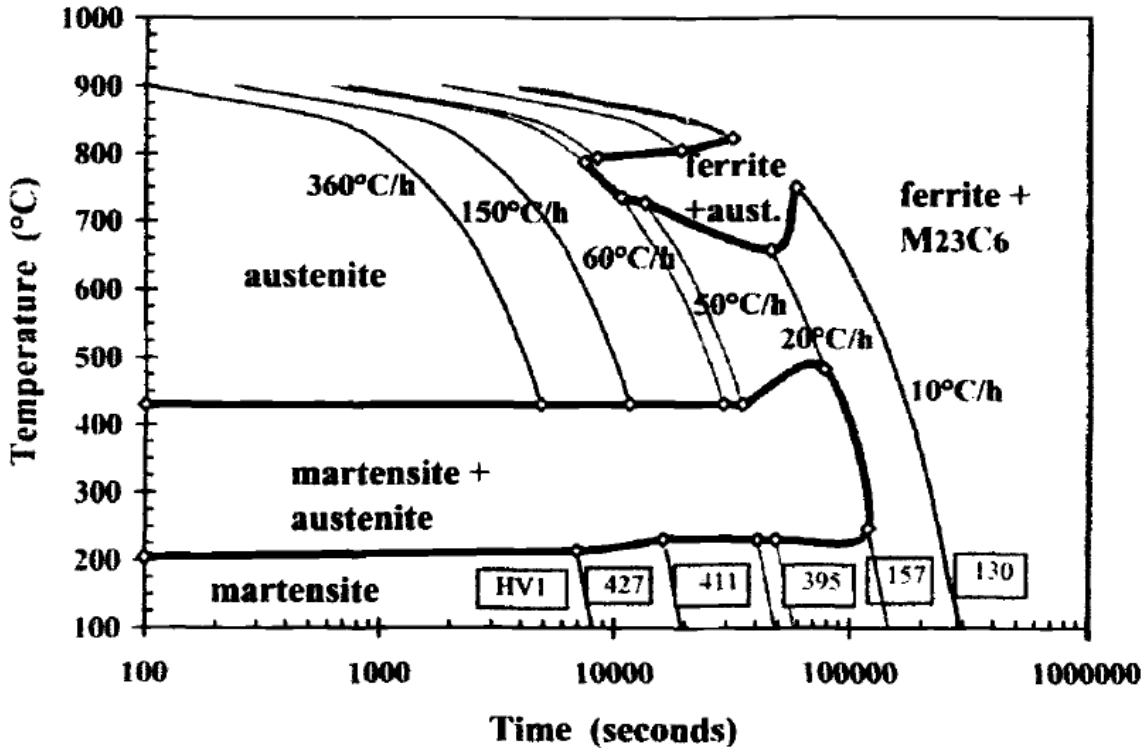

Figure 2.2. Continuous cooling transformation (CCT) diagram for low-carbon F82H (8Cr-2WVTa) steel determined after austenitization at 1050°C for 0.5 h, from [54].

The last step is tempering to improve toughness by refining the microstructure, which is conducted below the austenitization temperature to avoid re-austenitization and thereby achieve the optimum combination of strength and toughness [54]. Retarded softening occurs during tempering of a simple, low-carbon 12% Cr steel at temperatures up to about 500°C, while

pronounced softening occurs at 500°C to 550°C as shown in Figure 2.3 [54]. The rate of softening decreases progressively above 550°C. During tempering the dislocations recovery occurs reducing the overall density, and the laths become elongated sub-grains with small-angle lath boundaries. Meanwhile, undersized carbon atoms are pulled from the matrix to coarsen carbide and carbonitride precipitates, thus reducing the lattice strain. The result is that a good combination of strength, ductility and toughness of the HT9 steel can be obtained [51,60] with a proper selection of normalization and tempering heat-treatment conditions.

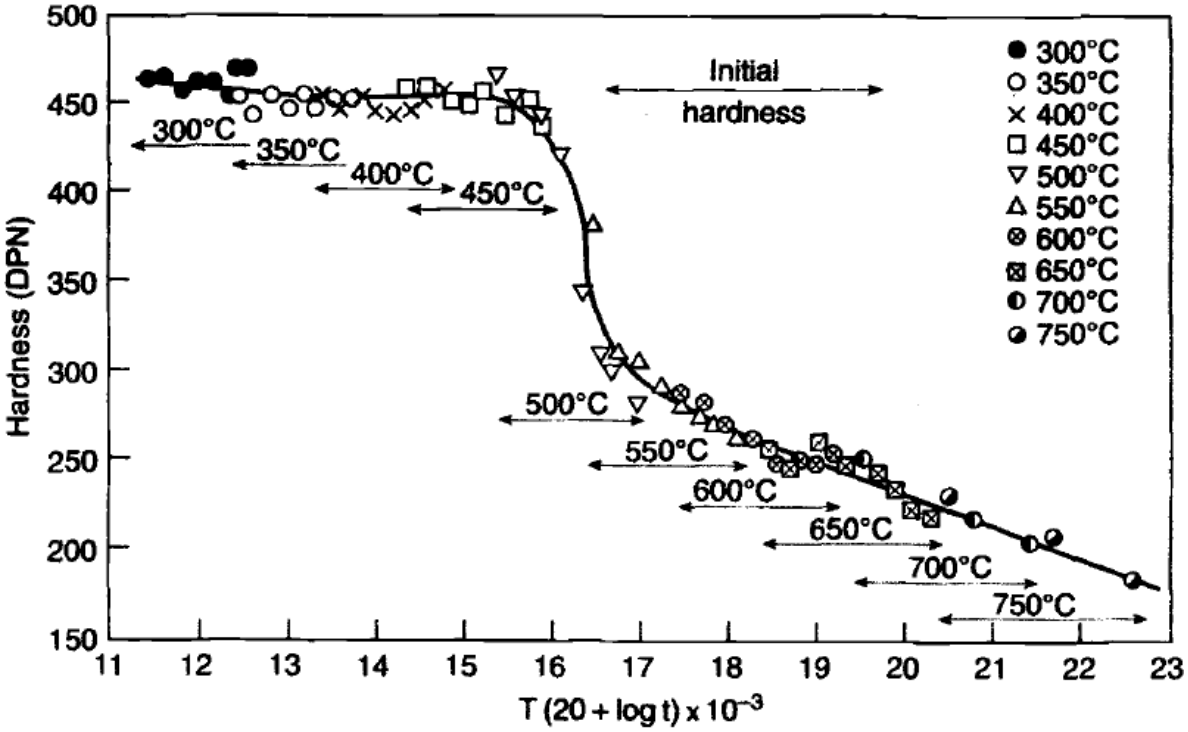

Figure 2.3. Tempering characteristics of a 12Cr-0.14C steel, from [54].

The hardness changes at different tempering temperatures can be correlated with the microstructural changes as follows [54]:

< 350°C – Fine dispersion of M_3C (Fe_3C) precipitates forms and grows to a dendritic morphology.

450-500°C – Fine needles of M_2X nucleate on the dislocations within the martensitic laths, retarding softening.

500-550°C – M_7C_3 and M_2X phases coarsen with a rapid decrease in hardness.

> *550°C* – M_7C_3 and M_2X are replaced by Cr-rich $M_{23}C_6$ precipitates on martensite lath and PAG boundaries.

> *650°C* – $M_{23}C_6$ precipitates grow, reducing dislocation density and forming sub-grains.

> *750°C* – Sub-cells grow into equiaxed sub-grains and M23C6 continues to grow.

It follows that over-aging during tempering of these steels is associated with the removal of M_2X from within the martensite laths and the growth of the grain boundary $M_{23}C_6$, these processes allow the dislocations to form polygonal networks. Typical line dislocation densities are on the order of 10^{14}-10^{15} m^{-2}. A schematic of the typical microstructure is presented in Figure 2.4 [3]. Further coarsening results in the sub-boundaries becoming unpinned and growth of equiaxed areas of ferrite occurs with the boundaries being composed of well-defined dislocation arrays. This has been referred to as recrystallization during tempering, but it is really only a form of sub-grain growth [54].

The addition of W, V, Mo and C promotes the precipitation of carbides and carbonitrides leading to secondary-phase strengthening [51–53]. Upon normalization the primary precipitate microstructure is the coarse (60-150 nm) $M_{23}C_6$ carbides formed on the PAGBs, whereas during tempering the primary precipitate microstructure is the much finer (20-80nm) MX precipitates (V- and Nb-rich) [51,61,62] on the lath boundaries and within the laths. The $M_{23}C_6$ carbides stabilize the PAGBs during normalization, while the MX precipitates serves to stabilize laths and pin mobile dislocations. These precipitates are important for improving both the creep resistance and the

radiation resistance, due to the precipitate-matrix interfaces that serve as point defect absorption sites [51].

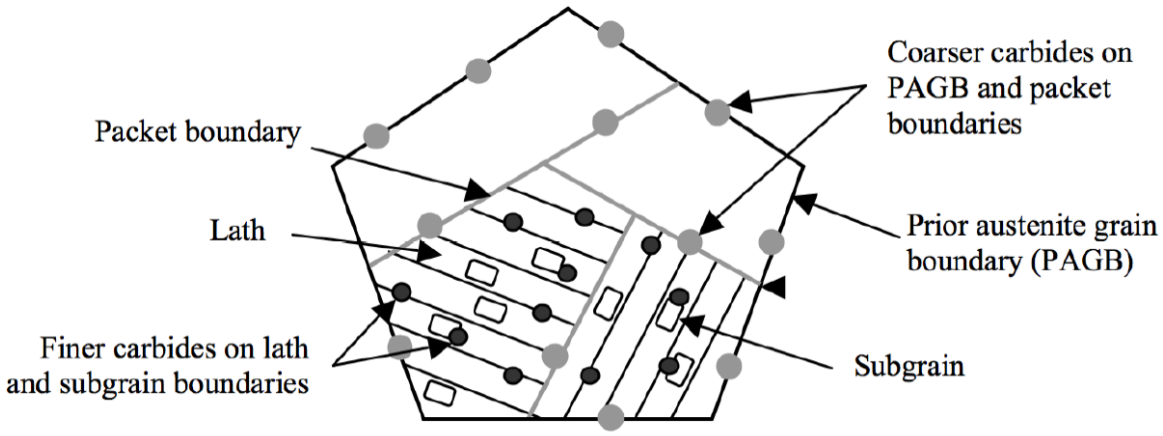

Figure 2.4. Typical F-M microstructure following tempering, from [3].

In summary, the microstructures of the high-chromium FM steels in the normalized-and-tempered condition are generally similar, as illustrated in Figure 2.5 [63]. They consist of: (a) martensite laths about 1 μm wide and > 5 μm long, containing dislocations with a Burgers vector $a/2\langle 111\rangle$ and a density of approximately $1\times10^{14}/m^2$ [54], and (b) coarse $M_{23}C_6$ particles located at prior austenite and δ-ferrite grain boundaries with finer precipitates within the laths and at the martensite lath and sub-grain boundaries; M_2X precipitates rich in chromium and isomorphous with $(CrMoWV)_2(CN)$ within the martensite laths and δ-ferrite phase; primary (Nb,Ta)X; and fine secondary (V,Nb,Ta)X [54]. Laths within a single packet usually have rather closely aligned crystal orientations with a few to less than 15 degrees of deviations.

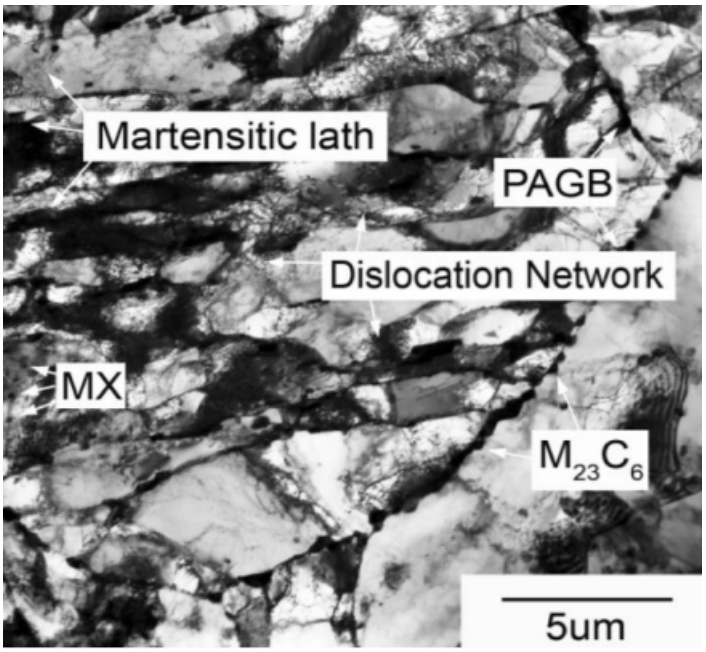

Figure 2.5. An example of a typical tempered martensite structure of a P92 steel, from [63].

2.1.2 Weld Processing

The use of a high-chromium martensitic steel for first wall and blanket structural component applications in a fusion reactor will require joining by welding or brazing. It is also envisaged that the construction and heat treatment of such large and complex structures cannot be carried out entirely in the fabrication shop and that some field fabrication will be necessary [54]. High-chromium martensitic steels are generally regarded as being more difficult to weld than, for example, austenitic steels, because it is often necessary to pre-heat before welding to avoid cracking, and it is essential to carry out a post-weld heat-treatment to temper the brittle martensitic structures formed in the fusion zone (FZ) and heat affected zones (HAZ) [54].

The microstructures of the FZ and HAZ in weldments of all metallic alloys are usually complex, but they are further complicated in air-harden-able steels of the type considered here due to the phase transformations that occur during the heating and cooling cycles of the fusion welding

process [64]. The various zones in a high-chromium FM steel fusion-welded joint are shown schematically in Figure 2.6; the microstructures of these respective zones in "as-welded" 0.1-0.2% C steels can be interpreted based on the temperatures (defined in Figure 2.6) achieved during welding and consideration of the phase fields in the equilibrium diagram for high-chromium alloys with low and high net Cr-equivalents (Figure 2.7) [54] as follows:

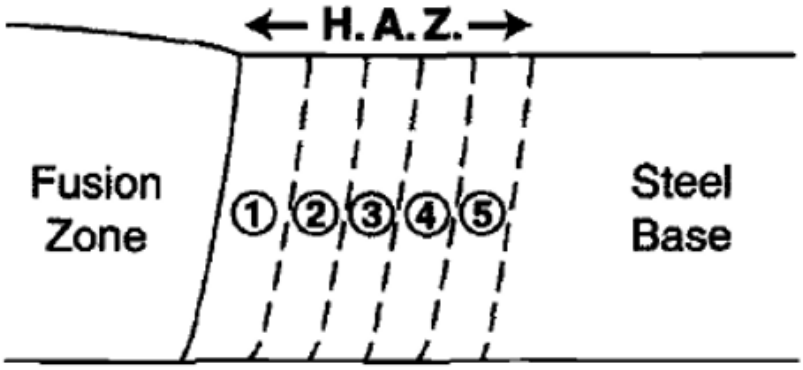

Fusion Zone (FZ): $T > T_m$

Heat-Affected-Zone (HAZ) [as-welded]:

Region 1:	$T_m > T > T_{\gamma\delta}$	$\gamma + \delta \rightarrow$ Martensite + δ
Region 2:	$T_{\gamma\delta} > T > A_{c3}$	Coarse grained $\gamma \rightarrow$ Martensite
Region 3:	$T_{\gamma\delta} > T > A_{c3}$	Fine grained $\gamma \rightarrow$ Martensite
Region 4:	$A_{c3} > T > A_{c1}$	$\gamma \rightarrow$ Martensite + Over-tempered Martensite
Region 5:	$A_{c1} > T > T_T$	Over-tempered Martensite

where T = temperature achieved during welding
T_m = melting point of steel
$T_{\gamma\delta}$ = temperature at which $\gamma \rightarrow \delta$ transformation is complete on heating
T_T = original tempering temperature of steel
A_{c1} = temperature at which $\alpha \rightarrow \gamma$ transformation starts on heating
A_{c3} = temperature at which $\alpha \rightarrow \gamma$ transformation is complete on heating

Figure 2.6. Schematic diagram of the heat-affected zone regions in a fusion weld of high-chromium FM steel.

FZ ($T > T_m$) – The first phase to form during solidification of the molten weld is δ-ferrite; the ferrite-to-austenite transformation occurs on further cooling, and the austenite transforms to martensite on cooling below the M_s temperature. Some δ-ferrite is usually retained in the FZ at ambient temperature, even when there is no ferrite present in the base and filler wire materials, as complete

transformation to austenite does not occur during cooling at the fast rates typical of the welding process [65,66]. Since the δ-ferrite can have detrimental effects on the mechanical properties, particularly strength and fracture toughness, of the high-chromium FM steels [67] and welds, the content should be controlled at <3% by balancing the concentrations of the austenite- and ferrite-forming elements in the base steels and filler wires. As noted previously, the formation of δ-ferrite can be inhibited in the high-chromium steels by maintaining the Cr-equivalent below approximately 9%; however, experimental data suggest the net Cr-equivalent concentration has to be reduced to <7.3 to avoid the presence of δ-ferrite in the FZ of autogenous TIG welds of the MANET-type steel made with a heat input of 1.1 MJ/m [67].

HAZ – Region 1 ($T_m > T > T_{\gamma\delta}$) – This region (see Figure 2.6) consists of martensite and δ-ferrite. The ferrite is formed along the PAGB as the region is heated into the two-phase (γ+δ) field during welding; some of the δ-ferrite is again retained at ambient temperature in a band typically 0.3 to 0.5 mm wide adjacent to the fusion line as a result of the rapid cooling after welding [65]. The δ-ferrite content and width of this region expands with increasing weld heat input and cooling rate; low heat input welding processes such as narrow gap, electron beam, and laser are consequently advantageous in minimizing the extent of the ferrite formation in this part of the HAZ.

HAZ – Region 2 ($T_{\gamma\delta} > T > A_{c3}$) – The microstructure is fully martensitic. This region is heated into the higher temperature part of the γ-phase field during welding, and the original carbide particles are dissolved, resulting in coarse prior austenite grain and martensite lath structures.

HAZ – Region 3 ($T_{\gamma\delta} > T > A_{c3}$) – The structure of this region, which is heated into the lower temperature part of the γ-phase field, is again martensitic, but it is finer grained than Region 2, as some of the original carbides are not dissolved and inhibit grain growth.

HAZ – Region 4 ($A_{c3} > T > A_{c1}$) – The structure consists of untampered and over-tempered martensite. Incomplete transformation to austenite and additional tempering of the original tempered martensite structure of the base steel occur during heating in this intercritical zone, with the austenite again transforming to martensite on cooling.

HAZ – Region 5 ($A_{c1} > T > T_T$) – The original tempered martensite in this narrow zone is further tempered during welding, but the microstructure is otherwise similar to that of the base steel.

A typical microstructure of a 9Cr-IMoVNb steel weld is illustrated in Figure 2.8 [68]. Four regions are delineated – the weld metal corresponds to the FZ of Figure 2.6, the transformed zone corresponds to Regions 1, 2, 3, and 4, the tempered zone corresponds to Region 5, and the base metal (BM) is the steel base which was unaffected during the welding process. Thin foil transmission and extraction replica electron microscopy of a welded and post-weld heat-treated 12Cr-IMoV steel [69] has shown larger sub-grains, lower dislocation densities, and larger and more spherical undissolved carbide particles in the intercritical Region 4 than in the base steel, indicating lower strength of the former. The carbide structure in the coarse-grained transformed Region 2 was similar to that in the original base steel, the carbides having been dissolved during welding and reprecipitated during PWHT. There were fairly large carbide particles on the PAGB,

and smaller carbides precipitated on the sub-grain boundaries within the relatively fine prior austenite grains in Region 3.

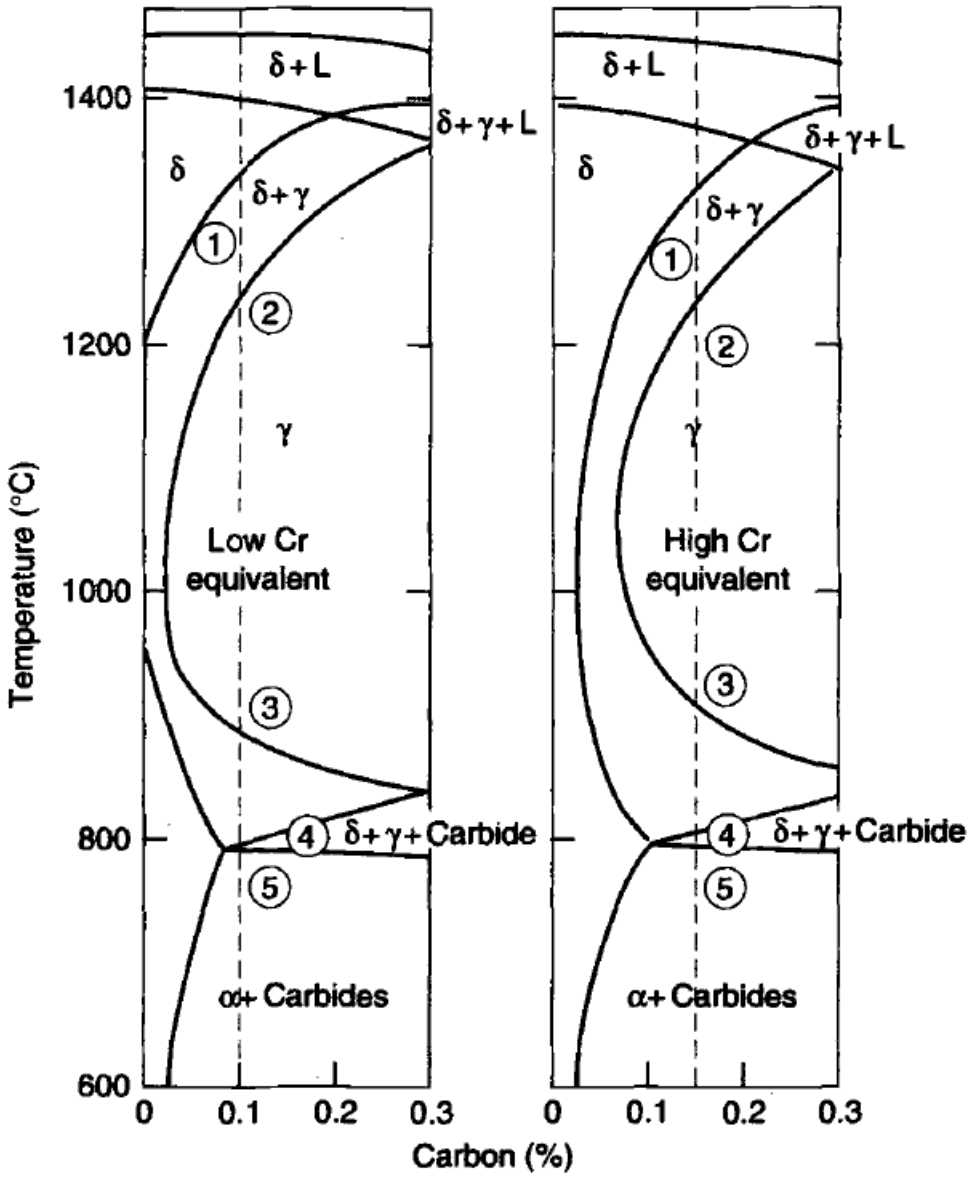

Figure 2.7. Phase diagram for high-chromium steels illustrating the effect of net Cr-equivalent and the relationship with the HAZ regions observed in fusion welds of 0.1% C low Cr-equivalent and 0.15% C high Cr-equivalent FM steels [54].

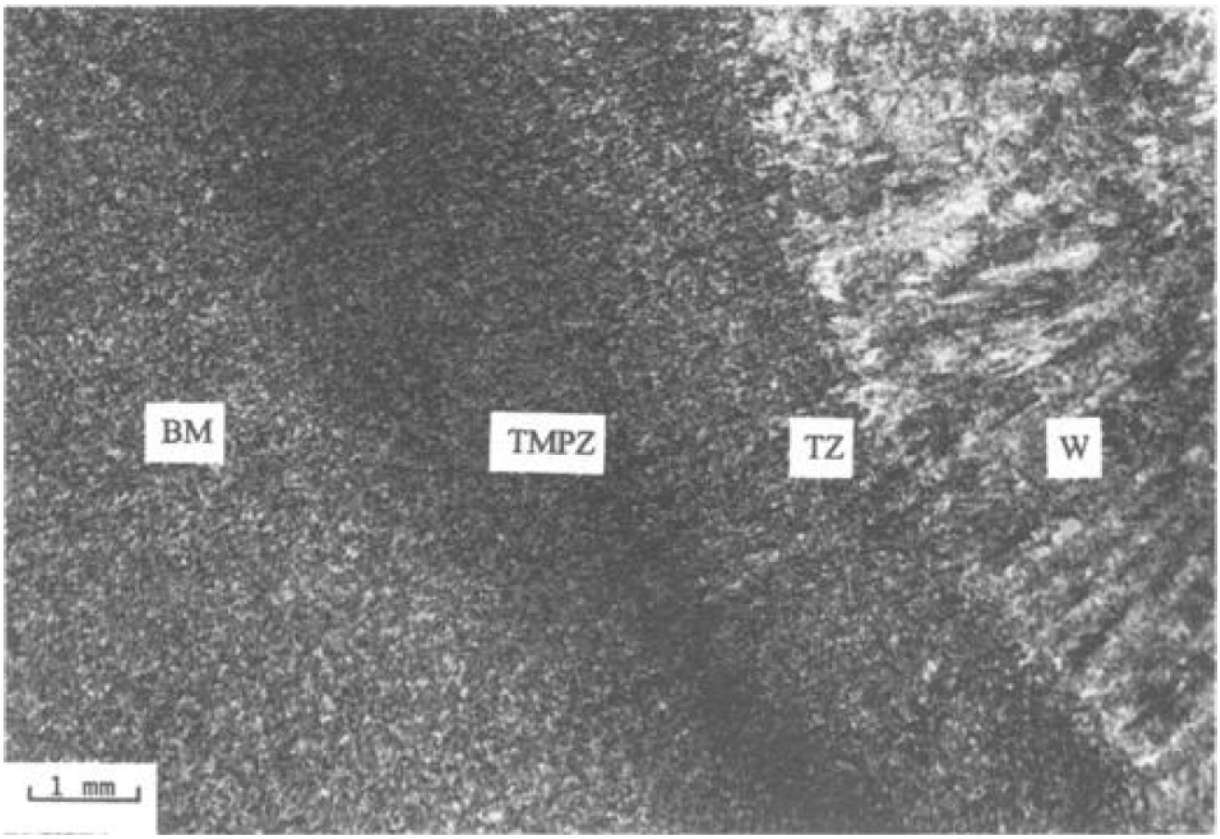

Figure 2.8. Typical microstructure of a modified 9Cr-lMo steel weld illustrating the weld and two regions of the HAZ [transformed zone (TZ) and tempered zone (TMPZ)] [68].

2.1.3 Laser-Blown Powder DED AM Material Processing

A typical DED machine consists of a nozzle mounted on a multi-axis appendage, which enables the deposition of melted material onto the specified surface. The process is similar to material extrusion or multi-pass welding, but the nozzle can move in multiple directions and is not fixed to a specific axis. The material, which can be deposited from any angle, is melted upon deposition with a laser, electron beam, or plasma arc [55,70,71]. The material feedstock is either metal wire, powder, or metal wire cored wire with powder, as shown in the schematics in Figure 2.9 [55].

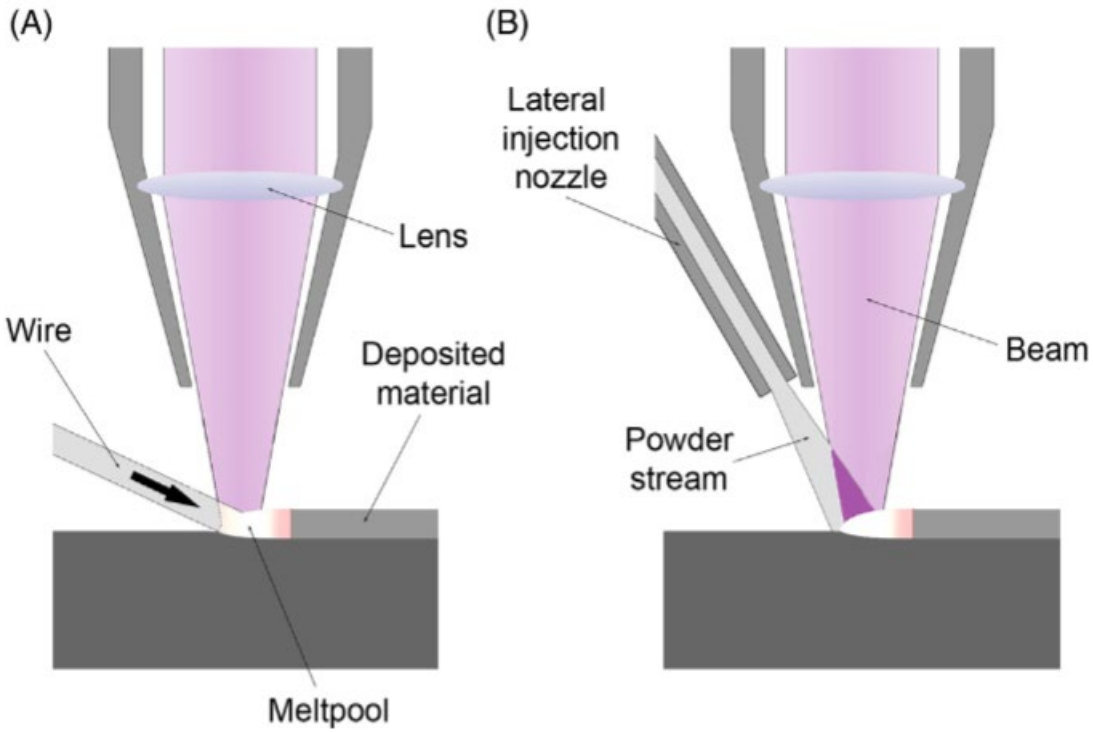

Figure 2.9. In DED, a metal feedstock is introduced to an energy source in the form of a wire (A) or as a powder (B), from [55].

In the case of using powder as material feedstock, the powder is delivered co-axially with the laser during fabrication. The nozzle is able to traverse three dimensions in the simplest configuration, resulting in layer-by-layer construction of a 3-dimensional component. The technique leads to repeated thermal cycling during fabrication, resulting in the possible formation of heterogeneous microstructures and a microchemistry leading to gradients in mechanical properties across or along the fabricated component. The complexity of the phase transformations that occur during the repeated reheating of deposited layers makes the microstructural evolution of FM steels significantly more complex compared with other alloy systems such as nickel-based alloys [49].

To a degree, most fusion-based AM processes are analogous to previously studied welding techniques, such as multi-pass laser-beam or electron-beam welding, among others. The results

show a synergy existing between the microstructures developed under welding and those observed during the AM process, which can be used to understand and exploit the process to form viable components using FM steels. As mentioned before, in typical welding processes for FM steels, the first primary phase to form during solidification is the δ-ferrite phase, which then can transform to austenite upon further cooling. For both welding and DED AM processing of FM steels, however, incomplete phase transformations can be detrimental to materials properties. For example, FM steels may contain some residual δ-ferrite in the microstructure after thermo-mechanical treatment because the transformation from δ-ferrite to austenite does not occur completely; the incomplete transformation is primarily due to the rapid cooling rates that the process involves [49,54,72].

Niyanth et al. [49] evaluated the feasibility of using AM to fabricate HT9 via the DED AM technique, coupled with post-built heat-treatments. The room-temperature and high-temperature mechanical property evaluation showed promising results compared to those of wrought HT9 alloy, warranting further scale-up studies. The characterization showed that the as-built microstructure consisted of a martensitic matrix with δ-ferrite present in the reheat zones between each pass during the sample fabrication process. The martensitic matrix consisted of an ultrafine dispersion of carbides and carbonitrides. In addition, between the two, the post-built heat-treatment with a higher austenitizing temperature and a lower tempering temperature resulted in a fine dispersion of the carbide structure and a fine-grained lath martensite, indicating the variability brought by heat-treatments. Low-temperature austenization, while it resulted in a finer prior austenite grain size, resulted in a significant coarsening of the carbide phases and the lath substructure, leading to the formation of an equiaxed ferrite structure.

2.2 Radiation Damage in Wrought FM Steels

Radiation damage can occur in FM steels induced by the bombardment of energetic particles including neutron, ion, and electron. The typical radiation damage process has been described in brief in Chapter 1, where point defects generated from the damage cascade event form the basis of radiation-induced microstructural changes. Some unique phenomena occur in irradiated wrought FM steels and will be discussed in this Section.

2.2.1 Cavity Swelling

The high swelling resistance of FM steels is the main reason for its application for high damage level applications, such as core materials for fast reactors. Therefore, extensive studies have been conducted on cavity evolution in FM steels. In radiation damage process, surviving irradiation-induced Frenkel pairs from recombination can get absorbed by various defect sinks. However, some types of defect sinks such as line dislocations and dislocation loops preferentially absorb interstitials over vacancies, which could result in higher concentration of vacancies in the matrix. With the thermo-vacancies that are accommodated within the matrix, excessive and over-saturated vacancies can agglomerate to form small clusters. The gas atoms in the material, such as He that forms from (n, α) transmutation reaction, are known to stabilize the small vacancy clusters and the nucleation of cavities.

The cavity swelling behaviors under irradiation as a function of damage levels are typically classified with three regimes: an incubation regime, a transient regime, and a linear steady-state swelling regime [3]. In the incubation regime, the swelling is very low with most cavities nucleated without significant coarsening. In the linear steady-state swelling regime, the swelling increases proportionally with the additional increase of damage levels on top of the damage level threshold of the incubation period. During the steady-state swelling regime, significant coarsening of cavities

occur that lead to the rapid increase of volumetric swelling. The cavity swelling is strongly affected by the size of cavities, as shown in Equation 2.1 below:

$$Swelling = \frac{\Delta V}{V_i} = \frac{\frac{\pi}{6}\sum d_{cav}^3}{V_i} \qquad \text{Equation 2.1}$$

where ΔV is the total material volume change due to the formation of cavities in the microstructure after irradiation, and V_i is the initial total material volume. The total material volume change is calculated further by summing the volume of each spherically-shaped cavity, with d_{cav} being the diameter of each cavity. As can be seen, the swelling has a cubic relationship against the cavity size. Therefore the coarsening of cavities strongly promote cavity swelling.

Between these incubation and steady-state swelling regimes is a transient period. As can be seen in Figure 2.10, several FM steels including HT9, T91 and T92 show the clear three-regime swelling behaviors as a function of damage level [9], with different incubation periods, and steady-state swelling rates. For the selected irradiation conditions with 10 He appm pre-implantation at 460°C in W-HT9, the incubation period is at about up to 75 dpa, with the steady-state swelling regime starting from about 130 dpa. The difference in the boundary conditions of three regimes in the three FM steels could be attributed to different compositions and sink strengths.

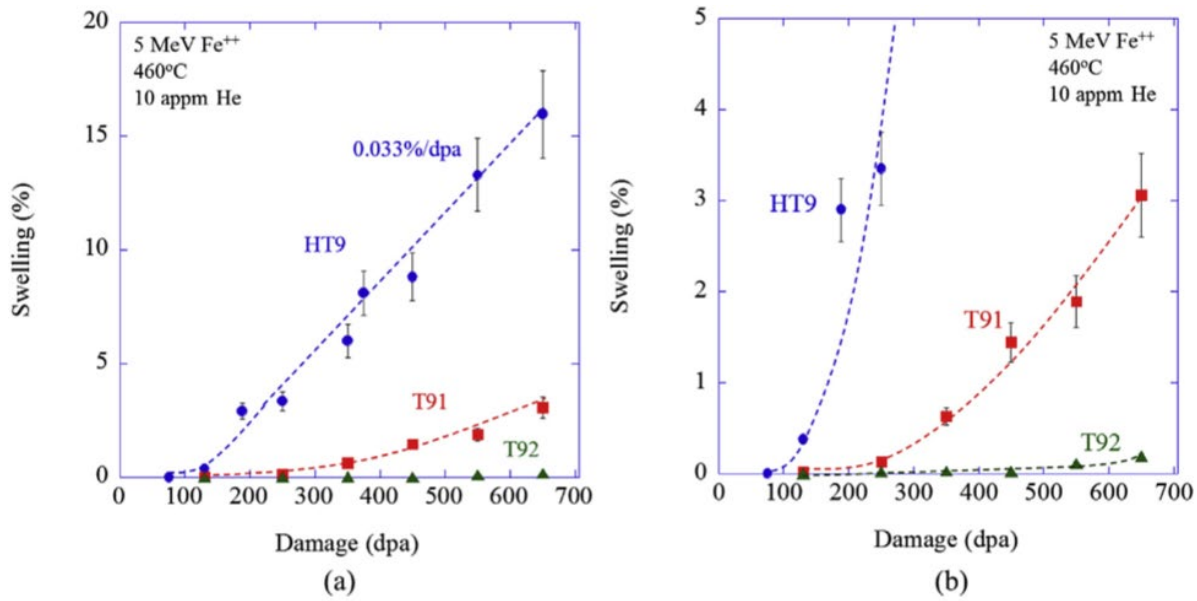

Figure 2.10. (a) Void swelling evolution in 5 MeV Fe^{2+}-irradiated HT9, T91 and T92 that are pre-implanted with 10 He appm and irradiated at 460°C, and (b) a more detailed view of the low swelling regime. From [9].

Besides damage levels, irradiation temperatures also strongly affect the cavity swelling behavior of FM steels. The vacancy super-saturation results in the precipitation of cavities, and the thermal equilibrium vacancy concentration is greatly affected by temperature. Theory has shown that the swelling behavior follows a bell-shaped relationship with temperature [73], based on the melting temperature, T_m, of the material [3,74]. Swelling reaches maximum within the irradiation temperature range between $0.3T_m$ to $0.5T_m$, and is called the peak swelling temperature. As the irradiation temperature deviates from the peak swelling temperature, the swelling goes down. At temperatures lower than the peak swelling temperature, vacancy mobility is too low to form cavity embryos so that cavity nucleation cannot occur. At higher temperatures than the peak swelling temperature, cavities are not stable and begin to emit thermal vacancies. The higher solubility of vacancies in the matrix provides the driving force to break down cavities or vacancy clusters.

Dvoriashin and colleagues [75] studied a ferritic-martensitic steel EP-450 after irradiation in a fast reactor. Swelling was studied as a function of temperature in the range of 275ºC - 690ºC.

A peak swelling rate is observed around 420ºC. Considering the lower damage data points at 11 dpa have a larger swelling rate than those at either 46 dpa or 89 dpa, it is likely that these swelling rates are representative are more representative of a nucleation rate rather than a growth rate, and therefore demonstrating that nucleation follows a similar bell-curve.

Ayrault [76] studied the effect of irradiation temperatures above 450°C on a 9Cr-1Mo steel. No swelling peak was found, but the highest swelling occurred at 450ºC. This may suggest that the tail-end of a temperature peak was caught in this study and the peak would appear somewhere close to 450ºC.

Hide et al. [77] studied the response to irradiation of six different ferritic alloys with 200keV C+ and 3 MeV Ni+: MA957 (an ODS alloy), HT9, Fe-12Cr, 12Cr-2Mo, 9Cr-8Mo-4Ni (solution anneal), 9Cr-8Mo-4Ni (aged). These metals were studied at damage levels ranging from 50 – 200 dpa and temperatures from 425-625°C. All of the samples were pre-injected with helium to a fixed ratio of 0.1 appm/dpa. All alloys exhibited peak swelling at 575°C. Although this value is higher than the previously suggested values between 400-500°C, the higher damage rate is expected to shift the swelling bell-curve to higher temperatures [78,79].

Kai and Kulcinski [80] studied HT9 irradiated with nickel ions at three different temperatures: 400ºC, 500ºC, and 600ºC. Cavities were only observed at 500ºC.

Schmidt et al. [81] observed a peak swelling temperature of 500ºC in HT9 and 550ºC in EM-12 after irradiation with 2.8 MeV Fe+ ions up to 250 dpa [60]. The dependence of swelling as a function of temperature is shown in Figure 2.8 [60].

Sencer et al. [33] irradiated HT9 in FFTF and found a peak swelling temperature at about 443ºC. However, it must be noted that the damage level was also highest at this temperature (155 dpa compared to 28 dpa at 384ºC), which may cloud the effect of temperature.

Wakai et al. [82] showed highest swelling at 470ºC, which then decreased with increasing temperature. Ferritic-martensitic steel F82H was irradiated with a triple beam system (Fe+, He+, and H+) at temperatures from 470ºC to 600ºC. It is likely that a peak swelling temperature is present at a temperature lower than that studied in this paper.

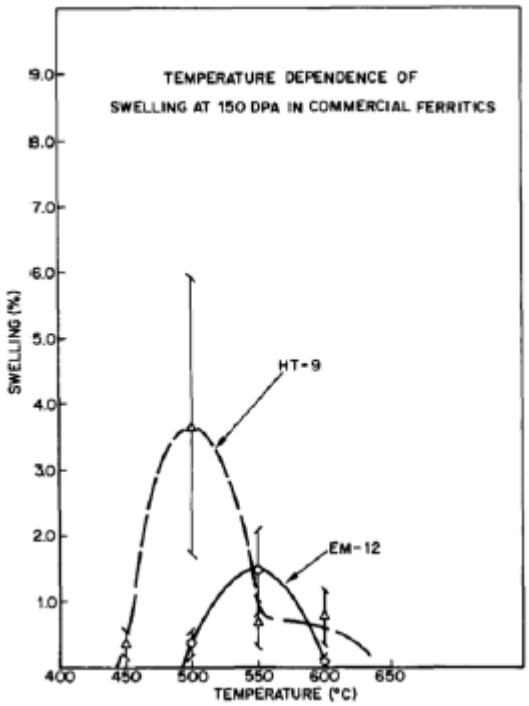

Figure 2.11. Temperature dependence of swelling at 150 dpa for EM-12 and HT9, with a clear bell-shaped swelling behavior near the peak swelling temperature observed. From [81].

Getto et al. [83] studied swelling in HT9 at temperatures ranging from 400°C to 480ºC after irradiation up to 375 dpa using Fe^{2+} ions and 10 or 100 appm helium pre-implanted. The peak swelling temperature was determined to be near 460ºC. At lower and higher temperatures 480ºC and 440ºC, it was determined that the onset of swelling was delayed relative to experiments performed at 460ºC. The swelling behavior as a function of temperature at 188 dpa is shown in Figure 2.12. This set of experiments suggested that cavity nucleation was enhanced closer to the peak swelling temperature [60].

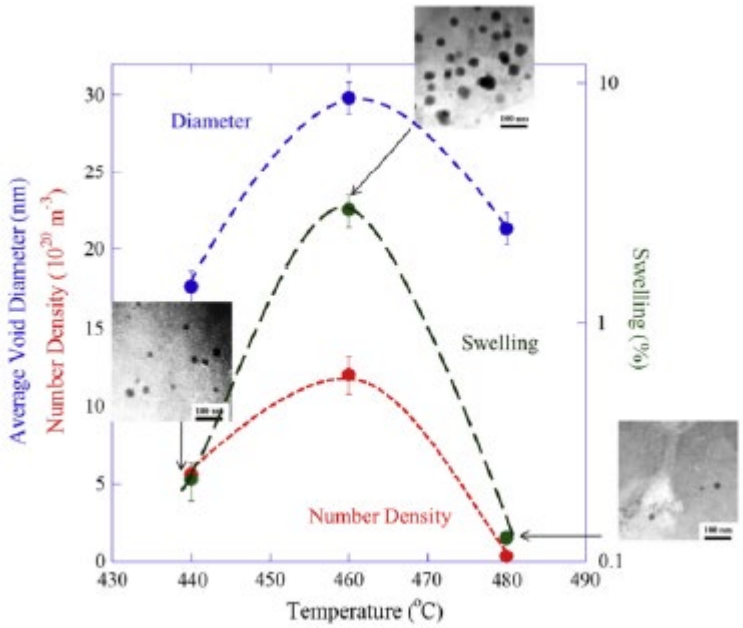

Figure 2.12. Temperature dependence of swelling, diameter, and number density at 188 dpa for HT9. From [83].

Cavities formed under irradiation are known to act as neutral defect sinks [84], having no preference for absorbing interstitials and vacancies [85]. Some recent simulation efforts [86,87], however, indicate that when cavities are small in size, they are potentially biased towards absorbing interstitials. Here, the vacancies are treated as neutral defect sinks due to the existing rate-theory models that were comprehensively established. Either way, the formation of cavities affects the swelling evolution with progressively higher damage levels under irradiation.

In addition, the co-injection rate of He in dual-ion irradiation experiments also affects the swelling behavior as a function of damage levels. Woodley [11,59] conducted a systematic study of the effects of helium co-injection rate and damage levels on the cavity evolution in terms of the diameter, density and swelling, as illustrated in Figure 2.13. It was shown that the helium-to-dpa ratio at which the maximum swelling occurs shifts to lower helium-to-dpa levels as the damage level increases in FM steels. In addition, the helium stabilized bubbles increase the cavity sink

strength of the microstructure and reduce the growth rate of voids, with this trend holding true for multiple heats and alloys of FM steels.

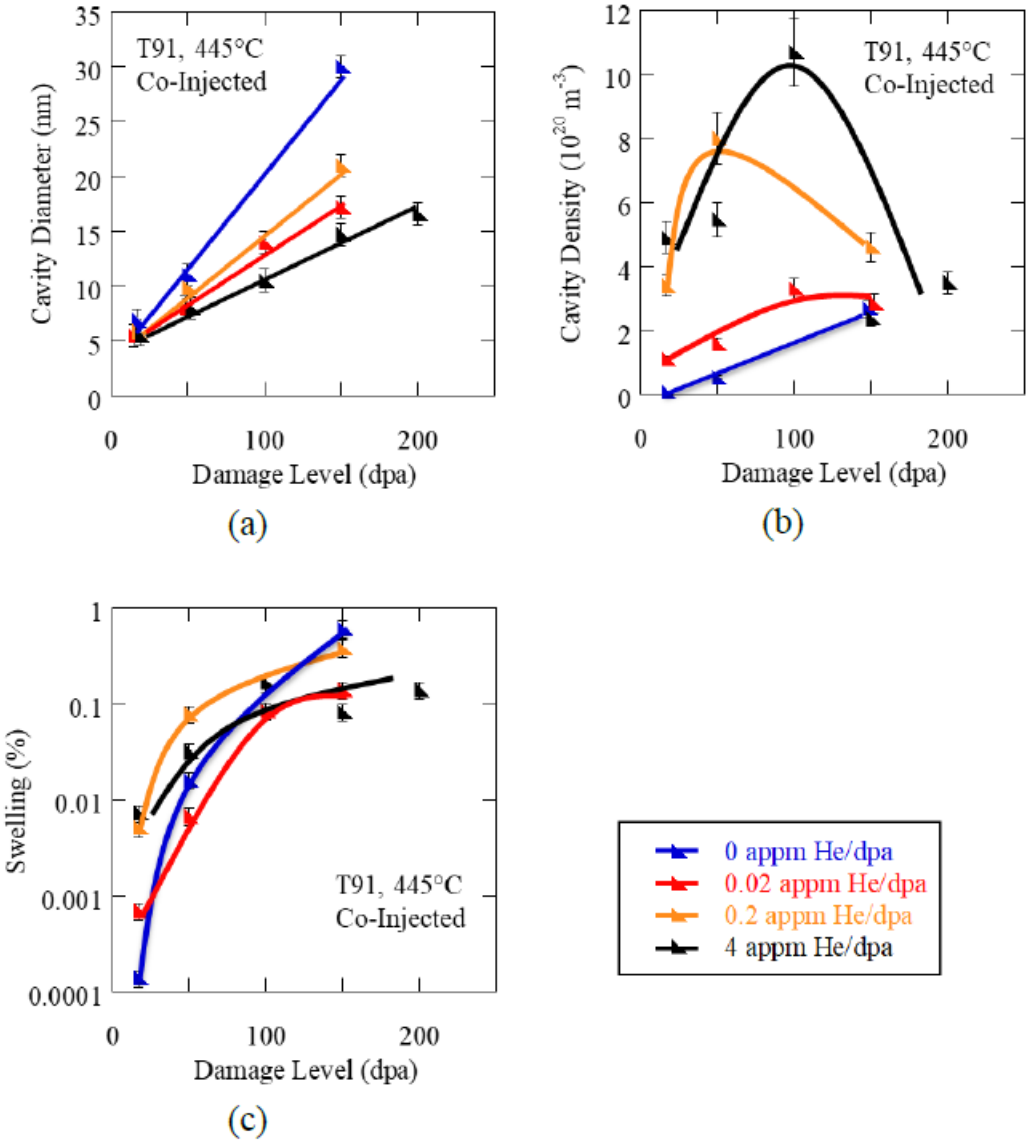

Figure 2.13. (a) Cavity diameter, (b) cavity density and (c) swelling in T91 as a function of damage level with 0 He appm/dpa (blue), 0.02 He appm/dpa (red), 0.2 He appm/dpa (orange) and 4 He appm/dpa (black) helium co-injection rate at 445°C with 7-8×10^{-4} dpa/s.

2.2.2 Dislocation Loops and Line Dislocations

The formation of dislocation loops originates from the point defect clusters of either interstitials or vacancies. These clusters form 2-dimentional configurations, preferentially aligned on certain crystallographic planes, called habit planes, in different material systems. In irradiated FM steels that are body-center-cubic (BCC) Fe-based, two types of dislocation loops are extensively observed: $a\langle 100\rangle\{100\}$ and $a/2\langle 111\rangle\{111\}$, where a is the lattice parameter, $\{100\}$ and $\{111\}$ are habit planes, and $a\langle 100\rangle$ and $a/2\langle 111\rangle$ are Burgers vectors of the two types of dislocation loops, respectively. These two types of dislocation loops in FM steels have different characteristics in many ways. First, $a\langle 100\rangle$ loops are considered sessile, whereas $a/2\langle 111\rangle$ loops are highly mobile [86] due to its Burgers vector along $\langle 111\rangle$, which is the close-pack direction within BCC materials. For this reason, $a\langle 100\rangle$ loops are considered to contribute more to irradiation hardening compared to mobile $a/2\langle 111\rangle$ loops [74]. Second, $a\langle 100\rangle$ loops are very stable at high irradiation temperatures, compared to $a/2\langle 111\rangle$ loops that can easily interact with each other or with line dislocations to form entangled dislocation networks. The formation mechanism and high-temperature stability of the $a\langle 100\rangle$ loops in irradiated BCC Fe-based materials have long been a puzzle in nuclear materials field, as computer simulation efforts tend to predict that $a/2\langle 111\rangle$ loops have a lower formation energy thus favorable configuration in theory [88], though there are other theories such as a direct punch-out from displacement cascade mechanism [89] that try to explain the formation of $a\langle 100\rangle$ loops.

The extensive nucleation of these dislocation loops occurs usually with low damage levels of well below 20 dpa. At higher damage levels, dislocation loops usually coarsen by absorbing more point defects or by interacting with each other or with line dislocations to open up and form entangled dislocation networks. Gliding line dislocations provide the plasticity and ductility for

FM steels, while they become undesirable when the density becomes too high such that strain hardening occurs to make materials hardened, brittle, and susceptible to fracture or failure. The annealing effect of high temperature can significantly decrease the line dislocation density with or without irradiation.

J.J. Kai et al. [90] conducted neutron irradiation in the Materials Open Test Assembly (MOTA) of the Fast Flux Test Facility (FFTF) at 420°C up to 35 dpa. The size of dislocation loops observed is about 100 nm and the loop density was about $5 \times 10^{20}/m^3$.

In another fast neutron irradiation study carried out at Phenix fast breeder reactor, Dubuisson et al. [91] observed a high density of dislocation loops in a group of high-Cr FM steels, including HT9, irradiated to ~100 dpa. Although no quantitative measurements were reported in the study, it was found that the dislocation structure became unstable above 500°C in FM steels and the dislocation density reduced rapidly with increasing irradiation temperature.

Sencer et al. [92] examined the HT9 fuel assembly duct material irradiated in FFTF at 443°C to 155 dpa. They found the network dislocation density was about $3 \times 10^{15}/m^2$. The majority of network dislocations were $a/2\langle 111\rangle$ type, and $a\langle 100\rangle$ type were about 1/4 of the total population. The density of dislocation loops (predominant $a\langle 100\rangle$ type) was $3 \times 10^{20}/m^3$ and the mean size was about 18 nm.

Zheng et al. conducted in-situ experiments and showed that in FM steels T91 [93] and HT9 [94] under irradiation with 1 MeV Kr^{2+}, both $a\langle 100\rangle$ loops and $a/2\langle 111\rangle$ loops nucleate with higher densities at low damage levels of less than 4 dpa, whereas they interact with line dislocations to form dislocation networks at higher damage levels. $a/2\langle 111\rangle$ loops are more affected by the interaction with line dislocations as compared to $a\langle 100\rangle$ loops, resulting in a decrease of dislocation loop density.

Line dislocations and dislocation loops have significant effects on microstructural evolution in irradiated FM steels. It is in generally considered that these features acting as defect sinks have slight bias toward absorbing interstitials over vacancies. Therefore, their existence could result in the over-saturation of vacancies in the matrix, which leads to the precipitation of cavities and subsequent swelling. In addition, dislocation cores are known to provide heterogeneous nucleation sites for precipitates, such as Ni/Si/Mn-rich clusters in FM steels, and Cu-rich clusters in RPV steels.

2.2.3 Precipitates and Segregation

Another important factor that affects microstructural evolution in FM steels is irradiation-induced precipitates and segregation. The most common irradiation-induced secondary phases include Cr-rich α', Fe/Mo-rich M_6X laves-phase (η), Fe/Si/Ni/Mo/P-rich χ-phase, Ni/Si/Mn-rich G-phase, and P-rich sigma-phase (σ) [54]. The precipitate-matrix interfaces provide defect sinks to annihilate point defects generated from irradiation. Evolution in the density and morphology of these precipitates can also contribute significantly to irradiation hardening by impeding motions of line dislocations.

Spencer et al. [17] and Anderoglu et al. [34] examined an HT9 duct after long-term exposure at FFTF up to 155 dpa between 380°C and 460°C. A high density of α' and Ni/Si/Mn-rich precipitates were observed. The precipitation was more sensitive to the irradiation temperature than neutron dose.

Radiation induced precipitation was also reported in an irradiation conducted at the Experimental Breeder Reactor II (EBR-II) [95] and some ion irradiation studies [80]. Klueh and Harries [54] reviewed a large amount of work on precipitates in various high-Cr FM steels. Table 2.1 summarizes the information concerning HT9 [38].

Table 2.1. Major Radiation-induced Precipitation in HT9 (after [54]*). From* [38]

Irradiation Facility	Precipitate	Temperature (°C)	Damage Level (dpa)	Reference
FFTF	α', χ	420	35	[90]
	η	407	47	[96]
	α', G	380−440	20−155	[92,97]
Phenix	α'	400−530	30−116	[91]
	η	419	79	[91]
EBR-II	α', χ, G	400, 425	25−60	[95]
HFIR	α', η	400	7.4	[98]
	G	300, 400, 500	10−12, 38	[95,96]
14 MeV Ni	α', χ	300−600	200	[80]

Zheng et al. [18] examined the self-ion irradiated HT9 steel to 1 and 10 dpa at 470°C and to 20 dpa at 420°C, 440°C and 470°C using ChemiSTEM and APT techniques. Radiation-induced Ni and Si segregation to defect sinks (grain boundaries, dislocation lines and carbide/matrix interface) was observed in all irradiation conditions. The formation of Ni/Si/Mn-rich precipitates were found in all conditions except 1 dpa at 470°C. Some of the Ni/Si/Mn-rich precipitates were found to nucleate heterogeneously at defect sinks.

Jiao et al. [99] showed that segregation of various elements at the grain boundary was detected in HCM12A following both proton irradiation to 7 dpa at 400°C and Fe^{2+} irradiations to 100 dpa at 500°C. Large variations (from depletion to enrichment) in Cr segregation at different grain boundaries were observed. Ni, Si and P were found to enrich at all grain boundaries. Segregation behavior of Cr, Ni and Si at dislocation lines/loops in T91 and HCM12A is consistent with that at the grain boundary. The magnitude of segregation is smaller at dislocation loops than that at dislocation lines.

In addition, the strong interaction between irradiation-induced point defects and solute atoms leads to the net influx or outflux to the defect sinks, such as grain boundaries, dislocation cores, cavity surfaces, and precipitate-matrix interfaces. As a result, certain minor elements enrich

or deplete near the defect sinks. For example, Ni and Si are often reported to enrich near grain boundaries and cavity surfaces, whereas Cr usually depletes [100,101]. The elemental segregation at dislocation loop cores could affect their growth as well [102]. These elemental redistribution and segregation are known to affect corrosion susceptibility in FM steels.

2.2.4 Heat-to-Heat Variability on Swelling

The heat-to-heat variability as well as the variability from different heat-treatments on the same heat of FM steels are well-known for their different cavity swelling behaviors under irradiation. Scattered data in the literature are available [14,33,90,92,103–107] from neutron irradiations at the Fast Flux Test Facility (FFTF) and the High Flux Isotope Reactor (HFIR), and are shown in Figure 2.14 [9]. The overall trend for the swelling rate is about 0.01%/dpa in the steady-state swelling regime. In addition, the maximum swelling observed is less than 3%, which highlights the good swelling resistance of FM steels. Chemical compositions and heat-treatments can significantly vary the starting microstructures and sink strength of these various FM steels, which then results in the different responses to cavity swelling.

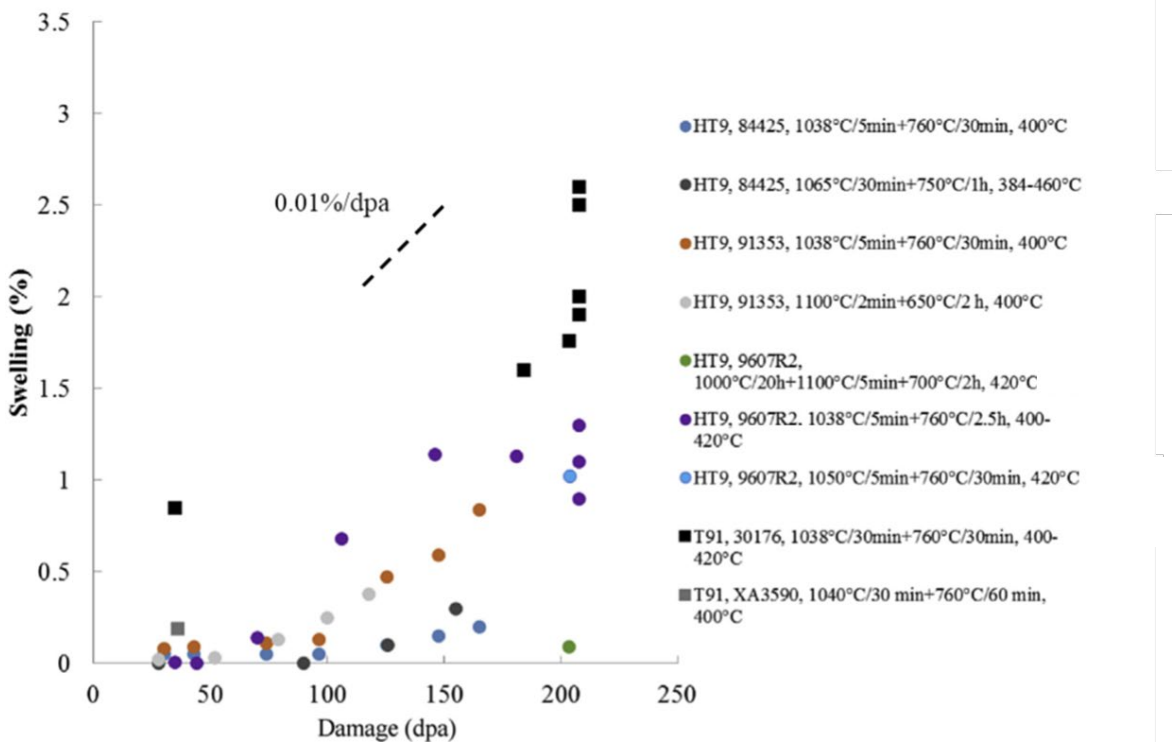

Figure 2.14. Summary of different heats of FM steels HT9 and T91 with varying heat-treatments irradiated in-reactor up to 208 dpa at temperatures varying from 400°C to 443°C, reproduced from [9].

2.2.5 Neutron and Heavy Ion Irradiation of FM Steels

Under neutron irradiation, the amount of helium generation via (n, α) reactions is affected by the neutron energy spectrum of a particular nuclear reactor, as well as the different reaction cross-section for each element and their concentration in the material [60]. Typical helium production has been estimated for fast reactors from 0.1 He appm/dpa to 1.0 He appm/dpa [108,109] but varies strongly with composition [60]. In order to understand the radiation responses of FM steels at an accelerated rate, ion irradiation experiments with significantly higher damage rates have been extensively used to simulate the effects of neutron irradiation damage, especially at high damage levels [60]. Using ion irradiation has the benefits of low cost, higher damage rate, and better experimental condition controls of beam current and temperature, as compared to

neutron irradiation. This Section reviews the heavy ion irradiation studies within literature, with similarity to [60].

The FM steel T91 was studied by Gigax et al. [110] using 3.5 MeV iron ions at 475°C up to 550 dpa at the region examined. The swelling response indicated low swelling (< 3%) up to 410 dpa but a sudden increase to 22% swelling at 550 dpa for a rate of 0.11%/dpa. Maximum swelling occurred at approximately half of the projected ion range, supposedly due to the defect imbalance effect [111]. Swelling of T91 had an incubation period of swelling of ~400 dpa at the depth of peak swelling, greater than incubation periods from neutron irradiated T91. However, in reactor the production of helium will drive cavity nucleation and therefore, decrease the incubation period for swelling. This ion irradiation study was conducted without considering the effects of helium and this may account for the delay in the incubation period.

The swelling and microstructure evolution of ferritic-martensitic alloys HT9, T91, and T92 were investigated by Getto et al. [9] using iron ions and 10 appm helium pre-implanted to obtain systematic evolution from 75 to 650 dpa. Contrary to the previous study, for the least swelling resistant alloy (HT9), a swelling rate of 0.033%/ dpa was observed from 188 to 650 dpa. Swelling resistance was higher in T91 at a rate 0.007%/ dpa. The decrease in swelling/swelling rate in T91 was primarily due to suppression of cavity nucleation, rather than growth, which proceeded at approximately 0.1 nm/dpa. Swelling resistance was highest in T92, which had not yet reached steady state swelling by 650 dpa due to a low density of small cavities, indicating suppression of both nucleation and growth. Analysis of additional heats of T91 indicated that alloy composition was not the primary factor in determining swelling resistance. In addition to swelling increasing with damage level, the volume fraction of Ni/Si/Mn-rich G-phase precipitates and line length of dislocation were found to evolve in the microstructure up to 650 dpa as shown in Figure 2.15,

though significant carbon contamination from irradiation experiments was observed and might affect microstructural evolution [9]. The use of ion irradiations has been instrumental in determining that the microstructure of ferritic-martensitic steels will continue to evolve with damage level beyond intended reactor lifetimes.

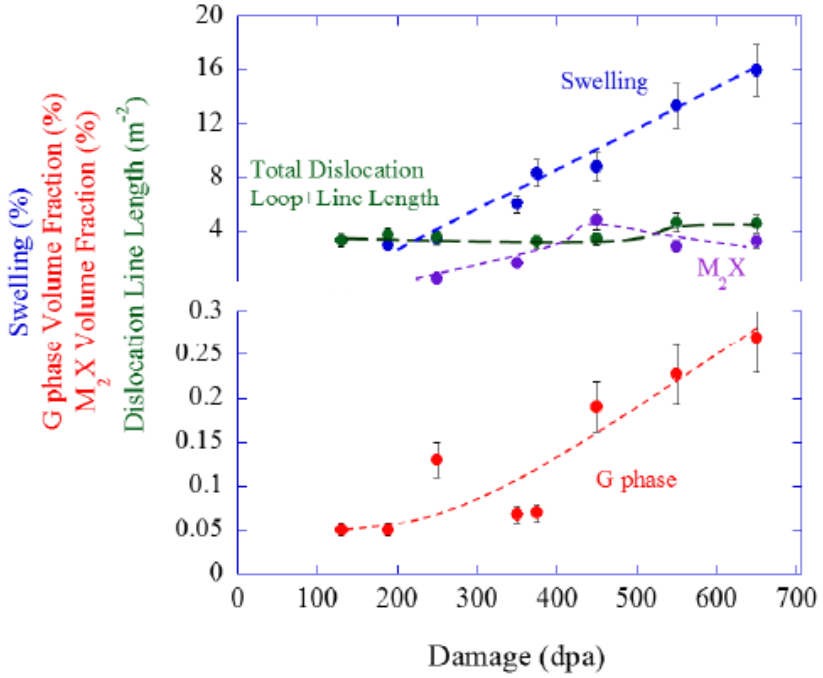

Figure 2.15. Microstructural evolution of HT9 irradiation with 5 MeV iron ions at 460°C from 130 to 650 dpa, from [9].

Chapter 3 Objectives

The objective of this work is to determine the effects of (i) the initial sink strength from as-received microstructures including line dislocations, lath boundaries and prior austenite grain boundaries, and (ii) the evolving sink strength from irradiation-induced features including precipitates/clusters, dislocation loops, and cavities, on the microstructural evolution of AM-HT9 alloys with and without post-build heat-treatments. This is ultimately evaluated by two primary irradiation campaigns, one where irradiation dose is increased from 16.6 dpa to 250 dpa at 445°C and all other irradiation parameters are held constant, and the other where the temperature is altered from 400°C to 500°C at 50 dpa with all other parameters held identical within the experimental variation. This design of experiment is developed to evaluate two primary hypotheses for the behavior of all microstructural evolution including cavities, dislocation loops, and precipitates as a function of damage levels and temperatures are presented as follows:

1. The radiation-induced swelling response as a function of damage level of AM fabricated HT9 components can be tailored through controlled evolution of the hierarchical microstructure of the alloy via conventional normalizing and tempering treatments. The prediction of this degree of swelling retardation can be made using a simplified theoretical model that accounts for starting and evolutional sink strengths, which are governed by all microstructural evolution under irradiation.

2. The peak swelling response as a function of temperature of AM fabricated HT9 can be tuned using the principals of sink strength tailoring permitting the ability to retard swelling in AM-fabricated materials at specific temperatures.

To test these hypotheses, the variability of radiation responses of three conditions of AM-HT9 alloys that were fabricated using DED technique are evaluated and determined, with (i) one as-built condition without post-built heat-treatment, and (ii) two conditions with similar but varying post-built heat-treatments. The drastically different starting microstructures between the two heat-treated conditions of AM-HT9 and the other as-built condition enabled gross and quick evaluation of the hypotheses for this complex material system. The investigation was achieved through a combination of dual-ion irradiation experiments with careful scanning/transmission electron microscopy (S/TEM) and atom-probe tomography (APT) characterization of the irradiated microstructures in the three conditions of AM-HT9 alloys.

For hypothesis 1, the characterization results at different damage levels were used to develop the evolution of sink strengths in order to calculate theoretical swelling rates and compare to those obtained from the experimental results. All microstructures were considered when the calculation of sink strengths was conducted – grain boundaries, cavities, dislocation loops, line dislocations, and precipitates induced by irradiation. Although the primary focus is on the cavity evolution and swelling behaviors of the three conditions of AM-HT9, the evolution of dislocation loops and precipitates will be closely examined as well as they contribute to both sink strength and cavity evolution, as well as mechanical property degradation.

The sink strength dependence of microstructural evolution will then be used to provide an explanation of the experimental observation obtained for Hypothesis 2.

Chapter 4 Experimental Procedures and Methodology

This chapter documents the experimental procedures used to prepare, irradiate, and characterize the AM-HT9 samples. In addition, the methodology used to calculate sink strength and theoretical swelling rate based on the characterization results is introduced in detail.

4.1 Alloy and Sample Preparation

The HT9 alloys used were fabricated using laser-blown powder DED additive manufacturing (AM-HT9) [49]. There are two HT9 powders developed to fabricate two heats of fabricated AM-HT9. One is developed by TerraPower LLC, or Heat A, and the other is developed by ORNL, or Heat B. The nominal compositions are listed in Table 4.1, as defined by ASTM A826/A826M-95 [112]. The composition of the powder was tailored to be identical to heats of HT9 recently studied by TerraPower LLC [113–115]. Gas-atomized HT9 powder in a size range of 40-120 μm diameter was used to fabricate samples [49]. Following powder procurement, samples for evaluation in the as-built condition and after post-build heat-treatment were fabricated using a DMD 103D blown-powder AM process housed at the Manufacturing Demonstration Facility [116] at ORNL. The DMD 103D was run with a 1 kW diode laser with a wavelength of 910 nm, a beam diameter of 1.5 mm, and a nominal layer height of 0.6-0.8 mm [49].

Table 4.1. Nominal composition in wt. % of the HT9 powder feedstock based on ASTM A826/A826M-95 standard [112].

Fe	Cr	C	Mn	P	S	Si	Ni	Mo	Nb	W	Al	V
Bal.	11.0-12.5	0.17-0.23	0.40-0.70	0.04 max	0.01 max	0.20-0.30	0.30-0.80	0.80-1.20	0.05 max	0.40-0.60	0.05	0.25-0.35

After obtaining the two heats of the as-built condition of AM-HT9 (ASB), additional post-built processing treatments were sought to alter the total effective sink density of the specimen prior to irradiation. An additional desire of the heat-treatments was to mimic traditional heat-treatment routes typically applied for fabricating W-HT9 [49], called ACO3 and FCRD, where (i) ACO3 stands for the ACO3 hex-duct irradiated in Fast Flux Test Facility (FFTF) (Heat 84425), and (ii) FCRD represents the Fuel Cycle Research and Development (FCRD) program [117], respectively. The heat-treatment used for the ACO3 condition of AM-HT9 consisted of normalizing at 1065°C for 30 min followed by air cooling and tempering at 750°C for 60 min followed by air cooling. The FCRD condition of AM-HT9 consisted of normalizing at 1040°C for 30 min followed by air cooling and tempering at 760°C for 60 min followed by air cooling. As discussed later, these two heat treatments led to similar but still varying sink strengths that were vastly different from that of the ASB samples in both heats. An additional benefit of the ACO3 and FCRD heat treatments was the reduction of the δ-ferrite phase compared to that of the ASB condition of AM-HT9, where the δ-ferrite phase formation was a result of incomplete transformation to austenite phase during the rapid cooling process [49,54]. Note, within this work the focus is on the tempered-martensite phase instead of the δ-ferrite phase persistent in the ASB conditions of AM-HT9.

After obtaining the three conditions, i.e., ASB, ACO3 and FCRD, of AM-HT9 alloys from the two different powder lots, bulk samples were cut into half-bars with dimensions of 1.5×1.5×10 mm using electrical discharge machining (EDM). Another ferritic-martensitic steel with comparable heat transferability was cut into full-bars with dimensions of 1.5×1.5×20 mm using EDM. All half- and full-bar samples were mechanically polished with a 1200-grit grinding-paper

finish, followed by electropolish to remove residual surface strain layer to achieve mirror-like surface conditions. Electropolish was conducted by using a mixture of solution containing 10% perchloric acid and 90% methanol, with temperatures between -40°C and -50°C. All samples were electropolished for 40s with a voltage of 40V applied between the sample (anode) and the conducting platinum mesh (cathode). This step of electropolish will remove the sample surface with thickness of a few microns, which is enough to remove all the surface strain layer with thickness of typically a few hundred nanometers. A schematic of the electropolishing setup before ion irradiation is shown in Figure 4.1.

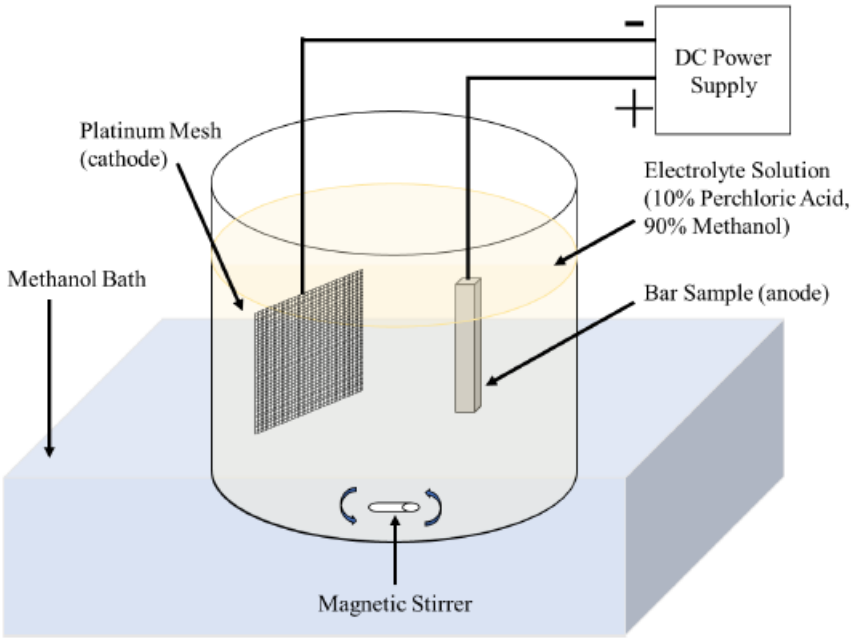

Figure 4.1. A schematic of the electropolishing setup used for samples prior to ion irradiation, from [60].

All the half-bar bulk samples were then used for (i) TEM sample preparation to characterize the as-received microstructures, and (ii) irradiation experiments. All the full-bar bulk samples were used to serve as guide bars for monitoring irradiation temperatures. More details about radiation experiments are discussed in Section 4.2. The procedures for characterization of both as-received

microstructures and irradiated microstructures are identical. Therefore, please refer to Section 4.3: post-irradiation examination (PIE) to find details on sample preparation and S/TEM characterization.

4.2 Ion Beam Irradiations

Ion beam irradiations were carried out at the Michigan Ion Beam Laboratory (MIBL). All three conditions of AM-HT9 of Heat A or Heat B were irradiated at the same time for each radiation condition. Defocused 5 MeV Fe^{2+} ions were used to create irradiation damage in all radiation conditions, and raster-scanned 2.85 MeV He^{2+} ions, with horizontal and vertical scan frequency of 117.19 Hz and 1019 Hz, respectively, were used to perform helium co-injection in dual-ion irradiations. The damage rate of 5.8×10^{-4} dpa/s was kept the same for all radiation conditions. To clarify, there are three groups of irradiations conducted:

(i) A single-ion irradiation with a damage level of 50 dpa at 460°C for Heat A

This single-ion irradiation served as a rapid screening study of the microstructural evolution for Heat A, with the emphasis on microchemical evolution. In addition, a similar condition had been used to irradiate a traditionally-made wrought HT9 alloy with ACO3 heat-treatment, therefore this single-ion irradiation campaign allowed cross-comparison of the radiation responses between the AM and wrought HT9 alloy without consideration of He effects. However, it was later identified that Cu impurities were introduced into the Heat A of AM-HT9 and formed extensive clustering after irradiation. Therefore, Heat B of AM-HT9, without significant amount of Cu detected, was then used for the following dual-ion irradiation experiments.

(ii) A series of dual-ion irradiations with varying damage levels of 16.6, 50, 75, 100, 150, and 250 dpa at 445°C for Heat B

This damage level series of dual-ion irradiation experiments were conducted to study the dose-dependence of the radiation responses in the AM-HT9 of Heat B without noticeable Cu impurities. In wrought HT9 it is known that 445°C is close to the peak swelling temperature in dual-ion irradiation, therefore the dose series of experiments at 445°C were conducted in AM-HT9. 16.6 dpa condition was used to compare with the results obtained from wrought HT9 with ACO3 heat-treatment, where cavity nucleation occurred significantly in the wrought HT9. 50 dpa and 75 dpa in wrought HT9 were known to be close to the end of incubation period and the start of stead-state swelling. 100 dpa, 150 dpa, and 250 dpa dose conditions were used to investigate the stead-state swelling behaviors of three conditions of AM-HT9 of Heat B.

(iii) A series of dual-ion irradiations with varying temperatures of 400, 445, 460, and 500°C with a damage level of 50 dpa for Heat B.

This temperature series of dual-ion irradiation experiments were conducted to study the temperature dependence of the radiation responses in the AM-HT9 of Heat B without noticeable Cu impurities. To study the peak swelling temperature of AM-HT9, temperatures ranging from 400°C and 500°C, which is believed to cover the peak swelling temperatures of AM-HT9, were used.

All irradiation conditions and corresponding completion dates are listed in Table 4.2.

Table 4.2. The experimental details for ion irradiations conducted as part of this thesis.

Date of completion	Damage (quick Kinchin-Pease model, dpa)	Temperature (°C)	Damage Rate (dpa/s)	Helium Co-Injection Rate (He appm/dpa)	He injected (appm)	Heat number of AM-HT9
12/13/2018	50	460 ± 4	5.8×10^{-4}	0	0	A
01/10/2020	16.6	443 ± 5	5.8×10^{-4}	4	66.4	B
03/05/2021	50	445 ± 3	5.8×10^{-4}	4	200	B
09/30/2020	75	445 ± 9	5.8×10^{-4}	4	300	B
11/01/2020	100	446 ± 4	5.8×10^{-4}	4	400	B
01/22/2021	150	445 ± 8	5.8×10^{-4}	4	600	B
05/10/2021	250	445 ± 4	5.8×10^{-4}	4	1000	B
08/13/2021	50	400 ± 3	5.8×10^{-4}	4	200	B
01/09/2021	50	460 ± 6	5.8×10^{-4}	4	200	B
08/05/2021	50	500 ± 5	5.8×10^{-4}	4	200	B
10/01/2020	50	460 ± 3	5.8×10^{-4}	0	0	B

4.2.1 Irradiation Stage Setup

The configuration of the stage setup is shown in Figure 4.2. A stage made of (i) copper for lower temperature irradiation (below 450°C) or (ii) stainless steel and nickel for higher temperature irradiation (above 450°C) was used for all the irradiations. At the back side of the irradiation stage, a heater was connected to heat up the stage. There was also a thermocouple mounted at the back of the stage to monitor the temperature near the heater. A cooling air flow was connected as well to quickly cool down the stage temperature immediately after the irradiation was finished, so that the post-irradiation thermal annealing was minimized in the samples.

At the front side of the irradiation stage, four half-bar samples containing all three conditions of a single heat (either Heat A or Heat B only) of AM-HT9 were positioned at the center of the stage, with two full-bar samples placed at both sides of the half-bar samples. A 0.25 mm thin ductile copper sheet was put in between the stage front surface and the bottom of the samples to ensure good thermal contact. The gaps among all six pieces of samples were minimized to ensure the best possible thermal contact, so that the front surface temperatures were consistent

among them. On top of the samples, a shim and two hold-down bars were positioned to apply pressure to further improve thermal contact between the samples and the stage. Finally, to monitor the temperature during the irradiation experiment, four J-type thermocouples with temperature detection range of 0°C to 750°C were welded on the surface of the two full-bar samples, with the caution of not shadowing the Fe^{2+} and He^{2+} beams to reach the surface of the four half-bar samples. Because of the previously mentioned procedures to ensure good thermal contact, the temperature readings on the two full-bar samples are reasonably representative of the four half-bar samples.

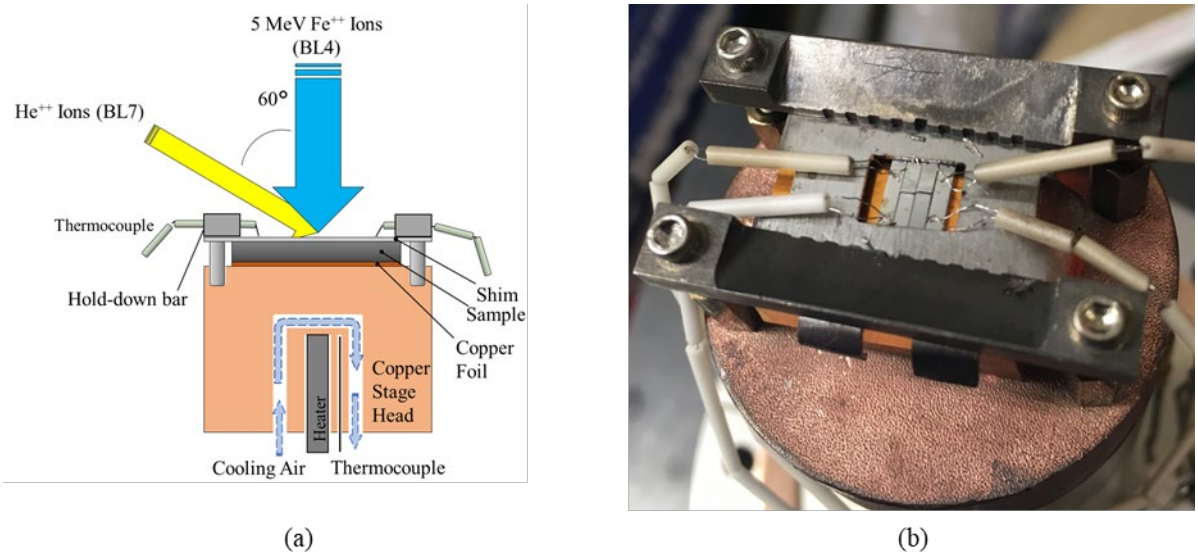

Figure 4.2. Stage setup schematics with (a) a cross-sectional view from the side of the stage, adapted from [52], and (b) a top-down photograph of a fully assembled stage.

4.2.2 Irradiation Setup

A multi-beam chamber (MBC) was used for all irradiations [59,60,118]. The MBC was designed to provide a fixed intersection point for each of the three accelerators at MIBL to achieve the multi-ion irradiation capability, with the schematic of the MBC provided in Figure 4.3. Radially directed ports around the MBC allowed direct access to the irradiation stage for the

accelerators and monitoring equipment and a flat back panel or easy access while minimizing chamber volume which is necessary to achieve high vacuum [59,60,118]. Two back panels were made for the chamber with different angles for the 6" ConFlat flange for the stage port to allow the stage to face any of the beam lines [59,60,118]. All of the irradiations within this thesis were performed with the sample surface and stage facing beamline 4 (BL4). BL4 delivers 5 MeV Fe^{2+} ion beam from the 3 MV Pelletron accelerator and is normal to the sample surface on the stage. BL7 delivers the 2.85 MeV He^{2+} helium ion beam from the 1.7 MV General Ionex Tandem Accelerator and it is 60° from BL4 in the horizontal plane, as shown in Figure 4.2 and Figure 4.3.

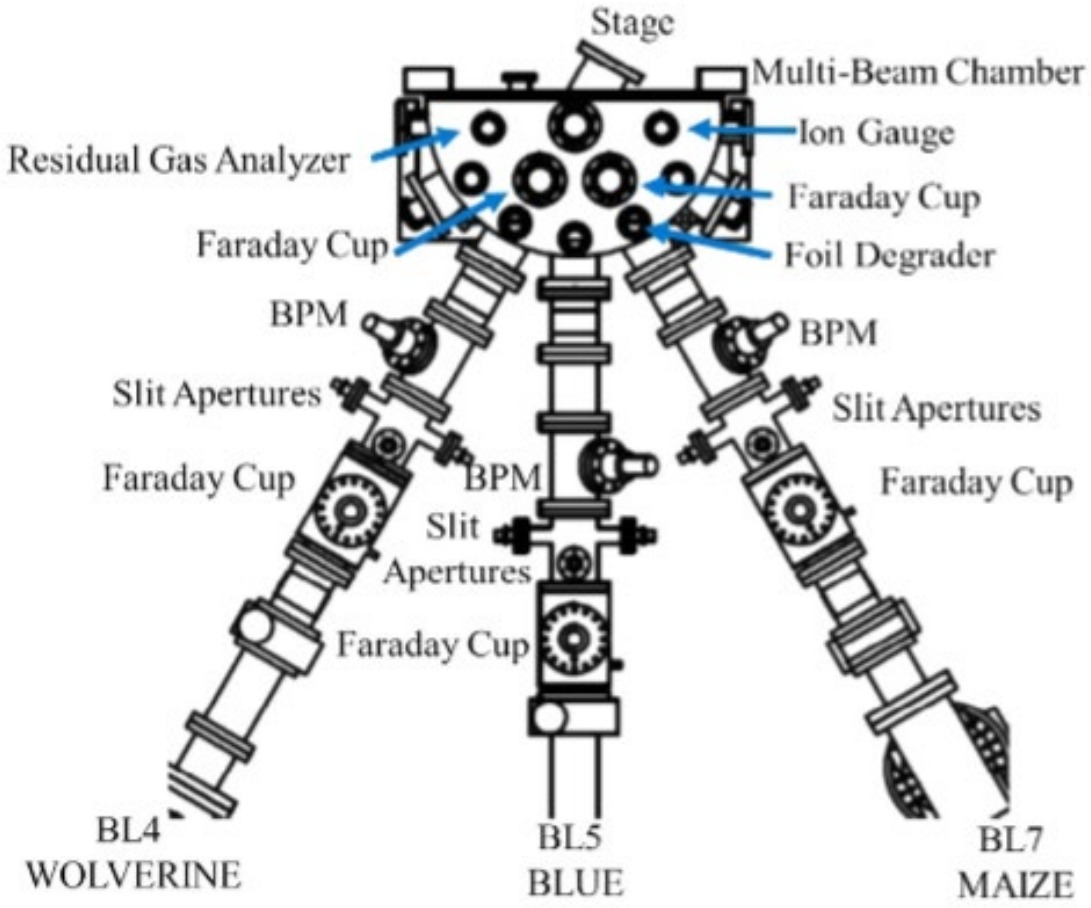

Figure 4.3. Multi-beam chamber with connecting beamlines. Each beamline is equipped with Faraday cups to record the ion beam current, slit apertures to define the irradiation area, and a beam profile monitor (BPM) to assess the beam shape. The image is adapted from [118].

The stage was mounted to the back panel of the chamber using a copper gasket and tightened down with nuts and bolts. Once mounted a resistive cartridge heater was inserted into the back of the stage. The cartridge heater was approximately 4 cm long and 1 cm in diameter, with a temperature rating of up to 760°C. The heat was then conducted from the back to the front of the stage, where samples were heated up to be a few °C lower than the target temperatures during the experiment. Minor beam heating of 2-5°C occurred when the Fe^{2+} beam was allowed to pass through the beamline and hit the sample surface. Additionally, a contact Type J thermocouple was inserted into the back of the stage into an approximately 1mm diameter hole to monitor the temperature close to the heater. Cables from a computer readout were attached to thermocouple feedthroughs, and the air lines for cooling the stage were also attached [59,60,118].

To ensure the quality of the irradiation experiments, several diagnostic instruments were connected to the MBC. An Evactron EP was used to plasma clean the chamber and the stage with samples, prior to irradiation to minimize carbon-contamination. A double-walled Dewar for liquid nitrogen was connected to a copper frame nearby the samples on the stage, acting as a cold trap before and during the irradiation to minimize contamination and oxidation with vapor at high irradiation temperatures. An Inficon Transpector® MPS Residual Gas Analyzer was used to monitor the partial pressure of each existing gas species in the MBC. An InstruTech Inc. model IGM402 hot cathode ionization vacuum gauge was used to monitor the pressure in MBC, and was maintained to be below 2×10^{-7} torr (2.67×10^{-5} Pa), as a result of the mentioned plasma cleaner and the use of the cold trap. The MBC has several quartz windows to allow live viewing of the irradiation stage. A Nikon digital camera was connected for the alignment of the ion beam position prior to irradiation, with detailed procedures to be discussed in Section 4.2.2. A 2D FLIR® infrared

thermal pyrometer was connected to MBC, together with thermocouples mounted on the sample surface, to monitor the sample surface temperatures on user-defined areas of interest at a rate of 3.125 Hz. Detailed procedures for temperature monitoring will be discussed in Section 4.2.4.

A slit aperture system with four slits that can be moved independently - on the top, bottom, left, and right side of the stage - was used on each beamline to perform the alignment of the ion beam position, define the irradiation area on the samples, and measure the current around the rectangular irradiation area defined by the four slits. For the defocused Fe^{2+} beam, irradiation area was kept at 5×5 mm so that all six samples on the stage can be irradiated. The raster-scanned He^{2+} beam needed to go through a rotating aluminum foil acting as an energy degrader so that the resulting ratio of implanted He concentration to damage was a constant, with more details discussed in Section 4.2.3. The scattering of the He^{2+} beam through the aluminum foil was sufficient that He^{2+} beam was able to cover all the area of interest on the irradiation stage.

4.2.3 SRIM Damage and Helium Injection Calculation

The Stopping and Range of Ions in Matter (SRIM) 2013 was used to calculate the damage and the injection of He as a function of depth from the sample surface, with the Quick Kinchin-Pease mode. An ion energy of 5 MeV and beam angle of 0° for the Fe^{2+} beam was entered as inputs. The displacement energy for each element from Table 4.1 was extracted from the ASTM Standard E591 [119] as inputs into the SRIM program. The atomic percentage inputs for each element was converted from the weight percent in Table 4.1 by using the median value from the composition ranges. At least 100,000 ions were used for calculation to obtain smooth profiles. The depth of 600 nm from the sample surface was used as the nominal damage for all irradiation experiments. This is because this depth is far from (i) the sample surface so that the surface effect

is minimized, and (ii) the depth of the peak injected interstitial profile so that the injected interstitial effect is also minimized [37]. To calculate the damage (dpa) profile, Equation 4.1 was used:

$$damage\ (dpa) = \frac{SRIM_{damage} \times \Phi}{N_{HT9}} \qquad \text{Equation 4.1}$$

where $SRIM_{damage}$ represents the SRIM damage event output values as a function of the depth, Φ represents the irradiation ion fluence, and N_{HT9} is the atomic density of the HT9 alloy, which is 8.34×10^{22} at/cm^3 [120]. Note, the damage caused by He^{2+} is orders of magnitude lower than that cause by Fe^{2+}, and thus was neglected during the calculation and experiment design.

Once the damage level at the target depth of 600 nm was designed for an irradiation experiment, the Φ can be calculated and subsequently used to derive two other key quantities for the radiation experiments: Fe injected interstitial concentration profile and Fe^{2+} ion current. The Fe injected interstitial concentration profile was calculated using Equation 4.2:

$$Fe\ (at\%) = \frac{SRIM_{range} \times \Phi}{N_{HT9}} \qquad \text{Equation 4.2}$$

where $SRIM_{range}$ is the SRIM range file output values as a function of depth. Note, $Fe\ (at\%)$ is a unitless quantity as a function of depth to measure the atomic percent of the injected Fe ion with respect to the matrix atoms. Another key quantity to calculate using Φ, coupled with the designed damage rate φ in dpa per second (dpa/s), is the Fe^{2+} current. The current was determined by the following equations:

$$I = \frac{Q}{t} \qquad \text{Equation 4.3}$$

$$I = \frac{Ne\Phi A}{t} \qquad \text{Equation 4.4}$$

$$I = \frac{Ne\Phi A}{damage/\varphi} \qquad \text{Equation 4.5}$$

where Q is the total charge of the Fe^{2+} particles, t is the amount of time during which the accumulative charge of Fe^{2+} reaches to Q, N is the number of electrons per Fe^{2+} particle which is 2, e is the charge per electron which is 1.6×10^{-19}C, and A is the irradiation area which is 5×5 mm. An example of calculated damage and injected Fe^{2+} interstitial profiles as a function of depth is shown in Figure 4.4, assuming the designed nominal damage level at 600 nm is 75 dpa.

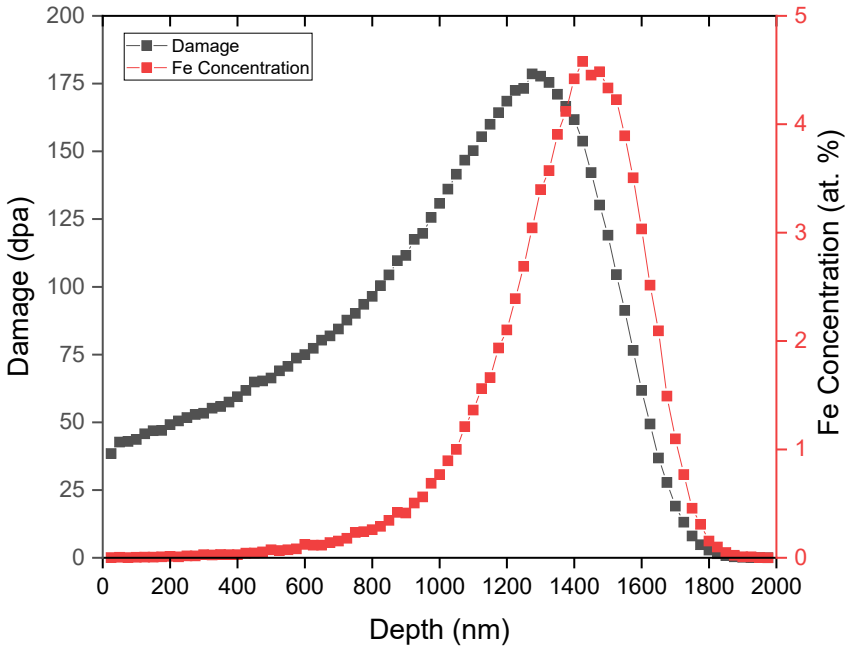

Figure 4.4. Calculated damage (in black) and injected interstitial concentration (in red) profile in AM-HT9 irradiated by 5 MeV Fe2+ ions.

The calculation of the He^{2+} beam for dual-ion irradiations was more complicated. Although the depth of 600 nm was used for nominal damage level, microstructures within the 500-700 nm range of depth was actually examined during the post-irradiation examination. Therefore, the design of the dual-ion irradiations intended to achieve a constant ratio of He injection concentration to damage level of 4 He appm/dpa within the depth range of 500-700 nm. This was achieved through the injection of He^{2+} ions with varying energy throughout the irradiation, so that

the superimposed injected He concentration profile matched with the intended shape. The varying He beam energy was achieved by a single-energy He ion beam with 2.85 MeV going through a rotating aluminum foil with 6.2 μm thickness, because the effective thickness thus traveling distance in the aluminum foil resulted in different energy loss of the He beam. The aluminum foil rotated in period from -60° to 60°, with the 0° being the position where the aluminum foil was normal to the Beamline 7 (BL7) – the He ion beam direction. The amount of time that the aluminum foil stayed at each angle can be digitally controlled. At 0°, the effective thickness of the aluminum foil was the lowest of 6.2 μm, resulting in the greatest depth of He injection. Note, He ion may get scattered in the aluminum foil, thus changing the traveling direction of the He beam as a function of the aluminum foil angle. SRIM was used to calculate (i) the reduced energy, position, and velocity of each exiting He ion from the foil at each foil angle, and (ii) the resulting He injection profile into the AM-HT9 samples. Python was used to automatically perform this series of calculations by propagating appropriate parameters into the SRIM program. Details regarding this methodology of customizing implantation profile can be found in the previous work by S. Taller [121].

After the injection profiles of He with different foil angle were obtained, different recipes of the foil control – with varying stopping time at each angle between -60° and 60° – were tried out, so that the resulting ratio of the He injection concentration to damage in the depth range of 500-700 nm is a constant of 4 He appm/dpa. The calculated He^{2+} injection profile, damage, and their ratio as a function of depth is shown in Figure 4.5.

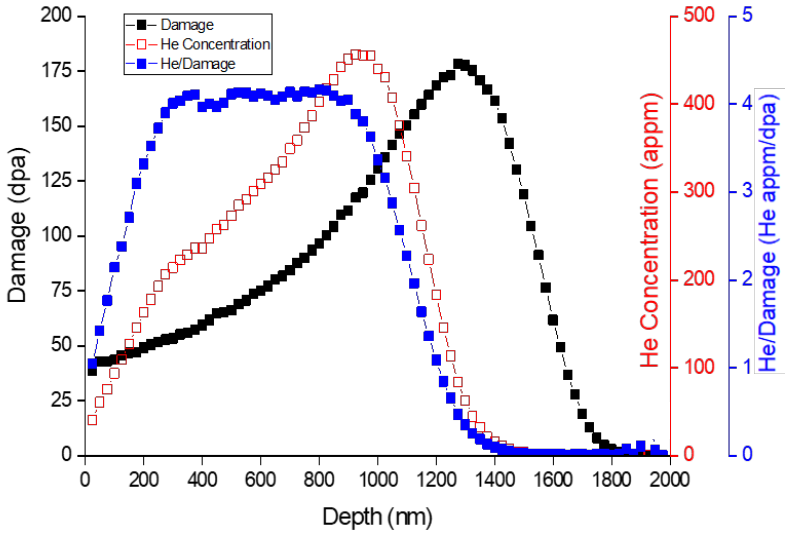

Figure 4.5. Injected He concentration (in red), calculated damage (in black), and their ratio (in blue) profiles in AM-HT9 irradiated by 5 MeV Fe2+ ions with 2.85 MeV He2+ injection using aluminum foil energy degrader.

As a result, with designed (i) damage rate of all the irradiation experiments of 5.8×10^{-4} dpa/s resulting from 5 MeV Fe^{2+} beam, and (ii) He injection rate of all the dual-ion irradiation experiments of 4 He appm/dpa resulting from 2.85 MeV He^{2+} beam coupled with an aluminum energy degrader, the ideal Fe^{2+} and He^{2+} current density was calculated as 4.4 nA/mm^2 and 2.25 nA/mm^2, respectively. Note, (i) the mentioned He^{2+} beam current density refers to the current density after He^{2+} beam going through the aluminum foil positioned at 0°, and (ii) the irradiation area defined by the position of slits were different for each beamline, and details can be found in Section 4.2.4.

4.2.4 Running the Irradiation

After the stage was mounted into the MBC, the chamber was first pumped down to $1\text{-}2\times10^{-1}$ torr with an oil-free scroll pump. An Evactron EP with a forward power of 15 W was then used for 2 hr to plasma clean the chamber by removing hydrocarbon contaminations. Afterwards, a cryopump was used for at least 10 hr to pump the pressure of the chamber down to the 1×10^{-7} torr

level. After that, the cold trap was then turned on to further drop the chamber pressure down to 6-7×10^{-8} torr by absorbing water vapor and minor contaminations. This last process could take more than 2-3 hours.

While the cold trap was turned on, the ion source was started and the ion beams in BL4 for Fe^{2+} and BL7 for He^{2+} were prepared, respectively, so that the designed current can be obtained. Very importantly, ion beams needed to be properly aligned by moving the four slit positions so that the desired region of interest (5×5mm) on the stage was hit by the ion beams. For the He^{2+} beam, because the targeted 4 He appm/dpa injection rate and the corresponding current density can be relatively easily achieved, the slit positions were set up so that the beam area was large enough to cover the whole stage without the necessity of a high accuracy alignment down to millimeter-level. Moreover, the scattering of the He^{2+} beam from the aluminum foil further increase the effective area covered by the He^{2+} ion beam. The left, right, top, and bottom slit (when the stage is viewed from the source and beamline) positions were set at 3, 3, 5, and 5 mm, respectively, resulting in the slit-defined area of 60 mm^2 and the He^{2+} current measured after the aluminum foil positioned at 0° of 135 nA.

The Fe^{2+} beam, however, requires very high accuracy alignment due to the fact that the desired Fe^{2+} beam current was slightly lower than the maximum amount of beam, which is governed by multiple factors, including (i) the beam production limit of the Peabody source, (ii) the beam loss due to the striper gas efficiency, and (iii) the beam loss due to the bending magnets and steering. In addition, the Fe^{2+} beam needed to be defocused and kept uniform with less than 10% variation in beam intensity across the 5×5 mm area. To reach this purpose, a pre-aligned laser beam and a piece of alumina ceramic right in front of the stage were used. The laser beam and the Fe^{2+} beam were pre-aligned to match with small positional offsets on the irradiation stage. The

procedure to align the beam was as follows: (i) the laser was turned on to illuminate the irradiation stage; (ii) slits position were moved so that the laser beam was centered on the area of interest on the stage, with the desired irradiation area; (iii) the alumina piece facing BL4 was inserted right in front of the stage so that the laser beam projected on the ceramic piece; (iv) the Fe^{2+} beam was turned on to be projected on the ceramic piece; and (v) move the slits position so that the new laser beam location matched the previous Fe^{2+} beam position, by a small amount. The Nikon digital camera was used during the processes to take high resolution images and monitor the laser and Fe^{2+} beam positions.

Once the beam alignment was completed, a beam profile monitor (BPM) was used to assess the beam profile. The quadrupoles at the high energy end and the Einzel lenses at the low energy end were adjusted to make profiles as flat and uniform as possible in both X and Y directions on the BPM. To confirm the uniformity (less than 10% variation), a moving 2D profiler in both X and Y directions were then used to measure the differential current in the irradiation area. Note that when the profilers entered the tested area with ion beam, there was anomaly arising from the electronic-irradiation interaction of the profiler that resulted in an artificial peak near the entering position in the plotted beam profile. To obtain the true beam profile, the forward-and-back movement mode of the 2D profiler was used to ensure at least one valid datapoint collection was made for every position tested.

Once this was completed, the irradiation was ready to start. The stage was then heated up by a digitally controlled cartridge heater inserted into the back side of the stage to quickly reach the target irradiation temperature, monitored by the four thermocouples. During the heat-up, outgas could occur and drive the pressure up to $3\text{-}5\times10^{-7}$ torr in MBC. The pressure would go back down

with the cryopump and cold trap functioning to reduce hydrocarbons and water vapor in the initial first two hours.

After the target temperature was reached, the thermal imager was then used to calibrate the temperature of each area of interest (AOI) by assigning an appropriate emissivity of each AOI. At least two AOIs were created for each half-bar sample, so that AOIs can cover most surface area of the sample, while the edge of all AOIs are slightly within the edges of the sample to avoid unstable and inaccurate emissivity readings. Figure 4.6 shows the typical thermal imager program with AOIs on the samples. Once the temperature was calibrated near the target value, the irradiation was started by removing the Faraday cup in each of the two beamlines and placing the beam on the stage.

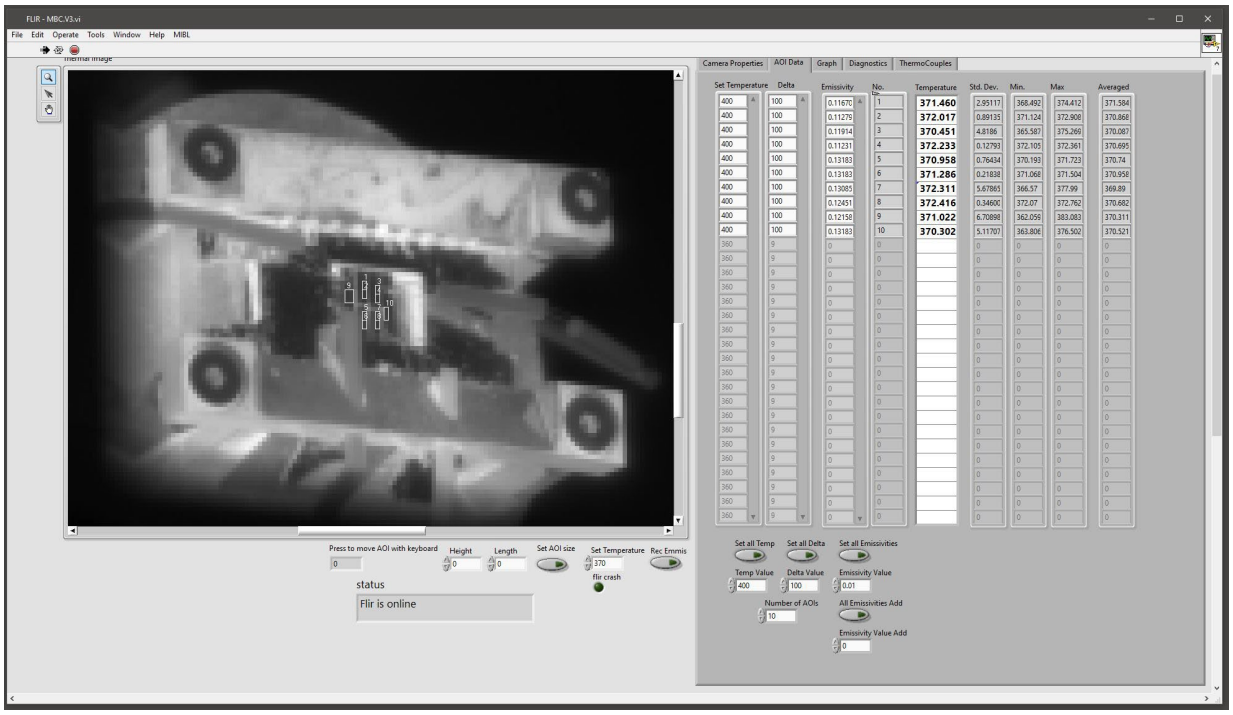

Figure 4.6. A typical thermal imager program used to monitor temperature with at least two AOIs set up on each half-bar samples.

Throughout the irradiation, several parameters were monitored to ensure a successful experiment. Temperatures were monitored by thermocouple readings, as well as AOI readings with maximum error of 10°C. The LabView™ program interfacing with the FLIR was set to alarm if any AOI temperature reading was more than ±10°C than the target temperature. The heater power was then adjusted so that the temperature went back to the set value. The current of the Fe^{2+} and He^{2+} ion beams were measured by inserting a Faraday cup located after the four slits for each beamline every 25-30 min. The measurement of the He^{2+} beam was conducted after pausing the rotation of the aluminum foil energy degrader at 0°. There were two goals for monitoring the ion beam: (i) the current value needed to be kept at an acceptable range of maximum 10% variation from the target value; and (ii) the beam shape remained the desired way. For the defocused Fe^{2+} beam, the beam profile from the BPM needed to stay flat so that the beam intensity was uniform throughout the irradiation area. For the raster-scanned He^{2+} beam, the slits current needed to be balanced between the left and right, as well as the top and bottom slits readings. If the balance of the beam was not acceptable, the bending magnet strength was used to balance the beam in X direction and the magnetic Y-steerer was used to balance the beam in Y direction. The pressure of the MBC chamber needed to be monitored as well. The steady-state pressure depended on the irradiation temperature and ranged from 6×10^{-8} torr to 3×10^{-7} torr for the irradiation temperature range of 400-500°C in this work. This pressure range below 3×10^{-7} torr normally resulted in acceptably small amount of surface oxidation, so that the bulk material surface quality was good enough for performing electron backscatter diffraction (EBSD) when completing a targeted lift-out TEM sample preparation. More details regarding EBSD experiments will be discussed in Section 4.3.1.1.

Once the cumulative fluence reached the target value, the irradiation was complete. All the Faraday cups in BL4 and BL7 were inserted to block the ion beams. The heater power was then turned down to 0, and the air cooling was turned on so that the stage temperature could be dropped to below 100°C within 3-5 min. Next, the cold trap was turned off, so that liquid nitrogen could evaporate and the cold trap was heated up to the room temperature before the chamber was finally vented. This step was used to avoid any condensation of the water steam from outside the chamber.

4.3 Post-Irradiation Examination (PIE)

After the irradiation, samples were removed from the MBC and the irradiation stage. The sample surface was observed to confirm the minor to minimum amount of oxidation during irradiation, which was usually the case for the low chamber pressure achieved. For the post-irradiation examination (PIE), microstructural responses before and after irradiation were obtained by advanced characterization techniques including S/TEM and APT.

4.3.1 S/TEM Sample Preparation

Unirradiated and irradiated bulk samples were adhered to scanning electron microscopy (SEM) stubs using a common carbon tape, so that the samples were electrically coupled to the SEM stubs. The "lift-out" method [122] was used to prepare cross-sectional electron-transparent S/TEM specimens of ~100 nm thick by using a dual-bream Thermo Fisher Helios 650 Nanolab Scanning Electron Microscope/Focused Ion Beam (SEM/FIB) system at Michigan Center for Materials Characterization (MC^2). The SEM/FIB system utilized an electron beam normal to the stage when the stage was tilted to 0° and a Ga ion beam 52° from the electron beam direction. Both beams were able to image the sample, and the ion beam was also used for milling and sputtering. The current and energy of both beams can be controlled independently. Depending on the

application, they were varied throughout the sample preparation process. For the purpose of this study, the Ga ion energy was kept at 30 kV. Besides the conventional "lift-out" method, several additional procedures were taken to ensure the production of S/TEM samples with the highest quality possible for the purpose of the next-step S/TEM characterization.

4.3.1.1 Electron Backscatter Diffraction (EBSD)

Before the "lift-out" procedure, the orientation of the extracted cross-sectional S/TEM sample was determined by the technique called EBSD, with an EBSD detector equipped on the SEM/FIB system. The crystallographic plane of the extracted S/TEM samples were selected to be close to the (001) orientation. The reason to prepare the S/TEM samples in this orientation was because of the ease of characterization of dislocation loop types in the irradiated microstructures at this orientation of [001] [123], which is further illustrated in Section 4.3.2.1.

The EDAX TEAM™ EDS Software Suite for SEM software was used to collect EBSD data. Several parameters within the software prior to data collection needed to be correctly set up. The working distance between the bulk material surface and the electron gun was 10.5 mm. The stage needed to be tilted to 60° angle facing the EBSD detector to increase the contrast in the resultant electron backscatter diffraction pattern. The software could also conduct the image tilt-correction based on the stage tilting angle, so that the resulting data sets were adjusted to plan-view of the sample surface. The electron beam energy was set to be at a maximum value of 30 kV to ensure enough penetration into the sample surface. The penetration depth can be calculated [124] using Equation 4.6:

$$ID_{BSE} = \frac{7AE^{1.67}}{\rho Z^{0.89}} cos\theta \qquad \text{Equation 4.6}$$

where ID_{BSE} (nm) is the information depth of the backscattered electron (BSE) emission, A (g/mol) is the atomic weight of the tested material, E (keV) is the energy of incident electrons, ρ (g/cm^3) is the density of the tested material, Z is the atomic number, and θ is the stage tilting angle. In this study, after plugging in the parameters of the AM-HT9 material, 30 keV maximum electron energy and 60° stage tilting angle, the maximum penetration depth is calculated to be about 400 nm, which is slightly shallower than the lower bound of the 500-700 nm target area of interest in the irradiated AM-HT9.

The electron beam current was ~6 nA or ~13 nA to ensure sufficiently high signal-to-noise ratio during data collection. The binning was set as 4×4 with gain at ~10, frame at ~167, and optimized exposure values based on selected electron beam current. Further, the candidate crystal structure of Fe-bcc-ferritic phase with the lattice constant of 2.87Å was pre-selected in the software database to help determine the grain orientation. After the background signal was subtracted and the target area was located, the data collection was ready to start. After the EBSD data collection, all the data were transferred to OIM Analysis™ software for the 3D visualization of the crystallographic orientation of the grain of interest. To determine the (001) orientation of the extracted TEM sample, the inverse pole figure (IPF) alone was not enough; the 3-dimensional information of how the BCC cubic crystal was placed for a grain at the sample surface was critical. For example, as shown in Figure 4.7, the EBSD-IPF mapping on the left indicates the "in" orientation of the grains where red, green and blue colors represents [100], [110] and [111] orientations, respectively. The cubic on the right indicating the crystal orientation for the grain with [100] "in" orientation in red highlighted with a white circle shows that there exists two possible ways of obtaining a {100} lift-out sample, when the extracted slice of material is along

the side of the cubic. Using this 3-dimensional EBSD information of a particular grain, in theory, a TEM sample on any common low-index crystallographic planes can be made by FIB.

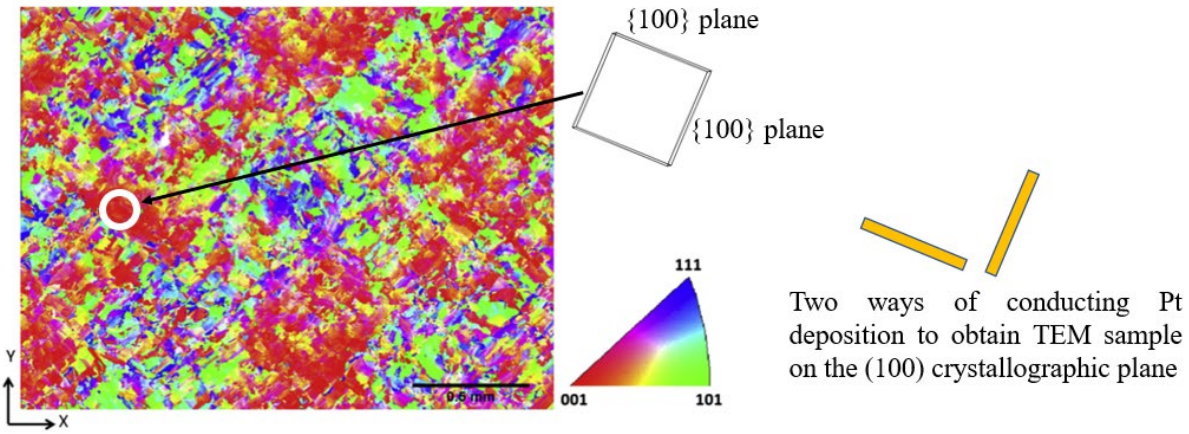

Figure 4.7. An example of using EBSD to determine how to extract a TEM sample using FIB that is along any crystallographic plane, and in this case, the {100} planes.

4.3.1.2 FIB Lift-out

The whole process is demonstrated in Figure 4.8, with detailed procedures described below.

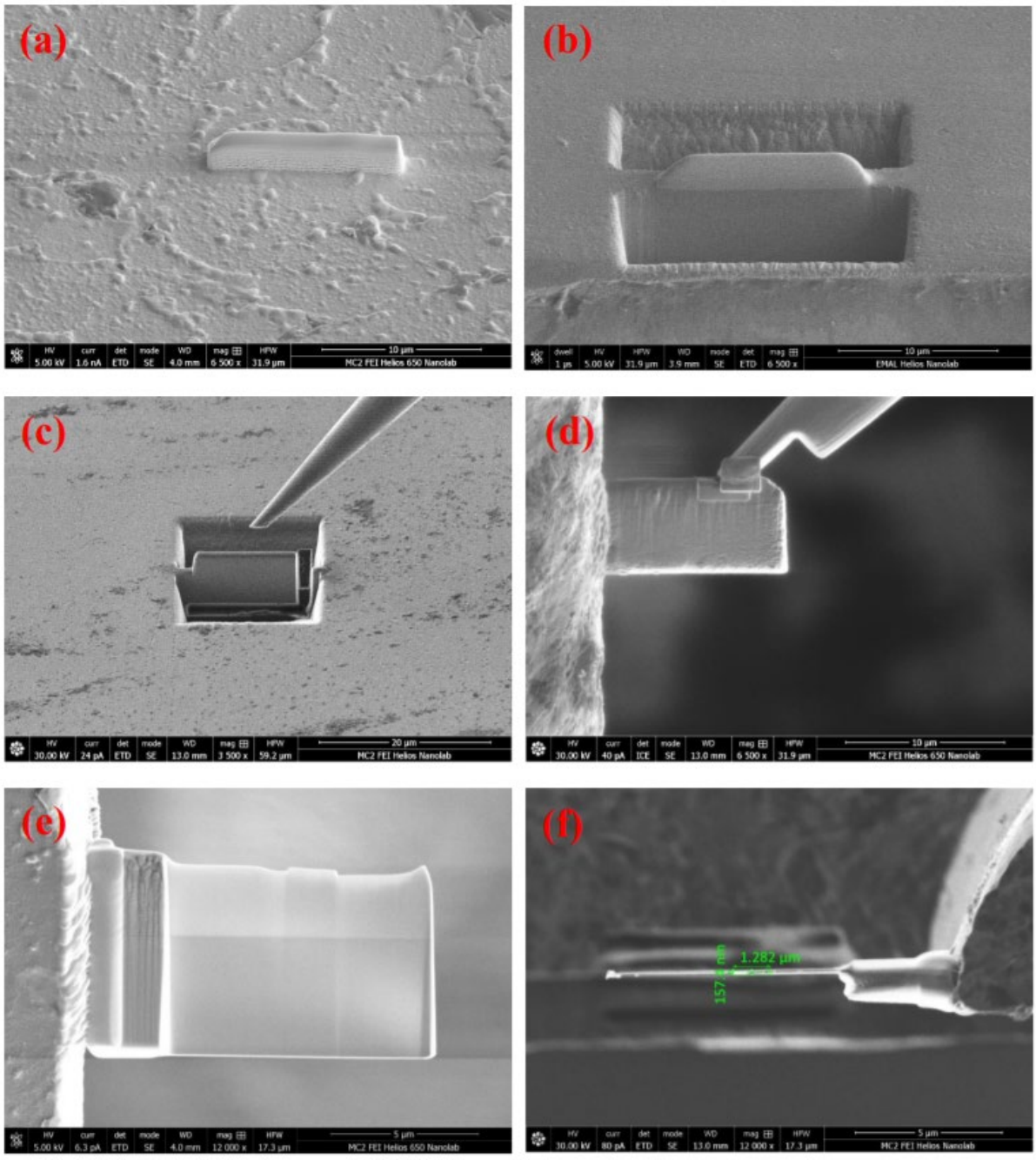

Figure 4.8. The "lift-out" process in the SEM/FIB system, adapted from [125]. *(a) A platinum protective layer deposited on the sample surface. (b) Two trenches were made along the long side of the platinum layer. (c) An inserted OmniProbe to lift out the S/TEM specimen. (d) The specimen attached to the TEM half grid (on the left). (e) A final view of the thinned S/TEM specimen, viewed in SEM. (f) A final view of the thinned S/TEM specimen, viewed using ion beam. The final thickness for all specimens was 150-180 nm.*

Once the (001) orientation of the lift-out was determined on a grain, the stage needed to be tilted to 52° with a working distance of ~4mm from the electron gun to the sample surface, which

was close to the eucentric height position of the SEM/FIB system. At this height, the same area of view on the sample using both electron and ion beams with a 52° angle provided a 3D full picture of the observed sample, to allow accurate operation in the lift-out process. The carbon gas injector needle was inserted to deposit a carbon layer with 0.2 μm thickness and 1.5 μm width, for the purpose of probe alignment in the STEM. The current of the ion beam was at 40 pA to ensure the production of a dense carbon layer. The direction of the deposited carbon layer matched the EBSD result so that the extracted S/TEM specimens were close to (001) crystallographic orientation. Afterwards, the platinum gas injector needle was inserted to further deposit a platinum layer with 3.5-4.0 μm thickness and 1.5 μm width to protect the sample surface from being damaged by the Ga ion beam. The ion beam current of 0.23 nA was used for the deposition of the platinum layer. The energy used for the Ga ion beam was 30 kV, and such thickness of a few micrometers of the platinum protective layer was more than enough to shield the materials beneath.

After that, two big trenches using a regular cross-section pattern were made along the long side of the platinum layer, with the ion beam current of 9.3 nA. The width and depth of the pattern were 8 μm and 4 μm, respectively. A lower current of 2.5 nA was then used to further clean the cross-sectional cut. The stage was then tilted back to 0° to make a near U-shape cut by using a regular rectangular pattern with 2.5 nA ion beam. The U-shape cut was not cut all the way through to have some remaining material connecting the S/TEM sample and the bulk material. An OmniProbe™ needle was then inserted and moved very close to the corner of the S/TEM sample. Platinum deposition was made to weld the sample and the OmniProbe together by using 40 nA ion beam. Finally, 2.5 nA ion beam was used to cut through the remaining joint between the specimen and the bulk material, so that the OmniProbe lifted the attached sample out of the bulk sample.

After the specimen was lifted out, the sample needed to be mounted on a TEM half grid for S/TEM characterization. The gold-coated TEM half grids, made by cutting a whole grid into halves, were used to ensure successful flash electropolishing experiments. Details on flash electropolishing are discussed in Section 4.3.1.3. The OmniProbe carrying the specimen was moved to approach the tip of the TEM half grid, and a platinum pattern was used to weld the specimen with the grid. Finally, the platinum joint between the specimen and the OmniProbe was cut off, so that the OmniProbe was moved back to its original parking position. The stage was then rotated 180° to deposit another platinum pattern at the back side of the specimen to ensure steady joint between the specimen and the grid. At this point, the specimen was still ~1.5 μm thick.

The specimen needed to be thinned down to 150-180 nm thickness prior to flash electropolishing. This was conducted by ion beam milling at the stage tilting angle of 52°±1°. At 52°, the specimen appeared edge-on when viewed from the ion beam image, which was an ideal position to measure the sample thickness. A slight tilting of 1° up or down would allow efficient removal of the materials to be thinned down to the final thickness, without completely removing the protective platinum protective layer. The ion beam current was 0.79 nA when the specimen thickness was greater than 800 nm, and 0.23 nA current was used to finally thin down the specimen to the targeted 150-180 nm thickness.

4.3.1.3 Flash Electropolishing

Unlike traditional final thinning method using 5 kV and 2 kV ion beams in the SEM/FIB system, flash electropolishing was used to serve several purposes. First, it was more time efficient to perform flash electropolishing as compared to the traditional low-energy FIB cleaning, especially when the final cleaning for more than two samples is needed. Second, flash electropolishing can remove the FIB induced damage layers on the two surfaces of the S/TEM

specimens. Third, the samples were kept flat during the flash electropolishing, rather than likely being bent during the low-energy FIB cleaning. The removal of the artifacts during the final thinning using flash electropolishing tremendously improved the quality of microstructural characterization with significantly higher signal-to-noise ratio of the S/TEM images. This was particularly important for dislocation loop characterization in irradiated samples, because ion beam in FIB induced small black dot defects that were small-size dislocation loops in-nature. The removal of these small features ensured all features captured during S/TEM characterization were indeed induced by irradiation to bulk materials, rather than artifacts. Several successes of applying this technique were reported in recent years on different material systems [7,102,126–135].

An example of the microstructure of an ion irradiated Ni-based high entropy alloy specimen before and after flash electropolishing is shown in Figure 4.9. As can be seen, before the flash electropolishing, the FIB induced black dot damages are visible throughout the whole region of the sample. After the flash electropolishing, a clear radiation-induced defect band is visible, indicating the radiation affected region, whereas a clean and undamaged deep region can be observed.

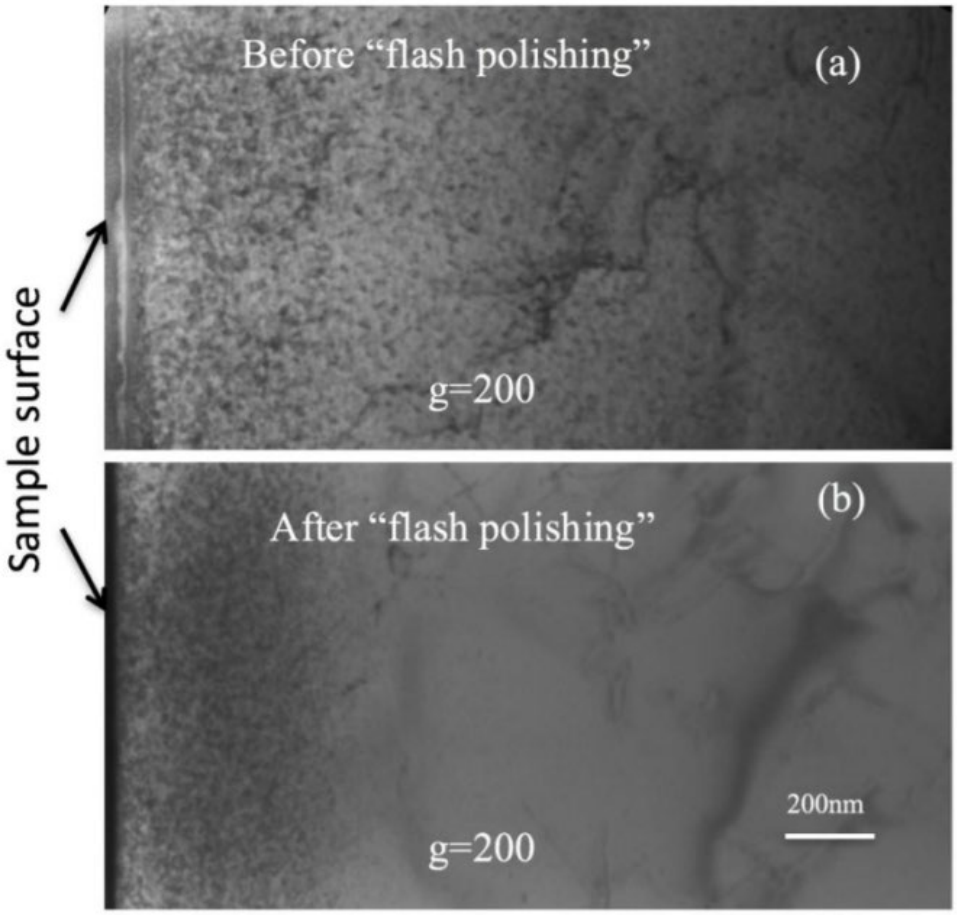

Figure 4.9. An example of an ion irradiated Ni-based high entropy alloy (a) before and (b) after flash electropolishing, adapted from [125].

A typical setup of the flash electropolishing experiment is shown in Figure 4.10. The working mechanism of flash electropolishing of S/TEM specimens and the regular flash electropolishing of bulk materials are same, but different parameters were used. The voltage was 15 V for the studied AM-HT9 material, and the polishing temperature was -40°C ~ -45°C. A mixture of solution containing 4% perchloric acid and 96% ethanol was used as the electrolyte. A self-closing gold-coated tweezer holding the grid acted as anode of the circuit, and a platinum mesh in a hollow square shape that was dipped into the electrolyte was used as conducting cathode of the circuit. The only difference in the circuit between bulk electropolishing and flash electropolishing was that the amount of time for flash electropolishing S/TEM specimens is ultra-

short, at around 0.1-0.3 s, because of the small amount of material to be removed. To accurately control this small amount of time, a timer relay was used to serve the purpose. A set amount of time can be programed into the timer, so that the circuit was connected for the set amount of time after the triggering by pressing a manual button, and automatically disconnected immediately afterwards. After the specimens were flash electropolished, the tweezer carrying the grid was put immediately in a successive fashion into four beakers containing reagent alcohol to clean and remove the residual electrolyte on the specimen and the grid to avoid corrosion. Cleaning lasted for 5 min for each specimen in the four beakers. After the flash electropolishing, the final thickness of the S/TEM specimen usually ranged from 70 nm to 100 nm.

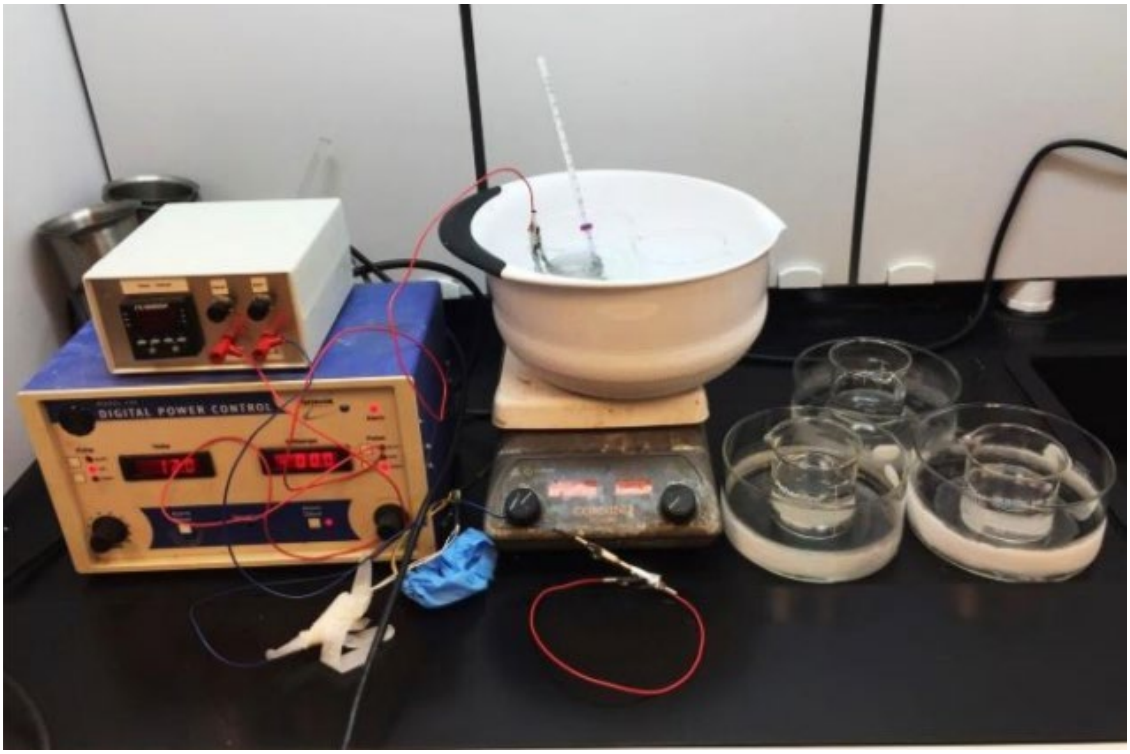

Figure 4.10. The setup for flash electropolishing of S/TEM specimens, adapted from [75].

4.3.2 S/TEM Characterization

All S/TEM characterization was conducted on a Thermo Fisher Talos F200X G2 S/TEM operated at 200kV, either housed at ORNL or MC^2. The Talos S/TEM was equipped with (i) a Gatan One View camera with 4K × 4K resolution to collect CTEM images and diffraction patterns; (ii) four STEM image detectors – bright field (BF), low-angle-annular-dark-field (LAADF), medium-angle-annular-dark-field (MAADF), and high-angle-annular-dark-field (HAADF) with 4K × 4K resolution as well with increasing collection angles to simultaneously collect four STEM images; (iii) four energy-dispersive X-ray spectroscopy (EDX) detectors to collect elemental distribution information with high efficiency; and (iv) a high-speed electron energy loss spectroscopy (EELS) DualEELS system to measure sample thickness.

After loading the S/TEM specimen on the sample holder with double tilt capability, the holder and the specimen were plasma cleaned using an Ar/O recipe for 5 min to remove residual carbon contaminations. Afterwards, the holder was carefully inserted into the S/TEM with caution of not breaking the vacuum of the system.

4.3.2.1 Dislocation Loop and Line Dislocation Imaging: On-Zone [001] STEM-BF

The on-zone STEM bright field (STEM-BF) technique was used for dislocation loop characterization. This technique has been demonstrated to be applicable to various irradiated material systems, including BCC ferritic-based alloys [37,123,136,137], face-center-cubic (FCC) Ni-based concentrated solid solution alloys [7,127,131,132,135,138], and uranium nitrides [139]. In this work, on-zone [001] STEM-BF was used, with the advantages [127] over the traditional kinematic two-beam condition imaging [102,126,129,130,133,140,141] in the CTEM mode: (i) improving signal-to-noise ratio due to suppressed bend contours and thickness fringes [142]; (ii) exhibiting all dislocation loop and line dislocation structures [143]; and (iii) enabling reliable and convenient identification of dislocation loop type from the morphology [127,144].

AM-HT9 has a BCC ferritic crystalline structure, and two types of dislocation loops with different Burgers vectors are well-known to form: $a\langle 100\rangle$ and $a/2\langle 111\rangle$ [123], where a represents the lattice parameter of the unit cell of AM-HT9. The projected dislocation loop morphology is demonstrated in Figure 4.11. As can be seen, dislocation loops with edge-on and in-plane morphology were identified as $a\langle 100\rangle$ type, whereas elliptical dislocation loops with major axes normal to each other were identified as $a/2\langle 111\rangle$ type.

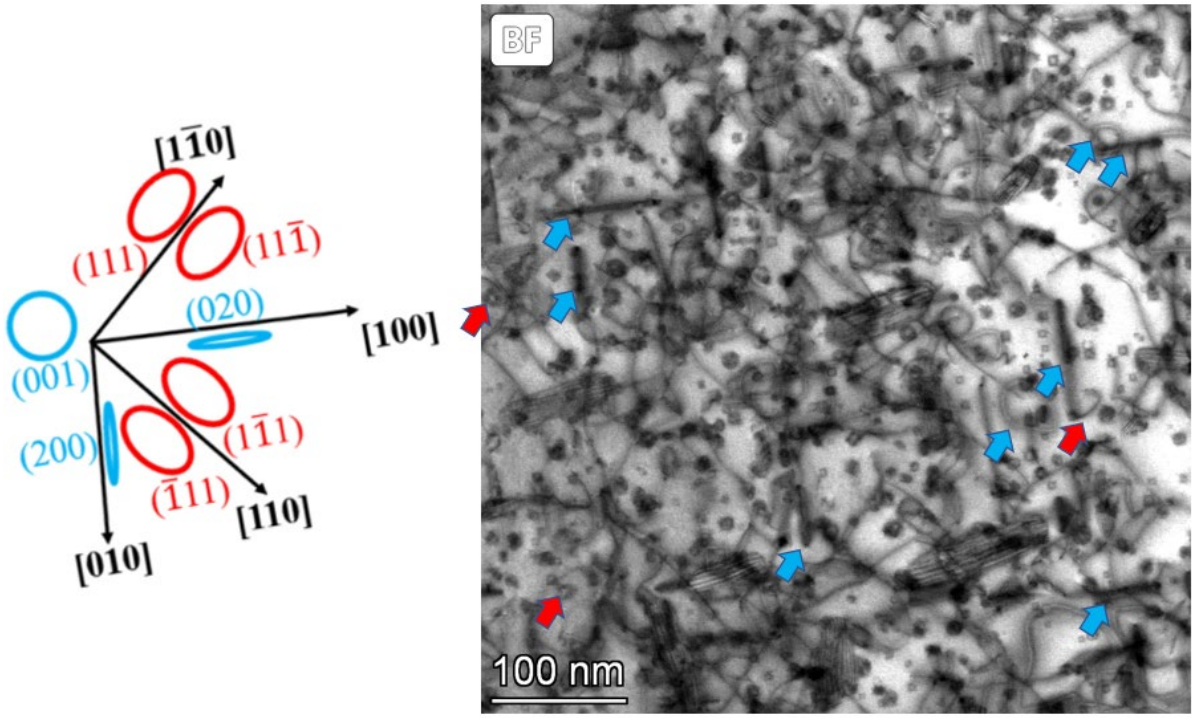

Figure 4.11. The developed dislocation loop morphology map developed by B. Yao [123]*, and an on-zone [001] STEM-BF image of an irradiated AM-HT9 alloy with loop type labeled: a/2⟨111⟩ in red and a⟨100⟩ in blue. Two images are rotated so that the orientation matches each other.*

After the sample holder with the specimen was loaded into the S/TEM, the stage was moved so that the specimen was brought into the field-of-view in the conventional TEM (CTEM) mode. The TEM was then aligned to ensure the best beam and imaging quality. As mentioned, the targeted depth of interest was 500-700 nm from the sample surface, or the interface between

platinum protective layer and the matrix. The grain at the target depth was then located, preferably has reasonably large grain size and close to [001] crystallographic orientation. The sample was then tilted to be exactly on-zone [001]. The diffraction pattern was then taken as a reference for later-on identification of dislocation loop types. Then, the S/TEM was switched to STEM mode for imaging dislocation loops. The 4K × 4K high resolution images were collected for all studied samples, with the vender-indicated magnification of 320 kx and the dwell time set up resulting in the collection time of 40 s.

After the image collection, ImageJ software was used to measure the diameters of all the observed dislocation loops. Regardless of the morphology of the dislocation loops (in-plane thus circular, inclined thus elliptical, or edge-on), the longest axes were measured as the diameter of each dislocation loop with the assumption that most dislocation loops are in circular shape. In this case, the length of the longest axes is always the length of the diameter. All reported dislocation loop sizes were measured in this way in diameter.

4.3.2.2 Clustering Imaging: STEM-EDX

The four STEM-EDX detectors were inserted to collect EDX signals at the same time. The magnification used was either 225 kx or 450 kx for all EDX data collection, with 1K × 1K resolution. The dwell time was selected so that each frame was completed within 5 s to minimize sample drifting within each frame. All elements in Table 4.1 were selected. Data collection usually took 10 min to develop significant visualization of elemental distributions in the specimen with a count rate of 100 kcps or greater. Spot size 1-2 (vendor indicated) within the Talos STEM was used to achieve this high count rate.

The Bruker ESPRIT software coupled with the Talos S/TEM at ORNL or the Velox software coupled with the Talos S/TEM in MC^2 was used for the STEM-EDX data collection. Two

types of images were generated in different ways. For the STEM-EDX maps that contained one element, images were directly obtained by a simple output using the Bruker ESPRIT or Velox software. For the Bruker ESPRIT-collected STEM-EDX maps containing four elements, as shown in Section 0, the overlay images were generated by data manipulation achieved by using a custom, in-house Python code [145], attached in We have been awarded a Nuclear Science User Facilities (NSUF) Rapid Turnaround Experiment (RTE) project entitled . The code was used to generate overlay images that highlight the various cluster populations found in the raw data. The code generates the images by completing the following steps [37]:

1) Individual text files for each element of interest (Cr, Nb, Ni, and Cu) that contain the integrated peak counts of the given element at each pixel were exported from the Bruker ESPRIT software.

2) A low-level threshold (e.g., <1–5 counts) for the counts at each pixel was applied to filter out systematic background for each element.

3) A Gaussian filter using the scikit-image package and a sigma value between 2 and 4.5 [146] was used to smooth out the elemental maps.

4) A single-color ramp was assigned to each element.

5) Final mapping was obtained by overlaying four maps together.

6) The zero channel in the integrated image color ramp was converted from black to white.

After the image collection, ImageJ software was used to measure the diameters of all the observed precipitates. All reported precipitate sizes were measured in this way in diameter.

4.3.2.3 Thickness Measurement: EELS

This method estimated the thickness of the sample by measuring the amount of electron energy loss as the beam passed through the sample, using a built-in algorithm in the

DigitalMicrograph® software. The BF, LAADF and MAADF detectors were taken out to avoid blocking the beam from going through to reach the EELS detector. After aligning and sharpening the zero-loss peak in the EELS spectrum collected by placing a stationary beam in the vacuum area so that there was no energy loss of the electrons, the exposure time was maximized to increase the signal-to-noise ratio of the spectrum, while the EELS camera was not over-exposed to avoid the damage cause by the strong beam. Then the area of interest on the specimen was selected to collect the mapping of the EELS spectrum by scanning the beam within this region. The step width of the EELS mapping was selected to be about 3-5 nm to ensure reasonably good spatial resolution. The average of the thickness spectrum within this region was then used as nominal thickness to compute feature volumetric density.

The thickness measurement is dependent on the selected divergence angle, collection angle, assumed specimen atomic mass, electron beam energy, and other factors. With the same procedure used every time, the error was consistent among all experiments and thus can be set to a fixed value of around 10% [62] as a result of systematic uncertainties in the assumed variables within the calculation.

4.3.2.4 Cavity Imaging: Through-Focus TEM

The Talos S/TEM was switched back to CTEM mode for cavity imaging. The off-zone through-focus method [147,148] was used for the purpose. The procedures are described as follows. The area of interest was first located at the region where the thickness was measured. The selected area aperture was then inserted to select this region. After switching the CTEM into diffraction mode, the diffraction pattern showed up. The objective aperture was then inserted to include only the transmitted beam, so that when switched back to CTEM, BF mode was chosen. If dislocation and dislocation loop contrast were visible, the sample was then randomly tilted

slightly to an off-diffracting condition, so that most of the diffraction contrast from these features disappeared. The sample was then brought to the eucentric height by moving the Z-height of the stage control. The focus knob was then turned to apply defocus in the TEM-BF images. Both under-focus and over-focus images were collected with the magnification of 190 kx and the resolution of 4K × 4K. The Fresnel contrast [126,130,133,149,150] around the edge of the cavities in the irradiated TEM samples developed as the image was brought out of focus. Images were then captured for statistical counting. Another commonly used imaging method of STEM high-angle-annular-dark-field (STEM-HAADF) was not used in this work. This method would work well for imaging large cavities by utilizing the Z-contrast, but it fails when used to image small cavities of a few nanometers in size, such as those that nucleated and had not undergone significant growth. On the other hand, the mentioned Fresnel contrast-based method in the CTEM mode allows effective imaging of both small and large cavities.

After the image collection, ImageJ software was used to measure the diameters of all the observed cavities. All reported cavity sizes were measured in this way in diameter.

4.3.3 Counting Statistics, Sink Strength Calculation, and Error Analysis

For all the reported statistics from counting, an effort was made to minimize the errors. There are three types of error that are needed to be accounted for: error due to TEM resolution, error due to EELS thickness measurements, and error due to counting statistics. The TEM image resolution is 0.08 nm/pixel, which is much lower than the measured feature size of a few nanometers or larger. Therefore, the error due to TEM resolution is considered negligible in this work. The fitting of the EELS zero loss method for measuring the sample thickness exhibits an error of 10%, as mentioned before. This thickness measurement affects the calculation of number density but is not dependent on any other factors,

$$\sigma_t = 10\% \times t = 0.1t \quad \text{Equation 4.7}$$

where t is the measured sample thickness using EELS zero loss method.

To compute density of features using area as two-dimensional information such as line dislocations,

$$\rho_{2D} = \frac{N_{2D}}{lt} \quad \text{Equation 4.8}$$

where N_{2D} is the number of intersections between line dislocations and the cross-sectional cut-plane defined by a randomly drew straight line on a TEM micrograph, l is the length of the line, and t is the thickness of the TEM sample. The error associated with it is calculated as

$$\sigma_{\rho_{2D}} = 0.1\rho_{2D} \quad \text{Equation 4.9}$$

To compute density of features using volume as three-dimensional information such as cavities, precipitates, and dislocation loops,

$$\rho_{3D} = \frac{N_{3D}}{abt} \quad \text{Equation 4.10}$$

where N_{3D} is the counted amount of a specific feature, a and b are the width and length of the area of interest. The error associated with the feature density is then

$$\sigma_{\rho_{3D}} = 0.1\rho_{3D} \quad \text{Equation 4.11}$$

For the computed swelling,

$$Swelling = \frac{\frac{\pi}{6}\sum d_{cav}^3}{abt - \frac{\pi}{6}\sum d_{cav}^3} \quad \text{Equation 4.12}$$

where d_{cav} is the measured diameter of each cavity. The error associated with the swelling is then computed as

$$\sigma_{Swelling} = Swelling \times \frac{0.1abt}{abt - \frac{\pi}{6}\sum d_{cav}^3} \quad \text{Equation 4.13}$$

To calculate the sink strength of cavities, which are considered neutral sinks, the following equation is used,

$$S_{cav\,i,v} = 2\pi \sum d_{cav}\rho_{cav} \quad \text{Equation 4.14}$$

$$S_{cav\,i,v} = \frac{2\pi}{abt} \sum d_{cav} \quad \text{Equation 4.15}$$

Therefore, the error associated with the cavity sink strength is

$$\sigma_{S_{cav\,i,v}} = 0.1 S_{cav\,i,v} \quad \text{Equation 4.16}$$

Similar to cavities, to calculate the sink strength of Ni-rich and Cr-rich precipitates, which are considered incoherent thus neutral sinks, the following equations are used,

$$S_{Ni\,i,v} = \frac{2\pi}{abt} \sum d_{Ni} \quad \text{Equation 4.17}$$

$$S_{Cr\,i,v} = \frac{2\pi}{abt} \sum d_{Cr} \quad \text{Equation 4.18}$$

where d_{Ni} and d_{Cr} are measured diameters of each Ni-rich and Cr-rich precipitate, respectively. Therefore, the error associated with the Ni-rich and Cr-rich precipitate sink strengths are

$$\sigma_{S_{Ni\,i,v}} = 0.1 S_{Ni\,i,v} \quad \text{Equation 4.19}$$

$$\sigma_{S_{Cr\,i,v}} = 0.1 S_{Cr\,i,v} \quad \text{Equation 4.20}$$

Dislocation loops are considered to be biased towards preferentially absorbing interstitials over vacancies. The sink strength of dislocation loops is as follows

$$S_{loop\,v} = \frac{\pi}{abt} \sum d_{loop} \quad \text{Equation 4.21}$$

$$S_{loop\,i} = z_{loop\,i} \times \frac{\pi}{abt} \sum d_{loop} \quad \text{Equation 4.22}$$

where d_{loop} is the measured diameters of each dislocation loop, regardless of $a/2\langle 111\rangle$ or $a\langle 100\rangle$ dislocation loop types, and $z_{loop\,i}$ is 1.25 [151–153]. The error associated with the sink strength of dislocation loops is

$$\sigma_{S_{loop\,i,v}} = 0.1 S_{loop\,i,v} \quad \text{Equation 4.23}$$

Similarly, line dislocations are also considered to be biased towards interstitial absorption. The sink strength of line dislocations is calculated by

$$S_{dis\,v} = \rho_{dis} \quad \text{Equation 4.24}$$

$$S_{dis\,i} = z_{dis\,i} \times \rho_{dis} \quad \text{Equation 4.25}$$

where ρ_{dis} is line dislocation density, and $z_{loop\,i}$ is 1.07 [151–153]. The error associated with the sink strength of line dislocations is

$$\sigma_{S_{dis\,i,v}} = 0.1 S_{dis\,i,v} \quad \text{Equation 4.26}$$

The total sink strength of vacancies, S_v, and interstitials, S_i, can then be calculated by summing up individual contributors such as line dislocations, dislocation loops, cavities, precipitates, and grain boundaries,

$$S_v = \sum_j S_{j\,v} \quad \text{Equation 4.27}$$

$$S_i = \sum_j S_{j\,i} \quad \text{Equation 4.28}$$

with the error calculated by

$$\sigma_{S_v} = \sqrt{\sum_j \sigma_{S_{j\,v}}^2} \quad \text{Equation 4.29}$$

$$\sigma_{S_i} = \sqrt{\sum_j \sigma_{S_{j\,i}}^2} \quad \text{Equation 4.30}$$

4.3.4 Numerical Solutions to the Cavity Growth Rate Equation and Error Analysis

Before discussing the results of the irradiation experiments, it is helpful to describe a common analytical framework in this section to be used in the analysis. The cavity growth rate equation depends on several parameters from the microstructure, the irradiation conditions, and the material properties. With the analytical solution from the defect balance equations, the theoretical swelling rate can be computed to compare with the experimental results and provide insights of the factors governing the swelling rate in the three conditions of irradiated AM-HT9 alloys. Starting from the defect balance equations [79],

$$\frac{dC_v}{dt} = K_0 - K_{iv}C_iC_v - D_vC_vS_v \qquad \text{Equation 4.31}$$

$$\frac{dC_i}{dt} = K_0 - K_{iv}C_iC_v - D_iC_iS_i \qquad \text{Equation 4.32}$$

where C_v and C_i are irradiation-induced vacancy and interstitial concentrations (dimensionless), respectively. K_0 is the damage rate in dpa/s or s^{-1}, and K_{iv} is the defect recombination rate in s^{-1}. D_v and D_i are vacancy and interstitial diffusion coefficients, respectively, and S_v and S_i are total sink strength for vacancy and interstitial absorption, respectively.

During the steady state, $\frac{dC_v}{dt}$ and $\frac{dC_i}{dt}$ are zero, giving

$$K_0 - K_{iv}C_iC_v - D_vC_vS_v = 0 \qquad \text{Equation 4.33}$$

$$K_0 - K_{iv}C_iC_v - D_iC_iS_i = 0 \qquad \text{Equation 4.34}$$

and the steady-state concentrations of irradiation-induced vacancies and interstitials can then be solved as

$$C_v = \frac{D_i S_i}{2K_{iv}}\left(\sqrt{1+\frac{4K_0K_{iv}}{D_iD_vS_iS_v}}-1\right) \quad \text{Equation 4.35}$$

$$C_i = \frac{D_v S_v}{2K_{iv}}\left(\sqrt{1+\frac{4K_0K_{iv}}{D_iD_vS_iS_v}}-1\right) \quad \text{Equation 4.36}$$

Note that among all the irradiation-induced vacancies that survive from either recombination or absorption by defect sinks, a small amount of thermal vacancies can be accommodated in the matrix of the material, resulting in a slightly lower amount of effective vacancies that are able to contribute to the cavity growth. Thus,

$$C_v^{effective} = C_v - C_v^{thermal} \quad \text{Equation 4.37}$$

where $C_v^{effective}$ is account for the effective vacancy concentration that actually contributes to cavity growth, and $C_v^{thermal}$ is the thermal vacancy concentration representing vacancies that are accommodated in the matrix without contributing to the cavity growth.

In order to calculate the cavity growth rate, Equation 4.38 is used,

$$\frac{d(\Delta V/V)}{d\Phi} = \frac{1}{K_0} \times \frac{d(\Delta V/V)}{dt} \quad \text{Equation 4.38}$$

where $\frac{d(\Delta V/V)}{d\Phi}$ is the swelling rate in dpa^{-1}, Φ is the damage level in dpa, $\Delta V/V$ is the swelling, t is the time in s, and the swelling rate with respect to time can be further expanded as

$$\frac{d(\Delta V/V)}{dt} = \frac{4\pi r_{cav}^2 \rho_{cav}}{\Omega} \times \dot{r_{cav}} \quad \text{Equation 4.39}$$

Here, r_{cav} is the average cavity radius, $\dot{r_{cav}}$ is the cavity radius growth rate with respect to time, ρ_{cav} is the cavity number density, Ω is the atomic volume, or, the volume taken by each atom.

Finally, with the last piece of equation below,

$$r_{cav}\dot{r_{cav}} = \Omega(D_v C_v^{effective} - D_i C_i) \quad \text{Equation 4.40}$$

the numerical solution of the theoretical swelling rate with respect to the damage level can be obtained by plugging in the above-mentioned solution of steady-state effective vacancy and interstitial concentrations:

$$\frac{d(\Delta V/V)}{d\Phi} = d_{cav}\rho_{cav}[\frac{\pi D_i D_v}{K_0 K_{iv}}\left(\sqrt{1+\frac{4K_0K_{iv}}{D_iD_vS_iS_v}}-1\right)(S_i - S_v) - \frac{2\pi D_v C_v^{thermal}}{K_0}] \quad \text{Equation 4.41}$$

Here, statistical results of d_{cav}, ρ_{cav}, S_i and S_v from experiments need to be introduced into Equation 4.41 to solve for the theoretical swelling rate from the current state, or damage level, to the next state, or the next higher damage level. For all the irradiations conducted within, the damage rates were kept at 5.8×10^{-4} dpa/s. Other parameters in the final solution can be calculated separately as detailed below.

$$K_{iv} = \frac{z_{iv}(D_i + D_v)}{a_0^2} \quad \text{Equation 4.42}$$

where K_{iv} of 500 is the combinatorial factor [3], a_0 is the lattice parameter of the material and in this case, is 2.89×10^{-10} m [79]. The interstitial and vacancy diffusion coefficient can be computed as,

$$D_i = D_{i0}^m \exp\left(-\frac{E_i^m}{k_B T}\right) \quad \text{Equation 4.43}$$

$$D_v = D_{v0}^m \exp\left(-\frac{E_v^m}{k_B T}\right) \quad \text{Equation 4.44}$$

where D_{i0}^m of 6.59×10^{-7} m^2/s and D_{v0}^m of 5.92×10^{-6} m^2/s are pre-exponential factors for Fe interstitial and vacancy diffusion respectively, E_i^m of 0.36 eV and E_v^m of 0.77 eV are activation energy for Fe interstitial and vacancy diffusivity respectively, in FM steels [154]. k_B is the

Boltzmann constant of 1.38×10^{-23} J/K, and T is the irradiation temperature in Kelvin. The thermal vacancy concentration is calculated by

$$C_v^{thermal} = \exp\left(-\frac{E_v^f}{k_B T}\right) \quad \text{Equation 4.45}$$

where E_v^f of 1.6 eV is the activation energy for Fe vacancy formation [155].

All the parameters used to obtain the computed theoretical swelling rate are listed in Table 4.3.

Table 4.3. Parameters used to compute the theoretical swelling rate.

Symbol	Physical meaning	Values
D_{i0}^m	pre-exponential factor for Fe interstitial diffusion	6.59×10^{-7} m^2/s
D_{v0}^m	pre-exponential factor for Fe vacancy diffusion	5.92×10^{-6} m^2/s
E_i^m	activation energy for Fe interstitial diffusivity	0.36 eV
E_v^m	activation energy for Fe vacancy diffusivity	0.77 eV
E_v^f	activation energy for Fe vacancy formation	1.6 eV
a_0	lattice parameter	2.89×10^{-10} m
K_0	damage rate	5.8×10^{-4} dpa/s
z_{iv}	combinatorial factor	500

Lastly, the error of the theoretical swelling rate $\frac{d(\Delta V/V)}{d\Phi}$, or if defined by f_1, is developed using error propagation,

$$\sigma_{f_1} = f_1 \times \sqrt{\left(\frac{\sigma_{d_{cav}}}{d_{cav}}\right)^2 + \left(\frac{\sigma_{\rho_{cav}}}{\rho_{cav}}\right)^2 + \left(\frac{\sigma_{f_2}}{f_2}\right)^2} \quad \text{Equation 4.46}$$

where f_2 is defined as

$$f_2 = \frac{\pi D_i D_v}{K_0 K_{iv}}\left(\sqrt{1+\frac{4K_0K_{iv}}{D_iD_vS_iS_v}}-1\right)(S_i - S_v) - \frac{2\pi D_v C_v^{thermal}}{K_0} \quad \text{Equation 4.47}$$

and its error is

$$\sigma_{f_2} = \frac{\pi D_i D_v}{K_0 K_{iv}}\left(\sqrt{1+\frac{4K_0K_{iv}}{D_iD_vS_iS_v}}-1\right)(S_i - S_v)\sqrt{\left(\frac{2K_0K_{iv}}{D_iD_vS_iS_v}\sqrt{\frac{\left(\frac{\sigma_{S_i}}{S_i}\right)^2+\left(\frac{\sigma_{S_v}}{S_v}\right)^2}{1+\frac{4K_0K_{iv}}{D_iD_vS_iS_v}}}*\frac{1}{\sqrt{1+\frac{4K_0K_{iv}}{D_iD_vS_iS_v}}-1}\right)^2+\left(\frac{\sqrt{\sigma_{S_i}^2+\sigma_{S_v}^2}}{S_i-S_v}\right)^2} \quad \text{Equation 4.48}$$

4.3.5 Atom-Probe Tomography

To fully quantify the composition of precipitates observed in STEM-EDX in Heat A, APT was performed using the CAMECA® LEAP 5000XS with an approximately 80% detection efficiency at the Northwestern University Center for Atom-Probe Tomography (NUCAPT) [37]. APT was performed in laser mode (355 nm wavelength ultraviolet laser) at 25 pJ laser pulse energy and a 50 K base temperature for the ASB specimens. For the ACO-3 and FCRD specimens, APT was performed at 30 pJ laser pulse energy and a 60 K base temperature with a 1–2% detection rate and a 250–500 kHz laser pulse repetition frequency. Two to three APT tips for each sample condition were run, and there were 20–70 million atoms for each run. Finally, the analyzed volumes were reconstructed, and the data were processed using CAMECA's Integrated Visualization and Analysis Software package, version 3.8. During sample reconstruction, the image compression factor (k) was held constant at 1.65, and the field factor (k) was tuned to provide correct interplanar distances for various identified crystallographic poles in the detector hit map. The k values ranged between 3.2 and 3.84 [37].

For global composition calculations, peak deconvolution was employed to separate mass spectra peaks for species such as $^{54}Cr^{2+}/^{54}Fe^{2+}$ and $^{58}Fe^{2+}/^{58}Ni^{2+}$. Precipitation was identified using

the isoconcentration method. Compositional information for the identified precipitates was obtained by employing the proximity histogram concentration profile methodology for APT and extracting the average “core” concentration of identified clusters [156]. Because few atoms at the core of the identified precipitates were available, peak deconvolution of the precipitate cores was not practical and some minor variation in Fe/Ni concentrations might be expected in reported precipitate compositions. Because few precipitates were identified in each specimen, size and dispersion information was not computed by this method and was instead computed using the STEM-EDX results as mentioned in Section 4.3.2.2 [37].

Chapter 5 Results

This chapter presents the results of the characterization of the ion irradiation-induced microstructures in three thermally-treated conditions of two heats of AM-HT9. The results are divided into three sections based on the irradiation campaign undertaken. The first section focuses on the screening results on microchemical responses across the three conditions of AM-HT9 of Heat A under single-ion irradiations. The second and the third sections focus on the results of dual-ion irradiation on the Heat B of three conditions of AM-HT9. Specifically, the second section focuses on the results with varying irradiation damage levels, while irradiation temperatures, damage rates, and helium co-injection rates are kept the same; the third section focuses on the results with varying irradiation temperatures, while damage levels, damage rates, and helium co-injection rates are kept the same.

5.1 Unirradiated Microstructures of AM-HT9

The unirradiated microstructures of three conditions (ASB, ACO3 and FCRD) of Heat A of AM-HT9 were characterized by Sridharan et al [49], as shown in Figure 5.1 and Figure 5.2 using optical microscopy, SEM, EBSD, and S/TEM respectively. The corresponding sink strengths of ASB, ACO3 and FCRD specimens were calculated as 12.2, 2.4, and $2.7 \times 10^{15}/m^2$, respectively [49].

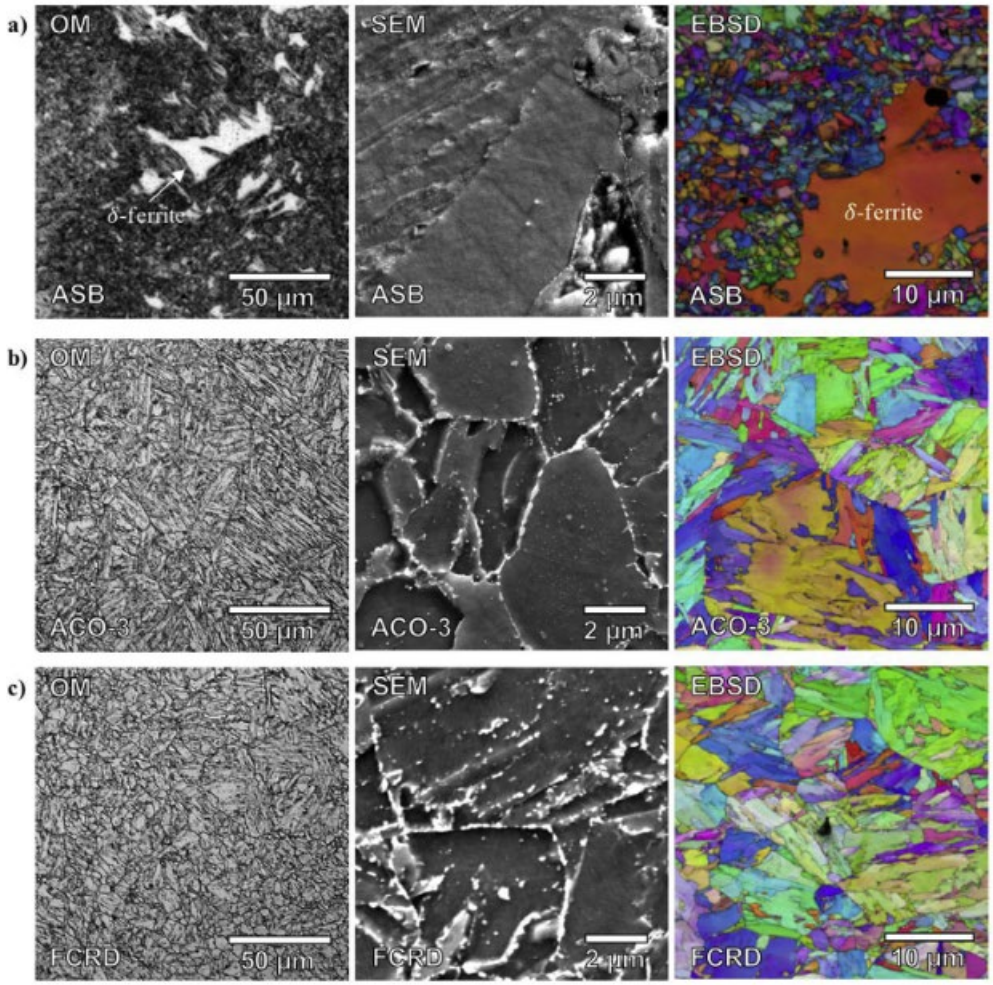

Figure 5.1. Optical micrographs showing the general martensitic structure, SEM secondary electron micrographs showing carbide decorations, and EBSD micrographs showing grain orientation relationships in the (a) ASB, (b) ACO3, and (c) FCRD conditions of AM-HT9 in Heat A. From [49]

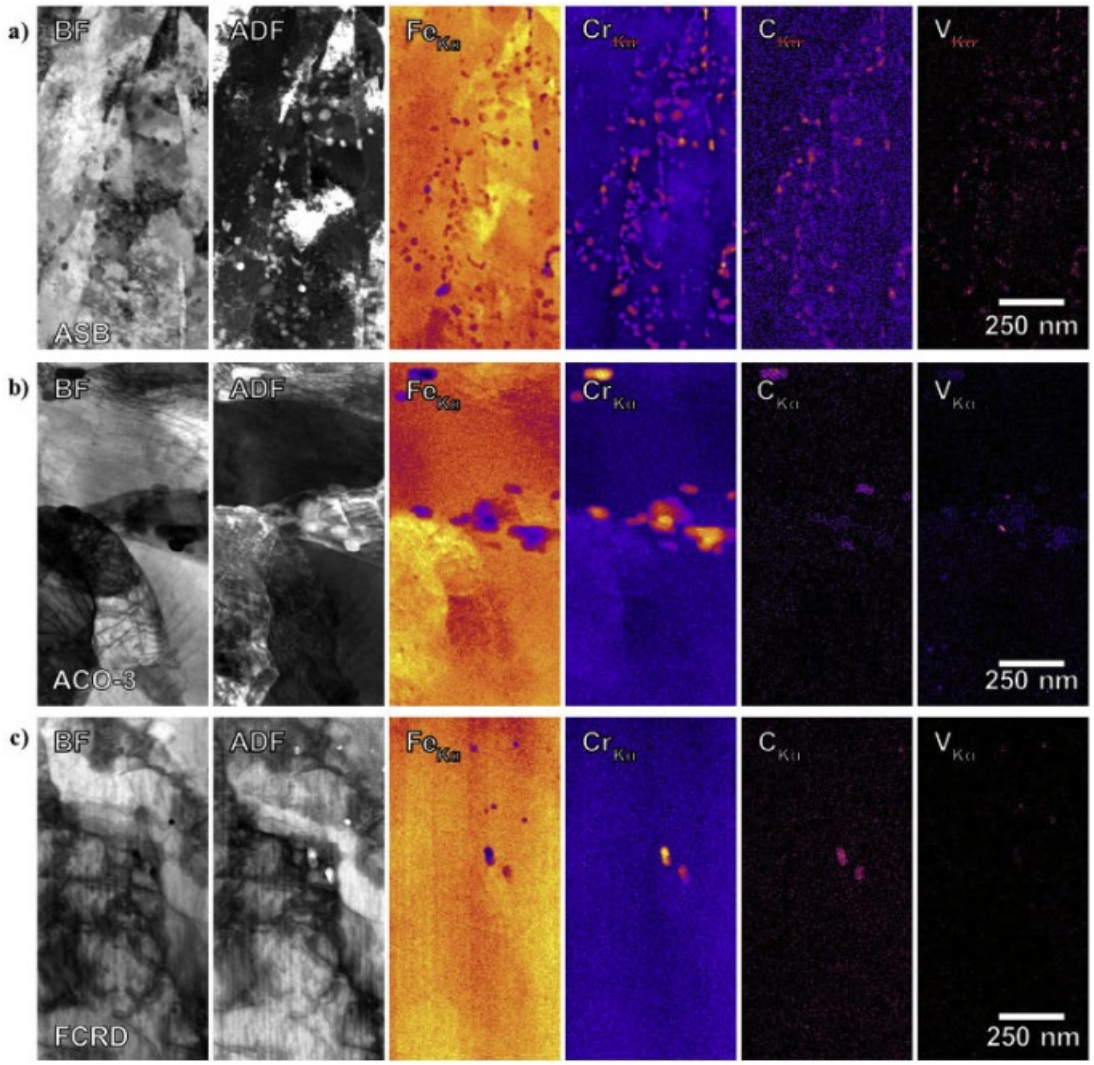

Figure 5.2. STEM micrographs and EDS maps showing the general lath structure and distribution of precipitates in the Heat A of AM-HT9 in (a) ASB, (b) ACO3, and (c) FCRD conditions. Color scale arbitrary, size scale identical for all images. From [49].

Due to the Cu uptake from the AM and processing history in Heat A, as discussed in Section 5.2 and Section 6.1, Heat B was fabricated with no observation of Cu uptake. Very similar grain structures between the Heat A and Heat B revealed by EBSD are shown in Figure 5.3 and optical micrographs in Figure 5.4. In addition, the in-grain dislocation microstructures within ACO3 and FCRD specimens of Heat B of AM-HT9 are shown in Figure 5.5, with ASB sample containing highly defective microstructures with high density of line dislocations and grain

boundary area. The sink strengths in three conditions of AM-HT9 in Heat B are calculated as 7.5, 1.9, and 2.4 × 10^{15} (/m^2) for ASB, ACO3, and FCRD respectively. The most dominant sink features are grain boundaries for ASB and line dislocations for ACO3 and FCRD, which are considered within as neutral and biased sinks, respectively.

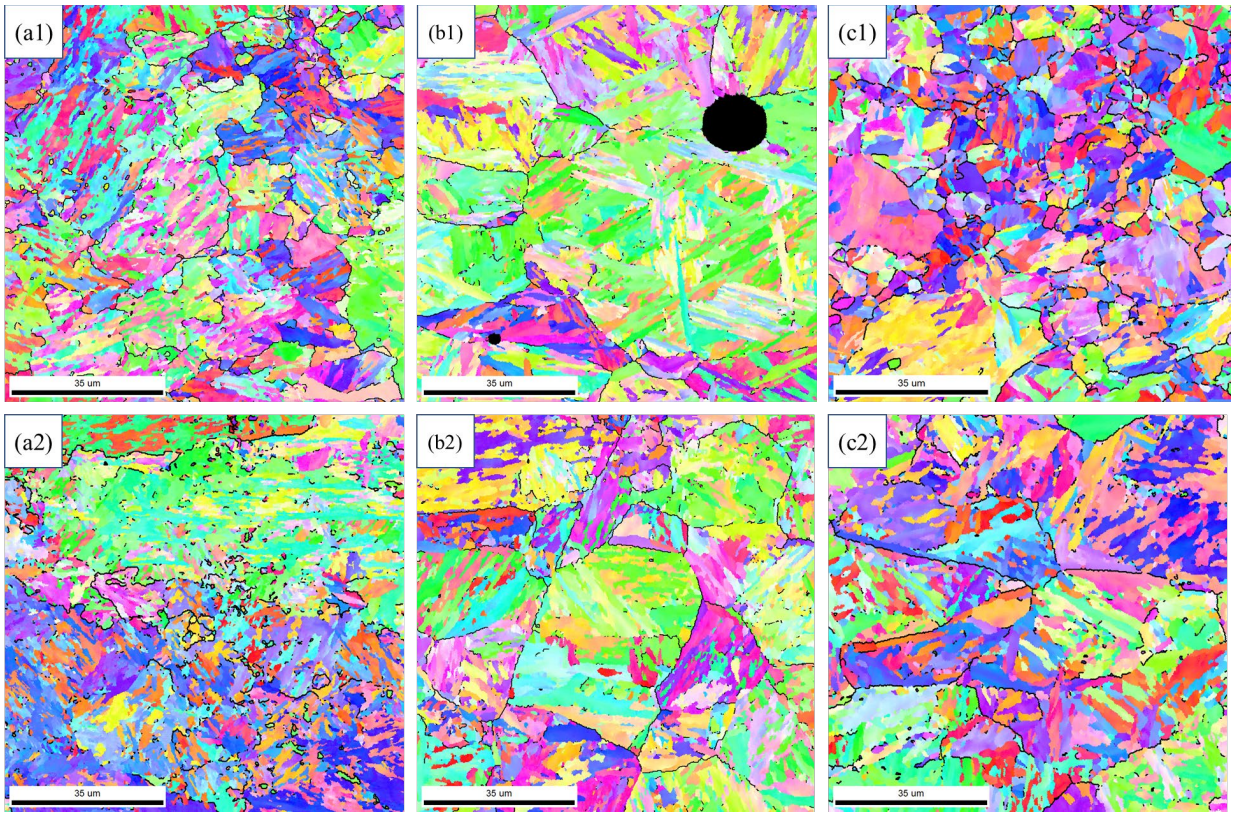

Figure 5.3. EBSD micrographs showing the similar grain structure of the two heats of AM-HT9: (a1) ASB (Heat A), (b1) ACO3 (Heat A), (c1) FCRD (Heat A), (a2) ASB (Heat B), (b2) ACO3 (Heat B), and (c2) FCRD (Heat B), respectively.

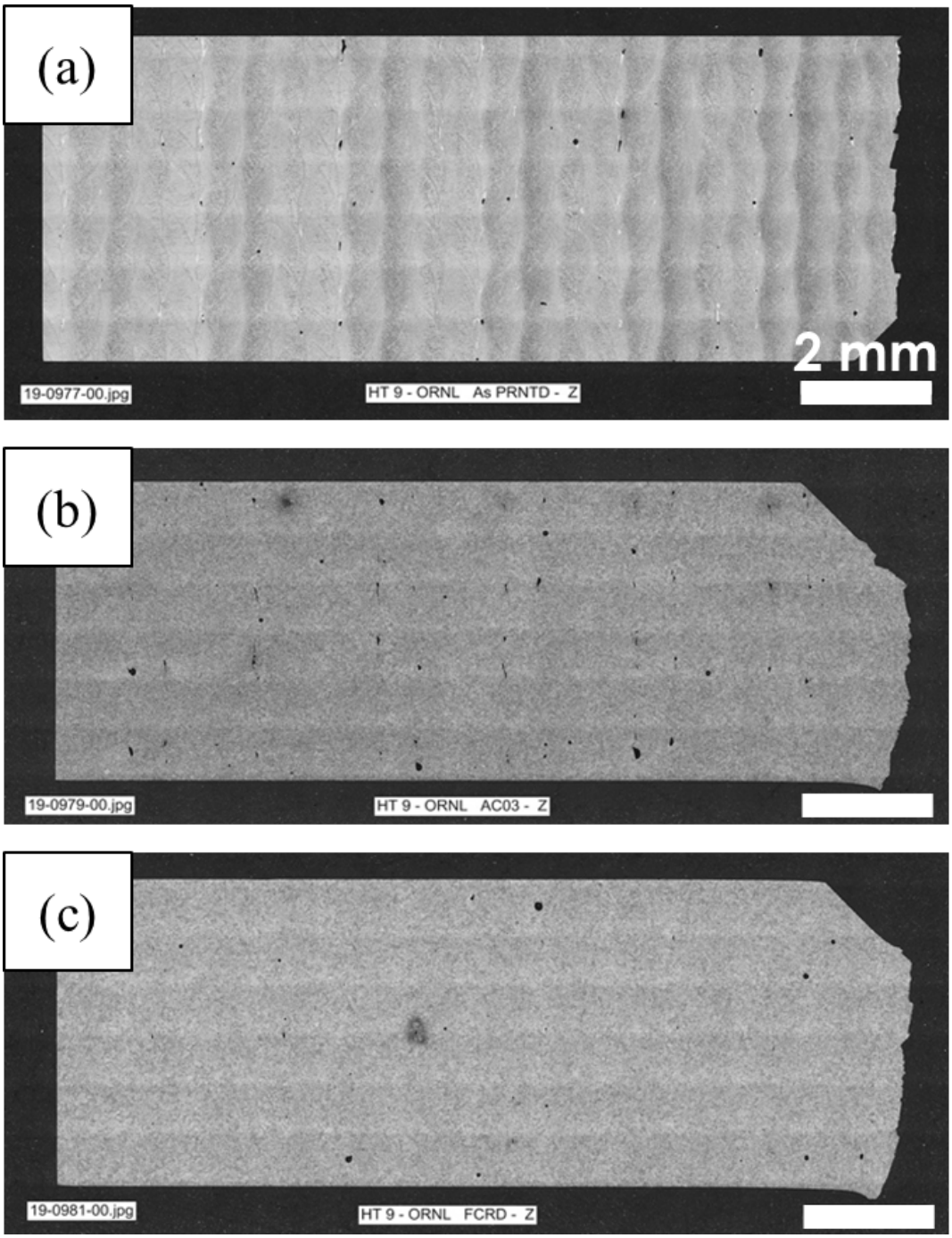

Figure 5.4. Optical micrographs showing the (a) layered structures within the ASB condition of AM-HT9 (Heat B), with microstructures homogenized after heat-treatments shown in (b) ACO3 and (c) FCRD. Build direction is left-to-right in the images.

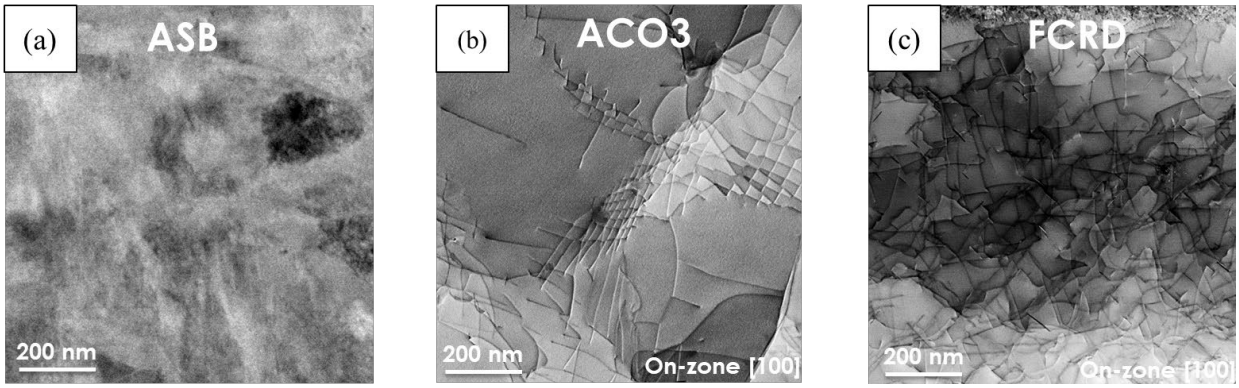

Figure 5.5. STEM-BF micrographs showing the in-grain microstructures in the Heat B of AM-HT9 in (a) ASB, (b) ACO3, and (c) FCRD conditions, respectively. The ACO3 and FCRD microstructures were characterized at on-zone [001] STEM-BF conditions showing all line dislocation structures.

5.2 Microchemical Responses in Heat A of AM-HT9 under Single-Ion Irradiation

The three conditions of Heat A of AM-HT9 were single-ion-irradiated with 5 MeV Fe^{2+} to 50 dpa at 460°C to cross-compare their microstructural responses. High-magnification (450 kx) STEM-EDX mapping coupled with STEM low-angle annular dark-field (LAADF) images was obtained to ascertain details of the microchemical evolution within the grain and matrix before and after irradiation. The results are shown for the ASB, ACO-3 and FCRD conditions of AM-HT9 (Heat A) in Figure 5.6. There are several points to note. First, STEM-LAADF images are reported here because they exhibit the best contrast among images obtained from all four detectors (BF, LAADF, MAADF, and HAADF) for the clustering present in the microstructures. Second, the following elements with significantly different distributions before and after irradiation are included in the STEM-EDX results: Ni, Cu, Nb, and Cr, because of the identification of V/Nb-rich, Ni/Si/Mn-rich, Cr-rich carbides and Cu-rich precipitates/clustering in some or all the samples either before or after irradiation. Third, the unirradiated STEM-EDX maps reported here were obtained past the irradiation-affected depth, which went through the thermal cycle during the 24 h

irradiation. Fourth, no significant differences in precipitate types or morphologies in the unirradiated microstructures were observed with and without the thermal cycle.

Ni/Si/Mn-rich clusters are observed to form in all irradiated conditions of AM-HT9 (Heat A) under single-ion irradiation with the damage level of 50 dpa at 460°C. In addition, Cu-rich clusters are observed to form only in the ACO3 and FCRD conditions, whereas no Cu-rich clusters are observed in the ASB condition of AM-HT9 (Heat A). Representative Ni/Si/Mn-rich and Cu-rich precipitates induced by irradiation are shown in Figure 5.6. The full statistics of Ni/Si/Mn-rich and Cu-rich precipitates are summarized in Table 5.1. As can be seen, the Ni/Si/Mn-rich precipitates have a size of 6.1 ± 1.7 nm, 9.7 ± 2.3 nm, 10.5 ± 3.1 nm and a density of 1.3 (± 0.2) × $10^{22}/m^3$, 2.9 (± 0.5) × $10^{21}/m^3$, 3.7 (± 0.8) × $10^{21}/m^3$ in the ASB, ACO3, and FCRD respectively. The Cu-rich precipitates have a size of 8.1 ± 2.1 nm, 10.0 ± 2.8 nm, and a density of 2.9 (± 0.5) × $10^{21}/m^3$, 3.8 (± 0.7) × $10^{21}/m^3$ in irradiated ACO3 and FCRD, respectively.

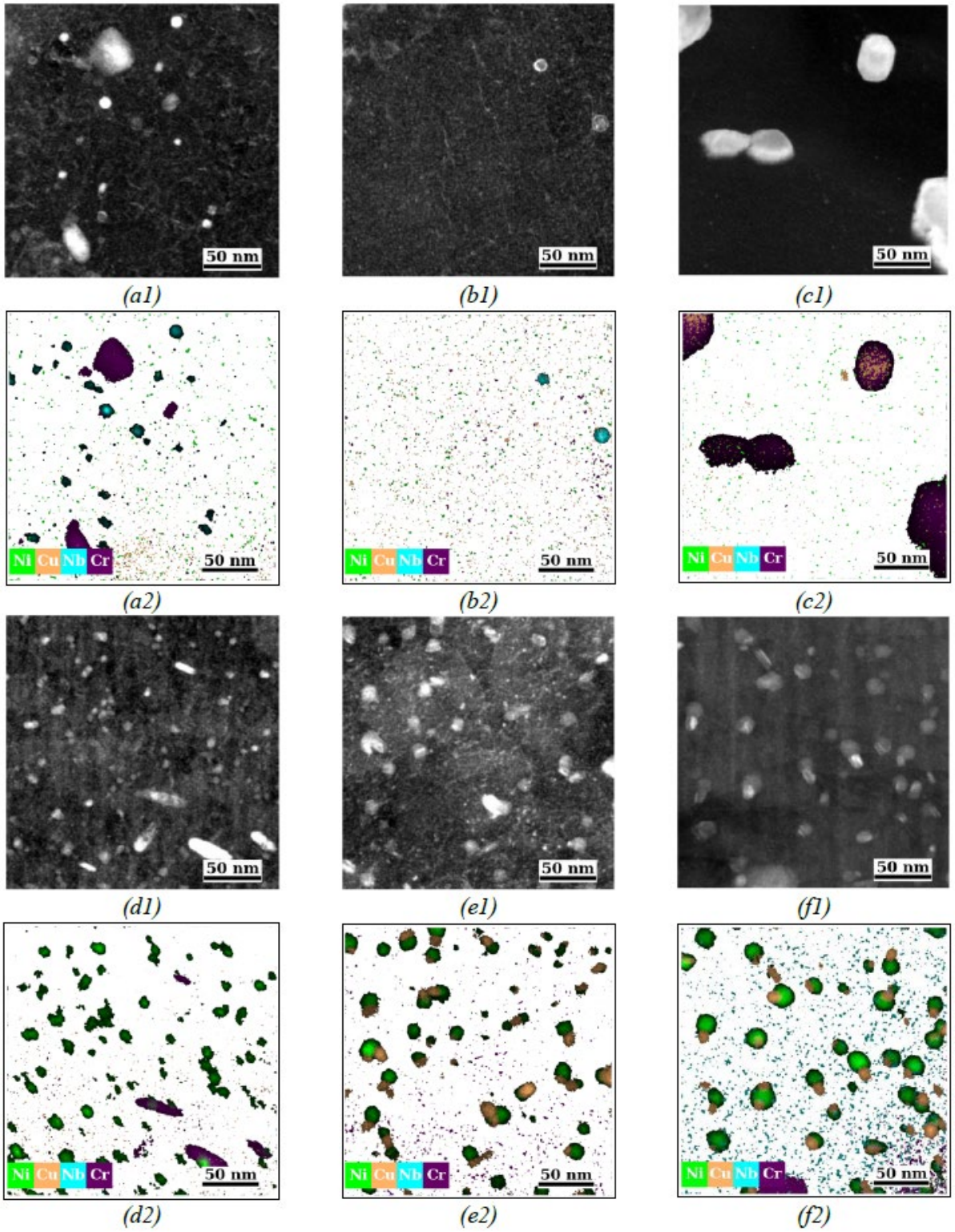

Figure 5.6. STEM-LAADF images in (a1) ASB, (b1) ACO3, and (c1) FCRD coupled with STEM-EDX mapping in (a2) ASB, (b2) ACO3, and (c2) FCRD show precipitates past the irradiated region in the TEM specimen, in which materials underwent the thermal cycle; STEM-LAADF images in (d1) ASB, (e1) ACO3, and (f1) FCRD coupled with STEM-EDX mapping in (d2) ASB, (e2) ACO3, and (f2) FCRD show precipitates after single-ion irradiation to 50 dpa at 460°C in Heat A of AM-HT9. From [37].

Table 5.1. Diameter size (d, in nm) and density (ρ, in /m^3) of Ni/Si/Mn-rich and Cu-rich precipitates/clustering in three conditions of AM-HT9 (Heat A) before and after irradiation to 50 dpa at 460°C [37].

			ASB	ACO3	FCRD
Ni/Si/Mn rich	Before irradiation	d	not observed	not observed	not observed
		ρ	not observed	not observed	not observed
	After irradiation	d	6.1 (± 1.7)	9.7 (± 2.3)	10.5 (± 3.1)
		ρ	1.3 (± 0.2) × 10^{22}	2.9 (± 0.5) × 10^{21}	3.7 (± 0.8) × 10^{21}
Cu rich	Before irradiation	d	not observed	4.9 (± 0.9)	6.6 (± 2.7)
		ρ	not observed	3.0 (± 0.5) × 10^{21}	1.1 (± 0.3) × 10^{21}
	After irradiation	d	not observed	8.1 (± 2.1)	10.0 (± 2.8)
		ρ	not observed	2.9 (± 0.5) × 10^{21}	3.8 (± 0.7) × 10^{21}

The APT reconstruction results are shown in Figure 5.7, where different elements of interest were represented using different color – Green for Ni, Grey for Si, Yellow for Mn, and Orange for Cu, respectively. To fully quantify the precipitates in the irradiated microstructure, the precipitate core compositions were measured using the proximity histogram method from the APT data. The proximity histograms averaged over all Ni/Si/Mn-rich and Cu-rich precipitates observed in three conditions of AM-HT9 specimens are shown in Figure 5.8. The measured precipitate core compositions in at. % are shown in Table 5.2. As can be seen, the Ni composition in Ni/Si/Mn-rich precipitates is 28.7 (± 2.1) at. %, 33.4 (± 0.8) at. %, and 35.3 (± 1.5) at. %, in irradiated ASB, ACO3, and FCRD, respectively. In addition, the Cu composition in Cu-rich precipitates is 75.7 (± 1.4) at. %, and 68.0 (± 1.5) at. % in irradiated ACO3 and FCRD, respectively.

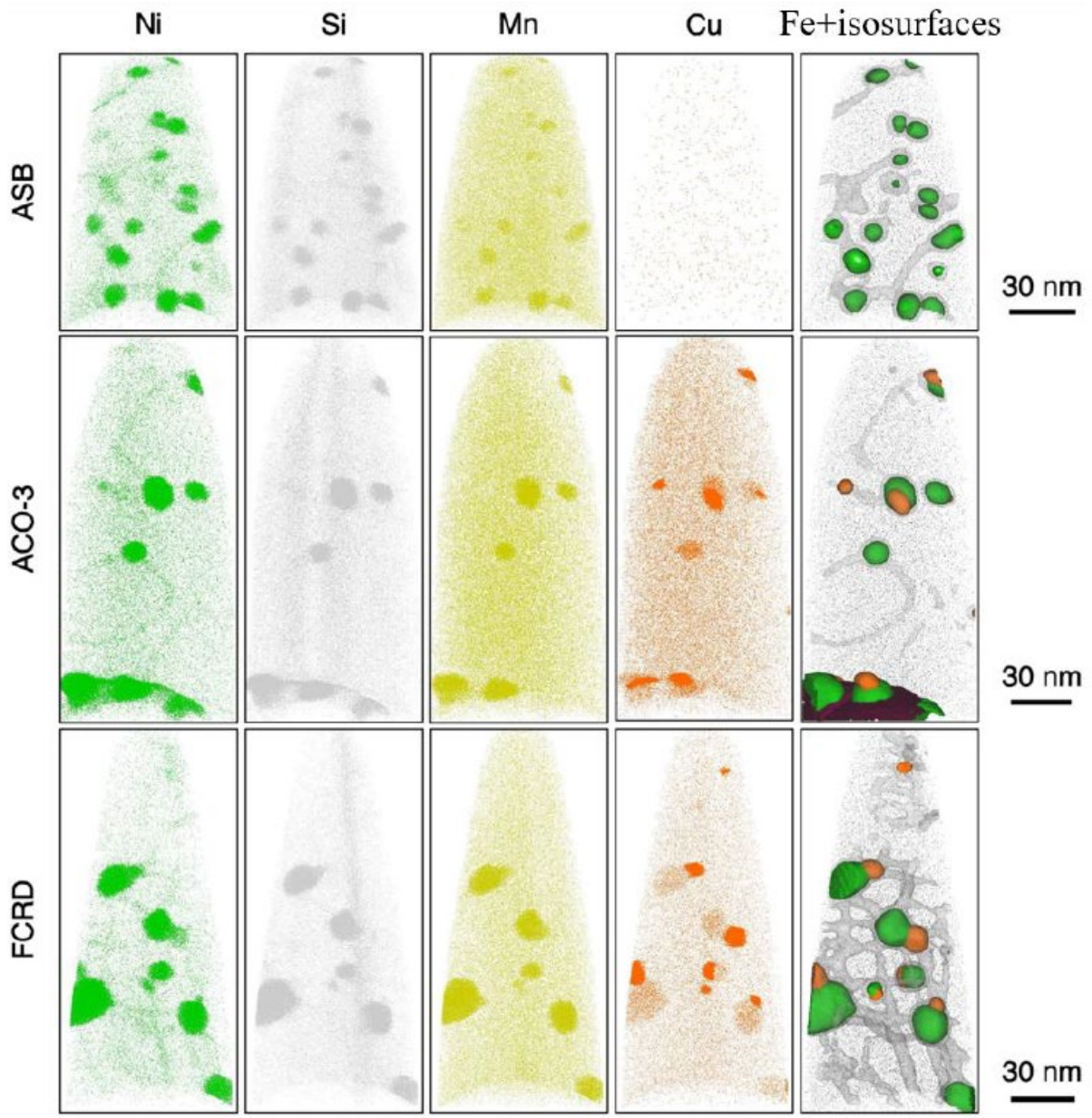

Figure 5.7. APT reconstructions of ASB, ACO3, and FCRD conditions of AM-HT9 (Heat A) after the irradiation. For each condition, ion maps of Ni, Si, Mn, and Cu are shown in Green, Gray, Yellow, and Orange, respectively. On the right, global maps highlight various microstructural features overlaid atop 0.1 at. % of black Fe atoms. In the "Fe+isosurfaces" maps, green features are isoconcentration surfaces containing at least 10 at. % of the combined Ni+Si+Mn ions; gray features are (Ni,Si)-enriched line dislocations (for ASB and ACO3) or low-angle grain boundaries (for FCRD), and are shown using 0.5 at. % Ni isoconcentration surfaces. Orange isoconcentration surfaces show Cu clusters with concentrations exceeding 5 at. %. Lastly, one brown 1 at. % C isoconcentration surface shows a $M_{23}C_6$ carbide in the ACO3 condition. From [37].

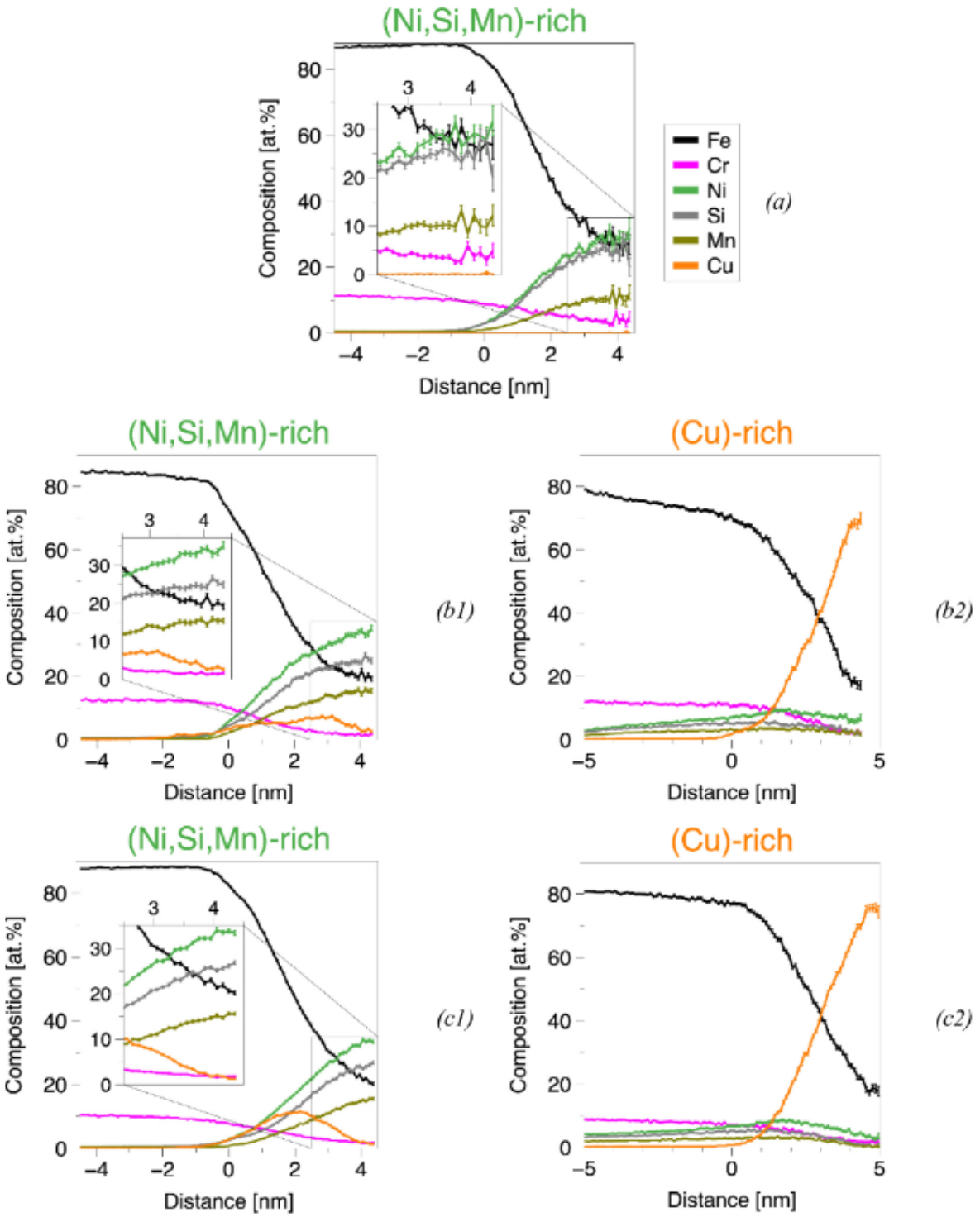

Figure 5.8. Proximity histograms obtained by averaging over all Ni/Si/Mn-rich (green) and Cu-rich (orange) precipitates observed in (a) ASB, (b) ACO-3, and (c) FCRD AM-HT9 (Heat A) specimens after the irradiation. The value of 0 nm on the x-axis represents the interface associated with isoconcentration surfaces using a threshold of 3 at. % Ni or Cu. Error bars indicate the standard deviation from the mean for elemental concentrations in each interval (bin width = 0.1 nm). The legend provided in (a) is applicable to all proximity histograms shown. From [37].

*Table 5.2. Measured precipitate core compositions in at. % in three conditions of AM-HT9 (Heat A) using the proximity histogram method** [37]. *N.O. indicates that the feature was not observed.*

Heat-treatment	Precipitate type	Fe	Cr	Ni	Si	Mn	Cu
ASB	Ni/Si/Mn-rich	25.6 ± 2.1	4.7 ± 1.0	28.7 ± 2.1	28.1 ± 2.1	10.0 ± 1.4	0.0 ± 0.0
	Cu-rich	N.O.					
ACO3	Ni/Si/Mn-rich	20.2 ± 0.8	1.8 ± 0.9	33.4 ± 0.8	26.9 ± 0.8	15.5 ± 0.9	1.3 ± 0.9
	Cu-rich	18.6 ± 1.3	1.7 ± 0.4	2.7 ± 0.5	0.4 ± 0.2	0.5 ± 0.2	75.7 ± 1.4
FCRD	Ni/Si/Mn-rich	19.2 ± 1.7	1.7 ± 1.9	35.3 ± 1.5	24.9 ± 1.6	15.4 ± 1.7	2.7 ± 1.9
	Cu-rich	17.3 ± 1.2	2.8 ± 0.5	6.2 ± 0.8	2.0 ± 0.4	2.7 ± 0.5	68.0 ± 1.5
*Balance elements (total <1 at. %) of Co, V, Nb, Mo, W, P, C, O, N not shown because of non-significant quantities measured							

Note from Figure 5.6 and Figure 5.7, that there is a clear spatial relationship between the Cu-rich and Ni/Si/Mn-rich precipitates in the heat-treated ACO3 and FCRD samples. The co-precipitation behavior will be discussed in Section 6.1.

Besides precipitation formation under irradiation, APT also revealed that Ni/Si enrichment occurs near common defect sinks, such as dislocations, dislocation loops, and low-angle grain boundaries after irradiation, as shown in Figure 5.7. This observation is supported by the low-magnification correlated STEM-BF, -DF2, and -EDX mapping covering the whole irradiated regions in ASB, ACO3, and FCRD, as shown in Figure 5.9. STEM-BF and -DF2 images present the grain and carbide structures, as well as Ni/Si/Mn-rich clusters with high diffraction contrast. Each STEM-EDX mapping contains at least one edge-on grain boundary that shows Ni enrichment near the grain boundary within the irradiated region. One detailed high-magnification STEM-EDX mapping was performed near an edge-on grain boundary in the ACO3 specimen, as shown in Figure 5.10.

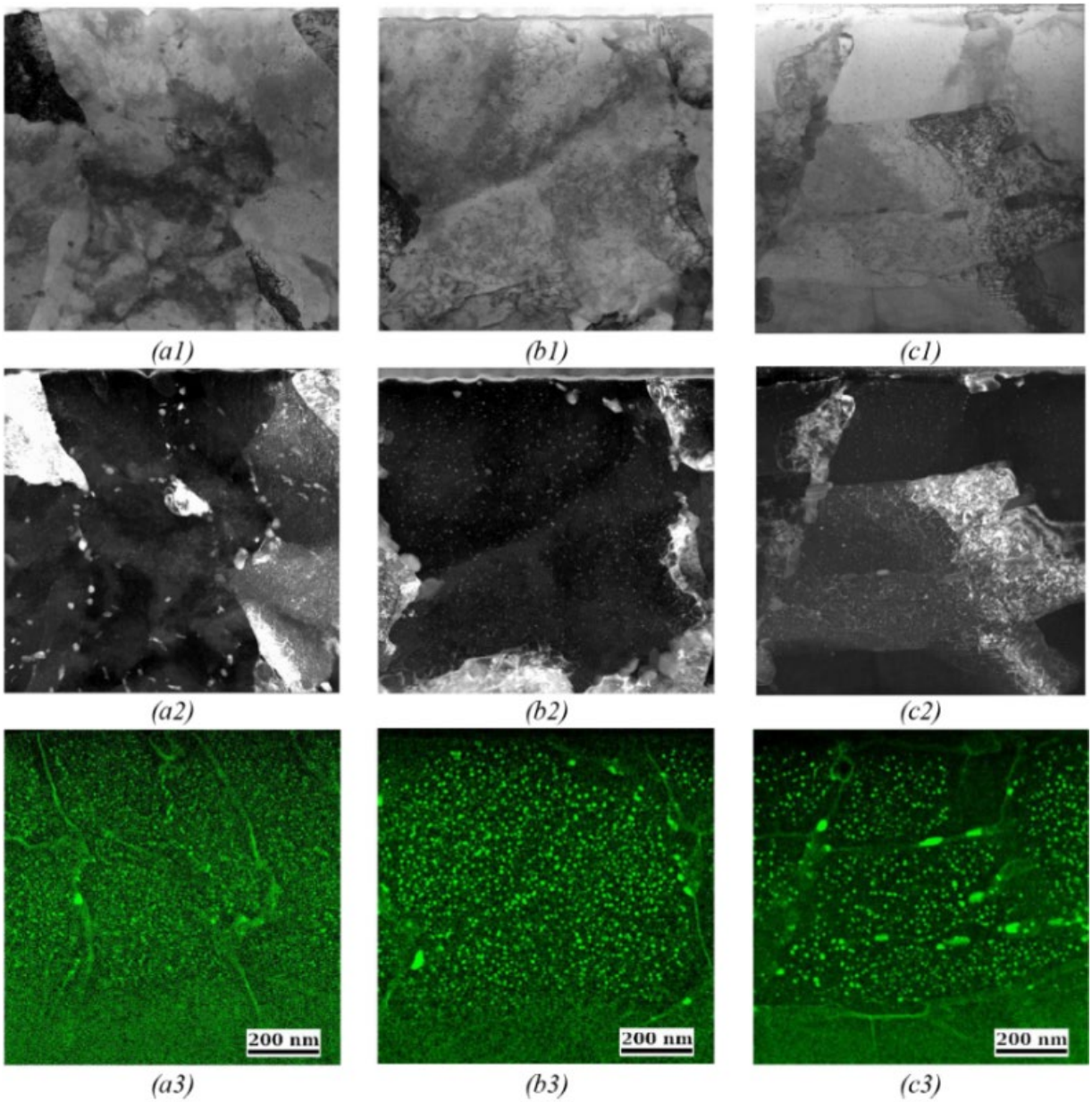

Figure 5.9. Low-magnification of correlated STEM-BF (in the first row), STEM-DF2 (in the second row), and STEM-EDX mapping (in the third row) images showing the RIS of Ni-enrichment near the edge-on grain boundaries in irradiated (a) ASB, (b) ACO-3 and (c) FCRD specimens. More defect sinks in the ASB specimen result in more trapping of Ni, whereas reduced sink density in the heat-treated specimens of ACO3 and FCRD enables higher content of Ni release into the matrix that form more mature Ni/Si/Mn-rich clusters under irradiation. From [37].

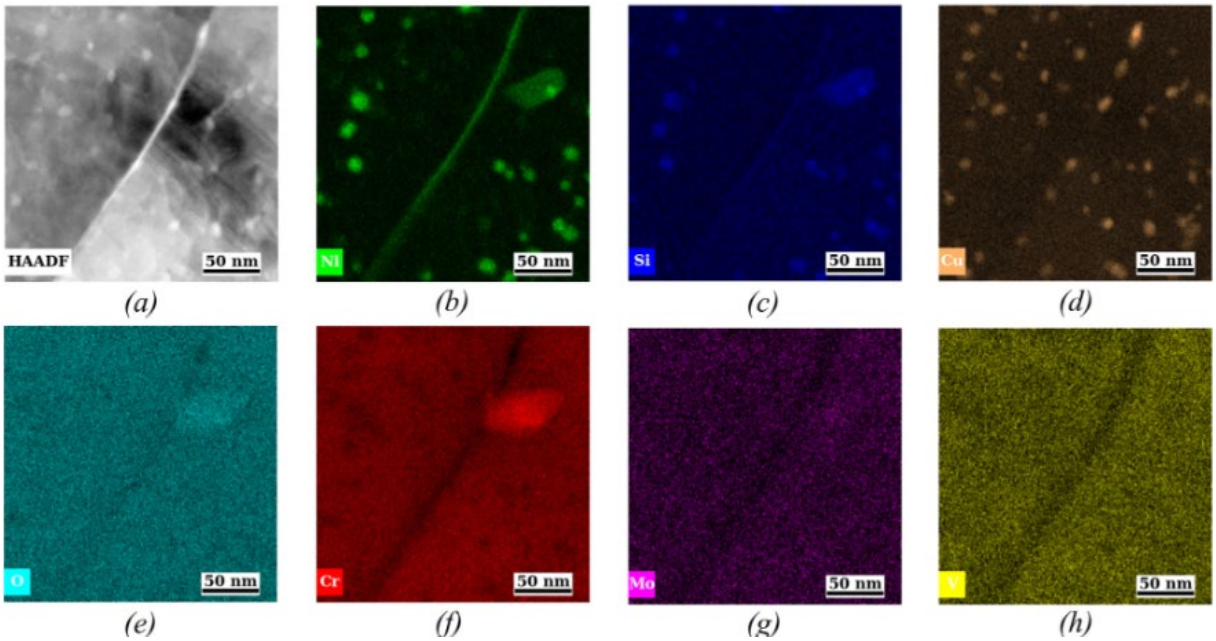

Figure 5.10. STEM-EDX mapping of ACO3 condition of AM-HT9 of Heat A after the irradiation. Selected representative elements show segregation near the grain boundary. (a) The HAADF STEM image with enriched elements including (b) Ni and (c) Si, as well as depleted elements, including (e) O, (f) Cr, (g) Mo, and (h) V. The (f) Cu map shows no segregation, whereas Cu-rich cluster nucleation was observed. From [37].

In addition, no cavity or swelling was observed within all three conditions of AM-HT9 of Heat A at this irradiation condition, indicating the damage level is still within the incubation period for swelling evolution.

5.2 Microstructure Evolution in Heat B of AM-HT9 under Dual-Ion Irradiation: Variable Damage Levels and Fixed Irradiation Temperatures (445°C)

This section of the results will be further broken up into three subsections: swelling and cavity evolution, dislocation loop evolution, and cluster evolution.

5.2.1 Swelling and Cavity Evolution

Cavities are observed to form in irradiated ACO3 and FCRD conditions of AM-HT9 (Heat B) regardless of the damage level from 16.6 dpa up to 250 dpa, while cavities are observed to form in ASB condition of AM-HT9 only with a damage level of 100 dpa or greater. Representative

cavity microstructures induced by irradiation are shown in Figure 5.11, where cavities are shown in the under-focus condition leading to white contrast centers with a dark Fresnel fringe. The manual counting results of cavity size (in diameter) with standard deviation, number density, and swelling are shown on each image where cavity formation is observed. A violin plot is made for each condition to show the size distribution of the irradiation-induced cavities, as shown in Figure 5.12. The swelling curve as a function of damage level in three conditions of AM-HT9 (Heat B) are shown in Figure 5.13. The full statistics of cavities and sink strength are summarized in Table 5.3.

As can be seen in Figure 5.12, Figure 5.13 and Table 5.3, in the ASB specimen, the cavities start to form at 100 dpa, with the average size remaining unchanged with further increasing damage levels to 250 dpa. Meanwhile, the cavity density increases from 5.3 (± 0.5) × $10^{21}/m^3$ at 100 dpa to 104.1 (± 10.4) × $10^{21}/m^3$ at 250 dpa, which results in the increase of overall cavity swelling from 0.01 ± 0.00% to 0.15 ± 0.02%.

In the ACO3 specimen, however, the cavity evolution is much more drastic. The average size of cavities in ACO3 doesn't seem to increase much according to Table 5.3, and this is because of the co-existence of both cavity nucleation of coarsening processes. According to Figure 5.12, highest population of nucleated cavities have the average size of less than 5 nm, which is represented by the peak in the violin plot and the peak position does not change with increasing damage levels. Meanwhile, the growth of cavities in ACO3 can be clearly seen in Figure 5.12, where a tale indicating the upper limit of size of all observed cavities in the microstructure becomes longer and longer with increasing damage levels. The former process of continuous nucleation leads to high population of small cavities, which decreases the average cavity size, while the later process leads to growth of cavities that results in the significant swelling increase. This can be

clearly seen in Figure 5.13, where the swelling of ACO3 specimen keeps increasing at higher damage levels within the steady-state swelling regime starting from 75 dpa or 100 dpa. The swelling at 75 dpa and 100 dpa are 0.25 ± 0.03% and 0.40 ± 0.04%, respectively, whereas the swelling significantly increases to 4.51 ± 0.45% at 250 dpa.

In another heat-treated FCRD specimen, however, a slower swelling increase is observed. Although the same trend of increasing upper bound of cavity size is reflected in the violin plot in Figure 5.12, the growth is much slower than ACO3. Even at 250 dpa, the largest cavity observed in FCRD is about 25 nm, as compared to 50 nm in the ACO3 specimen. Another interesting observation is that from 100 dpa to 250 dpa, within FCRD, the nucleation seems to slow down, with universal growth occurring. The high population of smaller cavities represented by the peak in Figure 5.12 have their size increased from 1-2 nm at 100 dpa to 4-6 nm at 250 dpa. As a result, the overall swelling increases from 0.51 ± 0.05% and 100 dpa to 0.74 ± 0.07% at 250 dpa.

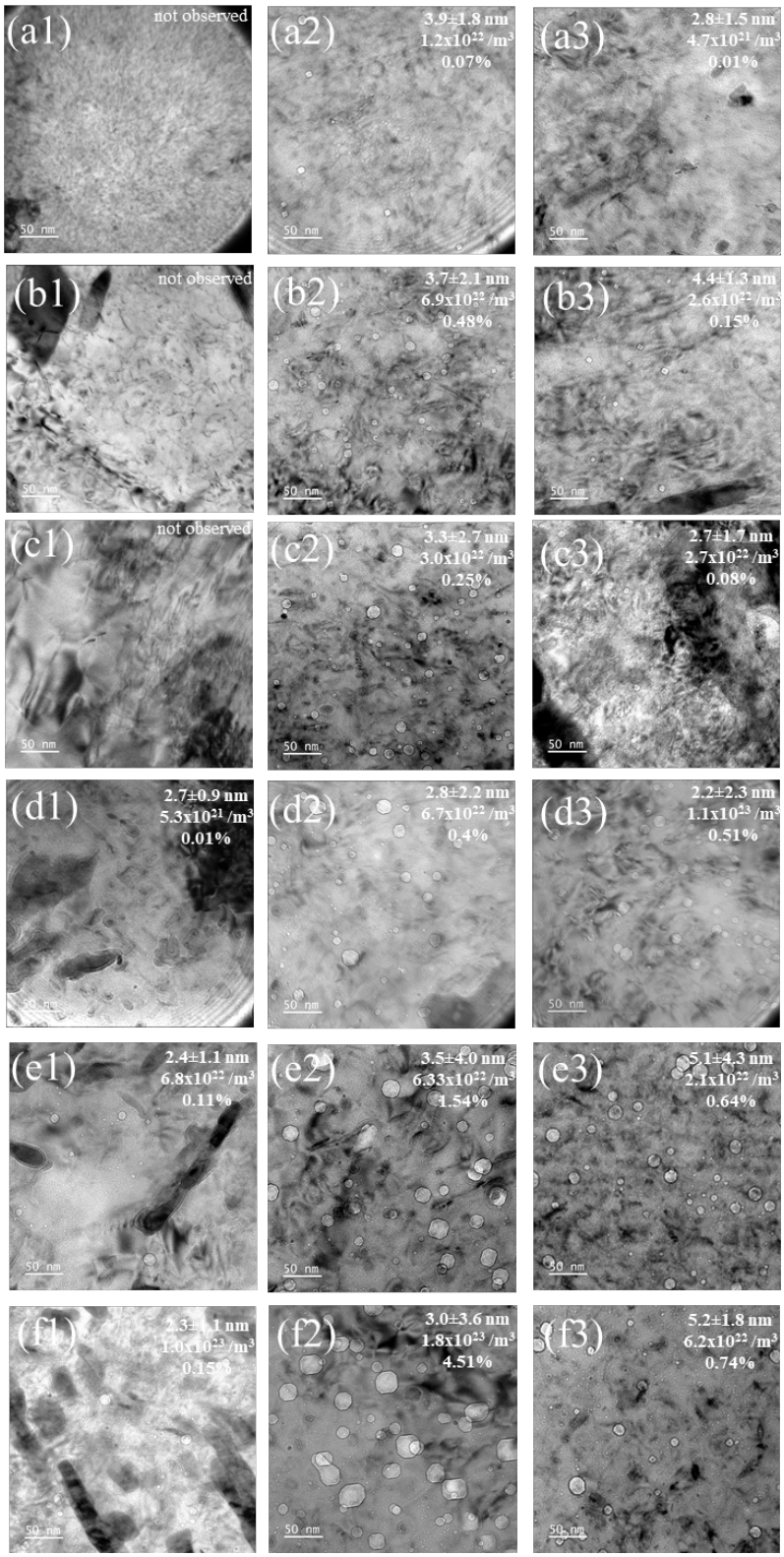

Figure 5.11. Cavity microstructures in dual-ion irradiated AM-HT9 (Heat B) alloys at 445°C with increasing damage level: (a) 16.6 dpa, (b) 50 dpa, (c) 75 dpa, (d) 100 dpa, (e) 150 dpa, and (f) 250 dpa, with the three columns representing ASB, ACO3, and FCRD from the left to the right, respectively. The cavity size (in diameter), the density, and the swelling are labeled on the top right corner of each image.

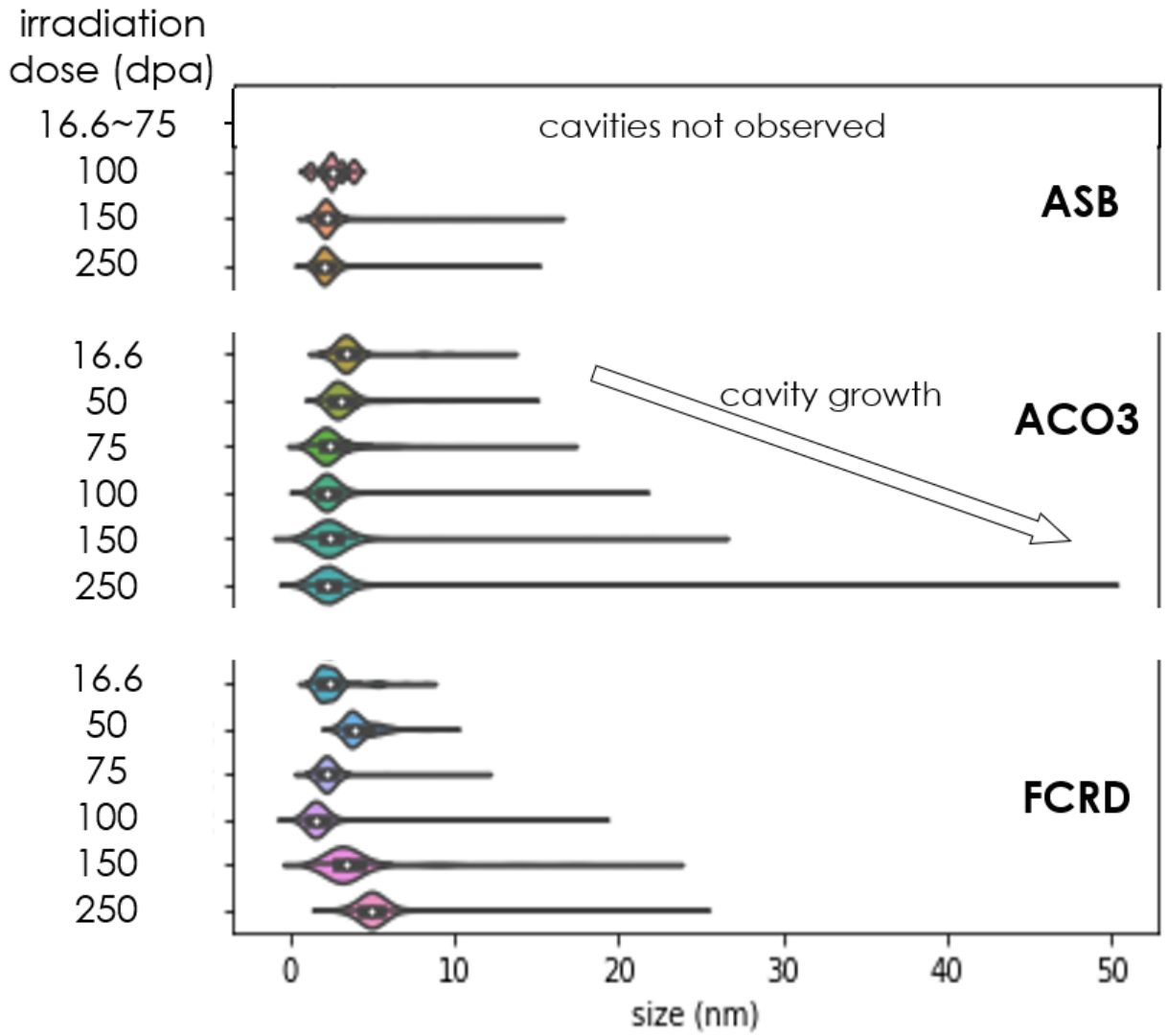

Figure 5.12. Cavity size (in diameter) distribution in dual-ion irradiated AM-HT9 (Heat B) alloys with increasing damage level from 16.6 dpa to 250 dpa at 445°C.

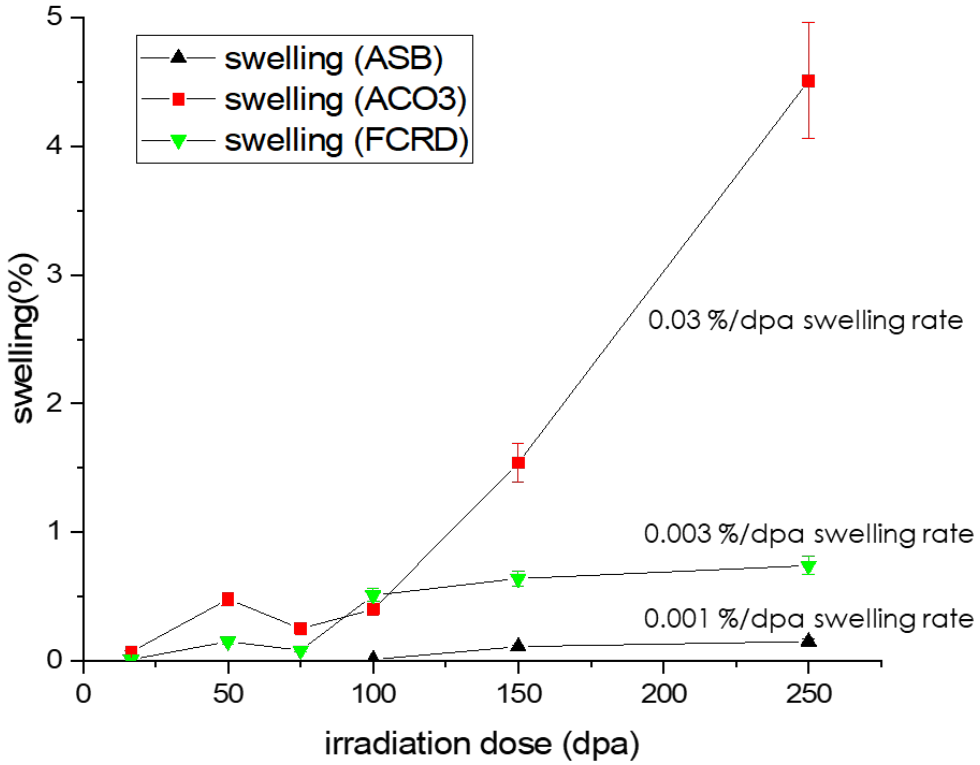

Figure 5.13. Swelling in three conditions of AM-HT9 (Heat B) as a function of damage levels at 445°C.

Table 5.3. Summary of characterization results for cavities in dual-ion irradiated AM-HT9 (Heat B) at 445°C with a damage rate of 5.8×10^{-4} dpa/s and a helium co-injection rate of 4 He appm/dpa. N.O. indicates that the feature was not observed.

	Damage (dpa)	Cavity Diameter (nm)	Cavity Density (10^{21} /m^3)	Swelling	Cavity Sink Strength i,v (10^{13} /m^2)
ASB	16.6	N.O.	N.O.	0	0
	50	N.O.	N.O.	0	0
	75	N.O.	N.O.	0	0
	100	2.7 ± 0.9	5.3 ± 0.5	0.01 ± 0.00 %	9.0 ± 0.9
	150	2.4 ± 1.1	67.8 ± 6.8	0.11 ± 0.01 %	100.8 ± 10.1
	250	2.3 ± 1.1	104.1 ± 10.4	0.15 ± 0.02 %	149 ± 14.9
ACO3	16.6	2.7 ± 0.9	12 ± 1.2	0.07 ± 0.01 %	30.2 ± 3.0
	50	3.8 ± 2.2	69.3 ± 7.0	0.48 ± 0.05 %	163 ± 16.3
	75	3.3 ± 2.7	29.7 ± 3.0	0.25 ± 0.03 %	62.4 ± 6.2
	100	2.8 ± 2.2	66.8 ± 6.7	0.40 ± 0.04 %	116 ± 11.6
	150	3.5 ± 4.0	63.4 ± 6.3	1.54 ± 0.15 %	140 ± 14.0
	250	3.0 ± 3.6	178.9 ± 17.9	4.51 ± 0.45 %	333 ± 33.3
FCRD	16.6	2.7 ± 1.5	4.7 ± 0.5	0.01 ± 0.00 %	8.1 ± 0.8
	50	4.4 ± 1.3	25.9 ± 2.6	0.15 ± 0.02 %	71.5 ± 7.2
	75	2.7 ± 1.7	26.9 ± 2.7	0.08 ± 0.01 %	45.8 ± 4.6
	100	2.2 ± 2.3	105.4 ± 10.5	0.51 ± 0.05 %	147.6 ± 14.8
	150	5.1 ± 4.3	20.7 ± 2.1	0.64 ± 0.06 %	66.2 ± 6.7
	250	5.2 ± 1.8	61.6 ± 6.2	0.74 ± 0.07 %	202 ± 20.2

5.2.2 Dislocation Loop and Line Dislocation Evolution

Dislocation loops of types $a\langle 100\rangle$ and $a/2\langle 111\rangle$ are observed to form in all irradiated AM-HT9 (Heat B) regardless of the damage level or the condition of the alloy. Representative dislocation loop microstructures induced by irradiation are shown in Figure 5.14. The dislocation loop size (in diameter) and density as a function of damage levels are plotted in Figure 5.15. The full statistics of dislocation loops and sink strength are summarized in Table 5.4.

As can be seen in Figure 5.15 and Table 5.4, in the ASB specimen, the dislocation loop size gradually increases and density decreases slightly with increasing damage levels, regardless of the dislocation loop type of $a\langle 100\rangle$ or $a/2\langle 111\rangle$. The $a\langle 100\rangle$ dislocation loop size of 4.6 ± 0.5 nm at 16.6 dpa increases to 24.7 ± 10.1 nm at 250 dpa with significant growth, with the density changing from 4.1 (± 0.4) × 10^{21}/m^3 at 16.6 dpa to 3.4 (± 0.3) × 10^{21}/m^3 at 250 dpa. Similarly, $a/2\langle 111\rangle$ dislocation loops grow significantly from 5.6 ± 1.6 nm at 16.6 dpa to 16.4 ± 3.1 nm at 250 dpa in size, with the density dropping from 4.7 (± 0.5) × 10^{21}/m^3 to 2.1 (± 0.2) × 10^{21}/m^3.

On the other hand, the dislocation loop size and density do not change much with increasing damage levels in the heat-treated ACO3 sample, as indicated in Figure 5.15 and Table 5.4. At 16.6 dpa, the $a\langle 100\rangle$ and $a/2\langle 111\rangle$ dislocation loops have a size of 27.9 ± 10.0 nm and 30.0 ± 5.0 and a density of 5.1 (± 0.5) × 10^{21}/m^3 to 0.7 (± 0.1) × 10^{21}/m^3, respectively. At 250 dpa, the $a\langle 100\rangle$ and $a/2\langle 111\rangle$ dislocation loops have a size of 19.7 ± 11.2 nm and 25.7 ± 7.9 and a density of 6.0 (± 0.6) × 10^{21}/m^3 to 0.8 (± 0.1) × 10^{21}/m^3, respectively. The average size of dislocation loops drop slightly with increasing damage levels for both type of dislocation loops

Similar to the ACO3 sample, no significant change of the size or density is observed in the heat-treated FCRD sample, according to Figure 5.15 and Table 5.4. At 16.6 dpa, the $a\langle 100\rangle$ and

$a/2\langle 111\rangle$ dislocation loops have a size of 21.5 ± 8.7 nm and 15.1 ± 5.6 and a density of 3.5 (± 0.4) × $10^{21}/m^3$ to 4.4 (± 0.4) × $10^{21}/m^3$, respectively. At 250 dpa, the $a\langle 100\rangle$ and $a/2\langle 111\rangle$ dislocation loops have a size of 14.9 ± 8.4 nm and 15.6 ± 5.5 and a density of 6.9 (± 0.7) × $10^{21}/m^3$ to 1.6 (± 0.2) × $10^{21}/m^3$, respectively.

Besides the dislocation loop evolution within each one of three conditions of AM-HT9 with increasing damage levels, interesting results are obtained when comparing the loop statistics across three specimens under the same irradiation conditions. The dislocation loop size reported to form in the irradiated ASB sample is in general much smaller than the ACO3 and FCRD samples, especially at relatively low damage levels of 16.6 dpa.

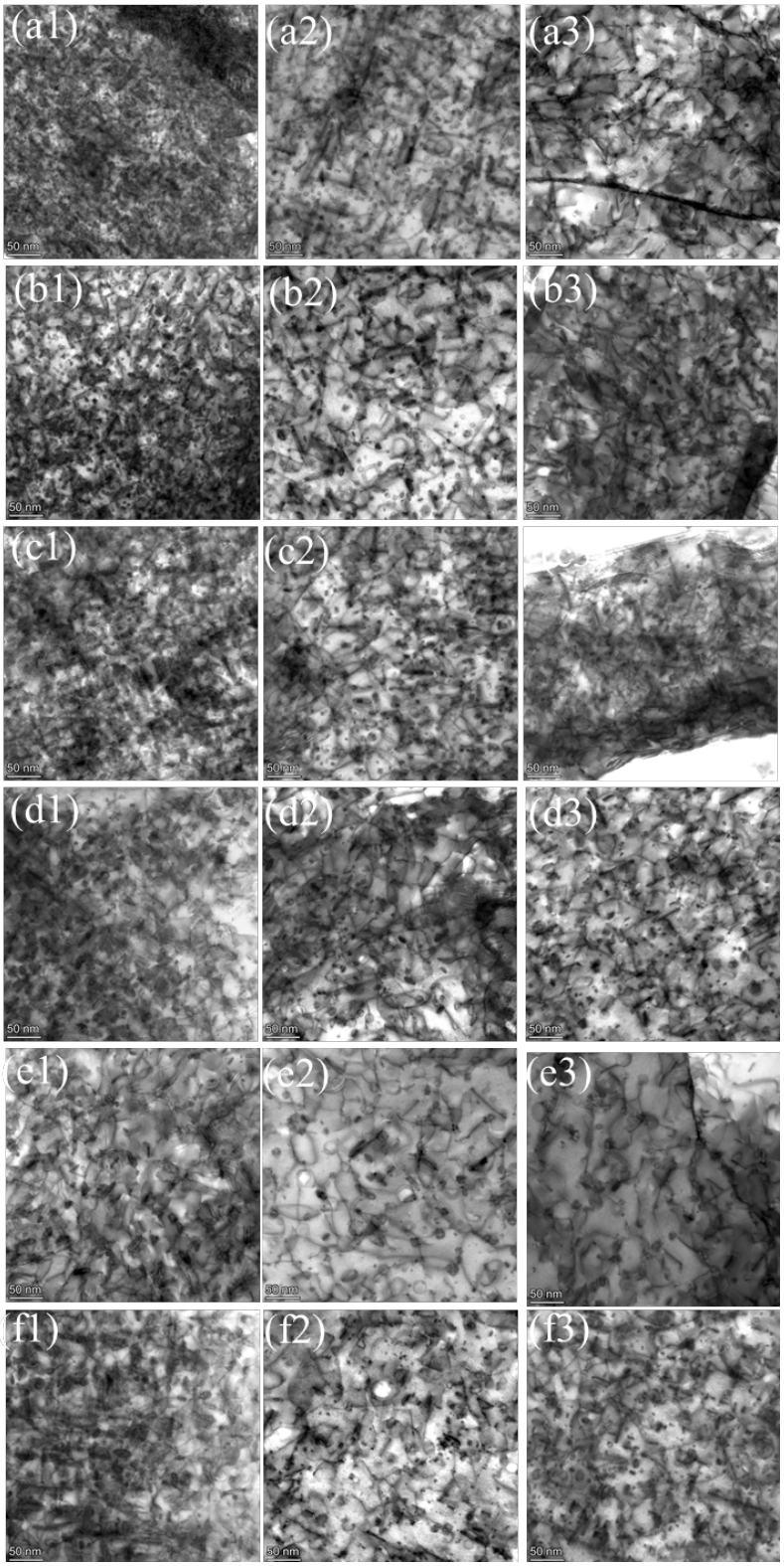

Figure 5.14. Dislocation loop microstructures in dual-ion irradiated AM-HT9 (Heat B) alloys at 445°C with increasing damage level: (a) 16.6 dpa, (b) 50 dpa, (c) 75 dpa, (d) 100 dpa, (e) 150 dpa, and (f) 250 dpa, with the three columns representing ASB, ACO3, and FCRD from the left to the right, respectively. All images were collected using on-zone [001] STEM-BF.

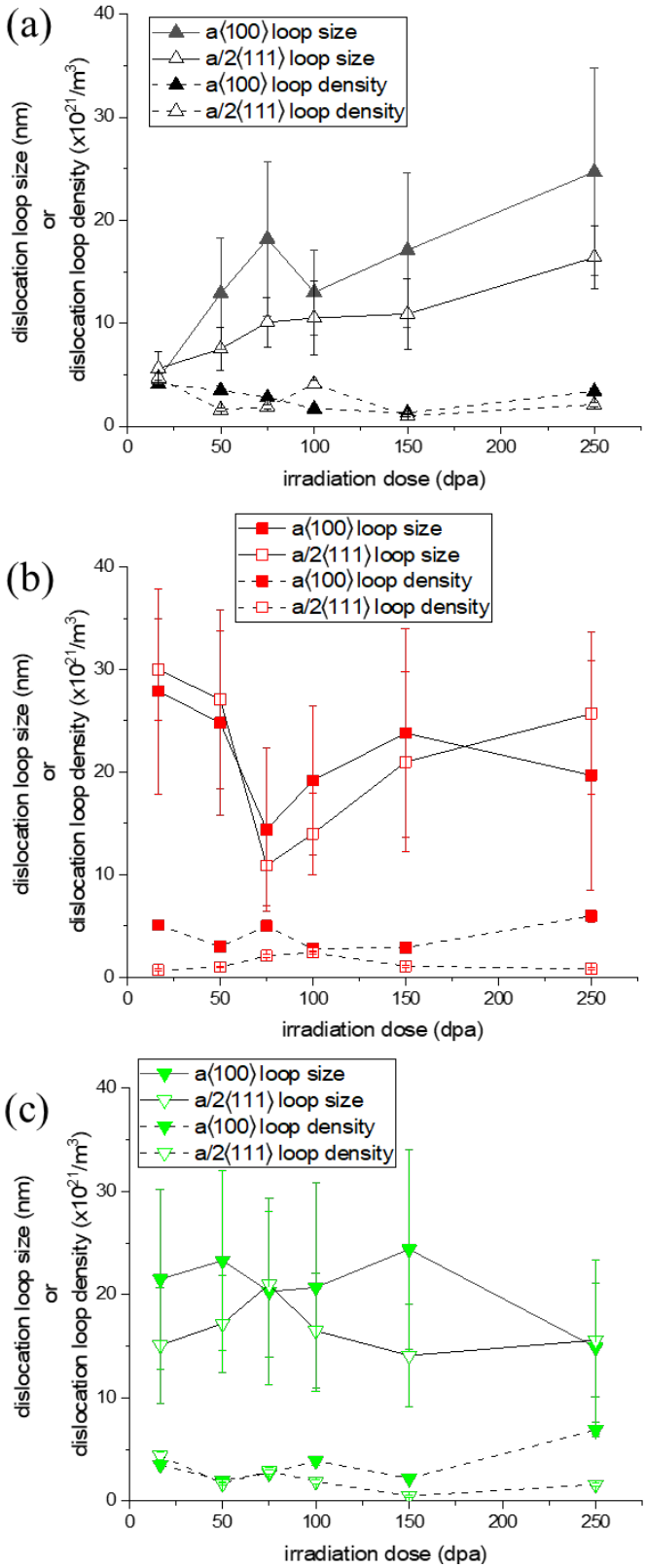

Figure 5.15. Dislocation loop size (in diameter) and density in dual-ion irradiated (a) ASB, (b) ACO3, and (c) FCRD conditions of AM-HT9 (Heat B) as a function of increasing damage level at 445°C.

Table 5.4. Summary of characterization results for dislocation loops in dual-ion irradiated AM-HT9 (Heat B) at 445°C with a damage rate of 5.8×10^{-4} dpa/s and a helium co-injection rate of 4 He appm/dpa.

	Damage (dpa)	$a\langle100\rangle$ Dislocation Loop Diameter (nm)	$a\langle100\rangle$ Dislocation Loop Density (10^{21} /m^3)	$a/2\langle111\rangle$ Dislocation Loop Diameter (nm)	$a/2\langle111\rangle$ Dislocation Loop Density (10^{21} /m^3)	Dislocation Loop Sink Strength i (10^{14} /m^2)	Dislocation Loop Sink Strength v (10^{14} /m^2)
ASB	16.6	4.6 ± 0.5	4.1 ± 0.4	5.6 ± 1.6	4.7 ± 0.5	1.8 ± 0.2	1.4 ± 0.1
	50	12.9 ± 5.4	3.5 ± 0.4	7.5 ± 2.1	1.6 ± 0.2	2.3 ± 0.2	1.8 ± 0.2
	75	18.2 ± 7.5	2.8 ± 0.3	10.1 ± 2.4	1.9 ± 0.2	2.7 ± 0.3	2.2 ± 0.2
	100	13.0 ± 4.1	1.7 ± 0.2	10.5 ± 3.6	4.1 ± 0.4	2.6 ± 0.3	2.0 ± 0.2
	150	17.1 ± 7.5	1.3 ± 0.1	10.9 ± 3.4	1.0 ± 0.1	1.3 ± 0.1	1.0 ± 0.1
	250	24.7 ± 10.1	3.4 ± 0.3	16.4 ± 3.1	2.1 ± 0.2	4.7 ± 0.5	3.8 ± 0.4
ACO3	16.6	27.9 ± 10.0	5.1 ± 0.5	30.0 ± 5.0	0.7 ± 0.1	6.4 ± 0.6	5.1 ± 0.5
	50	24.8 ± 9.0	3.0 ± 0.3	27.1 ± 8.7	1.0 ± 0.1	4.0 ± 0.4	3.2 ± 0.3
	75	14.4 ± 8.0	5.0 ± 0.5	10.9 ± 3.9	2.1 ± 0.2	3.7 ± 0.4	3.0 ± 0.3
	100	19.2 ± 7.3	2.8 ± 0.3	14.0 ± 4.0	2.4 ± 0.2	3.4 ± 0.3	2.7 ± 0.3
	150	23.8 ± 10.2	2.9 ± 0.3	21.0 ± 8.8	1.1 ± 0.1	3.7 ± 0.4	2.9 ± 0.3
	250	19.7 ± 11.2	6.0 ± 0.6	25.7 ± 7.9	0.8 ± 0.1	5.5 ± 0.6	4.4 ± 0.4
FCRD	16.6	21.5 ± 8.7	3.5 ± 0.4	15.1 ± 5.6	4.4 ± 0.4	5.5 ± 0.6	4.4 ± 0.4
	50	23.3 ± 8.7	2.0 ± 0.2	17.2 ± 4.7	1.7 ± 0.2	2.9 ± 0.3	2.4 ± 0.2
	75	20.3 ± 9.0	2.7 ± 0.3	21.0 ± 7.1	2.9 ± 0.3	4.5 ± 0.5	3.6 ± 0.4
	100	20.7 ± 10.1	3.9 ± 0.4	16.5 ± 5.6	1.9 ± 0.2	4.4 ± 0.4	3.5 ± 0.4
	150	24.4 ± 9.7	2.2 ± 0.2	14.1 ± 5.0	0.5 ± 0.1	2.4 ± 0.2	1.9 ± 0.2
	250	14.9 ± 8.4	6.9 ± 0.7	15.6 ± 5.5	1.6 ± 0.2	5.0 ± 0.5	4.0 ± 0.4

As expected, line dislocations exist in all irradiated AM-HT9 (Heat B) regardless of the damage level or the condition of the alloy. The full statistics of line dislocations and sink strength are summarized in Table 5.5. Quite scattered data on the line dislocation density are observed in all three conditions of AM-HT9 according to Table 5.5. Note that in general, line dislocation density is higher in the ASB specimen, as compared to the heat-treated ACO3 and FCRD specimens. Therefore, the sink strength in the ASB specimen is also higher than the ACO3 and FCRD at almost all damage levels.

Table 5.5. Summary of characterization results for line dislocations in dual-ion irradiated AM-HT9 (Heat B) at 445°C with a damage rate of 5.8×10^{-4} dpa/s and a helium co-injection rate of 4 He appm/dpa.

	Damage (dpa)	Line Dislocation Density (10^{14} /m^2)	Line Dislocation Sink Strength i (10^{14} /m^2)	Line Dislocation Sink Strength v (10^{14} /m^2)
ASB	16.6	23.2 ± 2.3	24.8 ± 2.5	23.2 ± 2.3
	50	5.1 ± 0.5	5.4 ± 0.5	5.1 ± 0.5
	75	30.4 ± 3.0	32.5 ± 3.2	30.4 ± 3.0
	100	12.4 ± 1.2	13.3 ± 1.3	12.4 ± 1.2
	150	6.8 ± 0.7	7.3 ± 0.7	6.8 ± 0.7
	250	9.8 ± 1.0	10.5 ± 1.1	9.8 ± 1.0
ACO3	16.6	10.4 ± 1.0	11.1 ± 1.1	10.4 ± 1.0
	50	2.6 ± 0.3	2.8 ± 0.3	2.6 ± 0.3
	75	9.3 ± 0.9	9.9 ± 1.0	9.3 ± 0.9
	100	5.3 ± 0.5	5.7 ± 0.6	5.3 ± 0.5
	150	2.0 ± 0.2	2.1 ± 0.2	2.0 ± 0.2
	250	4.2 ± 0.4	4.5 ± 0.5	4.2 ± 0.4
FCRD	16.6	8.2 ± 0.8	8.8 ± 0.9	8.2 ± 0.8
	50	5.6 ± 0.6	6.0 ± 0.6	5.6 ± 0.6
	75	6.9 ± 0.7	7.4 ± 0.7	6.9 ± 0.7
	100	3.7 ± 0.4	3.9 ± 0.4	3.7 ± 0.4
	150	4.2 ± 0.4	4.5 ± 0.5	4.2 ± 0.4
	250	3.1 ± 0.3	3.3 ± 0.3	3.1 ± 0.3

5.2.3 Precipitate Evolution

Ni/Si/Mn-rich clusters are observed to form in irradiated ACO3 and FCRD conditions of AM-HT9 (Heat B) regardless of the damage level from 16.6 dpa up to 250 dpa, whereas they are observed to form only at 75 dpa or higher in the ASB condition of AM-HT9. Representative Ni/Si/Mn-rich cluster microstructures induced by irradiation are shown in Figure 5.16. The Ni/Si/Mn-rich precipitate size (in diameter) and density as a function of damage levels are plotted in Figure 5.18. The full statistics of Ni/Si/Mn-rich precipitates and sink strengths are summarized in Table 5.6.

As can be seen in Figure 5.18 and Table 5.6, in the ASB specimen, the Ni/Si/Mn-rich precipitates only form at 75 dpa or higher damage levels, with the size increasing slightly and density decreasing slightly with increasing damage levels. The Ni/Si/Mn-rich precipitate size of 6.1 ± 2.4 nm at 75 dpa increases to 7.7 ± 2.8 nm at 250 dpa with mild amount of growth, and the

density decreases from 8.8 (± 0.9) × $10^{21}/m^3$ at 75 dpa to 5.3 (± 0.5) × $10^{21}/m^3$ at 150 dpa. In the ACO3 sample, the Ni/Si/Mn-rich precipitates form at all damage levels. The average size increases slightly with increasing damage levels, from 9.0 ± 1.9 nm at 16.6 dpa to 10.4 ± 4.3 nm at 250 dpa, according to Figure 5.18 and Table 5.6. On the contrary, the density decrease is much more significant, dropping from 12.1 (± 1.2) × $10^{21}/m^3$ at 16.6 dpa to 5.7 (± 0.6) × $10^{21}/m^3$ at 250 dpa. A more significant growth and coarsening process occurs in the FCRD sample. The average size of Ni/Si/Mn-rich precipitates rapidly increases from 5.2 ± 2.3 nm at 16.6 dpa to 10.5 ± 3.2 nm at 250 dpa, whereas the density drops from 16.7 (± 1.7) × $10^{21}/m^3$ at 16.6 dpa to 5.5 (± 0.6) × $10^{21}/m^3$ at 250 dpa.

Besides the Ni/Si/Mn-rich precipitate evolution within each one of three conditions of AM-HT9 with increasing damage levels, interesting results are obtained when comparing the precipitate statistics across three specimens under the same irradiation conditions. Table 5.6 shows that with increasing damage levels, Ni/Si/Mn-rich precipitate size does not change much in the ASB or ACO3 samples, though a consistently smaller size in ASB is observed compared to that in ACO3. On the other hand, the size change of Ni/Si/Mn-rich precipitates in FCRD is much more significant than either ASB or ACO3, while the maximum average size observed at 250 dpa is comparable with that of ACO3.

Cr-rich clusters are observed to form extensively in irradiated ASB condition of AM-HT9 (Heat B) regardless of the damage level from 16.6 dpa up to 250 dpa, whereas very minor if not negligible amount of Cr-rich clusters form in the ACO3 and FCRD conditions of AM-HT9. Representative Cr-rich cluster microstructures induced by irradiation in the ASB sample are shown in Figure 5.17. The Cr-rich precipitate size (in diameter) and density as a function of damage levels

are plotted in Figure 5.18. The full statistics of Cr-rich precipitates and sink strengths are summarized in Table 5.6.

As can be seen in Figure 5.18 and Table 5.6, in the ASB specimen, drastic evolution of Cr-rich precipitates occurs. The average size monotonically increases from 3.5 ± 1.1 nm at 16.6 dpa to 18.8 ± 11.8 nm at 250 dpa, whereas the density increases first from 16.1 (± 1.6) × $10^{21}/m^3$ at 16.6 dpa to 41.0 (± 4.1) × $10^{21}/m^3$ at 50 dpa, then significantly decreases to 5.5 (± 0.6) × $10^{21}/m^3$ at 250 dpa. Again, minimal Cr-rich clusters are observed in the heat-treated ACO3 and FCRD specimens.

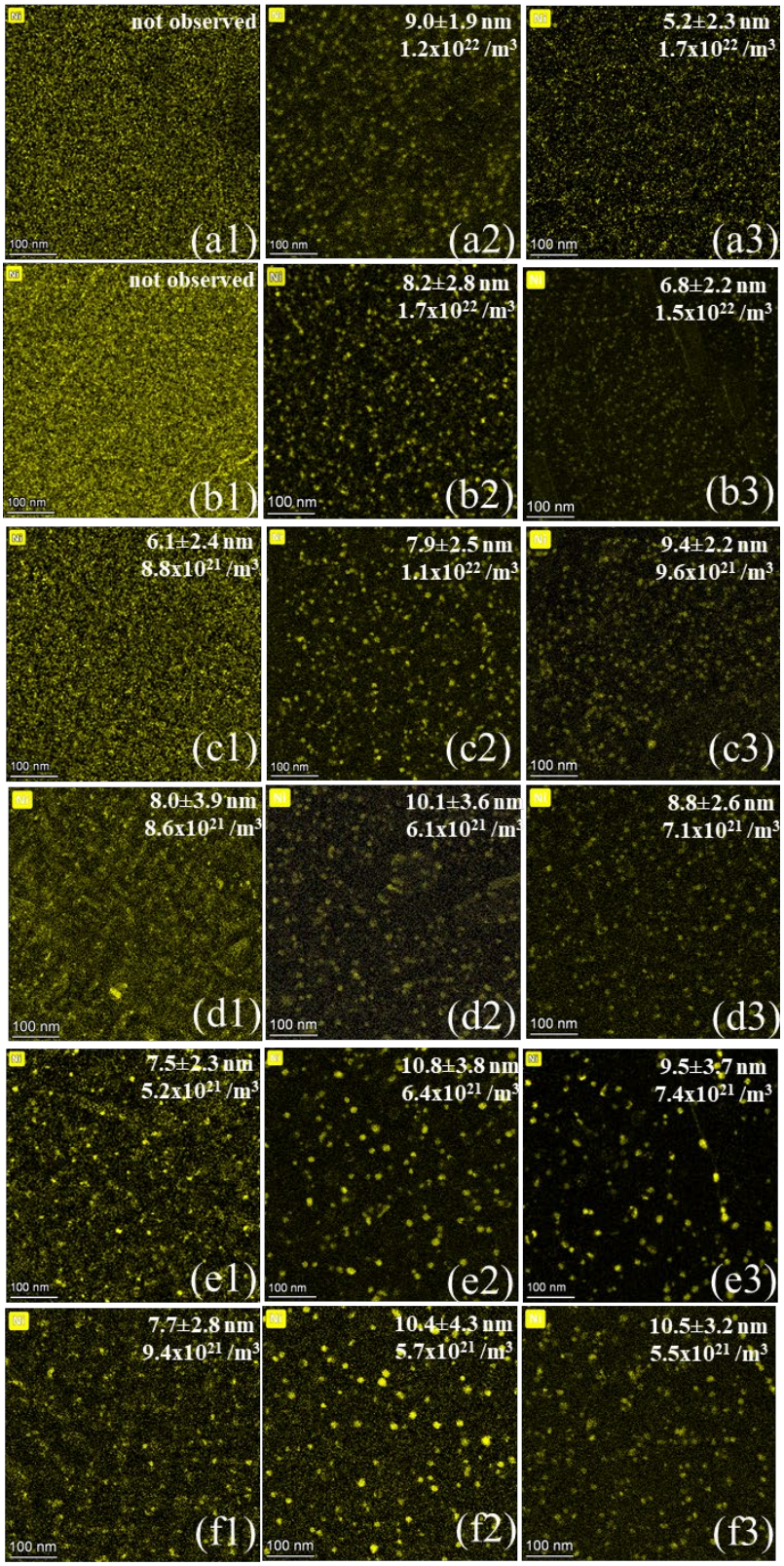

Figure 5.16. Ni/Si/Mn-rich cluster microstructures in dual-ion irradiated AM-HT9 alloys (Heat B) at 445°C with increasing damage level: (a) 16.6 dpa, (b) 50 dpa, (c) 75 dpa, (d) 100 dpa, (e) 150 dpa, and (f) 250 dpa, with the three columns representing ASB, ACO3, and FCRD from the left to the right, respectively.

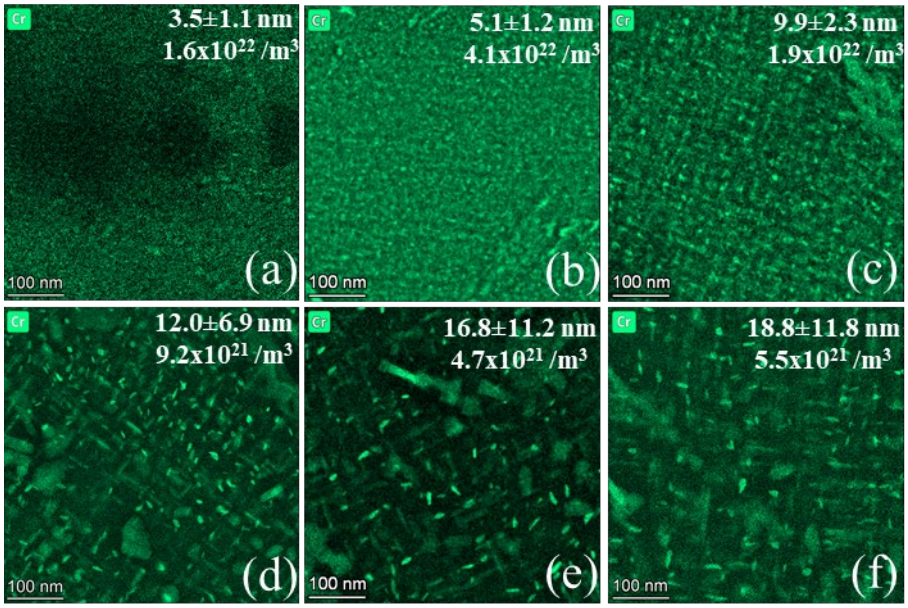

Figure 5.17. Cr-rich cluster microstructures in dual-ion irradiated ASB condition of AM-HT9 (Heat B) alloys at 445°C with increasing damage level: (a) 16.6 dpa, (b) 50 dpa, (c) 75 dpa, (d) 100 dpa, (e) 150 dpa, and (f) 250 dpa, respectively.

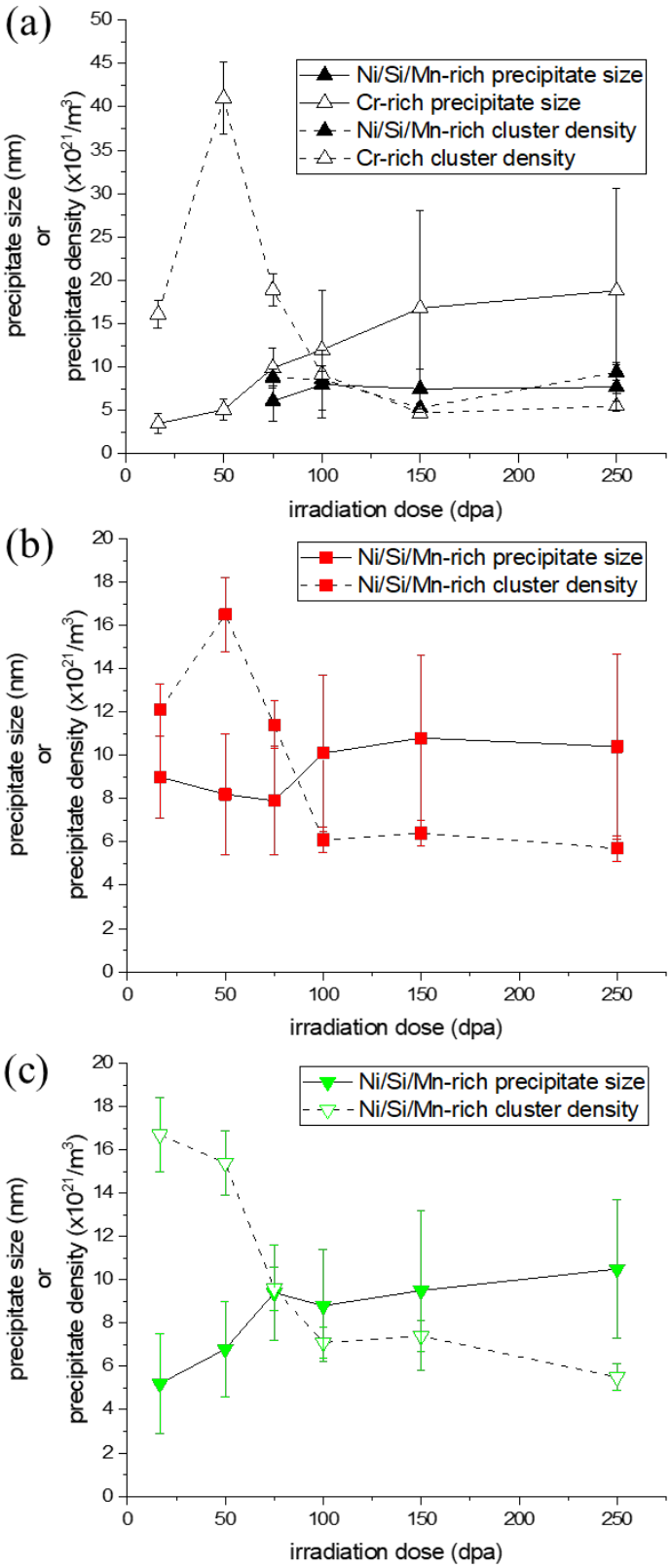

Figure 5.18. Precipitate size (in diameter) and density in dual-ion irradiated (a) ASB, (b) ACO3, and (c) FCRD conditions of AM-HT9 (Heat B) as a function of increasing damage level at 445°C.

Table 5.6. Summary of characterization results for Ni/Si/Mn-rich and Cr-rich precipitates in dual-ion irradiated AM-HT9 (Heat B) at 445°C with a damage rate of 5.8×10^{-4} dpa/s and a helium co-injection rate of 4 He appm/dpa. N.O. indicates that the feature was not observed.

	Damage (dpa)	Ni/Si/Mn-rich Precipitate Diameter (nm)	Ni/Si/Mn-rich Precipitate Density (10^{21} /m^3)	Ni/Si/Mn-rich Precipitate Phase Fraction	Cr-rich Precipitate Diameter (nm)	Cr-rich Precipitate Density (10^{21} /m^3)	Cr-rich Precipitate Phase Fraction	Precipitate Sink Strength i,v (10^{14} /m^2)
ASB	16.6	N.O.	N.O.	N.O.	3.5 ± 1.1	16.1 ± 1.6	0.05%	3.6 ± 0.4
	50	N.O.	N.O.	N.O.	5.1 ± 1.2	41.0 ± 4.1	0.34%	13.1 ± 1.3
	75	6.1 ± 2.4	8.8 ± 0.9	0.15%	9.9 ± 2.3	18.9 ± 1.9	1.11%	15.1 ± 1.5
	100	8.0 ± 3.9	8.6 ± 0.9	0.44%	12.0 ± 6.9	9.2 ± 0.9	2.46%	11.3 ± 1.1
	150	7.5 ± 2.3	5.3 ± 0.5	0.15%	16.8 ± 11.2	4.7 ± 0.5	3.59%	7.5 ± 0.8
	250	7.7 ± 2.8	9.4 ± 0.9	0.31%	18.8 ± 11.8	5.5 ± 0.6	5.18%	11.0 ± 1.1
ACO3	16.6	9.0 ± 1.9	12.1 ± 1.2	0.54%	N.O.	N.O.	N.O.	6.9 ± 0.7
	50	8.2 ± 2.8	16.5 ± 1.7	0.66%	N.O.	N.O.	N.O.	8.6 ± 0.9
	75	7.9 ± 2.5	11.4 ± 1.1	0.39%	13.2 ± 7.1	0.6 ± 0.1	0.15%	6.2 ± 0.6
	100	10.1 ± 3.6	6.1 ± 0.6	0.47%	11.2 ± 2.5	0.2 ± 0.0	0.02%	4.0 ± 0.4
	150	10.8 ± 3.8	6.4 ± 0.6	0.58%	N.O.	N.O.	N.O.	4.3 ± 0.4
	250	10.4 ± 4.3	5.7 ± 0.6	0.52%	N.O.	N.O.	N.O.	3.7 ± 0.4
FCRD	16.6	5.2 ± 2.3	16.7 ± 1.7	0.21%	N.O.	N.O.	N.O.	5.5 ± 0.6
	50	6.8 ± 2.2	15.4 ± 1.5	0.34%	N.O.	N.O.	N.O.	6.6 ± 0.7
	75	9.4 ± 2.2	9.6 ± 1.0	0.48%	N.O.	N.O.	N.O.	5.6 ± 0.6
	100	8.8 ± 2.6	7.1 ± 0.7	0.32%	8.2 ± 3.9	1.0 ± 0.1	0.05%	4.4 ± 0.4
	150	9.5 ± 3.7	7.4 ± 0.7	0.49%	21.5 ± 9.9	1.2 ± 0.1	1.07%	6.0 ± 0.6
	250	10.5 ± 3.2	5.5 ± 0.6	0.43%	18.0 ± 6.7	1.3 ± 0.1	0.57%	5.1 ± 0.5

As can be seen, the Ni/Si/Mn-rich clusters coarsen slowly with increasing damage levels, whereas the Cr-rich clusters coarsen significantly especially in the ASB condition of AM-HT9. It is worth noting that, unlike in Heat A, no Cu-rich precipitates were observed in irradiated Heat B of AM-HT9 regardless of the irradiation conditions.

5.2.4 Sink Strength and Swelling Rate

The total sink strengths for vacancy and interstitial absorption, S_v and S_i are calculated for each damage level. As can be seen in Figure 5.13, the end of incubation period and the start of steady-state cavity swelling in three conditions of AM-HT9 (Heat B) are around 75 dpa. Therefore, theoretical swelling rates at 75 dpa, 100 dpa, and 150 dpa are calculated from the experimental

input parameters including S_v, S_i, d_{cav}, and ρ_{cav}, and are then compared to the direct experimental swelling rate results, as listed in Table 5.7.

Table 5.7. Summary of total sink strength, average cavity radius and density, as well as theoretical and experimental swelling rates in dual-ion irradiated AM-HT9 (Heat B) at 445°C with a damage rate of 5.8×10^{-4} dpa/s and a helium co-injection rate of 4 He appm/dpa. N.C. indicates that the value was not calculated. N.O. indicates that the feature was not observed. N.A. indicates that the calculation was not applicable.

	Dam age (dpa)	Total Vacancy Sink Strength, S_v (10^{15} /m^2)	Total Interstitial Sink Strength, S_i (10^{15} /m^2)	Cavity Radius, d_{cav} (nm)	Cavity Density, ρ_{cav} (10^{21} /m^3)	Theoretical Swelling Rate (%/dpa)	Experimental swelling rate (%/dpa)	Ratio of Theoretical to Experimental Swelling Rate
ASB	16.6	5.7 ± 0.2	5.9 ± 0.3	N.O.	N.O.	N.C.	N.C.	N.A.
	50	4.8 ± 0.1	4.9 ± 0.1	N.O.	N.O.	N.C.	N.C.	N.A.
	75	7.6 ± 0.3	7.9 ± 0.3	N.O.	N.O.	0.000	0.0004	0
	100	5.5 ± 0.1	5.7 ± 0.2	2.7 ± 0.9	5.3 ± 0.5	0.001	0.0020	0.5
	150	5.4 ± 0.1	5.5 ± 0.1	2.4 ± 1.1	67.8 ± 6.8	0.004	0.0004	10
	250	6.8 ± 0.2	7.0 ± 0.2	2.3 ± 1.1	104.1 ± 10.4	N.C.	N.A.	N.A.
ACO3	16.6	3.3 ± 0.1	3.5 ± 0.1	3.9 ± 1.8	12 ± 1.2	N.C.	N.C.	N.A.
	50	3.8 ± 0.2	3.9 ± 0.2	3.8 ± 2.7	69.3 ± 7.0	N.C.	N.C.	N.A.
	75	3.2 ± 0.1	3.4 ± 0.1	3.3 ± 2.2	29.7 ± 3.0	0.005	0.0060	0.8
	100	3.1 ± 0.1	3.2 ± 0.1	2.8 ± 2.2	66.8 ± 6.7	0.007	0.0228	0.3
	150	3.1 ± 0.1	3.2 ± 0.2	3.5 ± 4.0	63.4 ± 6.3	0.007	0.0297	0.2
	250	5.3 ± 0.3	5.5 ± 0.3	3.0 ± 3.6	178.9 ± 17.9	N.C.	N.A.	N.A.
FCRD	16.6	2.8 ± 0.1	2.9 ± 0.1	2.8 ± 1.5	4.7 ± 0.5	N.C.	N.C.	N.A.
	50	3.0 ± 0.1	3.1 ± 0.1	4.4 ± 1.7	25.9 ± 2.6	N.C.	N.C.	N.A.
	75	2.9 ± 0.1	3.1 ± 0.1	2.7 ± 1.3	26.9 ± 2.7	0.004	0.0172	0.2
	100	3.5 ± 0.2	3.6 ± 0.2	2.2 ± 2.3	105.4 ± 10.5	0.009	0.0026	3.5
	150	2.7 ± 0.1	2.8 ± 0.1	5.1 ± 4.3	20.7 ± 2.1	0.003	0.0010	3
	250	4.1 ± 0.2	4.2 ± 0.2	5.2 ± 1.8	61.6 ± 6.2	N.C.	N.A.	N.A.

5.3 Microstructure Evolution in Heat B of AM-HT9 under Dual-Ion Irradiation: Variable Irradiation Temperatures and Fixed Damage Levels (50 dpa)

This section of the results will be further broken up into three subsections: swelling and cavity evolution, dislocation loop evolution, and cluster evolution.

5.3.1 Swelling and Cavity Evolution

Cavities are observed to form in irradiated ACO3 and FCRD conditions of AM-HT9 (Heat B) regardless of the irradiation temperature from 400°C up to 500°C, while cavities are only observed to form in ASB condition of AM-HT9 (Heat B) with irradiation temperature of 500°C. Representative cavity microstructures induced by irradiation are shown in Figure 5.19. The manual counting results of cavity size with standard deviation, number density, and swelling are shown on each image where cavity formation is observed. A violin plot is made for each condition to show the size distribution of the irradiation-induced cavities, as shown in Figure 5.20. The swelling curve as a function of irradiation temperature in three conditions of AM-HT9 (Heat B) are shown in Figure 5.21. The full statistics of cavities are summarized in Table 5.8.

As can be seen in Figure 5.20 and Table 5.8, in the ASB specimen, the cavities are not observed to form at the irradiation temperature between 400°C to 460°C. Very small amount of cavities are observed in ASB at 500°C, with the size and density to be 2.4 ± 0.5 nm and 35.1 (± 3.5) × $10^{21}/m^3$, respectively. Only the nucleation without any growth is observed, which leads to the low swelling of 0.03 ± 0.00% as shown in Table 5.8.

On the contrary, cavities are observed in ACO3 and FCRD at irradiation temperatures at 50 dpa. The violin plot in Figure 5.20 indicates that ACO3 has more cavity growth with increasing irradiation temperatures, with the upper bound of cavity size growing from around 6 nm at 400°C to 20 nm at 500°C. The overall swelling, however, undergoes a typical bell-shaped swelling behavior with varying irradiation temperatures, shown in Figure 5.21. The swelling increases from 0.19 ± 0.02% at 400°C to 0.62 ± 0.01% at 460°C, then decreases to 0.16 ± 0.02% at 500°C. In FCRD, a similar bell-shaped swelling behavior is observed, with the swelling increasing from 0.12 ± 0.01% at 400°C to 0.15 ± 0.02% at 445°C, then decreasing to 0.04 ± 0.00% at 500°C. In addition,

it is worth noting that the overall swelling in FCRD is consistently lower than ACO3 at all irradiation temperatures.

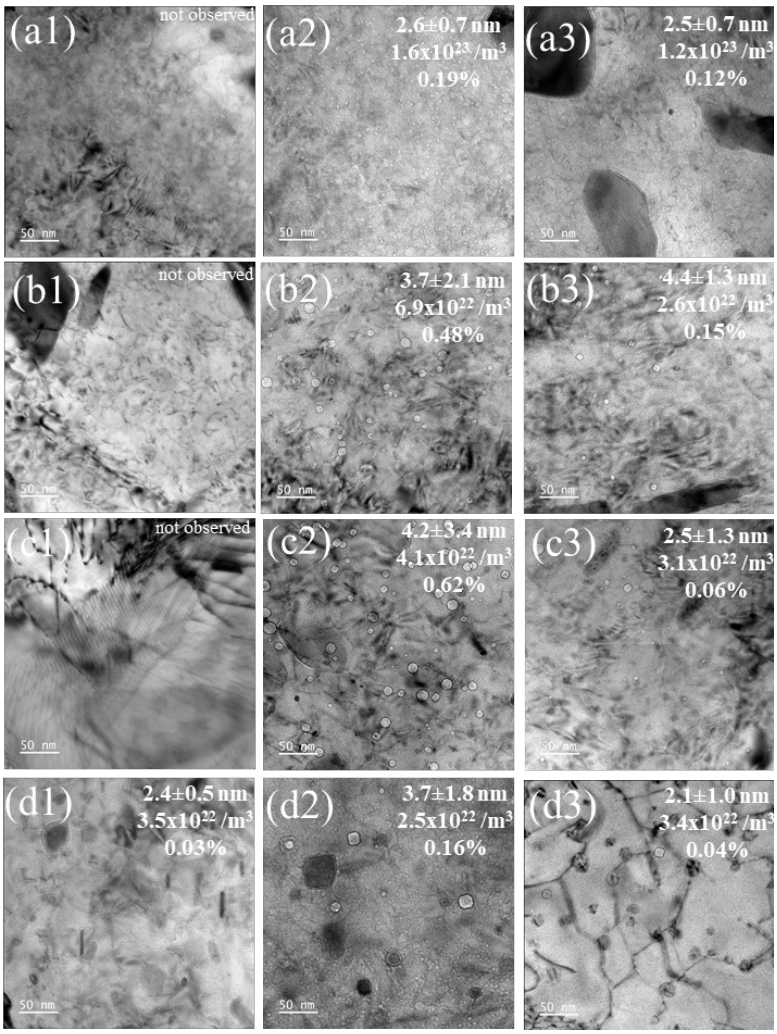

Figure 5.19. Cavity microstructures in dual-ion irradiated AM-HT9 (Heat B) alloys at 50 dpa with increasing irradiation temperature: (a) 400°C, (b) 445°C, (c) 460°C, and (d) 500°C, with the three columns representing ASB, ACO3, and FCRD from the left to the right, respectively.

Table 5.8. Summary of characterization results for cavities in dual-ion irradiated AM-HT9 (Heat B) at 50 dpa with a damage rate of 5.8×10^{-4} dpa/s and a helium co-injection rate of 4 He appm/dpa. N.O. indicates that the feature was not observed.

	Temperature (°C)	Cavity Diameter (nm)	Cavity Density (10^{21} /m^3)	Swelling
ASB	400	N.O.	N.O.	0
	445	N.O.	N.O.	0
	460	N.O.	N.O.	0
	500	2.4 ± 0.5	35.1 ± 3.5	0.03 ± 0.00 %
ACO3	400	2.6 ± 0.7	156.3 ± 15.6	0.19 ± 0.02 %
	445	3.8 ± 2.2	69.3 ± 7.0	0.48 ± 0.05 %
	460	4.2 ± 3.4	41.4 ± 4.1	0.62 ± 0.01 %
	500	3.7 ± 1.8	25.0 ± 2.5	0.16 ± 0.02 %
FCRD	400	2.5 ± 0.7	116.7 ± 11.7	0.12 ± 0.01 %
	445	4.4 ± 1.3	25.9 ± 2.6	0.15 ± 0.02 %
	460	2.5 ± 1.3	31.0 ± 3.1	0.06 ± 0.01 %
	500	2.1 ± 1.0	34.2 ± 3.4	0.04 ± 0.00 %

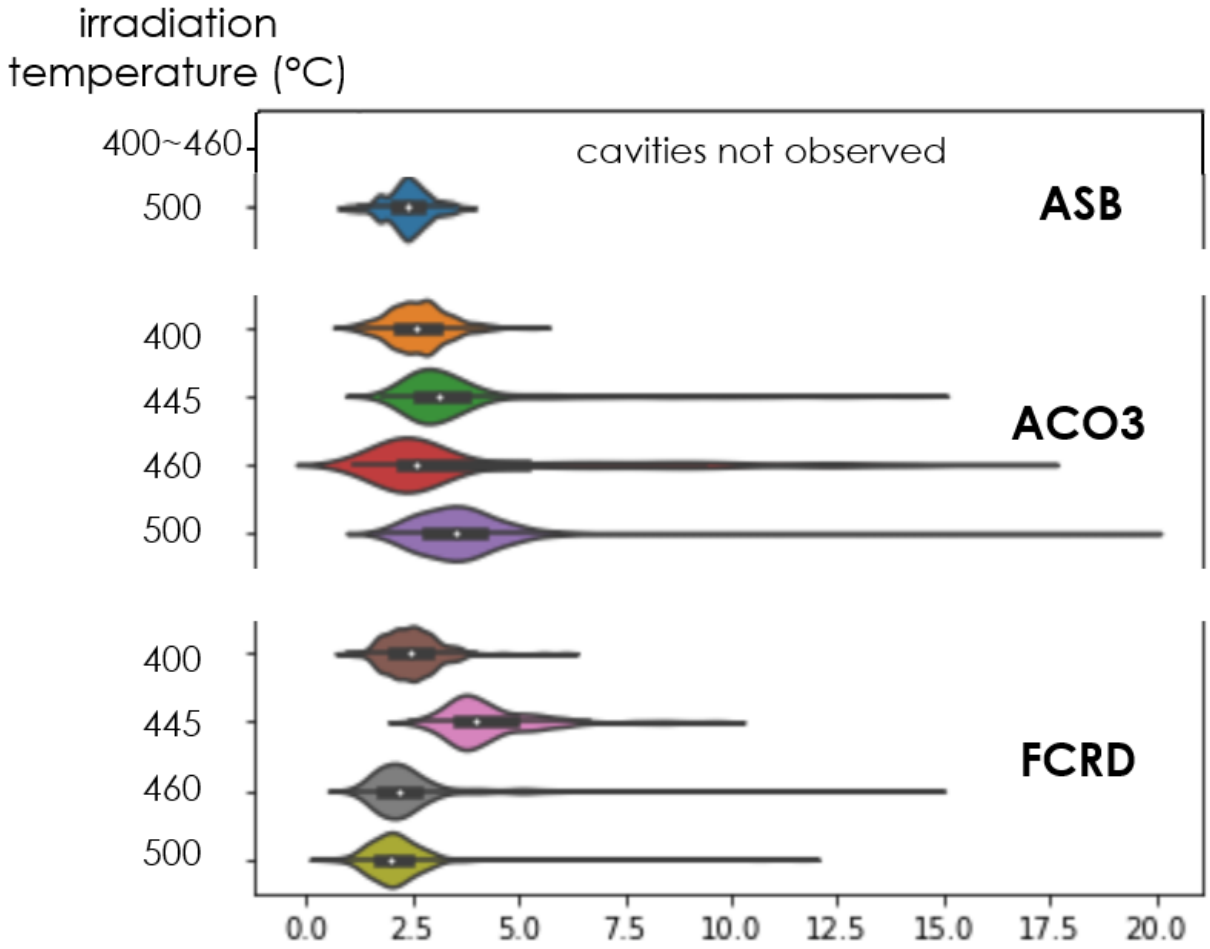

Figure 5.20. Cavity size distribution in dual-ion irradiated AM-HT9 (Heat B) alloys with increasing irradiation temperatures from 400°C to 500°C.

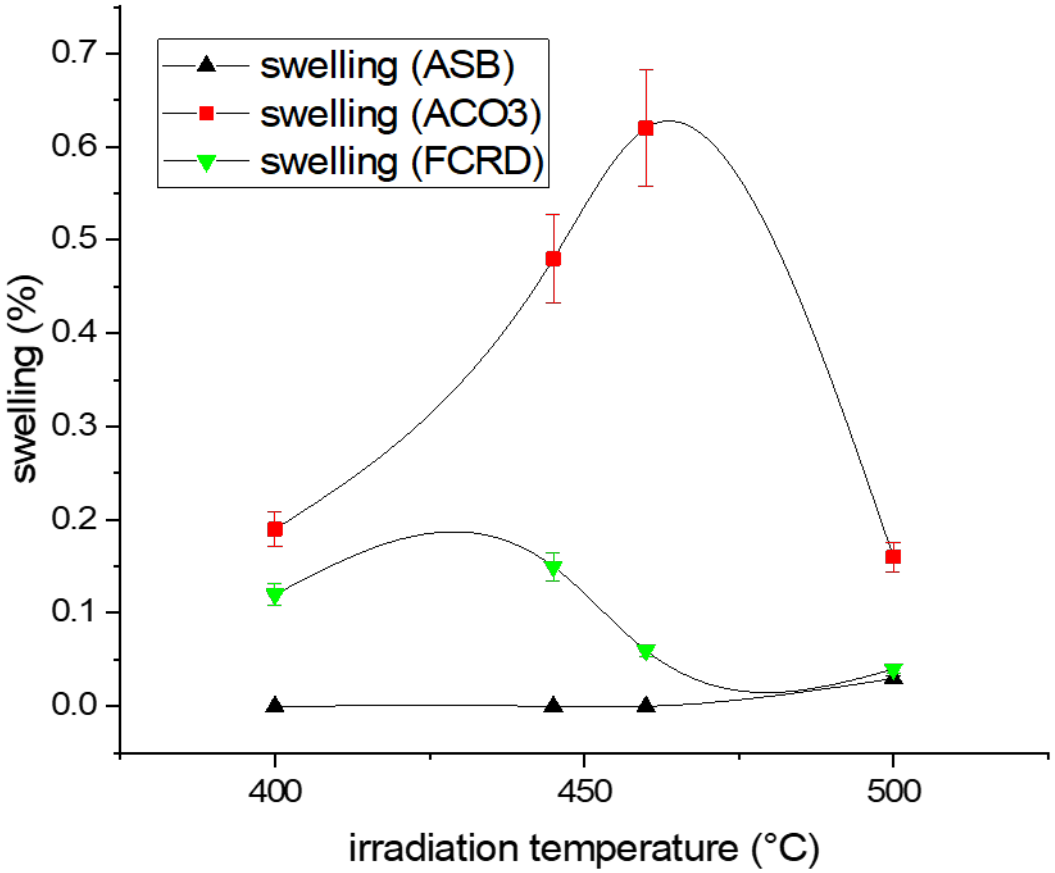

Figure 5.21. Swelling in three conditions of AM-HT9 (Heat B) as a function of irradiation temperatures to the damage level of 50 dpa.

5.3.2 Dislocation Loop Evolution

Dislocation loops of type and $a\langle 100\rangle$ are observed to form in all irradiated AM-HT9 (Heat B) regardless of the irradiation temperature or the condition of the alloy, whereas $a/2\langle 111\rangle$ loops are observed to form in all conditions of AM-HT9 (Heat B) with all irradiation temperatures except 500°C. Representative dislocation loop microstructures induced by irradiation are shown in Figure 5.22. The dislocation loop size (in diameter) and density as a function of damage levels are plotted in Figure 5.23. The full statistics of dislocation loops are summarized in Table 5.9.

As can be seen in Figure 5.23 and Table 5.9, the $a\langle 100\rangle$ dislocation loop size increases and density decreases significantly with increasing irradiation temperatures, regardless of the

conditions of AM-HT9. In the ASB specimen, the $a\langle 100\rangle$ dislocation loop size of 7.4 ± 1.9 nm at 400°C increases to 23.2 ± 7.9 nm at 500°C, with the density changing from 3.2 ± (0.3) × $10^{21}/m^3$ at 400°C to 0.3 (± 0.0) × $10^{21}/m^3$ at 500°C. In the ACO3 specimen, the $a\langle 100\rangle$ dislocation loop size of 11.5 ± 5.6 nm at 400°C increases to 38.1 ± 15.4 nm at 500°C, with the density changing from 6.4 (± 0.6) × $10^{21}/m^3$ at 400°C to 0.3 (± 0.0) × $10^{21}/m^3$ at 500°C. In the FCRD specimen, the $a\langle 100\rangle$ dislocation loop size of 10.3 ± 5.1 nm at 400°C increases to 42.2 ± 16.3 nm at 500°C, with the density changing from 5.9 (± 0.6) × $10^{21}/m^3$ at 400°C to 0.4 (± 0.0) × $10^{21}/m^3$ at 500°C. The growth of $a\langle 100\rangle$ dislocation loops in all three specimens is very significant with increasing temperatures, with their size increasing by three to four times. Besides the dislocation loop evolution within each one of three conditions of AM-HT9 with increasing irradiation temperatures, interesting results are obtained when comparing the loop statistics across three specimens under the same irradiation conditions. The $a\langle 100\rangle$ dislocation loop size reported to form in the irradiated ASB sample is in general smaller than the ACO3 and FCRD samples at all tested irradiation temperatures.

On the other hand, the statistics for $a/2\langle 111\rangle$ dislocation loops are more scattered. In the ASB sample, the size of $a/2\langle 111\rangle$ dislocation loops increases from 5.2 ± 1.9 nm at 400°C to 10.1 ± 4.1 nm at 460°C, with scattering data in density going down first from 5.5 (± 0.6) × $10^{21}/m^3$ at 400°C to 1.6 (± 0.2) × $10^{21}/m^3$ at 445°C, then going up again to 2.2 (± 0.2) × $10^{21}/m^3$ at 460°C. In the ACO3 sample, the size of $a/2\langle 111\rangle$ dislocation loops increases from 9.3 ± 3.6 nm at 400°C to 27.1 ± 8.7 nm at 445°C then decreases to 11.3 ± 5.6 nm at 460°C. The density of $a/2\langle 111\rangle$ dislocation loops in ACO3 specimen decreases consistently, from 4.2 (± 0.4) × $10^{21}/m^3$ at 400°C to 0.5 (± 0.1) × $10^{21}/m^3$ at 460°C. In the FCRD sample, both size and density of $a/2\langle 111\rangle$ dislocation loops vary consistently with increasing irradiation temperatures, with monotonical

increase of size from 9.3 ± 4.3 nm at 400°C to 22.0 ± 7.8 nm at 460°C and decrease of density from 2.5 (± 0.3) × $10^{21}/m^3$ at 400°C to 0.7 (± 0.1) × $10^{21}/m^3$ at 460°C. The disappearance of $a/2\langle 111\rangle$ dislocation loops at the highest test irradiation temperature of 500°C occurs across all three conditions of AM-HT9.

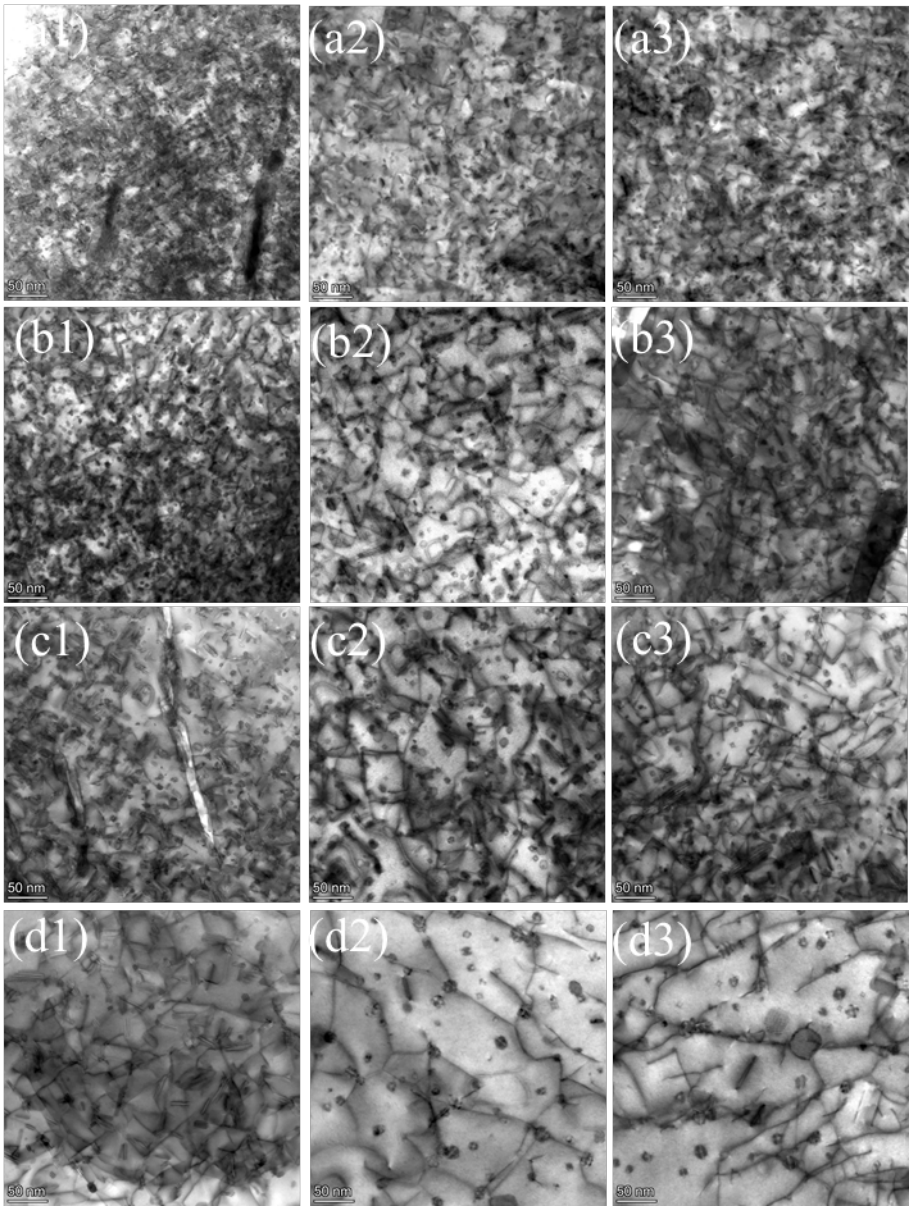

Figure 5.22. Dislocation loop microstructures in dual-ion irradiated AM-HT9 (Heat B) alloys at 50 dpa with increasing irradiation temperature: (a) 400°C, (b) 445°C, (c) 460°C, and (d) 500°C, with the three columns representing ASB, ACO3, and FCRD from the left to the right, respectively. All images were collected using on-zone [001] STEM-BF.

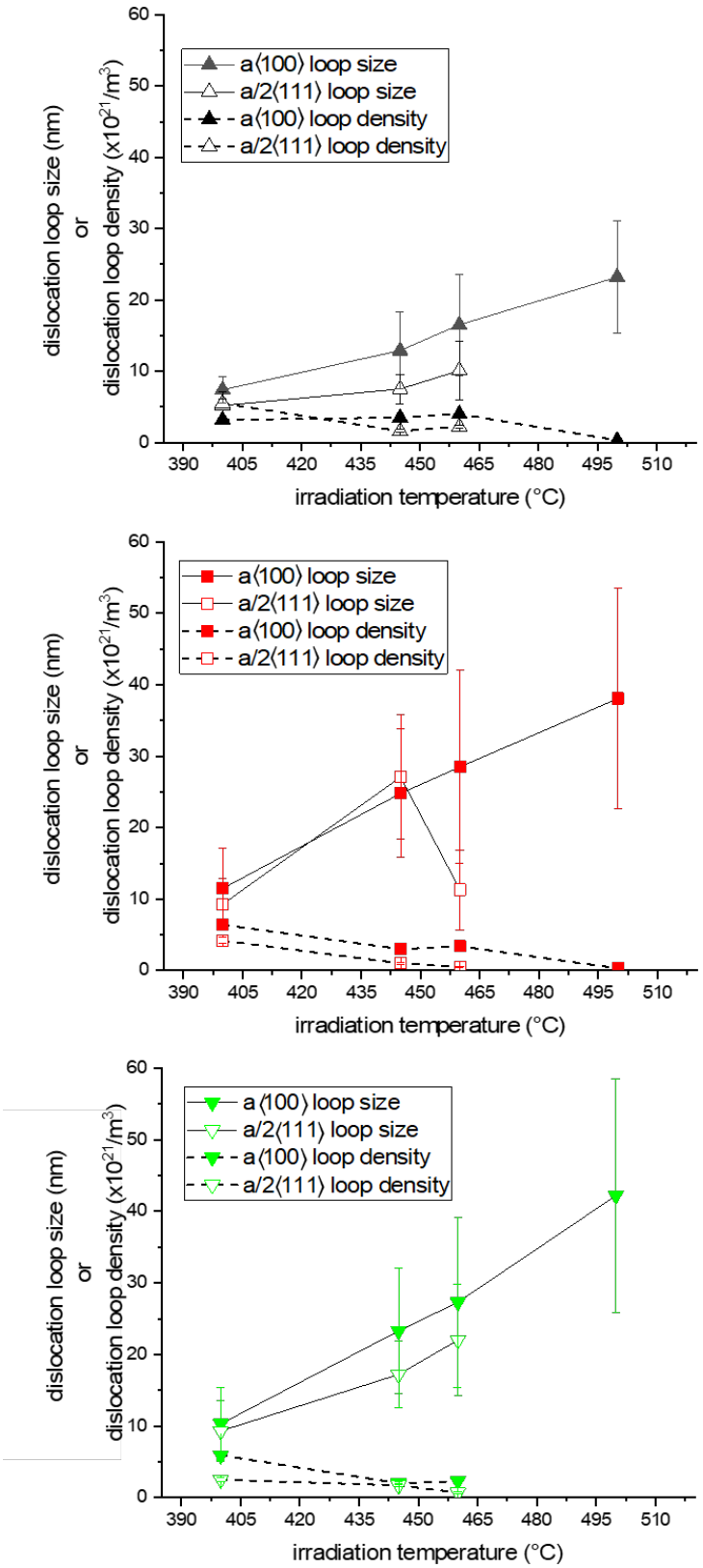

Figure 5.23. Dislocation loop size (in diameter) and density in dual-ion irradiated (a) ASB, (b) ACO3, and (c) FCRD conditions of AM-HT9 (Heat B) as a function of increasing irradiation temperature at 50 dpa.

Table 5.9. Summary of characterization results for dislocation loops in dual-ion irradiated AM-HT9 (Heat B) at 50 dpa with a damage rate of 5.8×10^{-4} dpa/s and a helium co-injection rate of 4 He appm/dpa. N.O. indicates that the feature was not observed.

	Temperature (°C)	$a\langle100\rangle$ Dislocation Loop Diameter (nm)	$a\langle100\rangle$ Dislocation Loop Density (10^{21} /m^3)	$a/2\langle111\rangle$ Dislocation Loop Diameter (nm)	$a/2\langle111\rangle$ Dislocation Loop Density (10^{21} /m^3)
ASB	400	7.4 ± 1.9	3.2 ± 0.3	5.2 ± 1.9	5.5 ± 0.6
	445	12.9 ± 5.4	3.5 ± 0.4	7.5 ± 2.1	1.6 ± 0.2
	460	16.5 ± 7.1	4.0 ± 0.4	10.1 ± 4.1	2.2 ± 0.2
	500	23.2 ± 7.9	0.3 ± 0.0	N.O.	N.O.
ACO3	400	11.5 ± 5.6	6.4 ± 0.6	9.3 ± 3.6	4.2 ± 0.4
	445	24.8 ± 9.0	3.0 ± 0.3	27.1 ± 8.7	1.0 ± 0.1
	460	28.5 ± 13.5	3.4 ± 0.3	11.3 ± 5.6	0.5 ± 0.1
	500	38.1 ± 15.4	0.3 ± 0.0	N.O.	N.O.
FCRD	400	10.3 ± 5.1	5.9 ± 0.6	9.3 ± 4.3	2.5 ± 0.3
	445	23.3 ± 8.7	2.0 ± 0.2	17.2 ± 4.7	1.7 ± 0.2
	460	27.3 ± 11.9	2.3 ± 0.2	22.0 ± 7.8	0.7 ± 0.1
	500	42.2 ± 16.3	0.4 ± 0.0	N.O.	N.O.

5.3.3 Precipitate Evolution

Ni/Si/Mn-rich clusters are observed to form in irradiated ACO3 and FCRD conditions of AM-HT9 (Heat B) regardless of the irradiation temperatures from 400°C to 500°C, whereas they are observed to form only at 460°C and 500°C in the ASB condition of AM-HT9 (Heat B). Representative Ni/Si/Mn-rich cluster microstructures induced by irradiation are shown in Figure 5.24. The Ni/Si/Mn-rich precipitate size (in diameter) and density as a function of damage levels are plotted in Figure 5.26. The full statistics of Ni/Si/Mn-rich precipitates and sink strengths are summarized in Table 5.10.

As can be seen in Figure 5.26 and Table 5.10, in the ASB specimen, the Ni/Si/Mn-rich precipitates only form at 460°C and 500°C, with the size increasing and the density decreasing significantly with higher irradiation temperatures. The Ni/Si/Mn-rich precipitate size of 6.6 ± 1.7 nm at 460°C increases to 14.7 ± 6.5 nm at 500°C, and the density decreases from 10.7 (± 1.1) ×

$10^{21}/m^3$ at 460°C to 2.4 (± 0.2) × $10^{21}/m^3$ at 500°C. In the heat-treated ACO3 and FCRD sample, the Ni/Si/Mn-rich precipitates form at all irradiation temperatures. In ACO3, the average size increases with increasing damage levels, from 5.6 ± 1.7 nm at 400°C to 12.4 ± 5.6 nm at 500°C, while the density drops from 20.5 (± 2.0) × $10^{21}/m^3$ at 400°C to 4.7 (± 0.5) × $10^{21}/m^3$ at 500°C, according to Figure 5.26 and Table 5.6. In the FCRD sample, similarly, the average size increases with increasing damage levels, from 6.5 ± 1.9 nm at 400°C to 14.8 ± 9.1 nm at 500°C. the density first increases from 11.4 (± 1.1) × $10^{21}/m^3$ at 400°C to 15.4 (± 1.5) × $10^{21}/m^3$ at 445°C, then decreases to 4.3 (± 0.4) × $10^{21}/m^3$ at 500°C.

Cr-rich clusters are observed to form at all irradiation temperatures in the ASB sample, whereas they are not observed to form in the ACO3 and FCRD conditions of AM-HT9. Representative Cr-rich cluster microstructures induced by irradiation in the ASB sample are shown in Figure 5.25. The Cr-rich precipitate size (in diameter) and density as a function of irradiation temperatures are plotted in Figure 5.26. The full statistics of Cr-rich precipitates and sink strengths are summarized in Table 5.10.

As can be seen in Figure 5.26 and Table 5.10, in the ASB specimen, drastic evolution of Cr-rich precipitates occurs. The average size first decreases from 8.1 ± 2.7 nm at 400°C to 5.1 ± 1.2 nm at 445°C, then increases significantly to 19.6 ± 15.2 nm at 500°C. Meanwhile, the Cr-rich precipitate density varies in the opposite way, where it first increases from 25.2 (± 2.5) × $10^{21}/m^3$ at 400°C to 41.0 (± 4.1) × $10^{21}/m^3$ at 445°C, then sharply decreases to 3.9 (± 0.4) × $10^{21}/m^3$ at 500°C.

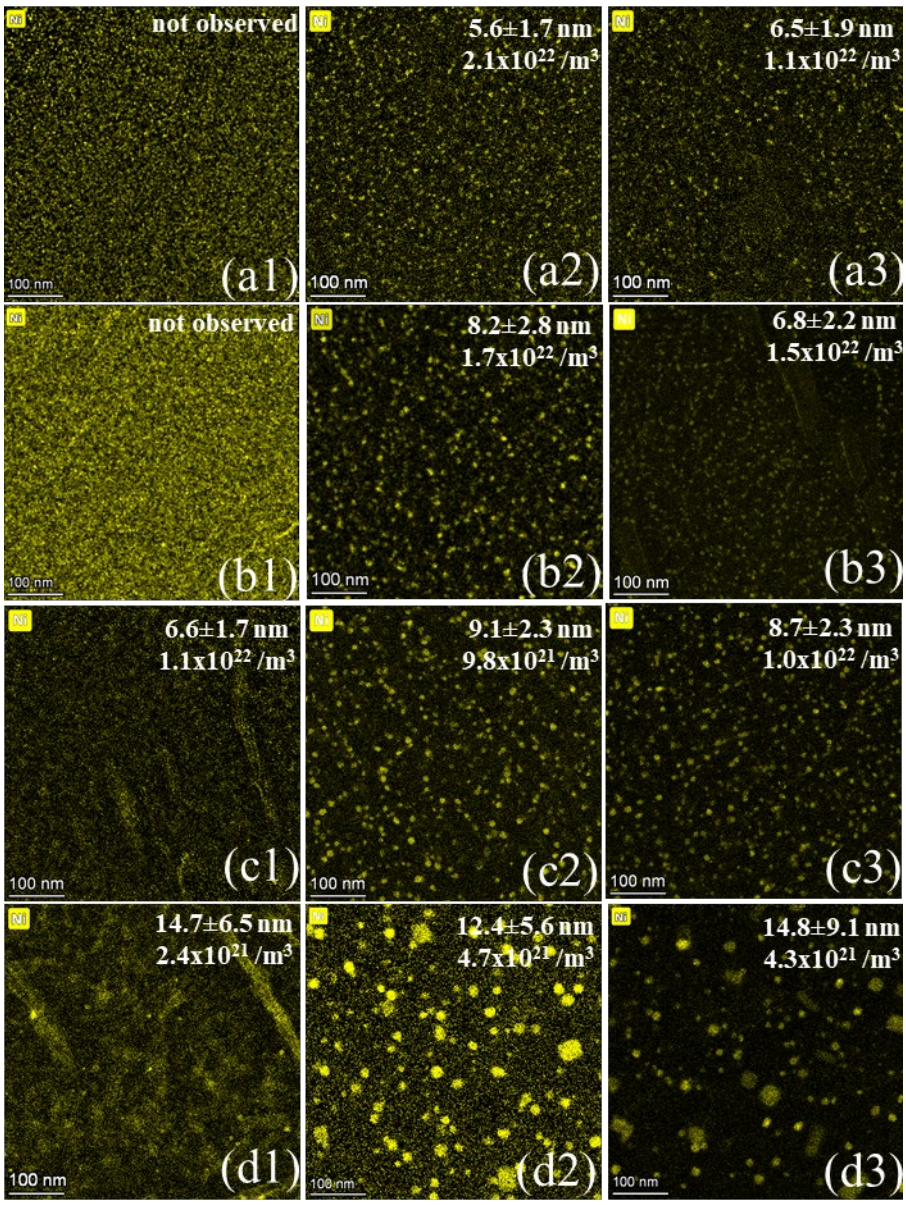

Figure 5.24. Ni/Si/Mn-rich cluster microstructures in dual-ion irradiated AM-HT9 alloys (Heat B) at 50 dpa with increasing irradiation temperature: (a) 400°C, (b) 445°C, (c) 460°C, and (d) 500°C, with the three columns representing ASB, ACO3, and FCRD from the left to the right, respectively.

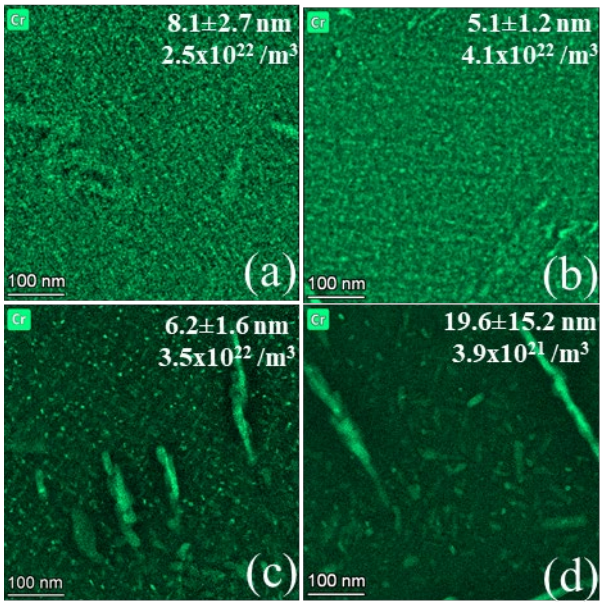

Figure 5.25. Cr-rich cluster microstructures in dual-ion irradiated AM-HT9 (Heat B) alloys at 50 dpa with increasing irradiation temperature: (a) 400°C, (b) 445°C, (c) 460°C, and (d) 500°C, with the three columns representing ASB, ACO3, and FCRD from the left to the right, respectively.

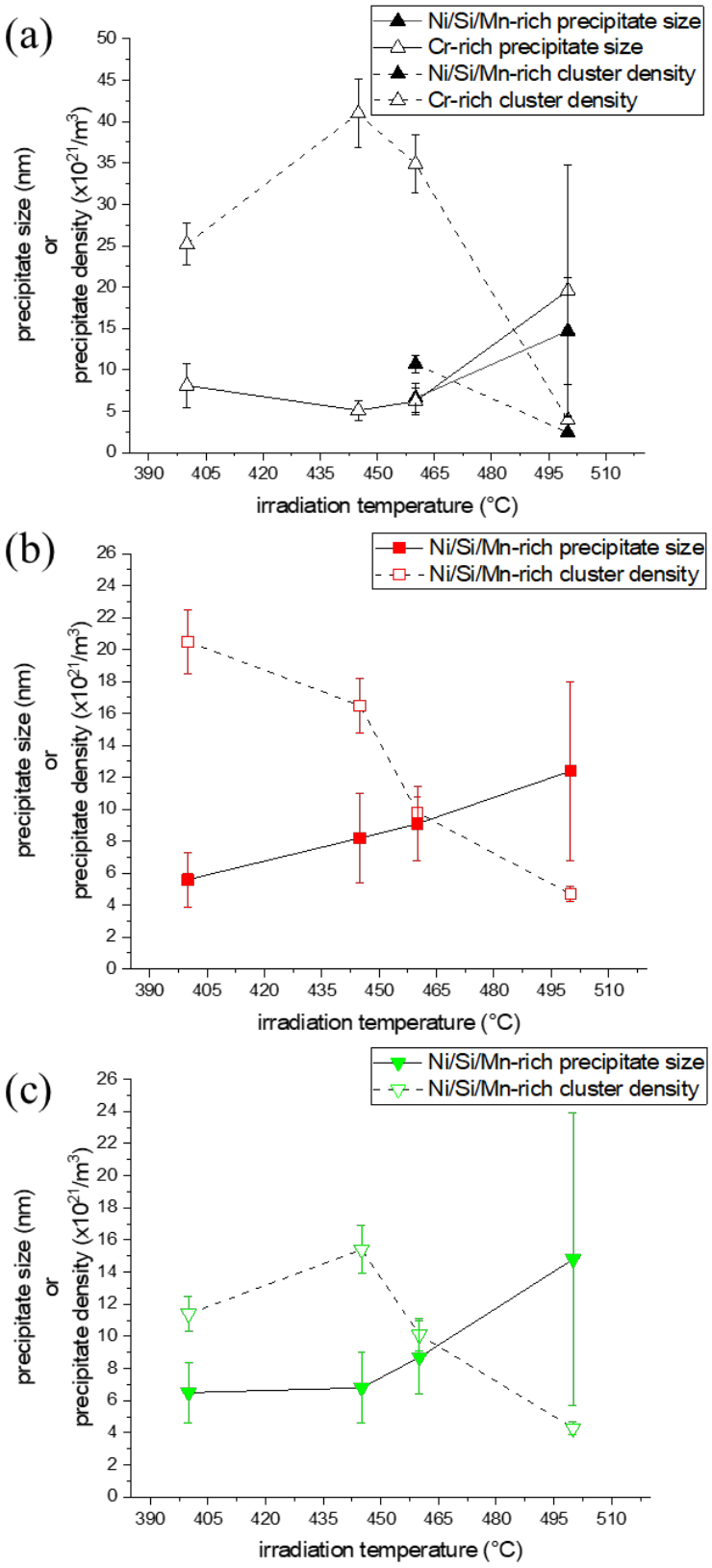

Figure 5.26. Precipitate size (in diameter) and density in dual-ion irradiated (a) ASB, (b) ACO3, and (c) FCRD conditions of AM-HT9 (Heat B) as a function of increasing irradiation temperature at 50 dpa.

Table 5.10. Summary of characterization results for Ni/Si/Mn-rich and Cr-rich precipitates in dual-ion irradiated AM-HT9 (Heat B) at 50 dpa with a damage rate of 5.8×10^{-4} dpa/s and a helium co-injection rate of 4 He appm/dpa. N.O. indicates that the feature was not observed.

	Temperature (°C)	Ni/Si/Mn-rich Precipitate Diameter (nm)	Ni/Si/Mn-rich Precipitate Density (10^{21} /m^3)	Ni/Si/Mn-rich Precipitate Phase Fraction	Cr-rich Precipitate Diameter (nm)	Cr-rich Precipitate Density (10^{21} /m^3)	Cr-rich Precipitate Phase Fraction
ASB	400	N.O.	N.O.	N.O.	8.1 ± 2.7	25.2 ± 2.5	0.96%
	445	N.O.	N.O.	N.O.	5.1 ± 1.2	41.0 ± 4.1	0.34%
	460	6.6 ± 1.7	10.7 ± 1.1	0.19%	6.2 ± 1.6	34.9 ± 3.5	0.52%
	500	14.7 ± 6.5	2.4 ± 0.2	0.63%	19.6 ± 15.2	3.9 ± 0.4	5.81%
ACO3	400	5.6 ± 1.7	20.5 ± 2.0	0.25%	9.3 ± 3.3	0.8 ± 0.1	0.04%
	445	8.2 ± 2.8	16.5 ± 1.7	0.66%	N.O.	N.O.	N.O.
	460	9.1 ± 2.3	9.8 ± 1.0	0.47%	12.2 ± 5.9	0.6 ± 0.1	0.09%
	500	12.4 ± 5.6	4.7 ± 0.5	0.86%	36.3 ± 10.0	0.1 ± 0.0	0.38%
FCRD	400	6.5 ± 1.9	11.4 ± 1.1	0.20%	N.O.	N.O.	N.O.
	445	6.8 ± 2.2	15.4 ± 1.5	0.34%	N.O.	N.O.	N.O.
	460	8.7 ± 2.3	10.1 ± 1.0	0.42%	20.7 ± 19.8	0.9 ± 0.1	1.84%
	500	14.8 ± 9.1	4.3 ± 0.4	1.93%	27.4 ± 7.2	0.5 ± 0.1	0.65%

Chapter 6 Discussions

The discussion of the results presented in Chapter 5 will be divided into three main sections. The first Section discusses the role of sink strength in the starting microstructures and varying damage levels and irradiation temperatures on precipitate evolution of AM-HT9 in both Heat A and Heat B, which directly addresses the objective of determining the mechanisms that govern microchemical evolution in the AM-HT9 steel. The second Section discusses the evolution of dislocation loops in irradiated AM-HT9 in Heat B with varying damage levels and irradiation temperatures, which are governed by both the sink strengths in the starting microstructures and irradiation conditions. The second Section directly addresses the objective of determining the mechanisms that govern dislocation loop evolution in the AM-HT9 steel. In the third Section, the cavity growth rate equation is used to examine the swelling behaviors with varying irradiation parameters to directly address both objectives. The first two Sections are used to assist the discussion of the third Section, so that all microstructural evolution are taken into consideration to evaluate swelling behavior. Because the damage levels achieved within this work reach the steady-state swelling regime, the discussion will mainly focus on cavity growth rather than the nucleation of cavities.

6.1 Effects of Sink Strength and Irradiation Parameters on Microchemical Evolution

The effects of sink strength and irradiation parameters on microchemical evolution in AM-HT9 are discussed here with three Sections. Similarity to [37], effects of sink strength in the starting microstructures on radiation-induced segregation and precipitate evolution with a single

irradiation condition in Heat A of AM-HT9 are discussed in the first two Sections. In the third Section, the combined effects of both sink strength and radiation parameters, with series of varying damage levels and temperatures, on precipitation evolution are discussed. As shown in Figure 5.1 and Figure 5.2, Sridharan et al. [49] showed that the ASB condition of AM-HT9 fabricated by the DED process contained a significantly higher density of defect sinks compared with heat-treated ACO3 and FCRD, such as smaller grain size and higher density of grain boundaries, higher density of line dislocations, δ-ferrite phases, and finer precipitates [37,49]. As shown in Section 5.1, the sink strength in the ASB condition of AM-HT9 is $1.22 \times 10^{16}/m^2$, about five times higher than that in the heat-treated conditions, ACO3 and FCRD, of AM-HT9. In the Section, the effects of sink strength on cluster evolution and radiation-induced segregation are discussed in detail.

6.1.1 Radiation-Induced Segregation in Heat A

As shown in Figure 5.7 and Figure 5.9, the higher density of grain boundaries in the ASB trapped more Ni-solute atoms, whereas reduced sink density in heat-treated ACO3 and FCRD specimens enabled more Ni existence in the matrix. As a result, more mature and more coarsened Ni/Si/Mn-rich clusters, as well as potentially stronger radiation-induced segregation (RIS) behavior per boundary, exist in the heat-treated ACO3 and FCRD specimens under irradiation. The irradiation-induced Ni enrichment near the grain boundaries was expected because it has been extensively reported [18,157–159] for RAFM steels in which undersized solutes of Ni and Si tend to enrich, whereas oversized solutes of Cr and Mo tend to deplete. From Figure 5.10, where a detailed high-magnification STEM-EDX mapping was performed near an edge-on grain boundary in the ACO3 specimen, confirms this expectation. Interestingly, several Cu-rich clusters are shown to be nucleated heterogeneously near the Ni-enriched grain boundaries without Ni/Si/Mn-rich clusters in the heat-treated specimens, whereas no obvious segregation of Cu at the grain boundary

is observed. This result indicates that Ni/Si/Mn-rich clusters might not necessarily have provided heterogeneous nucleation sites for the Cu-rich clusters, whereas grain boundaries and dislocations are very likely to do so. This is consistent with the APT observations in Figure 5.7 in which the coprecipitation between Ni/Si/Mn-rich and Cu-rich clusters occurs mostly at the line dislocations or at the grain boundaries.

6.1.2 Ni/Si/Mn-rich and Cu-rich Precipitate Evolution in Heat A

As shown in Figure 5.6 and Figure 5.7, Ni/Si/Mn-rich clusters form in all conditions of AM-HT9 of Heat A, whereas Cu-rich clusters only form in the heat-treated ACO3 and FCRD specimens. Although Cu was not included in the specification parameters for the HT9 powder, the presence of Cu is not unexpected because it is a common and inevitable impurity that is introduced from the fabrication and heat-treatment process [160]. Thus, its effects on microstructural evolution under irradiation are important to evaluate. The STEM-EDX mapping of the ASB sample in Figure 5.6 clearly shows that the pre-existing V/Nb-rich precipitates and very minor Cu-rich clustering before irradiation in Figure 5.6 (a2) get dissolved into the matrix after irradiation in Figure 5.6 (d2). At the same time, the Ni/Si/Mn-rich precipitates in Figure 5.6 (d2) form with irradiation with the size of 6.1 ± 1.7 nm and density of 1.3 (±0.2) × 10^{22}/m^3, as indicated in Table 5.1. However, in the ACO3 and FCRD samples shown in Figure 5.6, the precipitation of Ni/Si/Mn-rich clusters and Cu-rich clusters are much more extensive and coarser than those of the ASB sample. In the ACO3 condition, the size and number density of the Ni/Si/Mn-rich precipitates are 9.7 ± 2.3 nm and 2.9 (±0.5) × 10^{21}/m^3, and in the FCRD condition, the size and density are 10.5 ± 3.1 nm and 3.7 (±0.8) × 10^{21}/m^3. Significant differences in the Cu-rich clustering between the ASB and two heat-treated ACO3 and FCRD specimens were observed. Although no obvious Cu-clustering was observed in the ASB irradiated specimen, the ACO3 and FCRD specimens

contained significant amounts of Cu-rich clustering with number densities of 2.9 (±0.5) × $10^{21}/m^3$ and 3.8 (±0.7) × $10^{21}/m^3$, respectively, after irradiation. The average size of the Cu-rich clustering also increases by at least 50% in both the ACO3 and FCRD heat-treated specimens.

Another interesting observation from the STEM-EDX mapping regarding the Ni/Si/Mn-rich precipitates and Cu-rich clustering in the heat-treated ACO3 and FCRD samples is that they appear to exhibit correlated precipitation under irradiation, as shown in Figure 5.6 (e2) and Figure 5.6 (f2). As shown, most Ni/Si/Mn-rich and Cu-rich clusters form precipitation pairs under irradiation in the heat-treated ACO3 and FCRD specimens, whereas this formation is not observed in the ASB condition because of the nonexistence of Cu-rich clusters.

Detailed APT 3D reconstruction for the three irradiated conditions of AM-HT9 samples further confirms this coprecipitation behavior between the Ni/Si/Mn-rich and Cu-rich clusters in the ACO3 and FCRD heat-treated specimens, as shown in Figure 5.7. APT also confirmed the absence of Cu-rich clusters in the ASB specimen. Most of the precipitates in all three conditions of AM-HT9 were observed to occur at or near dislocations or grain boundaries, and a few occurred inside the matrix. This is likely a result of heterogeneous nucleation sites provided near or at the dislocations and grain boundaries. Additionally, the precipitates' size and density trend in ASB, ACO-3, and FCRD obtained by APT matches the STEM-EDX results presented in Table 5.1, both showing significant coarsening of Ni/Si/Mn-rich clusters with greater size and lower density.

The proximity histograms in Figure 5.8 fully quantified the core compositions of precipitates in the irradiated microstructure from the APT data. The proximity histograms averaged over all Ni/Si/Mn-rich and Cu-rich precipitates observed in three conditions of AM-HT9 specimens. Note that near the Ni/Si/Mn-rich precipitate-matrix interface in the ACO3 and FCRD specimens shown in Figure 5.8 (b1) and Figure 5.8 (c1), Cu enrichment at or near the interface can

also be observed. This is a direct result of the coprecipitation of Ni/Si/Mn- and Cu-rich clusters observed in the STEM-EDX and APT data presented in Figure 5.6 and Figure 5.7, respectively, rather than the Cu enrichment uniformly around the Ni/Si/Mn-rich clusters. The precipitate core compositions are shown in Table 5.2; minor elements are omitted because of their much lower significance in terms of quantities measured compared with the major elements identified in the precipitates.

As Table 5.2 shows, Cu-rich clusters are observed only in the irradiated heat-treated ACO3 and FCRD specimens with no other elements enriching in these clusters. As for the Ni/Si/Mn-rich clusters, the concentration of Ni is higher in the heat-treated ACO3 and FCRD specimens than in the ASB specimen. Additionally, Mn was found to have mild enrichment in the Ni/Si/Mn-rich clusters because its concentration is higher in ACO3 and FCRD as well. The results obtained using the proximity histogram method confirm that the heat-treated ACO3 and FCRD conditions of AM-HT9 contained more mature (i.e., increased Ni and Si concentrations, as shown in Table 5.2) and more coarsened (i.e., greater size and lower density, as shown in Table 5.1) Ni/Si/Mn-rich clusters than those observed in the ASB condition. One might expect that the excessive grain boundaries and dislocations have provided “highways” for fast solute pipe-diffusion in the ASB specimen under irradiation whereas slower bulk diffusion is more prominent in the heat-treated ACO3 and FCRD specimens because of the lower sink density. As a result, more solute atoms should reside near the defect sinks rather than the matrix. However, the observation of less mature Ni/Si/Mn clusters in the ASB condition of AM-HT9 suggests that a high density of defect sinks could provide faster diffusional pathways, but the higher density of isolated heterogeneous nucleation sites overweighs the diffusional-coarsening response for the Ni/Si/Mn-rich clusters as compared with the heat-treated ACO3 and FCRD specimen. As a result, the amount of solute atoms per Ni/Si/Mn

cluster decreased and led to less mature Ni/Si/Mn precipitates as indicated by Table 5.2, with higher density as shown in Table 5.1 in the ASB specimen. Although Cu-rich clustering has been extensively reported in reactor pressure vessel steels because of its well-known contribution to material hardening and embrittlement after irradiation [161–167], only a few studies have reported such cluster formation in FM steels, such as T91 [168–170], HCM12A [169], and HT9 [160] under irradiation. Moreover, the coprecipitation behavior between Cu-rich and Ni/Si/Mn-rich clusters was first reported by Jiao et al. [168,169]. The precipitation of Cu-rich clusters is likely enhanced through a radiation-enhanced diffusion mechanism of Cu atoms [167,171]. Additionally, the supersaturation and thus precipitation of Cu could be caused by the particularly low solubility in pure α-Fe of less than 0.1 wt.% at 460 °C [172].

Cu is a common impurity that can be introduced into BCC steels during fabrication and processing [173–177]. Unique to the DED process, Cu-rich alloys are routinely used in the components of the manufacturing device, such as the nozzle components, in which high-velocity powder can come into contact with and erodes Cu atoms from the nozzle, resulting in the Cu uptake of the AM-HT9 alloys. Thus, Cu uptake could be intrinsic to the AM process. An evaluation of the powder and build chemistry indicates this is the case in this study. A net increase of 19.30 ppm was observed after the DED process; the initial Cu level of the powder was measured at or below 1 ppm. Later experiments on various lots of HT9 further confirmed the possibility of Cu uptake, which also coincided with Zn uptake. These later studies indicated that the Cu uptake in the print of materials fabricated in the DMD 103D system was caused by the scrubbing process on brass components in the powder process stream. These results were initially unexpected but logical, and they highlight the unique future challenges of adopting AM processes in the fabrication of nuclear-grade components. For instance, the existence of Cu-rich clusters in the irradiated microstructure

resulting from Cu uptake from the manufacturing system should be considered because these clusters are well known to cause radiation hardening and embrittlement in BCC steels [162,178].

The coprecipitation behavior of Cu-rich clusters and Ni/Si/Mn-rich clusters that was mostly observed at the dislocations and grain boundaries in the ACO3 and FCRD specimens shown in Figure 5.7 can be partially explained by heterogeneous nucleation. Defect sinks including line dislocations, dislocation loops, and mature Ni/Si/Mn-rich clusters formed in ACO3 and FCRD specimens under irradiation could have provided a limited amount of heterogeneous nucleation sites for the Cu-rich clusters [179,180]. However, the highly dispersed Ni/Si/Mn-rich clusters with delayed evolution, as well as the high-density defect sinks containing dislocations and grain boundaries, could have provided an abundance of potential heterogeneous nucleation sites for the Cu-rich clusters. The abundance of these sites could have resulted in less Cu per site on average and thus no visible Cu-rich clusters that can be observed in the ASB specimen. Another factor that might contribute to the absence of Cu-rich clusters in the ASB specimen by both STEM-EDX and APT characterization is that the high-density defect sinks and traps in the ASB specimen could significantly decrease the diffusivity of the solute, resulting in reduced formation and coarsening kinetics of Cu-rich clusters at the irradiation temperature of 460°C. Both effects discussed could cause a highly dispersed distribution of Cu in the ASB specimen's microstructure.

Although the Cu-rich cluster evolution is speculated to be strongly delayed in the ASB specimen at the 50 dpa and 460°C test condition, the Cu-rich clusters might be able to nucleate and coarsen at a higher damage level. If so, then the clusters will affect the radiation responses of the ASB AM-HT9 specimen by providing even more defect sinks at the precipitate-matrix interface. Additionally, the post-build heat-treatments could release Cu from trapping sites before irradiation (e.g., leaching Cu from grain boundaries, precipitates, dislocations), resulting in a

greater amount of free Cu being present in the matrix of ACO3 and FCRD specimens before irradiation. As a result, significant amounts of Cu-rich clusters are more easily precipitated under irradiation, as observed in Figure 5.6.

6.1.3 Ni/Si/Mn-rich and Cr-rich Precipitate Evolution in Heat B

Within the Heat B of AM-HT9, the focus is on the formation of Ni/Si/Mn-rich precipitates in all conditions and Cr-rich precipitates in ASB condition. In any conditions of AM-HT9 (Heat B), no Cu-rich precipitates are observed, because they would have precipitated out under irradiation due to the low solubility of Cu in the ferritic Fe-based matrix [172]. The absence of Cu-rich precipitates indicates a success in significantly reducing, if not preventing, Cu uptake from the AM or heat-treatment processes, as compared to Heat A. This Section of discussion will be divided into two subsections with different focuses on the damage level effects and the temperature effects, coupled with the sink strength effects on the evolution of Ni/Mn/Si-rich and Cr-rich precipitates.

6.1.2.3 Damage Level Effects

According to Figure 5.18 and Table 5.6, the damage levels from 16.6 dpa to 250 dpa strongly affect the Ni/Si/Mn-rich precipitation behavior, especially in the heat-treated FCRD specimens with irradiation temperature of 445°C. The dependence on damage levels in ASB or heat-treated ACO3 specimens seem to be much lower. In the FCRD specimen, a typical precipitate growth behavior is observed from 16.6 dpa to 250 dpa, where average size increases and density decreases with increasing damage levels. Meanwhile, the phase fraction significantly increases with increasing damage levels.

The complete Ni/Si/Mn-rich precipitate growth process in FCRD specimen captured using the selected irradiation conditions indicates that at 16.6 dpa, nucleation occurs extensively without

significant growth. At the same time, a significant amount of Ni solute atoms still stays in the matrix without being extracted out to precipitate. With increasing damage levels (and increasing time at the irradiation temperature of 445°C) however, these solutes keep being pulled to precipitate out, potentially nucleating to form new Ni/Si/Mn-rich clusters; or more likely, these solutes or small clusters get absorbed by existing Ni/Si/Mn-rich precipitates to assist the growth behavior. The growth mechanism seems more dominant compared to the nucleation of new clusters, as the average size increases and the density decreases monotonically.

On the contrary, Ni/Si/Mn-rich precipitate evolution is much less drastic in the other heat-treated specimen, ACO3. At 16.6 dpa, a much larger size in ACO3 of 9.0 ± 1.9 nm as compared to 5.2 ± 2.3 nm in FCRD is observed. With damage levels higher than 100 dpa, the size or density do not change much further in ACO3, indicating a saturation is achieved at 100 dpa. The sharp comparison between the two heat-treated samples indicates that the cluster evolution is much faster in the ACO3 specimen, with significant growth already occurring at lower damage levels. At the highest damage level of 250 dpa, it is interesting to note that both size and density are nearly identical (with 1.0% and 3.5% difference for the size and density, respectively) for ACO3 and FCRD specimens. The primary difference is then the dose to reached Ni/Si/Mn-rich precipitate saturation (e.g., when nucleation and growth reach nearly asymptotic responses) where the much lower damage level of 100 dpa is needed for ACO3, as compared to 250 dpa for FCRD.

In the ASB specimen, damage levels also show weaker dependence on Ni/Si/Mn-rich precipitates. At 16.6 dpa and 50 dpa, no Ni/Si/Mn-rich precipitates are observed, indicating a sluggish nucleation behavior compared to ACO3 and FCRD. At 250 dpa, the Ni/Si/Mn-rich precipitate size of 7.7 ± 2.8 nm of ASB is significantly smaller than 10.4 ± 4.3 nm in ACO3 and 10.5 ± 3.2 nm in FCRD, with the density of 9.4 (± 0.9) × $10^{21}/m^3$ much higher than 5.7 (± 0.6) ×

$10^{21}/m^3$ in ACO3 and 5.5 (± 0.6) × $10^{21}/m^3$ in FCRD. Again, sluggish growth behavior is also observed in the ASB specimen as compared to both ACO3 and FCRD samples.

The drastically different Ni/Si/Mn-rich precipitation evolution as a function of damage levels within ASB, ACO3 and FCRD specimens can be explained, in part, by their sink strength in the starting microstructures. In the as-received ASB sample, high density of line dislocations and grain boundaries result in the sink strength of 7.5 × $10^{15}/m^2$, which is higher than 1.9 × $10^{15}/m^2$ in ACO3 and 2.4 × $10^{15}/m^2$ in FCRD. As illustrated in Section 6.1.1, a high-density of defect sinks provide heterogeneous nucleation sites for Ni/Si/Mn-rich precipitates in Heat A, which is likely to be the case within the ASB specimen here for Heat B. Although many more nucleation sites exist within ASB to promote the nucleation process, the average Ni solute composition per nucleated cluster decreases dramatically, so that much of the small clusters cannot be captured when STEM-EDX mapping was conducted with limited signals. In ACO3 and FCRD however, a lower density of defect sinks provides limited nucleation sites, but there are also increased free solute atoms within the matrix to diffuse and form extended Ni/Si/Mn-rich precipitates. This general mechanism explains why at 16.6 dpa and 50 dpa, Ni/Si/Mn-rich precipitates are not observed within the ASB specimen but are observed in the heat-treated specimens. A higher irradiation damage level of 75 dpa is needed in ASB to form Ni/Si/Mn-rich precipitates with appreciable Ni content within to be detected from the STEM-EDX images. Afterwards, the precipitate evolution seems to progress extremely slowly with further increase of damage levels, if saturation is not reached already. A limited amount of Ni/Si/Mn-rich precipitates are pinned by the high density of defect sinks, including those pre-existing prior to irradiation such as line dislocations and grain boundaries, and those form under irradiation such as dislocation loops, cavities and other secondary phases, like Cr-rich ones. The formation of Cr-rich precipitates, which will be discussed later on within this

Section, is actually believed to be a principle driving factor for the sluggish evolution of microstructures in ASB, including the Ni/Si/Mn-rich precipitate evolution. The strong pinning effects prevent further growth of Ni/Si/Mn-rich clusters at high damage levels such as 250 dpa, and result in the observed limited evolution progress.

A similar explanation can be applied to the comparison of different Ni/Si/Mn-rich precipitate evolution in the ACO3 and FCRD samples. The higher sink strength in FCRD than ACO3 in the starting microstructures retards the coarsening process. Below 16.6 dpa, significant growth occurs already in the ACO3 specimen, whereas in FCRD nucleation is more dominant than growth. Slightly higher sink strength and sink density in FCRD provides more heterogeneous nucleation sites for Ni/Si/Mn-rich clusters, and they also make the growth of these clusters sluggish. At higher damage levels, however, the annealing and the microstructural evolution under irradiation in FCRD at 445°C reduce the pinning effects. Line dislocation and dislocation loop density drop with longer irradiation time as shown in Figure 5.14 and Figure 5.15, so more Ni/Si/Mn solutes or small clusters are released from these defect sinks to assist with the coarsening process. That explains why ACO3 with lower sink strength sees early-on saturation and Ni/Si/Mn-rich precipitation, whereas FCRD catches up later at higher damage levels.

The similar catch-up behavior of Ni/Si/Mn-rich precipitation in ASB is not observed, for a few potential reasons. First, a potentially much higher damage level than 250 dpa is needed so that Ni/Si/Mn solutes can be released and contribute to coarsening. Second, new microstructures such as cavities, dislocation loops, and other secondary phases forming under irradiation, where Ni and/or Si segregation may occur, can contribute to the delayed evolution of Ni/Si/Mn-rich precipitates. Within the ASB specimen, limited cavity formation is observed under irradiation as shown in Figure 5.11 and Table 5.3, and dislocation loops tend to open up and form line

dislocations with higher damage levels that are susceptible to an annealing effect, both of which are believed to have limited contribution. However, as mentioned before, a high density of Cr-rich precipitates form in the ASB specimen, which could greatly contribute to the pinning effects of small Ni/Si/Mn-rich clusters.

As shown in Figure 5.18 and Table 5.6, Cr-rich precipitates form extensively within the ASB specimen. On the contrary, their formation in the heat-treated ACO3 and FCRD specimens is minimal. The result is expected, because Cr solutes mostly diffuse and are incorporated into Cr-rich carbides and carbonitrides form to stabilize PAGBs and martensitic lath structure developed during the heat-treatment processes for the ACO3 and FCRD. As a result, the Cr content of 12 wt.% within the matrix is much higher in ASB compared to ACO3 and FCRD specimens – note, this hypothesis will be confirmed in future, on-going work using APT. Under irradiation, Cr solutes easily precipitate out to form Cr-rich clusters within ASB. The large-size and low-density Cr-containing carbides and carbonitrides are not believed to contribute much to microstructural evolution within the matrix, as they primarily reside at grain boundaries and have limited precipitate-matrix interfacial area. This assumption is used in the sink strength calculations.

From 16.6 dpa to 50 dpa, both the size and the density of Cr-rich clusters increases, which indicates a mixture of on-going nucleation and growth processes. With further increase of damage levels, the average size keeps going up, while the density keeps going down, which is a typical precipitate growth process. These formed Cr-rich precipitates are dense and dispersed throughout the irradiated region within the matrix as shown in Figure 5.17, thus are believed to strongly affect other microstructural evolution within the ASB specimen. As can be seen in Table 5.6, the additional sink strengths provided by these formed Cr-rich precipitates and Ni/Si/Mn-rich

precipitates are about 3-4 times higher in ASB compared to ACO3 and FCRD, due to the extensive precipitate-matrix interfacial area.

6.1.2.4 Irradiation Temperature Effects

According to Figure 5.26 and Table 5.10, irradiation temperatures from 400°C to 500°C with the 50 dpa damage level drastically alters the precipitation responses in AM-HT9, regardless of the precipitate type (Ni/Si/Mn-rich or Cr-rich) or the sample condition (ASB, ACO3 or FCRD).

For the Ni/Si/Mn-rich precipitates, they are not observed in ASB at lower temperatures of 400°C and 445°C. Apparently, not enough kinetic energy at these relatively low temperatures is available to overcome the pinning effects previously discussed within the ASB specimen with high sink strength. At higher temperatures of 460°C and 500°C, however, Ni/Si/Mn-rich precipitates form with a typical precipitation behavior. The size increases, and the density decreases significantly in the ASB specimen at high temperatures. Note that, the Ni/Si/Mn-rich and Cr-rich precipitates seems to be in pairs with spatial relationships, which is similar to the co-precipitation behavior between Ni/Si/Mn-rich and Cu-rich observed and discussed for Heat A of AM-HT9.

On the contrary, Ni/Si/Mn-rich precipitates form at all selected irradiation temperatures in ACO3 and FCRD specimens with different evolution behaviors. In ACO3, the Ni/Si/Mn-rich precipitate size and density monotonically increase and decrease respectively, with increasing irradiation temperatures. In FCRD, the size of Ni/Si/Mn-rich precipitates increases from 400°C to 500°C, while the density first increases from 400°C to 445°C, then decreases all the way to 500°C. Very interestingly, although the similar growth behavior of Ni/Si/Mn-rich precipitates is observed in both ACO3 and FCRD, their differences can be linked to their sink strength in the starting microstructures.

At 400°C, the density of Ni/Si/Mn-rich precipitates in FCRD is only about the half of that in ACO3. The higher sink strength and sink density in FCRD than ACO3 are likely to provide more heterogeneous nucleation sites, but also lower the average solute compositions within each cluster. More importantly, 400°C is still a relatively low temperature regime, and not enough thermal energy is available to overcome the pinning effects and agglomerate small clusters. At 445°C, however, more kinetic energy in FCRD helps with the nucleation of Ni/Si/Mn precipitates that are visible within the STEM-EDX mapping, whereas the average size does not change much. At the same time in ACO3, extensive growth occurs at 445°C compared to 400°C. The average size increases from 5.6 ± 1.7 nm at 400°C to 8.2 ± 2.8 nm at 445°C, with the density dropping from 20.5 (± 2.0) × 10^{21}/m^3 to 16.5 (± 1.7) × 10^{21}/m^3. At even higher temperatures of 460°C and 500°C, the kinetic energy available is enough to completely overcome the pinning effects imposed by defects sinks in ACO3 and FCRD, thus a similar statistics and evolution progress of Ni/Si/Mn-rich precipitates are observed. At these high temperatures, the small difference in sink strengths in the starting microstructures between the two heat-treated conditions of AM-HT9 is not the determining factor anymore, on the contrary of the case of lower temperature of 400°C where sink strength effect is dominant.

For the Cr-rich precipitates in ASB, a similar two-regime behavior is observed. When the irradiation temperature increases from 400°C to 445°C, more heterogeneous nucleation of Cr-rich precipitates occurs, with the density going up. At higher-temperature regime of 460°C and 500°C, the Cr-rich precipitate size goes up and the density drops quickly. In ACO3 and FCRD, the amount of Cr solute atoms is significantly lower than ASB. Therefore, minimal Cr-rich precipitates form under irradiation, especially at low temperatures. FCRD contains more Cr-rich precipitate phase

fraction than ACO3 at 460°C and 500°C, possibly because of slightly higher Cr-content in the matrix as a result of the heat-treatment history.

6.2 Effects of Sink Strength and Irradiation Parameters on Dislocation Loop Evolution

The effects of sink strength and irradiation parameters on dislocation loop evolution in AM-HT9 (Heat B) are discussed here with two Sections, with two series of varying damage levels and irradiation temperatures.

6.2.1 Damage Level Effects

According to Figure 5.15 and Table 5.4, both a⟨100⟩ and a/2⟨111⟩ types of dislocation loops form under irradiation at all damage levels from 16.6 dpa to 250 dpa at 445°C. In the ASB specimen, the growth behavior of dislocation loops is observed. The size of both a⟨100⟩ and a/2⟨111⟩ types of dislocation loops increase with increasing damage levels, with the density decreasing slightly. As can be seen in Figure 5.14 and Table 5.5, the line dislocation density in the ASB specimen about twice as high compared to ACO3 and FCRD. Together with a high density of grain boundaries, as well as Ni/Si/Mn-rich and Cr-rich precipitates, the elevated sink strength in the ASB specimen results in increased annihilation of irradiation-induced point defects over a defined period of time or damage levels. The reduced density of surviving point defects in the ASB specimen leads to less point defects for agglomeration and the lower size of dislocation loops at 16.6 dpa. With the course of irradiation damage with more point defect generation, these dislocation loops grow and then coarsen in the ASB specimen. In the ACO3 and FCRD specimens, however, a/2⟨111⟩ dislocation loop size and density remain relatively unchanged, and this is because the lower initial sink strength allows for saturation in the a/2⟨111⟩ loop evolution process to occur before 16.6 dpa. The a/2⟨111⟩ dislocation loops achieve saturation at lower damage levels,

and the dependence of damage levels becomes weak at higher damage levels. The a⟨100⟩ dislocation loops, however, increase their average size slightly in ACO3 and FCRD specimens.

The properties between a⟨100⟩ and a/2⟨111⟩ types of dislocation loops are very different. Besides their difference in Burgers vector and habit plane, their stabilities are different as well. The a/2⟨111⟩ type of dislocation loops is known to be more mobile, because their Burgers vector is along the close-pack direction in the BCC material system. Upon heating, they also tend to coarsen more quickly or interact with gliding line dislocations, to open up themselves and form entangled dislocation networks. The a⟨100⟩ type of dislocation loops, however, is more stable, especially at higher temperatures [181]. The observation made within this work proves that the a⟨100⟩ type of dislocation loops can slowly coarsen even at high damage levels of 250 dpa or potentially more, whereas a/2⟨111⟩ dislocation loops easily become entangled dislocation networks rather than keeping their growth. The exhibition of the dislocation loop growth behavior in the ASB specimen shows that the high sink strength in the ASB specimen greatly delays the dislocation loop evolution of both types.

6.2.2 Irradiation Temperature Effects

As shown in Figure 5.23 and Table 5.9, a⟨100⟩ type of dislocation loops forms at all selected irradiation temperatures from 400°C to 500°C at 50 dpa in all conditions of AM-HT9. On the contrary, a/2⟨111⟩ dislocation loops form at all temperatures except 500°C at 50 dpa, also in all conditions of AM-HT9. Irradiation temperatures have a strong impact on the dislocation loop evolution [181]. In general, both types of dislocation loops grow up in size, and the density decreases rapidly with higher temperatures.

Within the ACO3 specimen, a decrease of a/2⟨111⟩ dislocation loop size from 445°C to 460°C is observed, and that is simply because larger a/2⟨111⟩ dislocation loops open up to form

entangled dislocation networks at the higher temperature of 460°C. At the same time, new and small a/2⟨111⟩ dislocation loops nucleate and form, which drags down the average a/2⟨111⟩ dislocation loop size. At 500°C, a/2⟨111⟩ dislocation loop growth is so fast that they are no longer stable in any conditions of AM-HT9.

Meanwhile, a⟨100⟩ type of dislocation loops remains to be stable, especially at higher temperatures. In all three conditions of AM-HT9, a⟨100⟩ dislocation loops grow larger consistently. Interestingly, sink strength greatly tailors the a⟨100⟩ dislocation loops evolution. At all selected irradiation temperatures, a⟨100⟩ dislocation loop size in the ASB specimen is consistently lower than that in the ACO3 and FCRD specimens. This result is expected, because the higher sink strength results in smaller amount of surviving point defects.

6.3 Effects of Sink Strength and Irradiation Parameters on Swelling Behaviors

The effects of sink strength and irradiation parameters on dislocation cavity and swelling evolution in AM-HT9 (Heat B) are discussed here with three Sections, with two series of varying damage levels and irradiation temperatures. For the damage level series, calculation of theoretical swelling rate as well as the effect of a microstructural-based parameter, Q, on swelling evolution are discussed in another Section.

6.3.1 Damage Level Effects

According to Figure 5.12 and Table 5.3, cavities form under irradiation in the two heat-treated ACO3 and FCRD conditions of AM-HT9 at all damage levels from 16.6 dpa to 250 dpa at 445°C, while in the ASB specimen cavities form only at 100 dpa or higher damage levels.

From the size distribution shown in Figure 5.12, the notable growth, reflected by the long tail at the higher end of the size distribution, of cavity size with increasing damage levels can be

observed in ACO3 and FCRD specimens. Much slower growth of cavities is observed in the ASB specimen from 100 dpa to 250 dpa. Note that there is always a peak showing high density and population of small cavities with size (in diameter) smaller than 5 nm. These cavities represent the ones that are newly nucleated under irradiation, which indicates that significant nucleation of cavities always occurs even in the ACO3 specimen at high damage levels, where cavity growth is also significant. Although the two processes occur at the same time, among these cavities that have a rather broad size distribution, those nucleated without significant coarsening do not contribute much to the overall volumetric swelling of the materials. Larger size cavities contribute significantly more to the volumetric swelling, because volume has a cubic relationship against the cavity size.

The overall swelling presented in Figure 5.13 shows the consistent trend with the size distribution in Figure 5.12, where the most coarsened cavities in ACO3 result in higher swelling at high damage levels. The typical three regimes for swelling evolution are observed from Figure 5.13. The whole tested damage level of 0-250 dpa for the ASB sample is likely within the incubation and the transient regime at the irradiation temperature of 445°C, where barely any cavity or swelling is observed. Most nucleated cavities do not experience significant coarsening. The transient regime for the ASB sample could extend to much higher damage levels above 250 dpa, followed by the linear steady-state swelling regime which is not observed here. In ACO3, the incubation regime is likely to be around 75 dpa, followed by a short transient regime between 75 dpa to 100 dpa. Above 100 dpa, the steady-state swelling regime is achieved, with the high swelling rate of about 0.03 %/dpa. During the steady-state swelling regime, significant coarsening of cavities occurs, which leads to the rapid increase of volumetric swelling. In FCRD, the swelling

rate is much lower at around 0.003 %/dpa, with the three swelling regimes pretty much the same as the ones of ACO3.

The theoretical swelling rates within the steady-state swelling regime are calculated using Equation 4.39, with the comparison of theoretical and experimental swelling rate listed in Table 5.7. As can be seen, the calculated swelling rates match reasonably well (within one order of magnitude of difference) with experimental swelling rates. The key variables governing the theoretical swelling rate calculations are cavity density, cavity size, and steady-state equilibrium vacancy and interstitial concentrations. The last two terms are obtained by solving the defect balance equation pairs shown in Equation 4.33 and Equation 4.34, which is related to all the sinks existing in the microstructure. The theoretical swelling rate calculation takes all the microstructural features or defect sinks, some are pre-existing, the others are irradiation-induced, into consideration. It is worth noting that, in this work, both Ni/Si/Mn-rich and Cr-rich precipitates are treated as neutral sinks and the sink strength calculation is therefore conducted with the same formula. However, the sink strength of precipitates depend on the lattice mismatch between the precipitates and matrix, as well as the precipitate type and composition [3]. Therefore the calculation in theory ideally should take the difference between different precipitate type into consideration. In this work, such distinction is not made due to the lack of modeling efforts to enable such quantitative calculation.

The dependence of experimental and theoretical swelling rates in three conditions of AM-HT9 irradiated at 445°C is shown in Figure 6.1. The swelling rates are experimentally measured or theoretically calculated at 75 dpa, 100 dpa, and 150 dpa. Interestingly, data points for ACO3 locate at the left side of the y = x black line, which reflects that the experimental swelling rate is higher than the theoretical one. This could be explained by how the experimental data obtained by

characterization are used as inputs into the equations. In the previously mentioned equations that are used to calculate theoretical swelling rate, the average cavity size was used. However, the major contributor to the overall swelling are larger cavities. ACO3 has more coarsened cavities than FCRD and ASB, therefore the calculation can underestimate the theoretical swelling rate if sufficient counting statistics are not acquired. In this work, an average of 375 cavities are counted per condition. In addition, the use of the average cavity size could "smear out" or reduce the large cavity contributions. To confirm the validity of it, more data points are needed to complete the full picture of the comparison between the experimental and theoretical swelling rate data. In addition, the differences in the sink strength of Ni/Si/Mn-rich and Cr-rich precipitate structures in the ACO3 and the FCRD specimen are not accounted for in the theoretical calculation, as discussed previously, which could be a significant driving factor in the observed disparity. Additional studies on the coherency of precipitates as a function of composition and size are needed to complete the full picture study of the swelling response under irradiation.

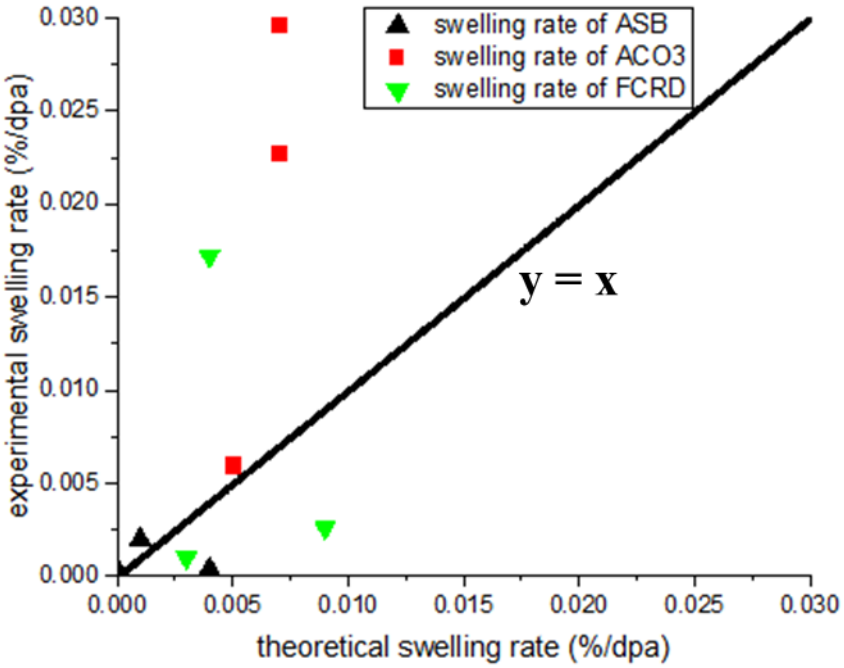

Figure 6.1. Dependence of experimental and theoretical swelling rates in three conditions of AM-HT9 irradiated at 445°C. The swelling rates are experimentally measured or theoretically calculated at 75 dpa, 100 dpa, and 150 dpa. The black line indicates the equal values between the two.

6.3.2 Relationship between Experimental Swelling Rate and Q-Value

Besides the swelling rate calculation done in Section 6.3.1, Mansur [109] proposed using a microstructural-based quantity, Q, to predict the swelling rate of materials under irradiation:

$$Q_{i,v} = \frac{z_{d\ i,v}\,\rho_d}{2\pi d_{cav}\rho_{cav}z_{cav\ i,v}} \qquad \text{Equation 6.1}$$

where $z_{d\ i,v}$ is the bias factor of line dislocations, ρ_d is the line dislocation density, $z_{cav\ i,v}$ is the bias factor of cavities. Essentially, the ratio of sink strength of biased (line dislocations) against neutral (cavities) sinks controls the $Q_{i,v}$ value that further determines swelling rate. The cavity swelling rate is proportional to $\frac{Q}{(1+Q)^2}$ [109]. Mathematically, the swelling approaches the maximum when the Q value approaches 1, meaning that when the biased and neutral sink strengths are approximately equal, or comparable to each other, the maximum swelling rate can be achieved.

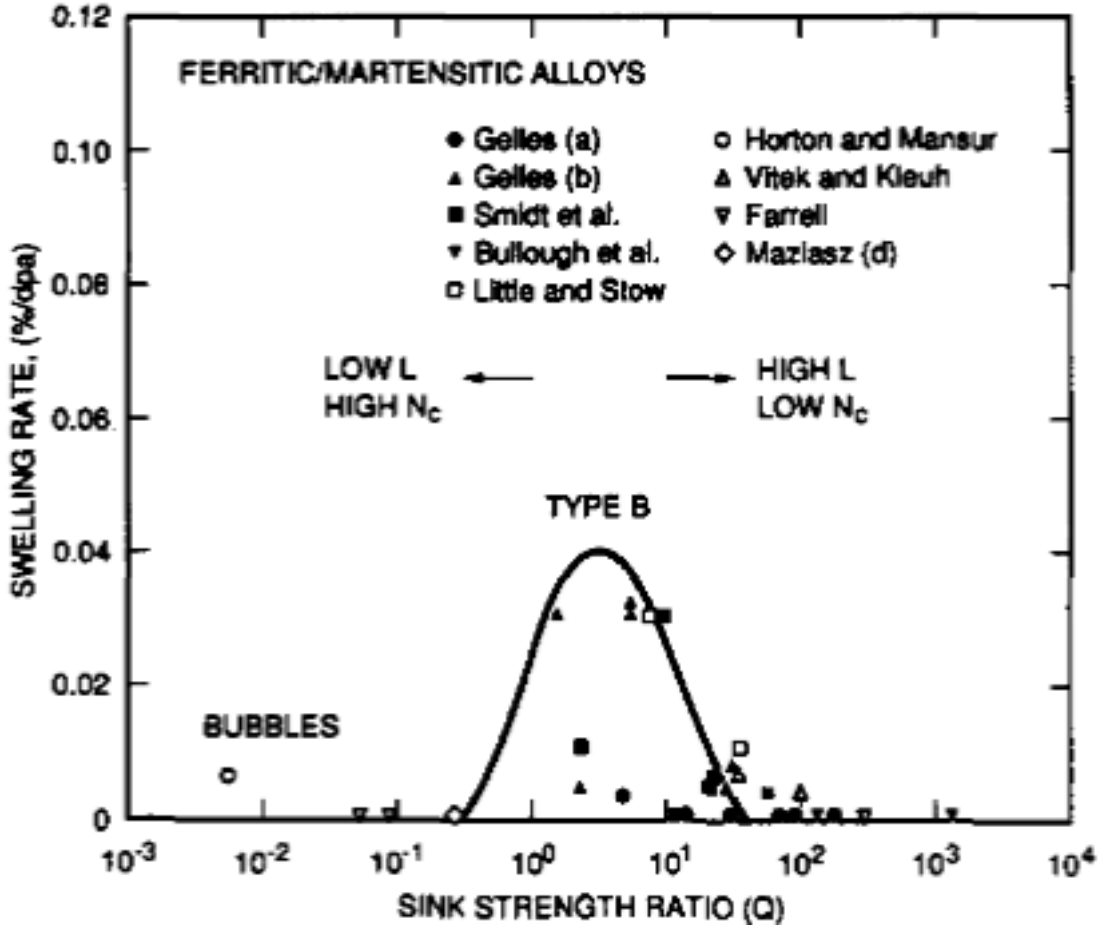

Figure 6.2. Experimentally observed swelling rates as a function of Q for FM steels in literature. Points are swelling rates calculated from swelling data and curves are drawn to aid the eye. From [109].

As shown in Figure 6.2 [109], various data points for experimental swelling rates as a function of their Q values from microstructures are plotted, with a curve indicating the general trend of theoretical swelling rate as a function of Q. At low damage levels, dislocations typically are the dominant sink, and $Q \gg 1$. At high damage levels, cavities become the dominant sink in the microstructure, and $Q \ll 1$. In either case, the swelling rate decreases, as Q deviates away from 1 when the maximized Q is reached.

The swelling rates and Q values calculated using Equation 6.1 for three conditions of AM-HT9 of Heat B are then plotted together with the data in the literature, as shown in Figure 6.3. As shown, the data points obtained in this work is consistent with the original Mansur's theory [109], with larger swelling rates achieved when the Q values approach 1.

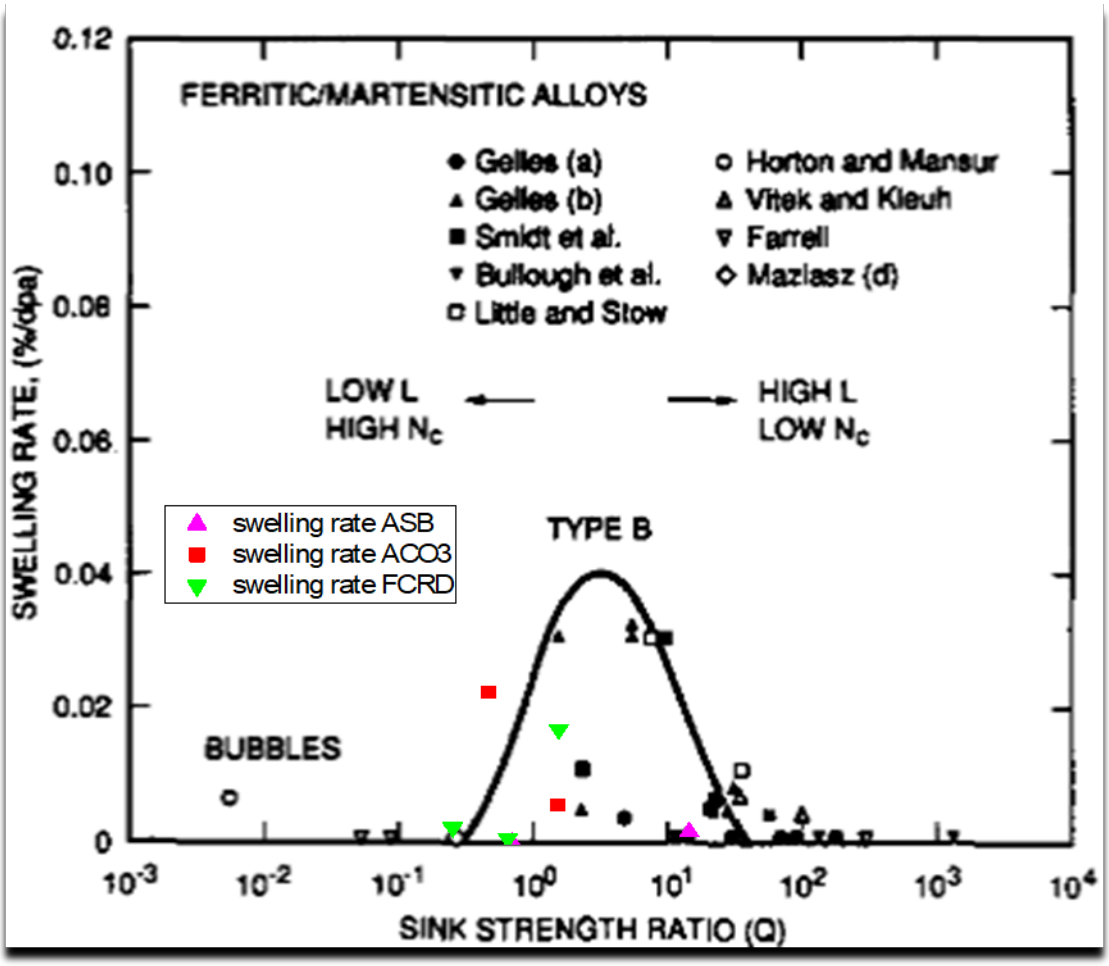

Figure 6.3. Experimentally observed swelling rates as a function of Q for FM steels in literature, together with swelling rates with Q calculated by Equation 6.1.

The model described in Equation 6.1, however, was developed assuming that the only biased sinks exist in the microstructure are line dislocations, and the only neutral sinks are cavities. In reality, additional biased sinks such as both types of dislocation loops, together with additional neutral sinks such as incoherent precipitates form under irradiation. Also, the previously

mentioned model does not consider the contribution of grain boundaries as neutral sinks, either. To generalize this equation, the full microstructure features are taken into consideration: biased sinks include line dislocations, a⟨100⟩ and a/2⟨111⟩ types of dislocation loops; neutral sinks include cavities, Ni/Si/Mn-rich precipitates, Cr-rich precipitates (excluding large carbides), and grain boundaries. The generalized equation is then used to calculate the Q values as shown in Figure 6.4. As can be seen from Figure 6.4, maximum swelling rates occur with Q values of 0.2 to 0.3 in ACO3, which are lower than the Q values calculated and shown in Figure 6.3 using the original model developed by Mansur [109]. In fact, all the Q calculated using the generalized model observe a shift towards lower values as compared to the original model. This is an indication that the full effects of neutral sinks on tailoring the Q, and thus swelling rate, should be accounted for.

In addition, some recent simulation work [87] showed that small cavities have bias towards absorbing interstitials over vacancies, making small cavities potentially biased sinks rather than neutral sinks. If that is the case, then a further correction on the generalized model as described previously, resulting in an increase of calculated Q values as expected. This is due to the increase of biased sink strength and the decrease of neutral sink strength when small cavities are treated differently from being neutral to biased. The shift of Q value calculation due to small, biased cavities is expected to affect the ACO3 specimen the most, due to the fact that high density of small cavities keeps nucleating in the microstructure even at high damage levels with large-size cavities existing, according to Figure 5.12 where 2-3 nm size of small cavities exist from 100 dpa to 250 dpa. On the other hand, small cavities in the FCRD specimen increase in size from 2-3 nm at 100 dpa to about 5 nm at 250 dpa. Therefore, more small size cavities that are potentially biased in ACO3 could result in a higher amount of increase of Q value calculation, as compared to FCRD.

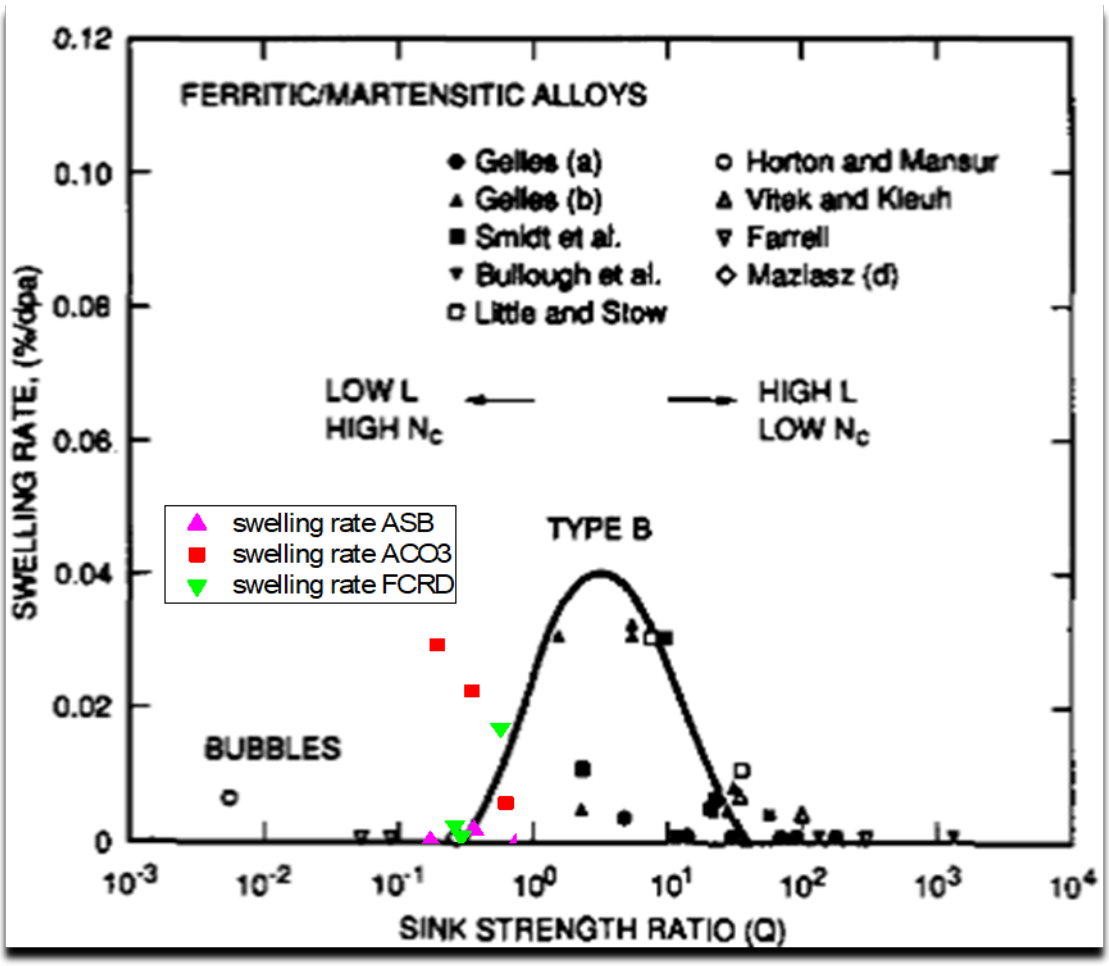

Figure 6.4. Experimentally observed swelling rates as a function of Q for FM steels in literature, together with swelling rates with Q calculated by using the generalized model considering all microstructural features, including line dislocations, a⟨100⟩ and a/2⟨111⟩ types of dislocation loops as biased sinks; cavities, Ni/Si/Mn-rich precipitates, Cr-rich precipitates, and grain boundaries as neutral sinks.

Another factor to consider is the impact of RIS on grain boundaries and their sink strength. In AM-HT9, most common grain boundaries are lath boundaries, which are low-angle grain boundaries as compared to PAGB that are of high-angle characteristics. Previous work by Field et al. [100,182,183] indicated a reduction of sink strength of laths boundaries compared to PAGB or high angle grain boundaries due to likely RIS, such as Ni near the grain boundaries. This reduction of grain boundary sink strength will further increase the calculated Q values, and the increased amount is expected to be the highest for the ASB specimen with the highest density of grain

boundaries. The RIS around dislocation loops and cavities also can have an impact on sink strength, thus more work is needed to identify the RIS on these various features and simulation efforts are needed to investigate how sink strength of these features is affected by RIS.

6.3.3 Comparison between the Swelling Behaviors of AM-HT9 and W-HT9

The swelling evolution of AM-HT9 is compared with that of tradionally-made W-HT9 or wrought FM steels [160] under irradiation, as shown in Figure 6.5. As can be seen, under neutron irradiation in the test reactors, the common swelling rate ranges from 0.002%/dpa to 0.01%/dpa. The swelling rates observed in this work for AM-HT9 (Heat B) however, are 0.001%/dpa, 0.003%/dpa, and 0.03%/dpa for ASB, FCRD, and ACO3, respectively. The heat-to-heat variability of W-HT9 results in a range of swelling rates; while the heat-treatment variability following the AM-DED process in this work results in much broader range of swelling rate. The drastically different starting microstructures and sink strengths lead to this very wide range of materials performance under irradiation. The comparison between AM-HT9 and W-HT9, though, is not strictly “apple-to-apple”, because the irradiation temperatures, He contents, or irradiating particles thus damage rates, are all different. However, a much wider deviation of swelling behaviors in AM-HT9 still shows very promining applications of AM techniques on fabrication structural materials for nuclear applications. AM process followed by potential heat-treatments allows for much greater flexibility of materials responses under irradiation, which in this case the swelling is significantly tailored by the sink strength in starting microstructures.

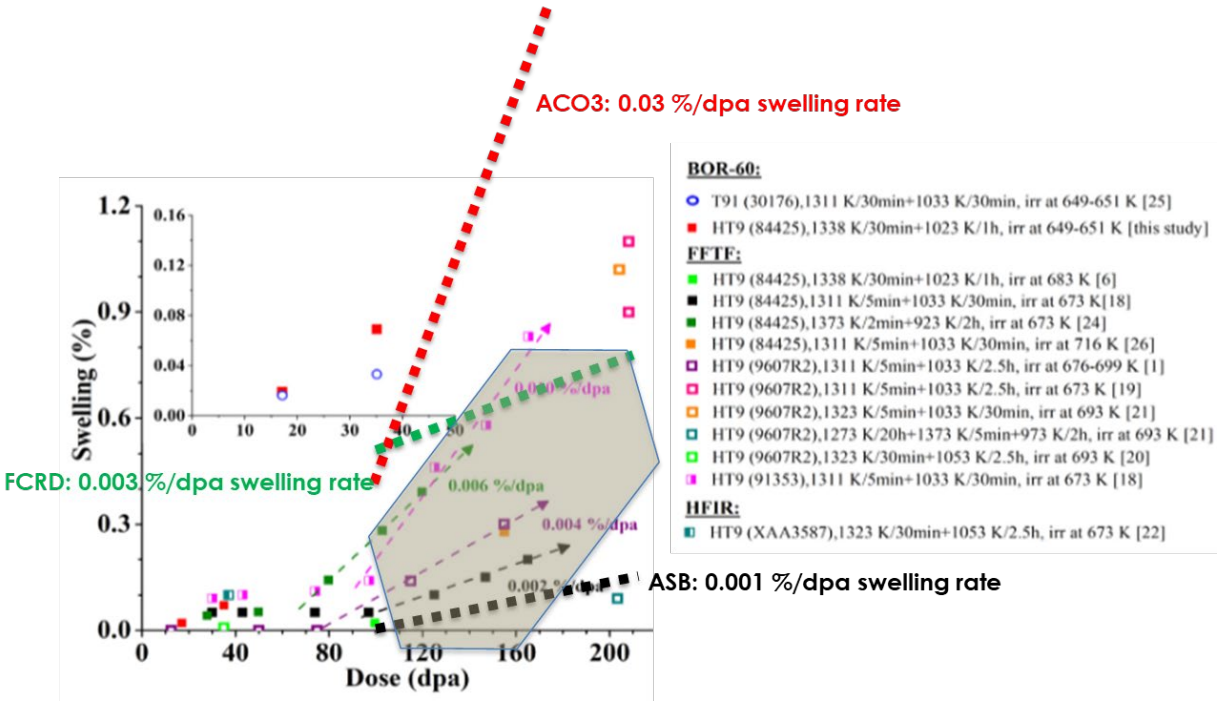

Figure 6.5. Swelling as a function of damage levels in W-HT9 irradiated in test reactors, from [160]*, with three lines overlapped showing experimental swelling curve in this work of AM-HT9 irradiated using dual-ion at 445°C.*

6.3.4 Irradiation Temperature Effects

According to Figure 5.20 and Table 5.8, cavities form under irradiation in the two heat-treated ACO3 and FCRD conditions of AM-HT9 at all irradiation temperatures from 400°C to 500°C at 50 dpa, while in the ASB specimen few cavities form only at 500°C.

The high sink strength in the ASB specimen is responsible for the suppression of cavity nucleation under irradiation. In the ACO3 and FCRD specimens, the density of cavities drops quickly with increasing irradiation temperatures. At the same time, ACO3 have consistently higher density than FCRD, indicating that the nucleation of cavities is suppressed by higher sink strength in FCRD. The size distribution of cavities in Figure 5.20 indicates significant growth of cavities in the ACO3 and FCRD specimens at higher irradiation temperatures. Similar to the size distribution of cavities with varying damage levels shown in Figure 5.12, there are also peaks

showing high density of small, nucleated cavities with average size (in diameter) lower than 5 nm in all three conditions of AM-HT9 with varying irradiation temperatures.

The overall swelling as a function of irradiation temperatures is presented in Figure 5.21. It is very interesting to notice that, although the bell-shaped curve for swelling behavior with varying irradiation temperatures is obtained in ACO3 and FCRD, their peak swelling temperatures seem to shift between the two. The peak swelling temperature of ACO3 may be close to 460°C, whereas the peak swelling temperature of FCRD may be lower than 445°C. Alloying elements and impurities are well known to modify the swelling behavior of a material [184–187], with possible impact on the peak swelling temperature. In addition, microstructure also plays a key role on the swelling behavior [91]. Different post-build heat-treatments could change the matrix compositions of ACO3 and FCRD; in addition, the microstructures are demonstrated to be changed by heat-treatments as discussed previously. Therefore, a combination of different microstructures and matrix compositions are responsible for the peak swelling shift between ACO3 and FCRD.

Chapter 7 Conclusions

This chapter presents the significant conclusions drawn from the results presented in Chapter 5 and the discussions in Chapter 6. The conclusions first focus on addressing the objective proposed in Chapter 3 to determine the effects of sink strength on microstructural evolution in ion irradiated AM-HT9 steel over a range of damage levels and irradiation temperatures. Additionally, several other conclusions are presented.

- Cyclic thermal history used in the AM DED process enable higher initial sink strength of $12.2 \times 10^{15}/m^2$ in the as-built condition of AM-HT9. Post-build heat-treatments result in about 5-time reduced sink strengths of $2.4 \times 10^{15}/m^2$ and $2.7 \times 10^{15}/m^2$ for ACO3 and FCRD, respectively compared to the as-built state of AM-HT9, with much lower density of line dislocations, grain boundaries, and precipitate-matrix interfaces. Although the overall gross irradiation response of swelling, dislocation loop, and Ni/Si/Mn-rich precipitate evolution remains the same between conventional and AM processes, the detailed evolution and quantitative magnitude of these responses are ultimately different between conventional and AM-HT9. Thus, a greater ability exists to fine tune the irradiation response of AM-HT9 over conventional means due to the higher initial sink strength in the as-built conditions.
- Solute atoms, such as Cr, diffuse and are precipitated out from the matrix to form large-size carbides near the grain boundaries during the post-build heat-treatments leading to coarsening based on precipitation thermodynamics and kinetics. Conversely, the lack

of post-build heat-treatments in the as-built condition of AM-HT9 prevents Cr diffusion leading to a high remaining content of Cr in the matrix of the as-built state of AM-HT9. The increased Cr matrix concentration is then precipitated out to form extensive Cr-rich secondary phases under irradiation in the as-built AM-HT9. Cr-rich precipitation in the as-built state further increases the sink strength at high dose driving increased point defect annihilation and significantly delaying additional microstructural evolution under irradiation.

- High sink strength ($>10 \times 10^{15}/m^2$) provides significant amount of heterogeneous nucleation sites for precipitation under irradiation. This includes Ni/Si/Mn-rich, Cu-rich, and Cr-rich precipitate formation, with the type and population depending on the initial alloy composition and thermal history of the alloy. As the damage levels increase, defect sinks significantly delay the coarsening process by pinning the nucleated clusters and retarding coalescence. As the irradiation temperatures increase, the pinning effects are reduced because of the higher kinetic energy available to overcome the energy barrier.
- High sink strength strongly suppresses the growth of dislocation loops of both a⟨100⟩ and a/2⟨111⟩ types with increasing damage levels, and a⟨100⟩ loops show significant growth and stability with higher irradiation temperatures. This response is identical in both additive manufactured and traditionally processed high-Cr steels.
- The complicated and varying microstructural evolution of dislocation loops, precipitates, and cavities in the as-built and heat-treated AM-HT9 results in drastically different swelling behavior with increasing damage levels. 0.03 %/dpa, 0.003 %/dpa, and 0.001 %/dpa swelling rates in ACO3, FCRD, and ASB respectively are obtained

with increasing damage levels. A 30°C peak swelling temperature shift between the two heat-treated specimens is also obtained. The complicated microstructural evolution including all mentioned features contribute to evolving defect sinks with irradiation dose that collectively tailor the swelling behavior in the three conditions of AM-HT9, which is verified using a simplified and a generalized rate-theory model and Q value calculation. It was found through this analysis that a simplified or generalized approach for AM-HT9 is not sufficient to ascertain a 1:1 prediction of the swelling rate, but the analytical model does highlight that both the overall sink strength as well as the balance between biased and neutral sinks are strong indicating factors for increased swelling resistance in AM-HT9.

- A high variability of microstructural responses under ion irradiation is obtained in HT9 fabricated using AM DED techniques coupled with different post-build heat-treatment routes. The tuning of higher sink strength in the starting and the irradiated microstructures greatly affects the defect evolution by retarding the coarsening of cavities, dislocation loops, and precipitates. These insights obtained within this work will stimulate further research and development of using AM to fabricate tailored-response materials, including but not limited to FM steels, that are highly radiation resistant for advanced nuclear reactor applications.

Chapter 8 Future Work

The results and findings of this dissertation provide insights into the roles of (i) sink strength in the starting and irradiated microstructures, as well as (ii) the irradiation parameters such as damage levels and irradiation temperatures on microstructural evolution in AM-HT9 under ion irradiation. However, there are many unanswered questions and areas which merit further study.

First, the full compositions of irradiation-induced precipitates in dual-ion irradiated AM-HT9 of Heat B have not been studied. We have been awarded a Nuclear Science User Facilities (NSUF) Rapid Turnaround Experiment (RTE) project entitled "The sink strength and radiation parameter effects on microchemical evolution in dual-ion irradiated additively manufactured and wrought HT9". This project focuses on detailed APT studies on the microchemical evolution in AM-HT9 under various irradiation conditions, and with results obtained under one of the irradiation conditions compared with W-HT9 to probe into the variability of precipitation and chemical-segregation responses of HT9 under irradiation.

Second, the varying ion irradiation conditions studied in this work have been concentrating on damage levels and irradiation temperatures. Within the damage levels of 250 dpa, a high swelling rate, thus a steady-state swelling behavior is observed in the heat-treated ACO3 specimen; however, in the FCRD and ASB specimens, such behavior is not observed. A potentially much higher damage level needs to be achieved to fully exhibit the full three-regime swelling behavior in these two samples. In addition, many other irradiation conditions can be varied to study the radiation responses of the three conditions of AM-HT9 in order to reflect the effects on sink

strength on the microstructural evolution. For example, the variation of helium co-injection rate and the damage rate can be applied during ion irradiation. Neutron irradiation experiments using test reactors such as High Flux Isotope Reactor (HFIR) will also provide valuable data directly with neutron irradiation environment, with closer to in-service low damage rate as compared to ion irradiations. The precipitate evolution is well-known to be strongly affected by damage rates. For example, Cr-rich α' only form with low enough damage rates and will undergo ballistic dissolution at higher damage rates such as those used in typical ion irradiations. The additional sink strength provided by these precipitates could further affect swelling behavior of the three conditions of AM-HT9.

Finally, the calculation of sink strengths of various features in this work is based on theory in the literature. For example, Ni/Si/Mn-rich and Cr-rich precipitates are both incoherent with the matrix, thus their sink strength calculation is treated the same. However, the exact sink strength of precipitate-matrix interface is affected by the lattice mismatch, as a higher degree of lattice mismatch can accommodate more point defects. High-resolution S/TEM characterization may need to be conducted to fully quantify the lattice mismatch. Similarly, grain boundaries with different mismatch angle could also change the sink strength. Different types of dislocation loops may also have different bias factor of absorbing interstitials and vacancies. Ideally, model alloys with single sink type need to be fabricated to isolate its effects on absorbing point defects; meanwhile, simulation needs to be conducted to further the understanding of sink strength of different defect types. All of these efforts, if made, will greatly benefit the calculation, therefore understanding, of sink strength in nuclear structural materials.

Appendices

Appendix A. Python Code Used for Generating STEM-EDX Overlay Images with Scalebars

```
# credit: Kevin G. Field (kgfield@umich.edu) wrote this code, Pengyuan Xiu (xiupy@umich.edu) modified it

from matplotlib import pyplot as plt
from PIL import Image
import numpy as np
import pandas as pd
import seaborn as sns
import cv2 as cv
from skimage.filters import threshold_otsu
from skimage.filters import threshold_triangle
from skimage.filters import threshold_minimum
from skimage.filters import threshold_yen
from skimage.filters import threshold_li
from skimage import filters

def read_data(file_name):
    n = []
    with open(file_name,'r') as file:
        for line in file:
            n.append(
                line.strip().split(';'))
    df = pd.DataFrame(n)
    matrix = df.astype(int).to_numpy()

    return matrix

def NormalizeData(data):
    return (data - np.min(data)) / (np.max(data) - np.min(data))

### Read data and make pixel value dataframe

# add in the elements of interest
Ni_file = 'ASB-unirradiated_Ni.txt'
Cr_file = 'ASB-unirradiated_Cr.txt'
Cu_file = 'ASB-unirradiated_Cu.txt'
Nb_file = 'ASB-unirradiated_Nb.txt'
Si_file = 'ASB-unirradiated_Si.txt'

Ni_cts = read_data(Ni_file)
Cr_cts = read_data(Cr_file)
```

```
Cu_cts = read_data(Cu_file)
Nb_cts = read_data(Nb_file)
Si_cts = read_data(Si_file)

Perform simple threshold to remove background/noise in data:


# apply a low count threshold to filter noisy data, may need to change depending on the elements selected
Cu_cts[Cu_cts<5] = 0
Ni_cts[Ni_cts<2] = 0
Cr_cts[Cr_cts<5] = 0
Nb_cts[Nb_cts<2] = 0
Si_cts[Si_cts<1] = 0

Perform a gaussian blur on each map to help with noise to signal ratio, then convert to 0-255 value scale

#Norm_Ni=NormalizeData(cv.blur(Ni_cts,(5,5)))*255
#Norm_Cr=NormalizeData(cv.blur(Cr_cts,(5,5)))*255
#Norm_Cu=NormalizeData(cv.blur(Cu_cts,(5,5)))*255
#Norm_Nb=NormalizeData(cv.blur(Nb_cts,(5,5)))*255

# apply gaussian filter to smooth out the map. may need to change the sigma values here. higher the sigma, more smooth/blurred the image will be

Norm_Ni=NormalizeData(filters.gaussian(Ni_cts,sigma=3))*255
Norm_Cr=NormalizeData(filters.gaussian(Cr_cts,sigma=3))*255
Norm_Cu=NormalizeData(filters.gaussian(Cu_cts,sigma=2))*255
Norm_Nb=NormalizeData(filters.gaussian(Nb_cts,sigma=4.5))*255
Norm_Si=NormalizeData(filters.gaussian(Si_cts,sigma=3))*255

Norm_Ni[np.isnan(Norm_Ni)]=0
Norm_Cr[np.isnan(Norm_Cr)]=0
Norm_Cu[np.isnan(Norm_Cu)]=0
Norm_Nb[np.isnan(Norm_Nb)]=0
Norm_Si[np.isnan(Norm_Si)]=0

Perform adaptive thresholding (triangle alogrithm) to remove background  and apply false color for each map, could be map as loop

if np.any(Norm_Ni):
  Norm_Ni[Norm_Ni<threshold_triangle(Norm_Ni)] = 0
colNi=np.repeat(Norm_Ni[:, :, np.newaxis], 3, axis=2)
col=np.array((0,1,0))
colNi=col*colNi

colNi=colNi.astype(int)

#colNi[np.all(colNi<1, axis=2)] = 255

fig1, ax = plt.subplots(1,3)
ax[0].imshow(Ni_cts)
ax[0].axis('off')
ax[1].imshow(Norm_Ni)
ax[1].axis('off')
ax[2].imshow(colNi)
ax[2].axis('off')
```

```
plt.subplots_adjust(wspace=0, hspace=0, left=0, right=2, bottom=0, top=1)
plt.show()

if np.any(Norm_Cu):
  Norm_Cu[Norm_Cu<threshold_triangle(Norm_Cu)] = 0

colCu=np.repeat(Norm_Cu[:, :, np.newaxis], 3, axis=2)
colCu[:,:,0]=colCu[:,:,0]*(255/255)
colCu[:,:,1]=colCu[:,:,1]*(178/255)
colCu[:,:,2]=colCu[:,:,2]*(102/255)

colCu=colCu.astype(int)

#colCu[np.all(colCu<1, axis=2)] = 255
fig2, ax = plt.subplots(1,3)
ax[0].imshow(Cu_cts)
ax[0].axis('off')
ax[1].imshow(Norm_Cu)
ax[1].axis('off')
ax[2].imshow(colCu)
ax[2].axis('off')
plt.subplots_adjust(wspace=0, hspace=0, left=0, right=2, bottom=0, top=1)
plt.show()

if np.any(Norm_Cr):
  Norm_Cr[Norm_Cr<threshold_triangle(Norm_Cr)] = 0

colCr=np.repeat(Norm_Cr[:, :, np.newaxis], 3, axis=2)
colCr[:,:,0]=colCr[:,:,0]*(103/255)
colCr[:,:,1]=colCr[:,:,1]*(0/255)
colCr[:,:,2]=colCr[:,:,2]*(103/255)

colCr=colCr.astype(int)
#colCr[np.all(colCr<1, axis=2)] = 255
fig2, ax = plt.subplots(1,3)
ax[0].imshow(Cr_cts)
ax[0].axis('off')
ax[1].imshow(Norm_Cr)
ax[1].axis('off')
ax[2].imshow(colCr)
ax[2].axis('off')
plt.subplots_adjust(wspace=0, hspace=0, left=0, right=2, bottom=0, top=1)
plt.show()

#if np.any(Norm_Nb):
#  Norm_Nb[Norm_Nb<threshold_yen(Norm_Nb)] = 0

if np.any(Norm_Nb):
  Norm_Nb[Norm_Nb<threshold_triangle(Norm_Nb)] = 0

colNb=np.repeat(Norm_Nb[:, :, np.newaxis], 3, axis=2)
colNb[:,:,0]=colNb[:,:,0]*0
colNb[:,:,1]=colNb[:,:,1]*1
colNb[:,:,2]=colNb[:,:,2]*1

colNb=colNb.astype(int)
```

```
#colNb[np.all(colNb<1, axis=2)] = 255

fig2, ax = plt.subplots(1,3)
ax[0].imshow(Nb_cts)
ax[0].axis('off')
ax[1].imshow(Norm_Nb)
ax[1].axis('off')
ax[2].imshow(colNb)
ax[2].axis('off')
plt.subplots_adjust(wspace=0, hspace=0, left=0, right=2, bottom=0, top=1)
plt.show()

if np.any(Norm_Si):
  Norm_Nb[Norm_Si<threshold_yen(Norm_Si)] = 0

colSi=np.repeat(Norm_Si[:, :, np.newaxis], 3, axis=2)
colSi[:,:,0]=colSi[:,:,0]*1
colSi[:,:,1]=colSi[:,:,1]*0
colSi[:,:,2]=colSi[:,:,2]*1

colSi=colSi.astype(int)

#colNb[np.all(colNb<1, axis=2)] = 255

fig2, ax = plt.subplots(1,3)
ax[0].imshow(Si_cts)
ax[0].axis('off')
ax[1].imshow(Norm_Si)
ax[1].axis('off')
ax[2].imshow(colSi)
ax[2].axis('off')
plt.subplots_adjust(wspace=0, hspace=0, left=0, right=2, bottom=0, top=1)
plt.show()

Perform additive color mixing of maps of interest and then annonate the image with necessary outputs

interim_1=np.maximum(colNb,colCu)
interim_2=np.maximum(interim_1,colNi)
test=np.maximum(interim_2,colCr)
#test=colNi + colCu + colNb +colCr +colNb
print(test)

#test=colNi + colCu + colNb +colCr #+colNb

#Convert background from black to white
test[np.all(test<10, axis=2)] = 255

#Adding color block legend
test[900:1000,0:100,0]=0
test[900:1000,0:100,1]=255
test[900:1000,0:100,2]=0

test[900:1000,100:200,0]=255
test[900:1000,100:200,1]=178
test[900:1000,100:200,2]=102
```

```
test[900:1000,200:300,0]=0
test[900:1000,200:300,1]=255
test[900:1000,200:300,2]=255

test[900:1000,300:400,0]=103
test[900:1000,300:400,1]=0
test[900:1000,300:400,2]=103

#White background for scale bar
test[915:1000,740:960,0]=255
test[915:1000,740:960,1]=255
test[915:1000,740:960,2]=255

#Make a scale bar - this needs to change for the given pixel/nm
test[975:990,743:957,0]=0
test[975:990,743:957,1]=0
test[975:990,743:957,2]=0

#Scaled for 10 in by 10 in
fig2 = plt.figure(figsize = (10,10))

plt.imshow(test)

#Add text to colorblock legend and scale bar
plt.text(50,950,'Ni',color='white', horizontalalignment='center',verticalalignment='center',
fontsize=30,fontfamily='serif',fontweight='bold')
plt.text(150,950,'Cu',color='white', horizontalalignment='center',verticalalignment='center',
fontsize=30,fontfamily='serif',fontweight='bold')
plt.text(250,950,'Nb',color='white', horizontalalignment='center',verticalalignment='center',
fontsize=30,fontfamily='serif',fontweight='bold')
plt.text(350,950,'Cr',color='white', horizontalalignment='center',verticalalignment='center',
fontsize=30,fontfamily='serif',fontweight='bold')
plt.text(850,950,'50 nm',color='black', horizontalalignment='center',verticalalignment='center',
fontsize=30,fontfamily='serif',fontweight='bold')
plt.axis('off')
```

Appendix B. Python Code Used for Generating STEM-BF/LAADF/MAADF/HAADF Greyscale Images with Scalebars

```
# credit: Pengyuan Xiu (xiupy@umich.edu) wrote the code

from PIL import Image
from numpy import asarray
import numpy as np
from matplotlib import pyplot as plt
import pandas as pd
import seaborn as sns
import cv2 as cv
from skimage.filters import threshold_otsu
from skimage.filters import threshold_triangle
from skimage.filters import threshold_minimum
from skimage.filters import threshold_yen
from skimage.filters import threshold_li
from skimage import filters

# To normalize the counts data based on the min and max of all the pixel counts by using a 256 full scale for
greyscale plot
def NormalizeData(data):
    return (data - np.min(data)) / (np.max(data) - np.min(data)) * 255

# This function takes in an image file (tiff for example), trim out the data to make a squre-shaped dataframe
(1024 by 1024 for example)
def process_img(file_name):
    tiff = Image.open(file_name)
    numpydata = asarray(tiff)
    num1 = numpydata.shape[1]
    num2 = numpydata.shape[0]
    #this step removes the excessive data from the scale bar added by the TIA software when outputting the tiff
images
    trimmed_data = np.delete(numpydata, slice(num1,num2), 0)
    #to normalize the data and convert it to 255 scale with 1 dimension
    Norm_data = NormalizeData(trimmed_data)
    #increase the dimension to 3d array from 1d, and keep the grey scale (r=g=b)
    Norm_3d_data = np.repeat(Norm_data[:, :, np.newaxis], 3, axis=2)
    #convert all data to integer
    Norm_3d_data = Norm_3d_data.astype(int)

    #add white background for scale bar
    Norm_3d_data[915:1000,740:960,0]=255
    Norm_3d_data[915:1000,740:960,1]=255
    Norm_3d_data[915:1000,740:960,2]=255
```

```
    #make a black scale bar. Here, 50 nm = 215 pixel for a 1024 x 1024 pixel image, affecting left2 and right2
values!
    Norm_3d_data[975:990,743:957,0]=0
    Norm_3d_data[975:990,743:957,1]=0
    Norm_3d_data[975:990,743:957,2]=0

    plt.text(850,950,'50 nm',color='black', horizontalalignment='center',verticalalignment='center',
fontsize=30,fontfamily='serif',fontweight='bold')

    return Norm_3d_data

plt.figure(figsize=(20, 20))
ASB = process_img('DF2_FCRD_UN_Z.tif')
plt.imshow(ASB)
plt.axis('off')
plt.show()

plt.savefig('ACO3_unirr_test.png', format='png', dpi=1200)
```

Appendix C. Raw Data for Irradiation Experiments

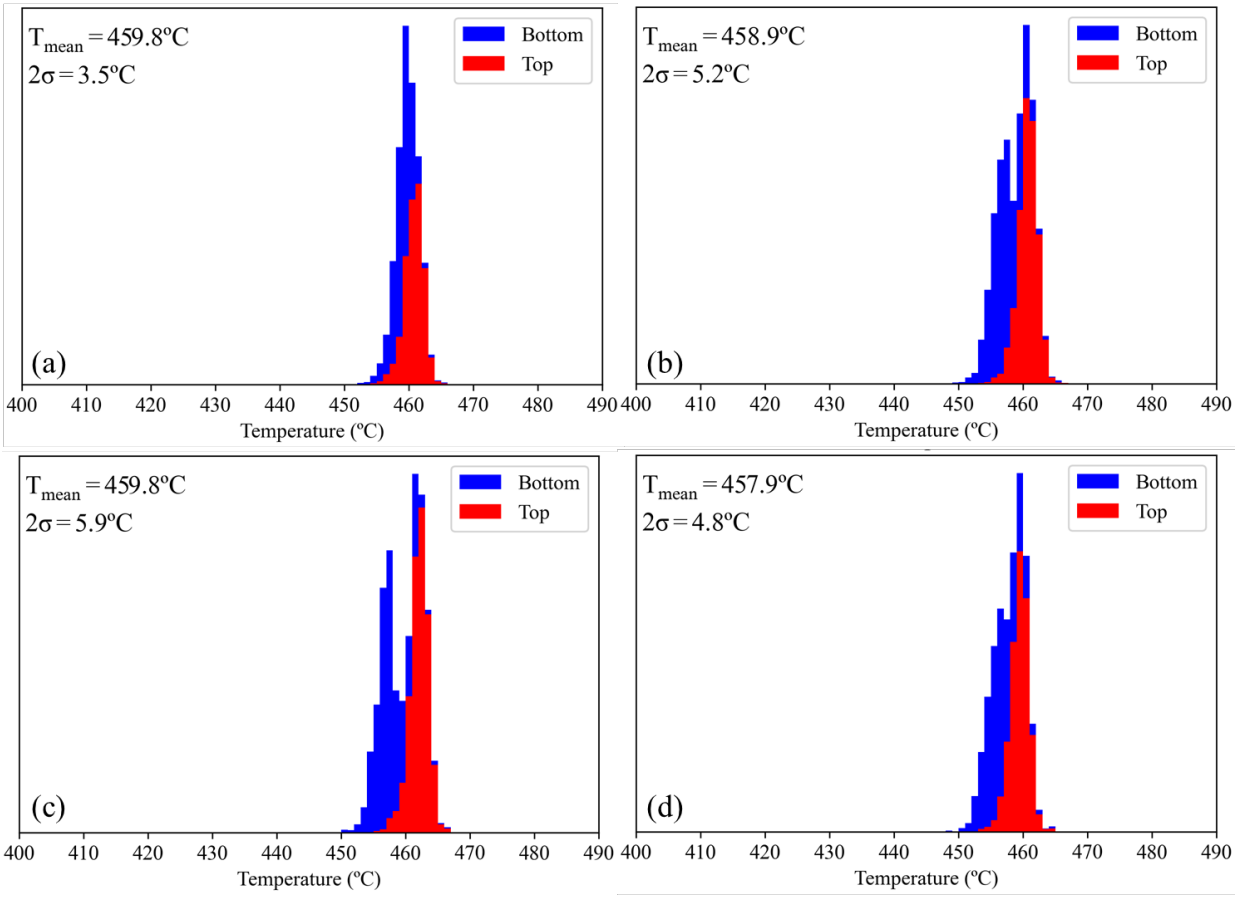

Appendix Figure 1. Temperature histograms for the 50 dpa, 460°C irradiation of Heat A of AM-HT9 with 5 MeV Fe^{2+} ions without He implantation.

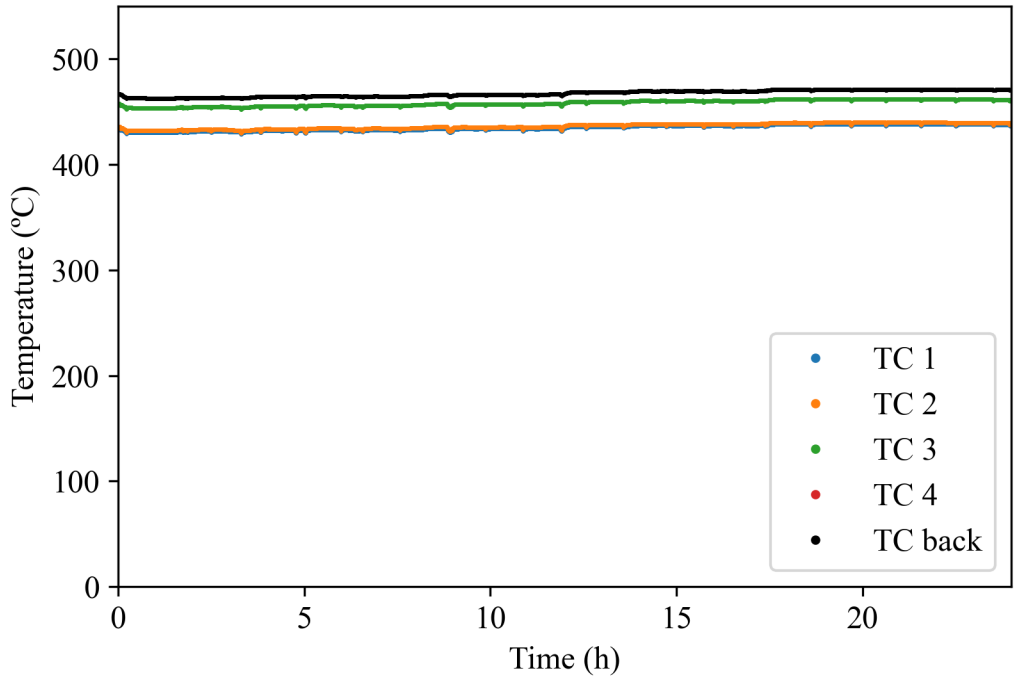

Appendix Figure 2. Thermocouple readings of temperature for the 50 dpa, 460°C irradiation of Heat A of AM-HT9 with 5 MeV Fe^{2+} ions without He implantation.

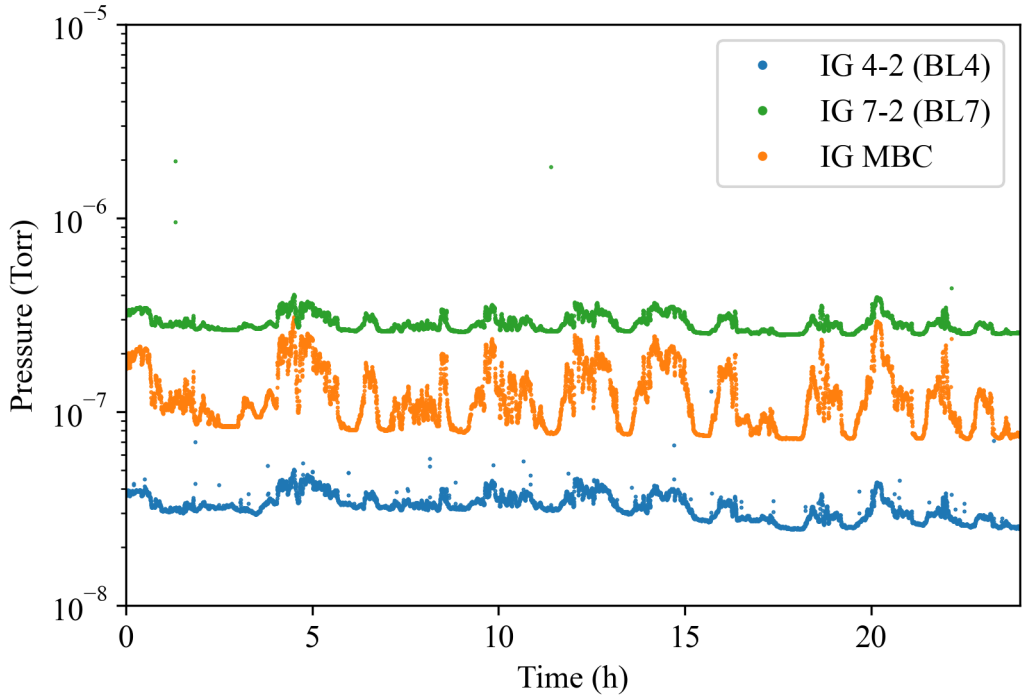

Appendix Figure 3. Pressure history for the 50 dpa, 460°C irradiation of Heat A of AM-HT9 with 5 MeV Fe^{2+} ions without He implantation.

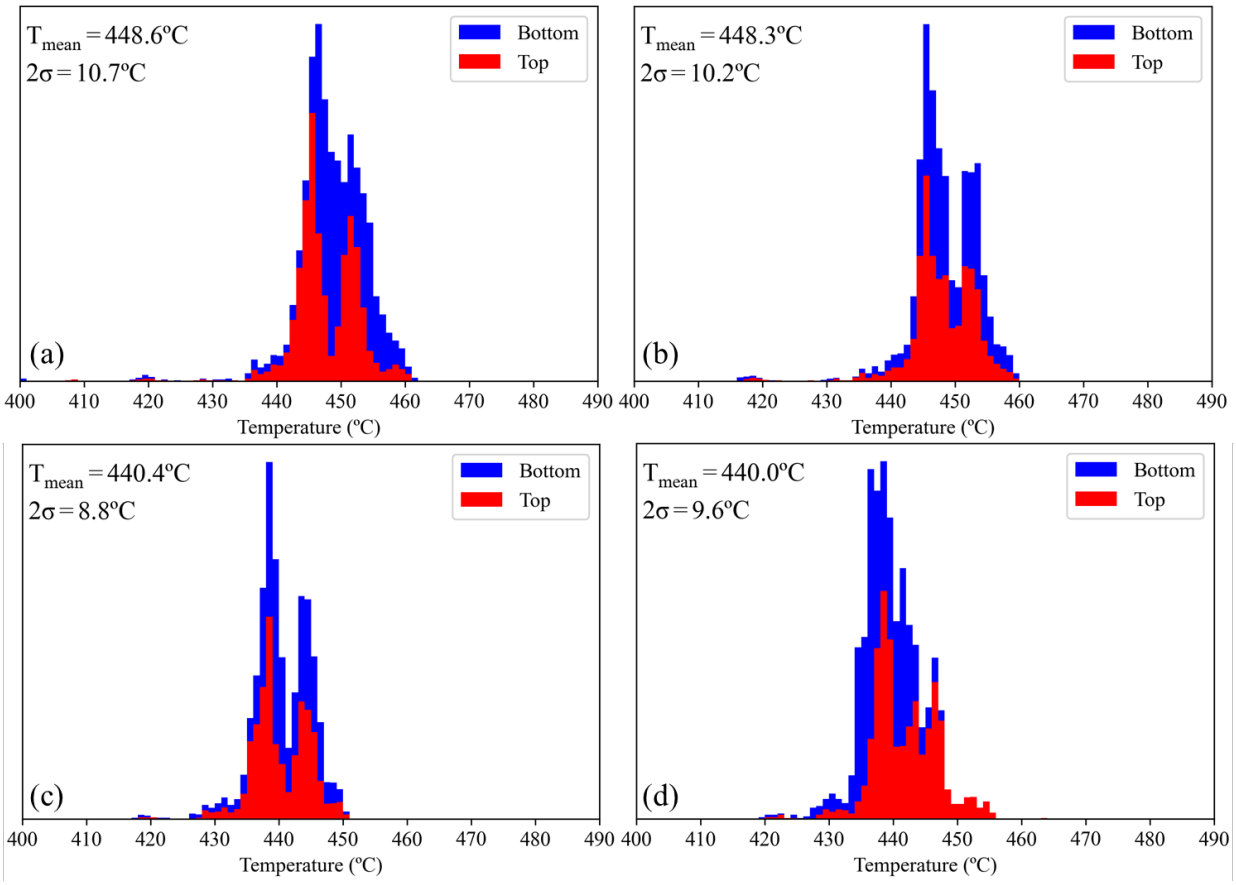

Appendix Figure 4. Temperature histograms for the 16.6 dpa, 445°C irradiation of Heat B of AM-HT9 with 5 MeV Fe^{2+} ions for implanted He levels of 4 appm/dpa.

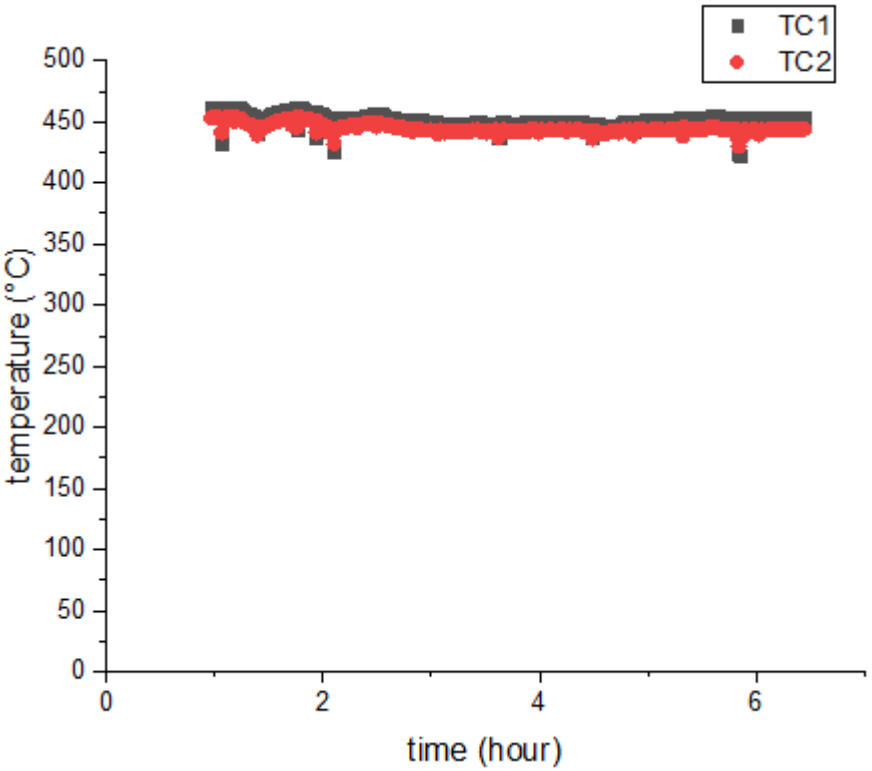

Appendix Figure 5. Thermocouple readings of temperature for the 16.6 dpa, 445°C irradiation of Heat B of AM-HT9 with 5 MeV Fe^{2+} ions for implanted He levels of 4 appm/dpa.

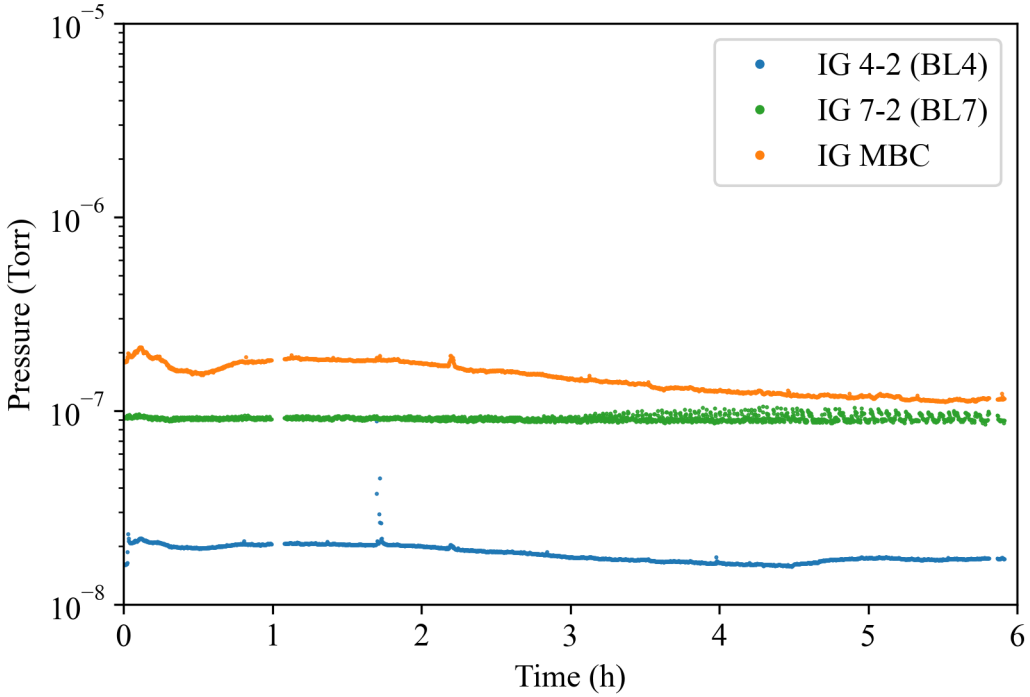

Appendix Figure 6. Pressure history for the 16.6 dpa, 445°C irradiation of Heat B of AM-HT9 with 5 MeV Fe^{2+} ions for implanted He levels of 4 appm/dpa.

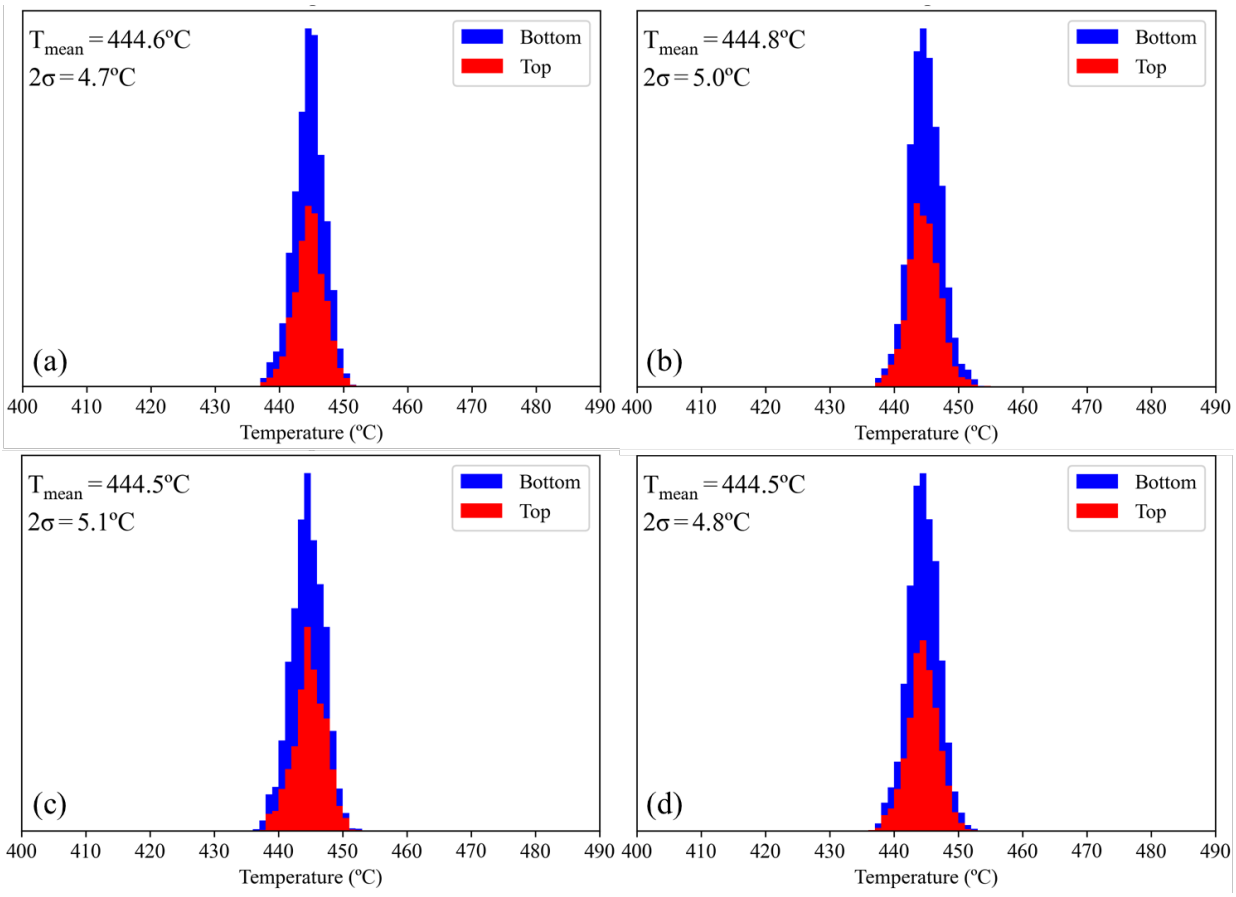

Appendix Figure 7. Temperature histograms for the 50 dpa, 445°C irradiation of Heat B of AM-HT9 with 5 MeV Fe^{2+} ions for implanted He levels of 4 appm/dpa.

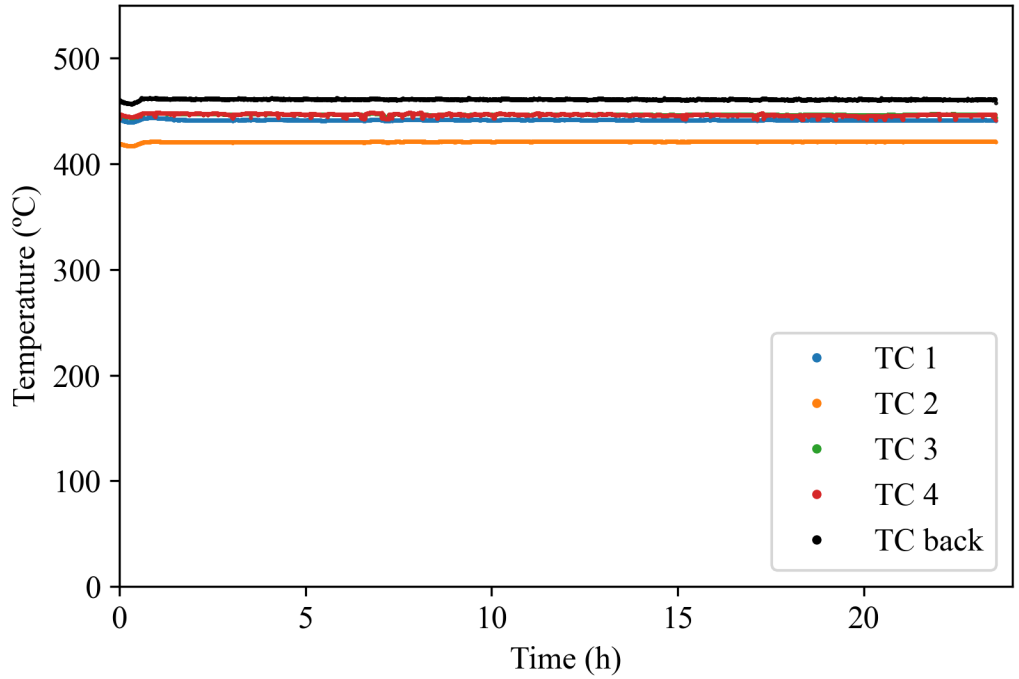

Appendix Figure 8. Thermocouple readings of temperature for the 50 dpa, 445°C irradiation of Heat B of AM-HT9 with 5 MeV Fe^{2+} ions for implanted He levels of 4 appm/dpa.

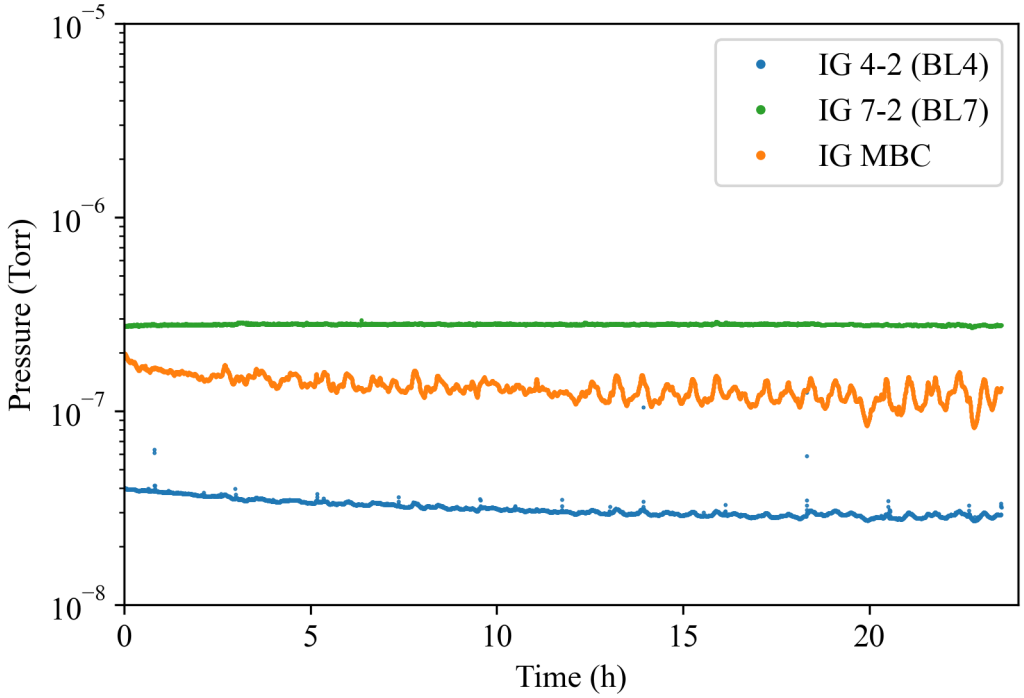

Appendix Figure 9. Pressure history for the 50 dpa, 445°C irradiation of Heat B of AM-HT9 with 5 MeV Fe^{2+} ions for implanted He levels of 4 appm/dpa.

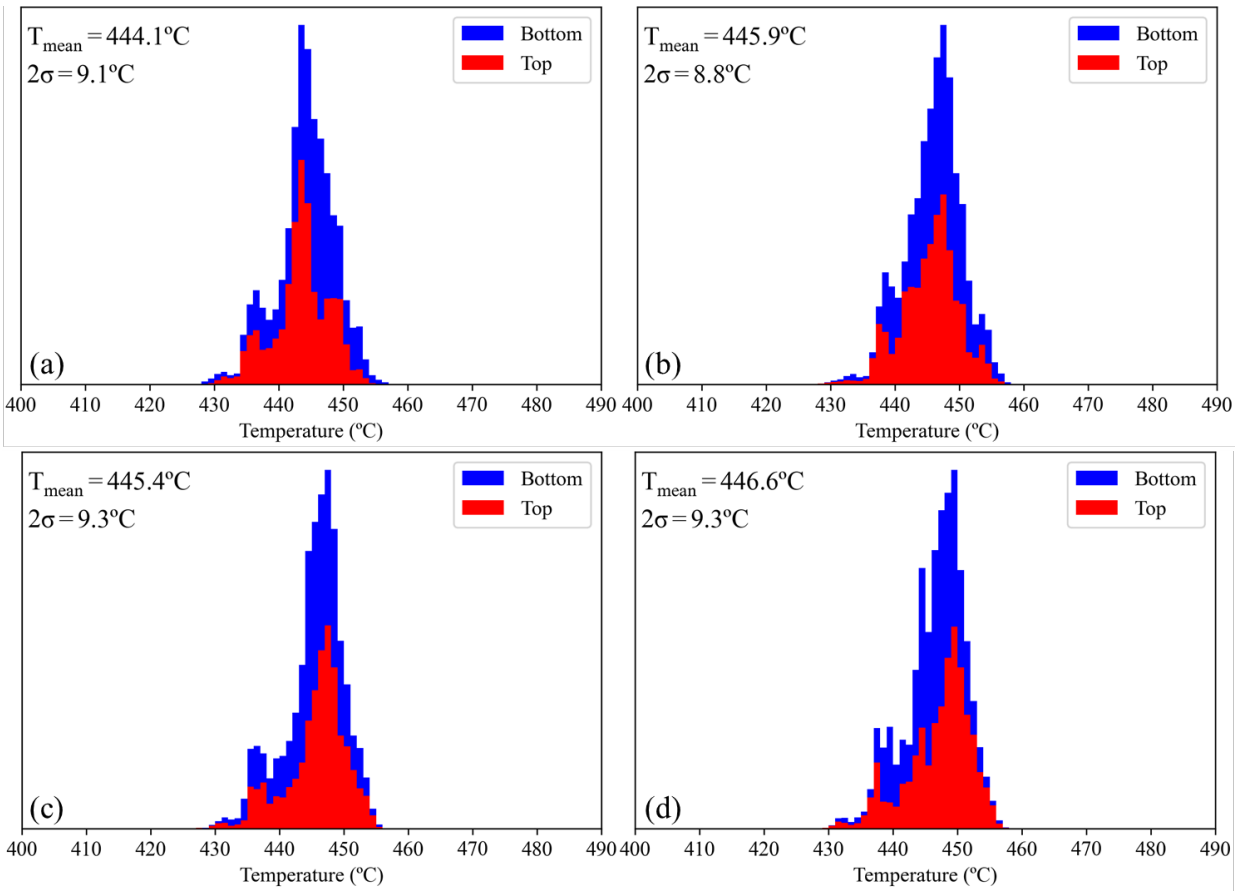

Appendix Figure 10. Temperature histograms for the 75 dpa, 445°C irradiation of Heat B of AM-HT9 with 5 MeV Fe^{2+} ions for implanted He levels of 4 appm/dpa.

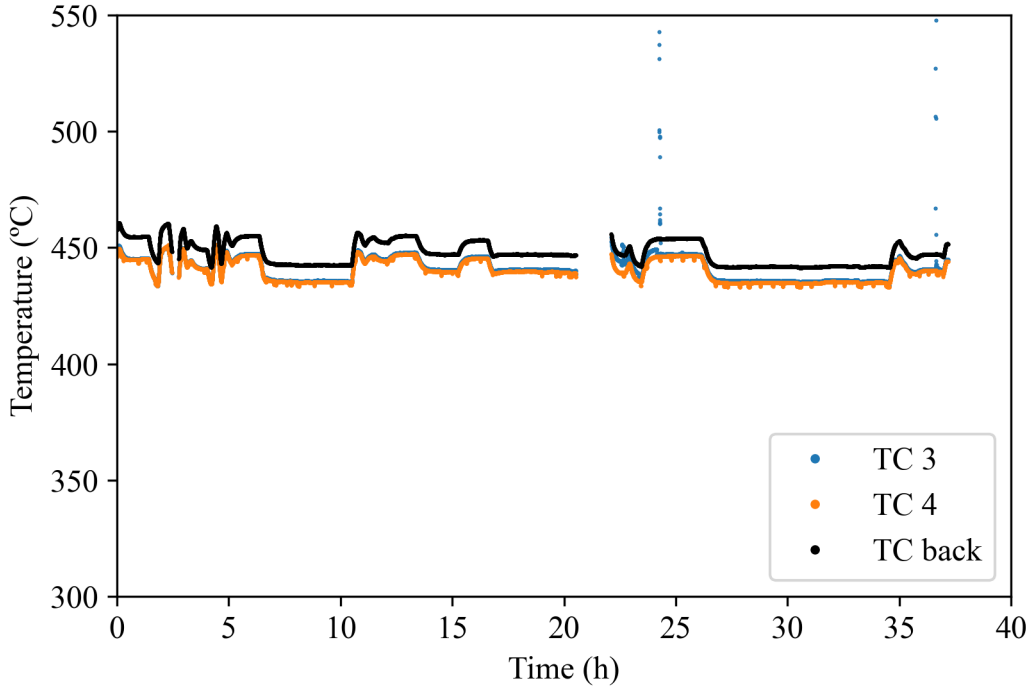

Appendix Figure 11. Thermocouple readings of temperature for the 75 dpa, 445°C irradiation of Heat B of AM-HT9 with 5 MeV Fe^{2+} ions for implanted He levels of 4 appm/dpa.

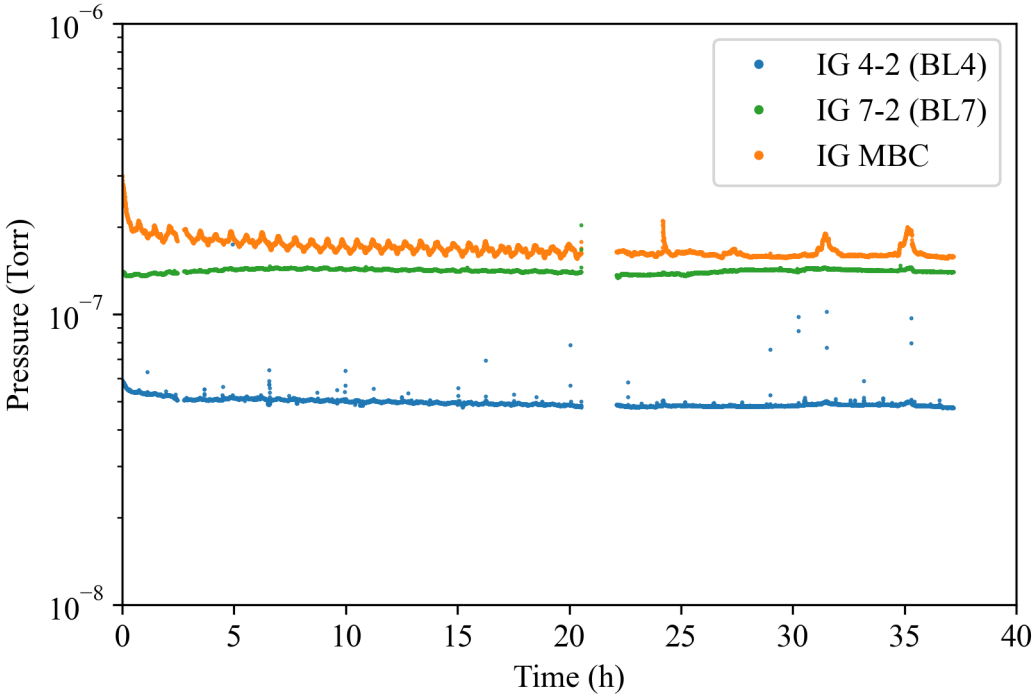

Appendix Figure 12. Pressure history for the 75 dpa, 445°C irradiation of Heat B of AM-HT9 with 5 MeV Fe^{2+} ions for implanted He levels of 4 appm/dpa.

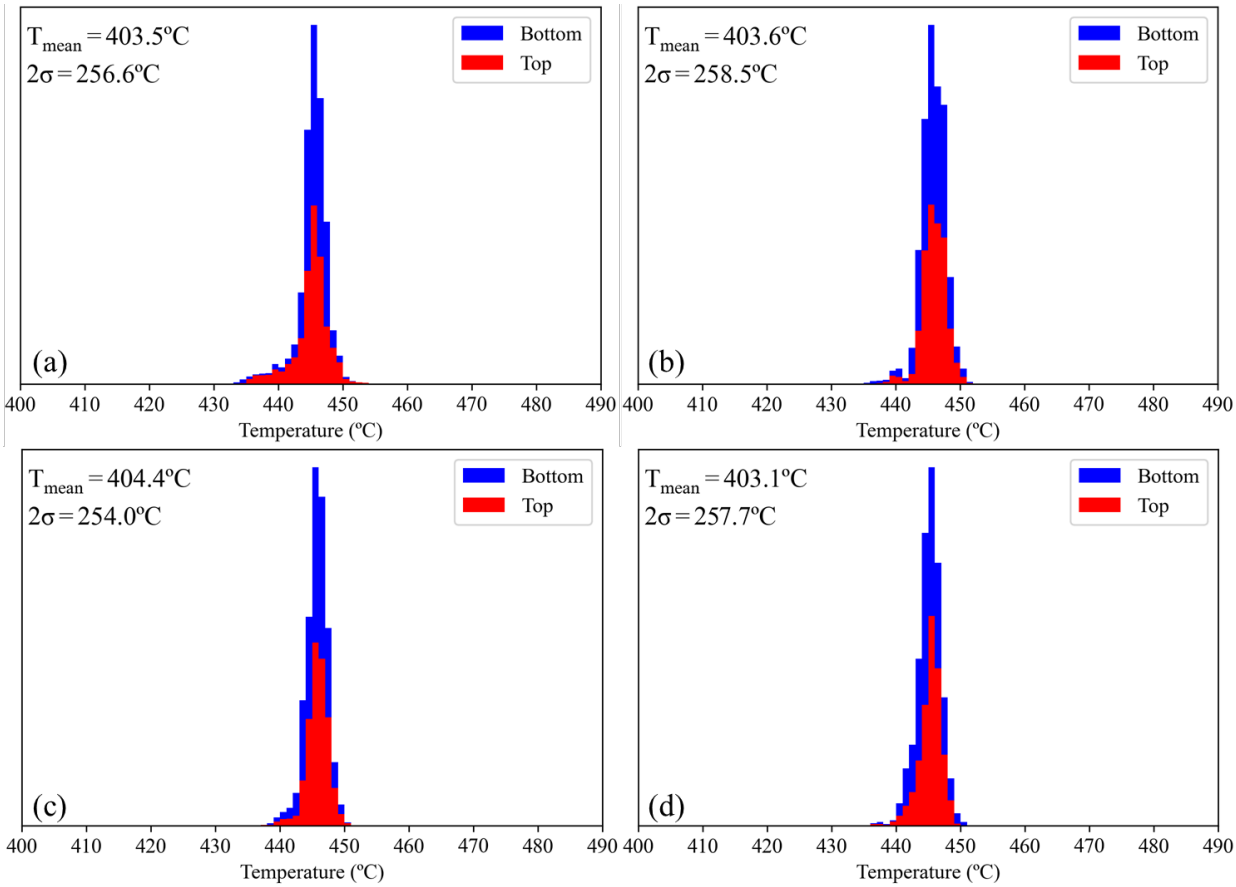

Appendix Figure 13. Temperature histograms for the 100 dpa, 445°C irradiation of Heat B of AM-HT9 with 5 MeV Fe^{2+} ions for implanted He levels of 4 appm/dpa.

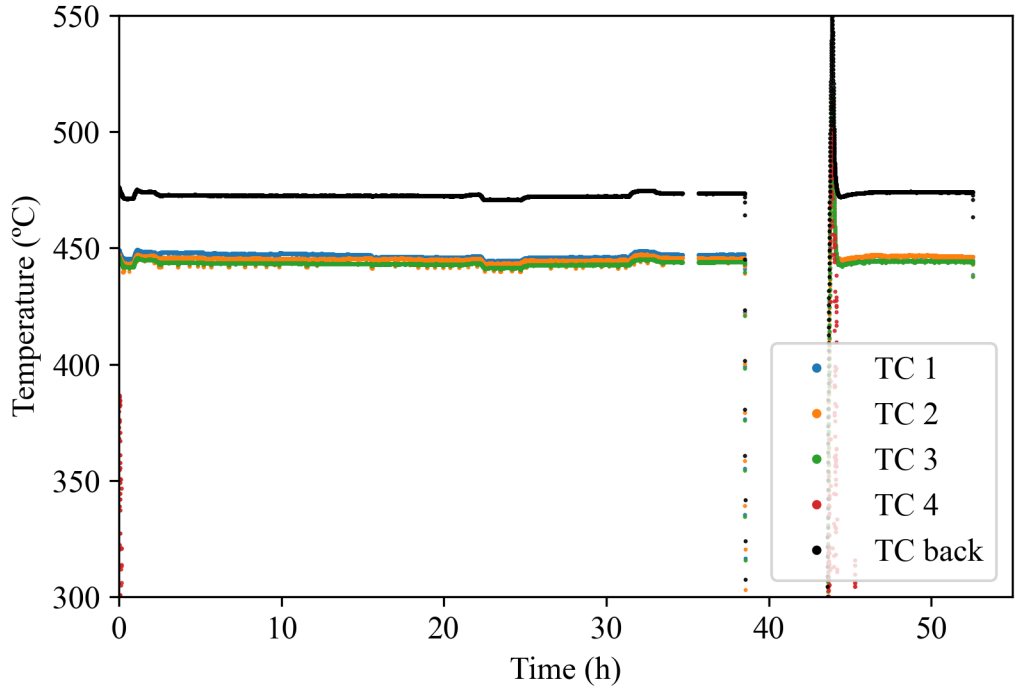

Appendix Figure 14. Thermocouple readings of temperature for the 100 dpa, 445°C irradiation of Heat B of AM-HT9 with 5 MeV Fe^{2+} ions for implanted He levels of 4 appm/dpa.

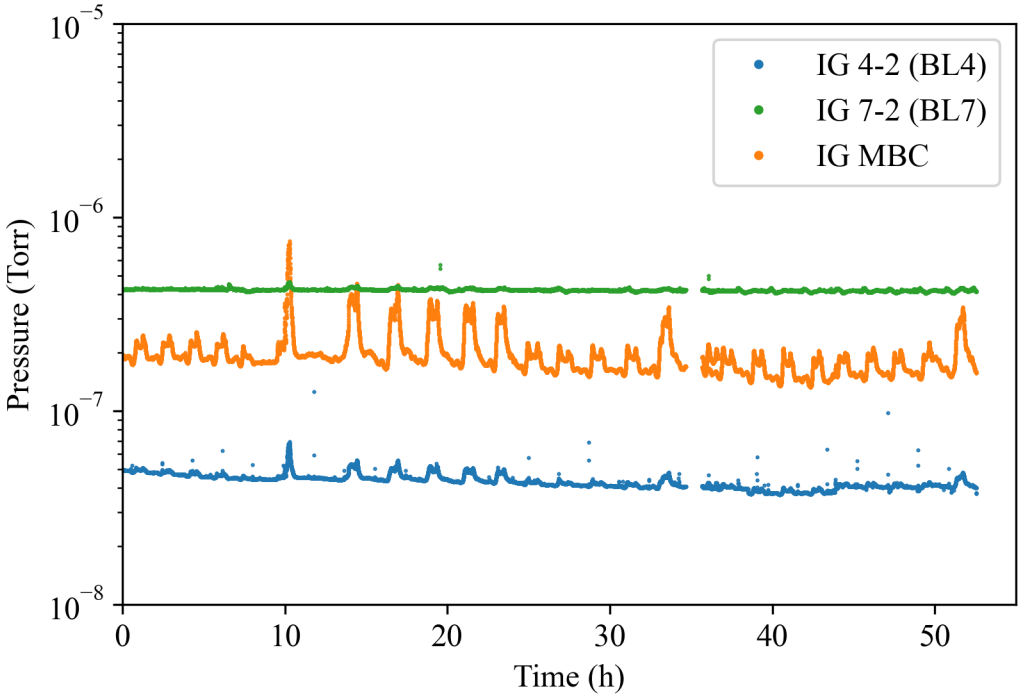

Appendix Figure 15. Pressure history for the 100 dpa, 445°C irradiation of Heat B of AM-HT9 with 5 MeV Fe^{2+} ions for implanted He levels of 4 appm/dpa.

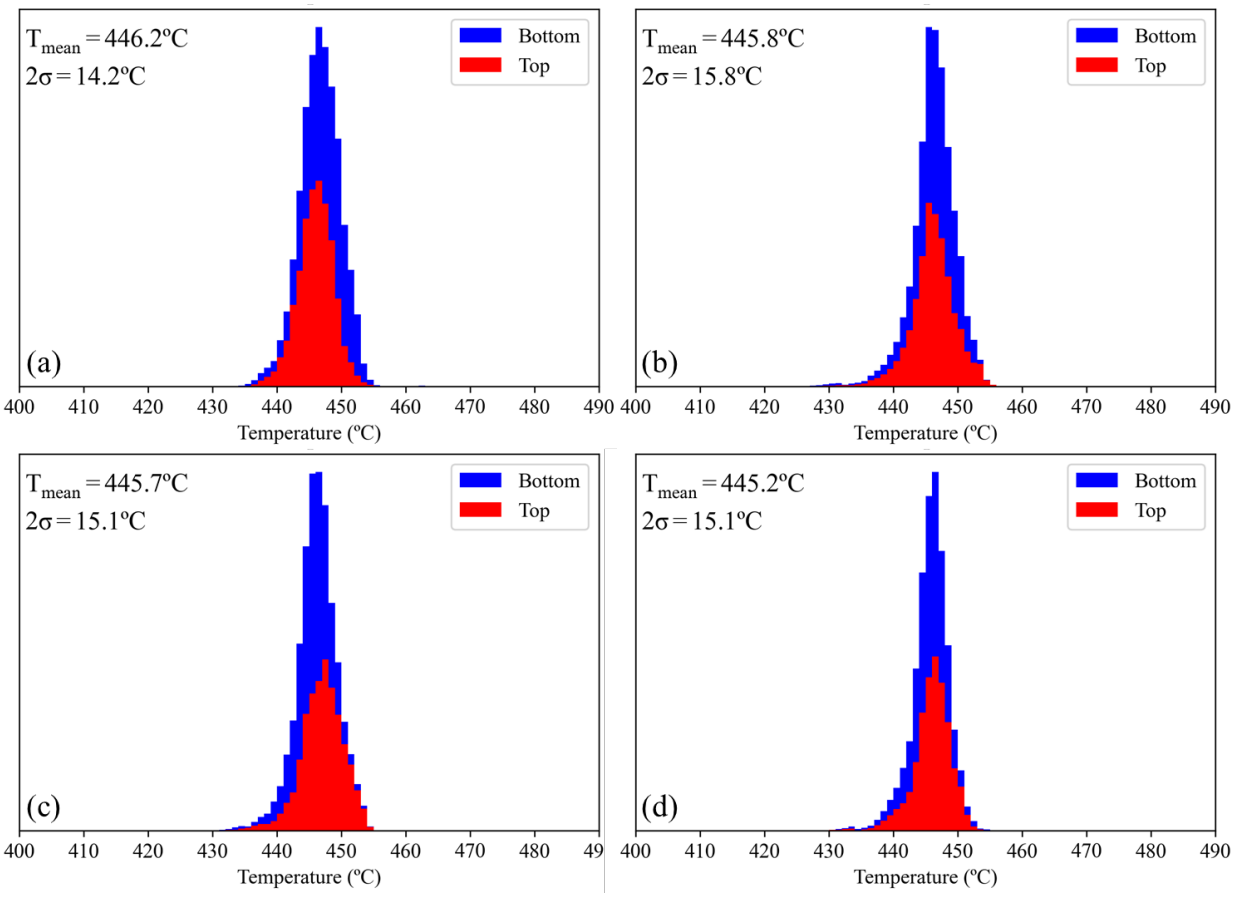

Appendix Figure 16. Temperature histograms for the 150 dpa, 445°C irradiation of Heat B of AM-HT9 with 5 MeV Fe^{2+} ions for implanted He levels of 4 appm/dpa.

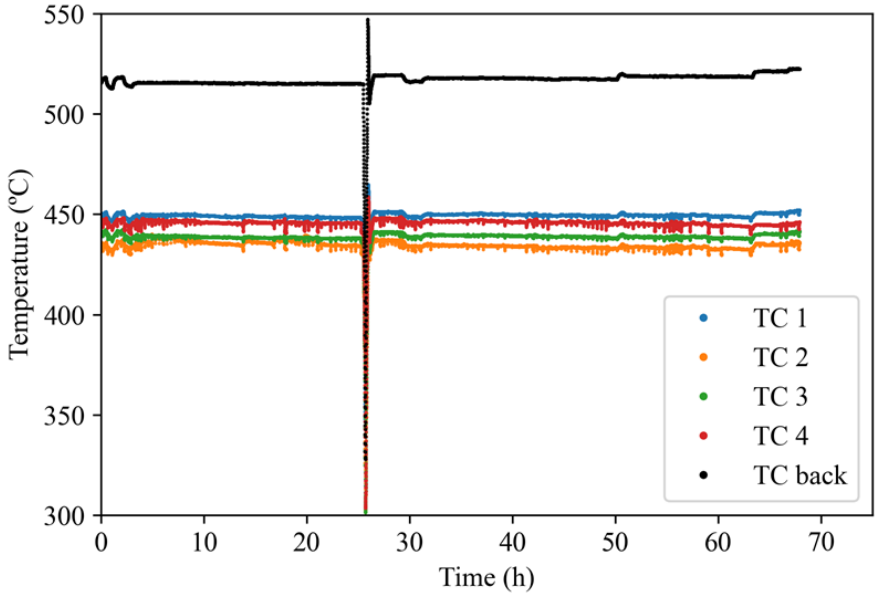

Appendix Figure 17. Thermocouple readings of temperature for the 150 dpa, 445°C irradiation of Heat B of AM-HT9 with 5 MeV Fe^{2+} ions for implanted He levels of 4 appm/dpa.

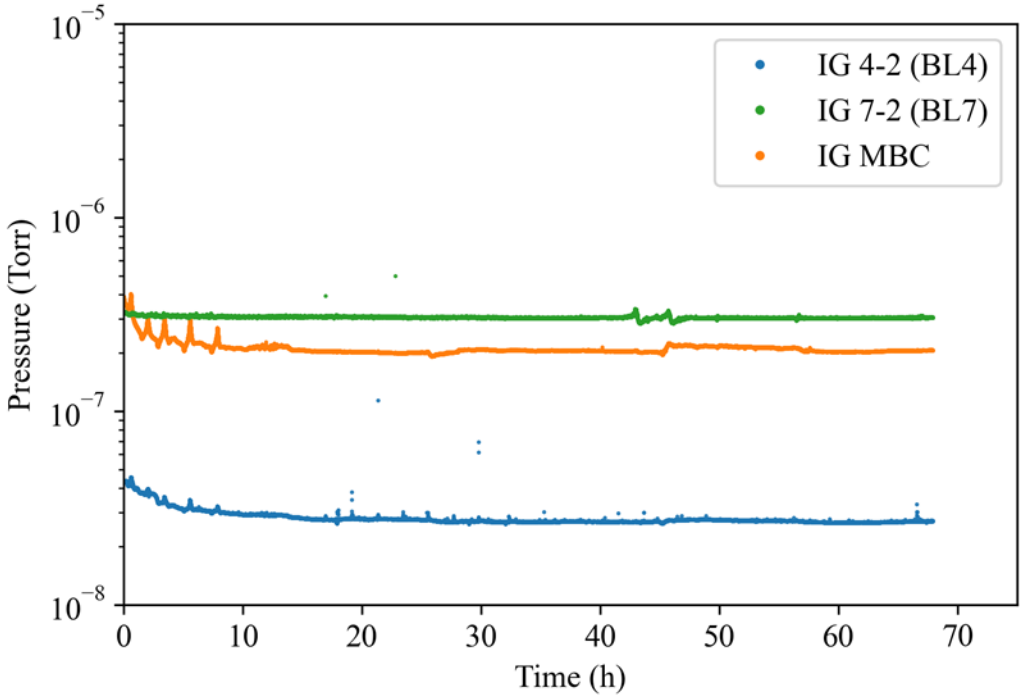

Appendix Figure 18. Pressure history for the 150 dpa, 445°C irradiation of Heat B of AM-HT9 with 5 MeV Fe^{2+} ions for implanted He levels of 4 appm/dpa.

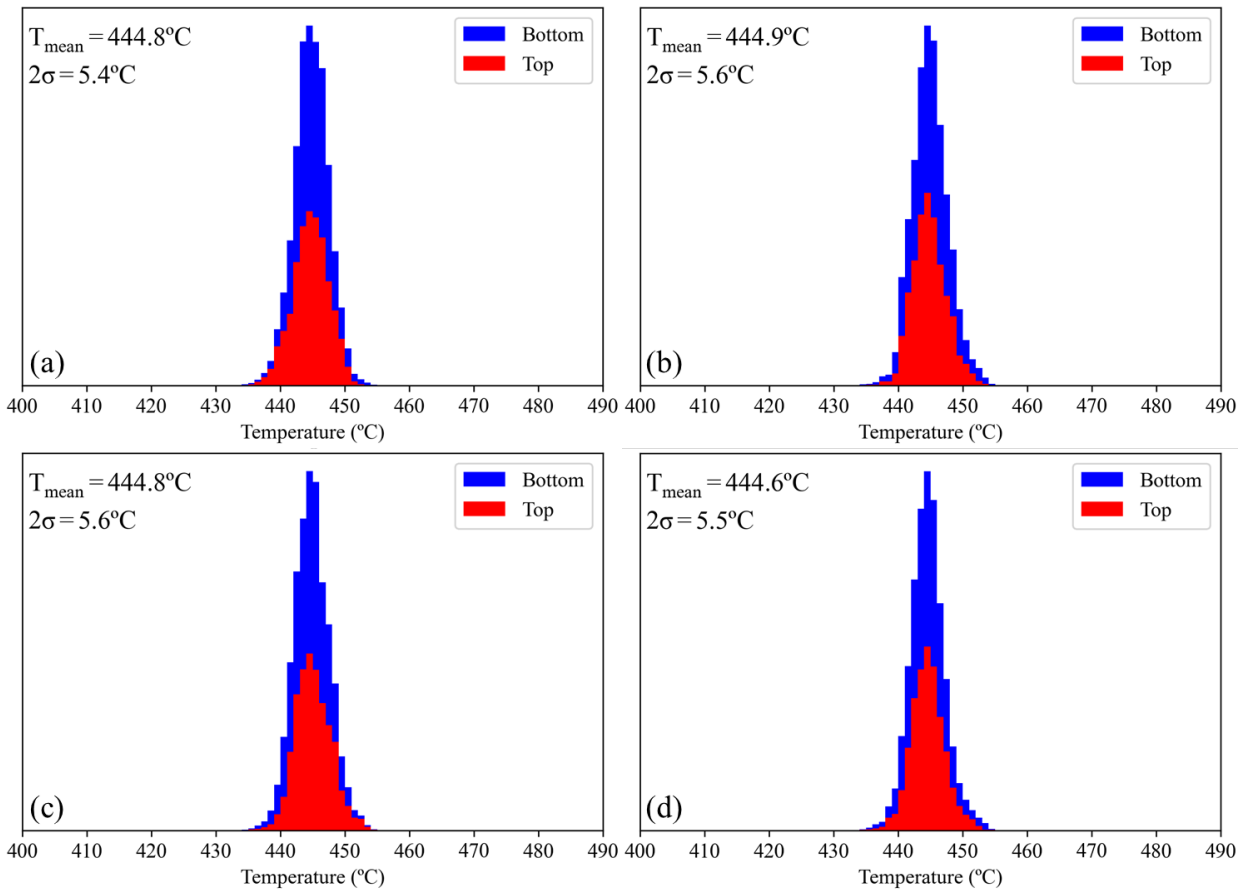

Appendix Figure 19. Temperature histograms for the 250 dpa, 445°C irradiation of Heat B of AM-HT9 with 5 MeV Fe^{2+} ions for implanted He levels of 4 appm/dpa.

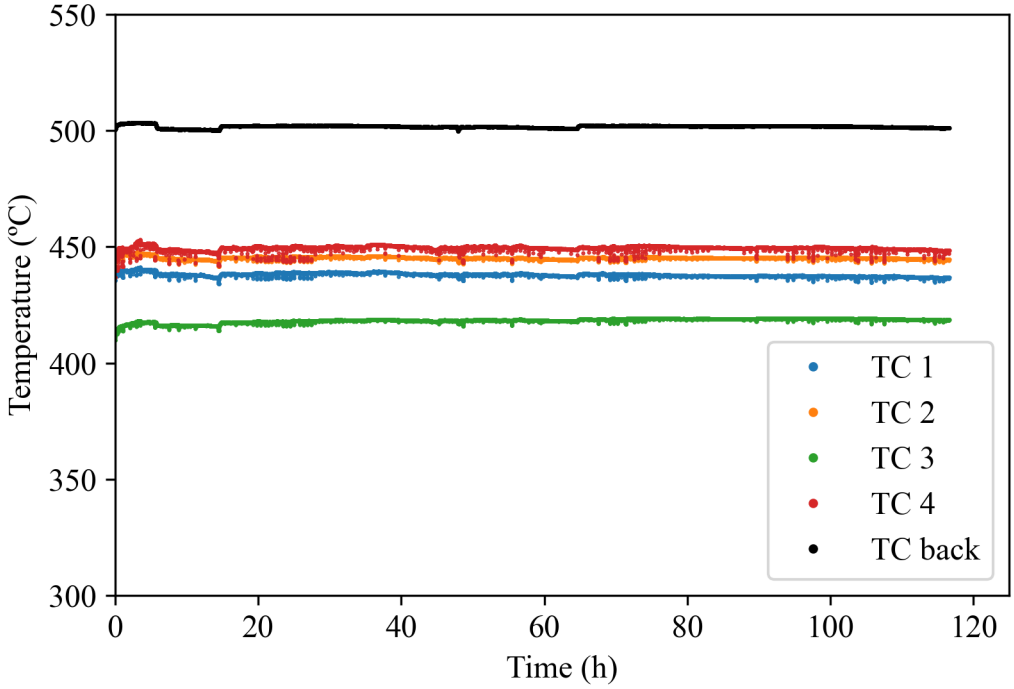

Appendix Figure 20. Thermocouple readings of temperature for the 250 dpa, 445°C irradiation of Heat B of AM-HT9 with 5 MeV Fe^{2+} ions for implanted He levels of 4 appm/dpa.

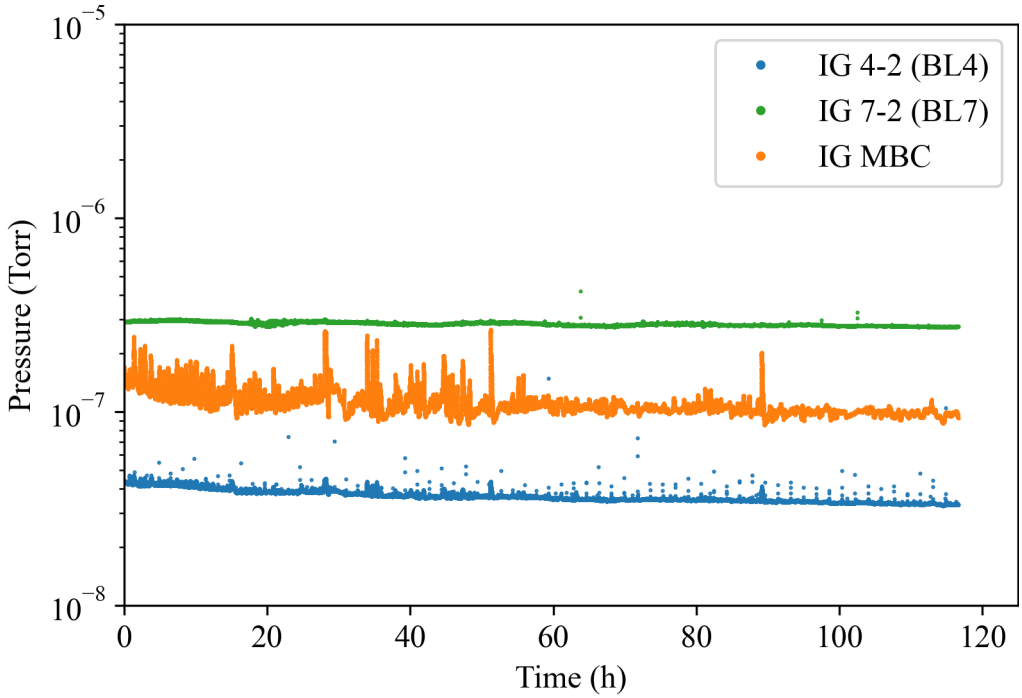

Appendix Figure 21. Pressure history for the 250 dpa, 445°C irradiation of Heat B of AM-HT9 with 5 MeV Fe^{2+} ions for implanted He levels of 4 appm/dpa.

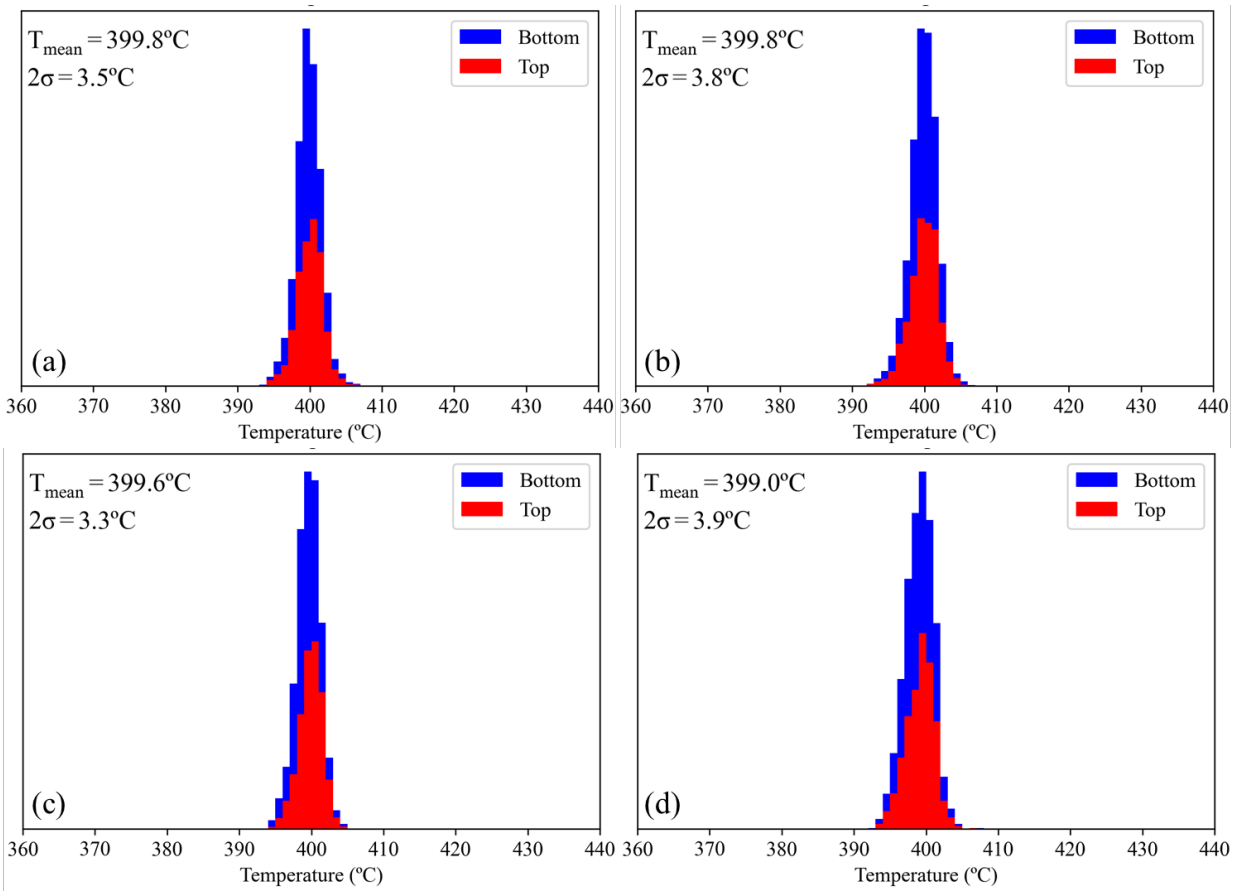

Appendix Figure 22. Temperature histograms for the 50 dpa, 400°C irradiation of Heat B of AM-HT9 with 5 MeV Fe^{2+} ions for implanted He levels of 4 appm/dpa.

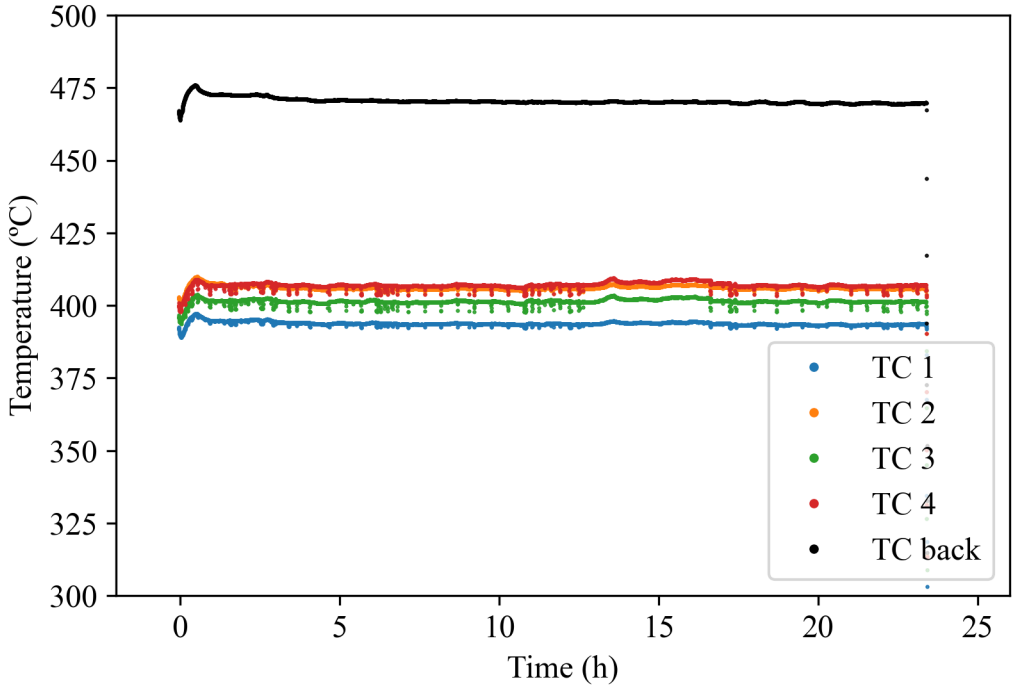

Appendix Figure 23. Thermocouple readings of temperature for the 50 dpa, 400°C irradiation of Heat B of AM-HT9 with 5 MeV Fe^{2+} ions for implanted He levels of 4 appm/dpa.

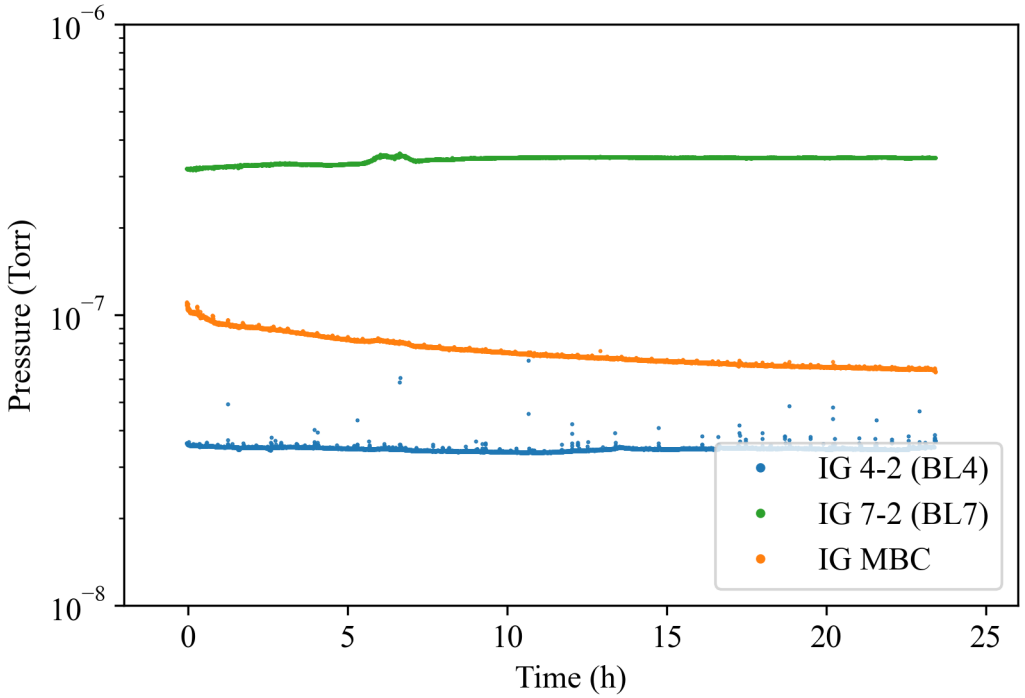

Appendix Figure 24. Pressure history for the 50 dpa, 400°C irradiation of Heat B of AM-HT9 with 5 MeV Fe^{2+} ions for implanted He levels of 4 appm/dpa.

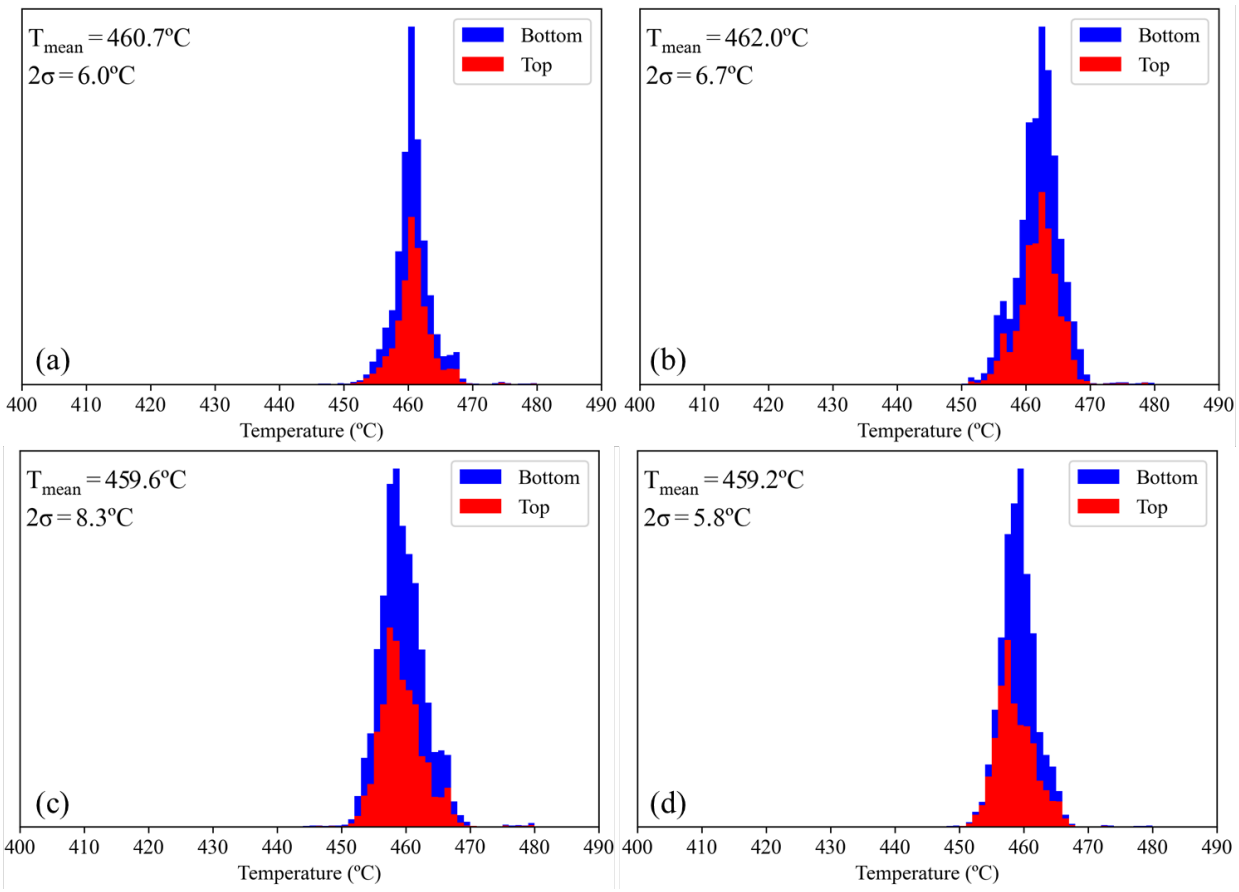

Appendix Figure 25. Temperature histograms for the 50 dpa, 460°C irradiation of Heat B of AM-HT9 with 5 MeV Fe^{2+} ions for implanted He levels of 4 appm/dpa.

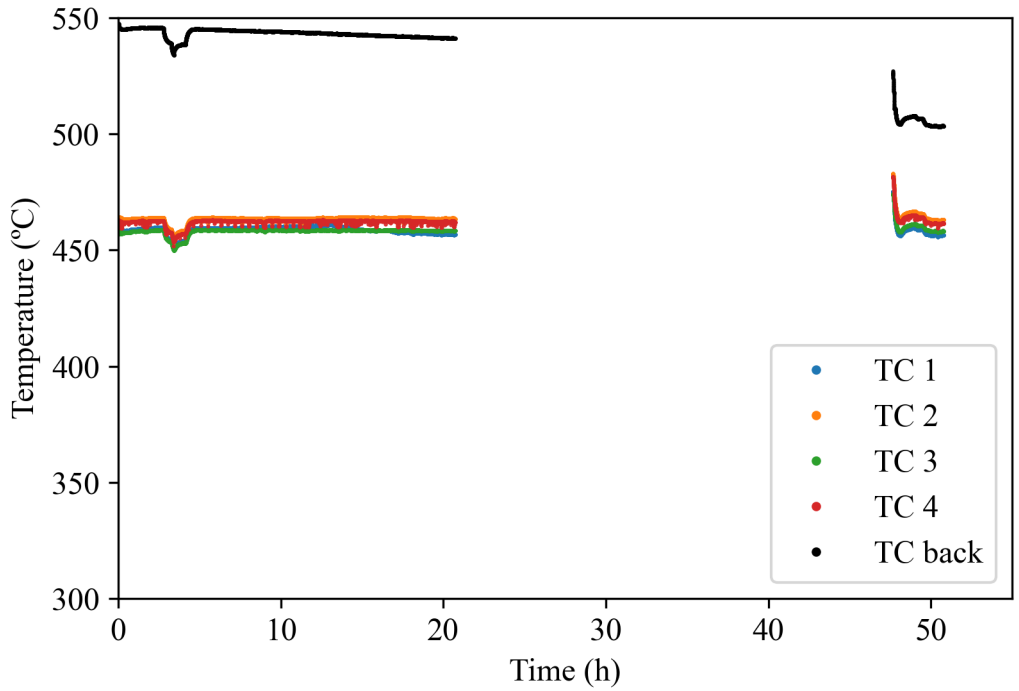

Appendix Figure 26. Thermocouple readings of temperature for the 50 dpa, 460°C irradiation of Heat B of AM-HT9 with 5 MeV Fe^{2+} ions for implanted He levels of 4 appm/dpa.

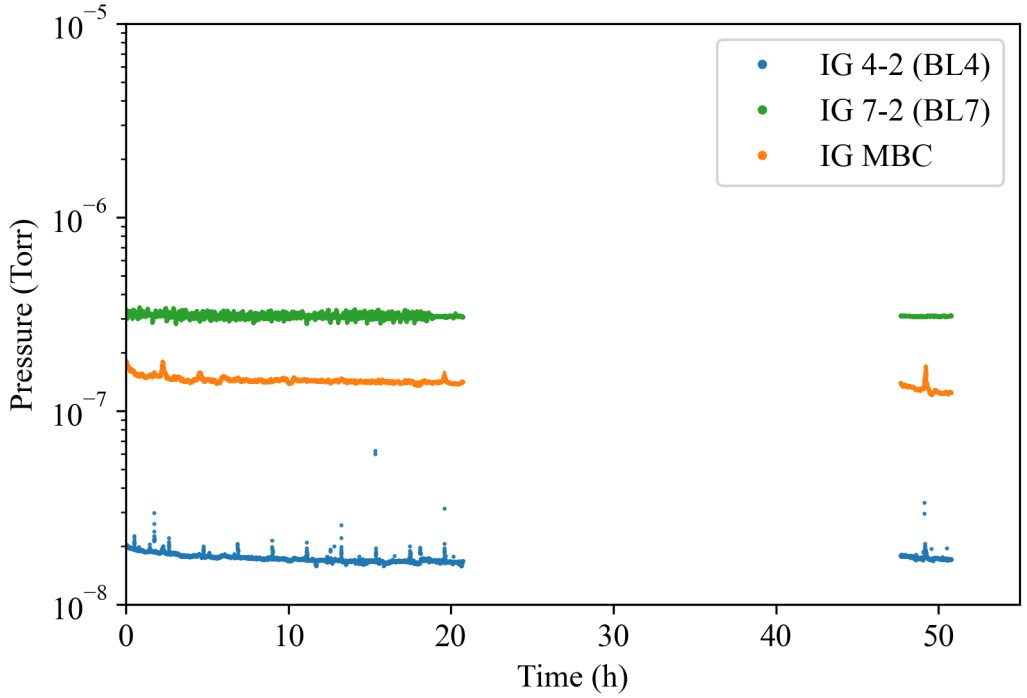

Appendix Figure 27. Pressure history for the 50 dpa, 460°C irradiation of Heat B of AM-HT9 with 5 MeV Fe^{2+} ions for implanted He levels of 4 appm/dpa.

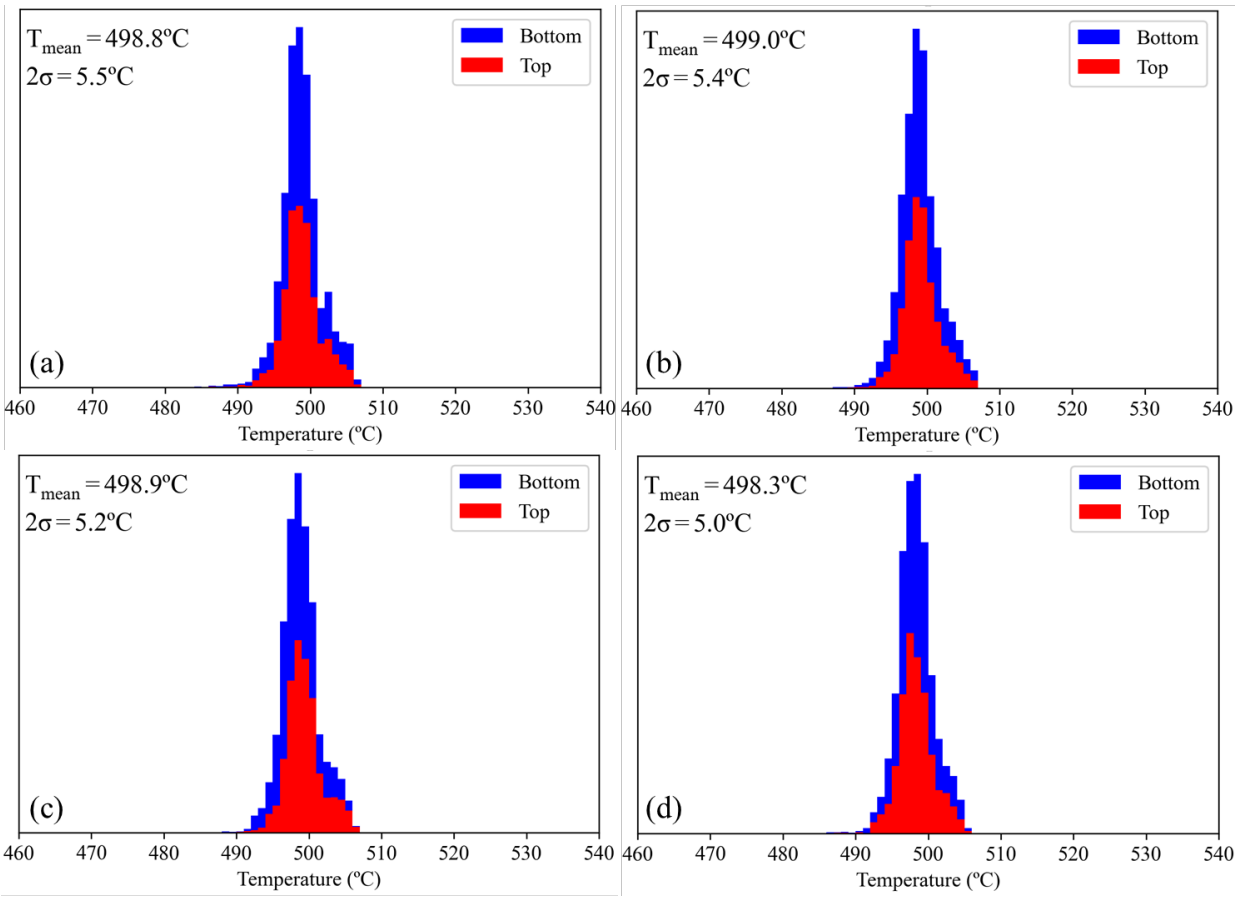

Appendix Figure 28. Temperature histograms for the 50 dpa, 500°C irradiation of Heat B of AM-HT9 with 5 MeV Fe^{2+} ions for implanted He levels of 4 appm/dpa.

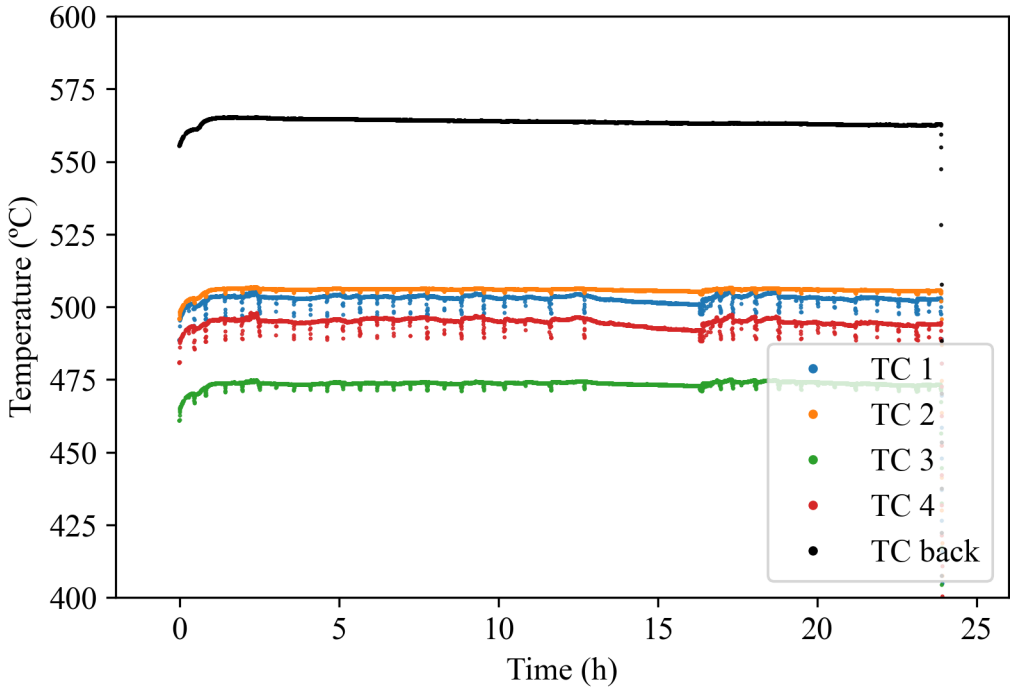

Appendix Figure 29. Thermocouple readings of temperature for the 50 dpa, 500°C irradiation of Heat B of AM-HT9 with 5 MeV Fe^{2+} ions for implanted He levels of 4 appm/dpa.

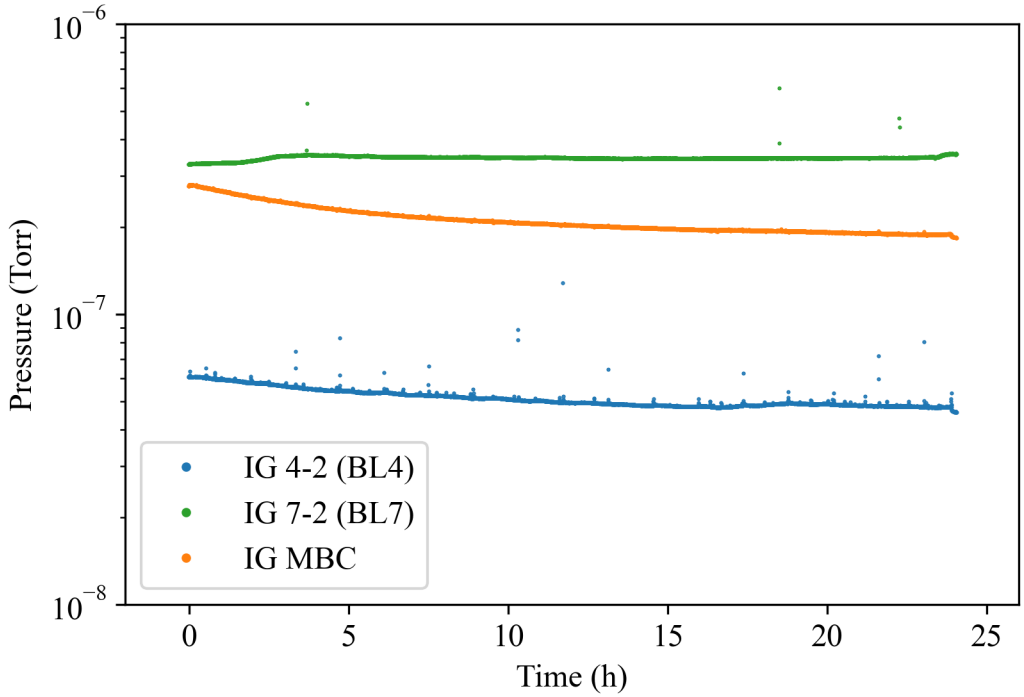

Appendix Figure 30. Pressure history for the 50 dpa, 500°C irradiation of Heat B of AM-HT9 with 5 MeV Fe^{2+} ions for implanted He levels of 4 appm/dpa.

Appendix D. Full Feature Statistics and Q Calculations in the Damage Level Series

	PAGB Grain Size (μm)	Lath Size (nm)	Damage (dpa)	Dislocation Density (10^{14}/m^2)	Cavity Diameter (nm)	Cavity Density (10^{21}/m^3)	$a\langle100\rangle$ Dislocation Loop Diameter (nm)	$a\langle100\rangle$ Dislocation Loop Density (10^{21}/m^3)	$a/2\langle111\rangle$ Dislocation Loop Diameter (nm)	$a/2\langle111\rangle$ Dislocation Loop Density (10^{21}/m^3)	Ni/Si/Mn-rich Precipitate Diameter (nm)	Ni/Si/Mn-rich Precipitate Density (10^{21}/m^3)	Cr-rich Precipitate Diameter (nm)	Cr-rich Precipitate Density (10^{21}/m^3)	Q with simplified model	Q with generalized model
ASB	32 ± 1	247.4 ± 66.0	0	8.48 ± 0.8	N.O.	N.O.	N.O.	N.O.	N.O.	N.O.	N.O.	N.O.	N.O.	N.O.	∞	0.3
			16.6	23.2 ± 2.3	N.O.	N.O.	4.6 ± 0.5	4.1 ± 0.4	5.6 ± 1.6	4.7 ± 0.5	N.O.	N.O.	3.5 ± 1.1	16.1 ± 1.6	∞	0.8
			50	5.09 ± 0.5	N.O.	N.O.	12.9 ± 5.4	3.5 ± 0.4	7.5 ± 2.1	1.6 ± 0.2	N.O.	N.O.	5.1 ± 1.2	41.0 ± 4.1	∞	0.2
			75	30.4 ± 3.0	N.O.	N.O.	18.2 ± 7.5	2.8 ± 0.3	10.1 ± 2.4	1.9 ± 0.2	6.1 ± 2.4	8.8 ± 0.9	9.9 ± 2.3	18.9 ± 1.9	∞	0.7
			100	12.4 ± 1.2	2.7 ± 0.9	5.3 ± 0.5	13.0 ± 4.1	1.7 ± 0.2	10.5 ± 3.6	4.1 ± 0.4	8.0 ± 3.9	8.6 ± 0.9	12.0 ± 6.9	9.2 ± 0.9	13.8	0.4
			150	6.82 ± 0.7	2.4 ± 1.1	67.8 ± 6.8	17.1 ± 7.5	1.3 ± 0.1	10.9 ± 3.4	1.0 ± 0.1	7.5 ± 2.3	5.3 ± 0.5	16.8 ± 11.2	4.7 ± 0.5	0.7	0.2
			250	9.81 ± 1.0	2.3 ± 1.1	104.1 ± 10.4	24.7 ± 10.1	3.4 ± 0.3	16.4 ± 3.1	2.1 ± 0.2	7.7 ± 2.8	9.4 ± 0.9	18.8 ± 11.8	5.5 ± 0.6	0.7	0.2
ACO 3	22 ± 7.8	377.6 ± 19.5	0	1.92 ± 0.2	N.O.	N.O.	N.O.	N.O.	N.O.	N.O.	N.O.	N.O.	N.O.	N.O.	∞	0.3
			16.6	10.4 ± 1.0	2.7 ± 0.9	12 ± 1.2	27.9 ± 10.0	5.1 ± 0.5	30.0 ± 5.0	0.7 ± 0.1	9.0 ± 1.9	12.1 ± 1.2	N.O.	N.O.	3.4	0.9
			50	2.62 ± 0.3	3.8 ± 2.2	69.3 ± 7.0	24.8 ± 9.0	3.0 ± 0.3	27.1 ± 8.7	1.0 ± 0.1	8.2 ± 2.8	16.5 ± 1.7	N.O.	N.O.	0.2	0.2
			75	9.27 ± 0.9	3.3 ± 2.7	29.7 ± 3.0	14.4 ± 8.0	5.0 ± 0.5	10.9 ± 3.9	2.1 ± 0.2	7.9 ± 2.5	11.4 ± 1.1	13.2 ± 7.1	0.6 ± 0.1	1.5	0.6
			100	5.32 ± 0.5	2.8 ± 2.2	66.8 ± 6.7	19.2 ± 7.3	2.8 ± 0.3	14.0 ± 4.0	2.4 ± 0.2	10.1 ± 3.6	6.1 ± 0.6	11.2 ± 2.5	0.2 ± 0.0	0.5	0.3
			150	1.98 ± 0.2	3.5 ± 4.0	63.4 ± 6.3	23.8 ± 10.2	2.9 ± 0.3	21.0 ± 8.8	1.1 ± 0.1	10.8 ± 3.8	6.4 ± 0.6	N.O.	N.O.	0.1	0.2
			250	4.22 ± 0.4	3.0 ± 3.6	178.9 ± 17.9	19.7 ± 11.2	6.0 ± 0.6	25.7 ± 7.9	0.8 ± 0.1	10.4 ± 4.3	5.7 ± 0.6	N.O.	N.O.	0.1	0.2
FCR D	7.0 ± 2.5	368.1 ± 114	0	3.31 ± 0.3	N.O.	N.O.	N.O.	N.O.	N.O.	N.O.	N.O.	N.O.	N.O.	N.O.	∞	0.4
			16.6	8.22 ± 0.8	2.7 ± 1.5	4.7 ± 0.5	21.5 ± 8.7	3.5 ± 0.4	15.1 ± 5.6	4.4 ± 0.4	5.2 ± 2.3	16.7 ± 1.7	N.O.	N.O.	10.1	0.8
			50	5.62 ± 0.6	4.4 ± 1.3	25.9 ± 2.6	23.3 ± 8.7	2.0 ± 0.2	17.2 ± 4.7	1.7 ± 0.2	6.8 ± 2.2	15.4 ± 1.5	N.O.	N.O.	0.8	0.4
			75	6.89 ± 0.7	2.7 ± 1.7	26.9 ± 2.7	20.3 ± 9.0	2.7 ± 0.3	21.0 ± 7.1	2.9 ± 0.3	9.4 ± 2.2	9.6 ± 1.0	N.O.	N.O.	1.5	0.6
			100	3.66 ± 0.4	2.2 ± 2.3	105.4 ± 10.5	20.7 ± 10.1	3.9 ± 0.4	16.5 ± 5.6	1.9 ± 0.2	8.8 ± 2.6	7.1 ± 0.7	8.2 ± 3.9	1.0 ± 0.1	0.2	0.3
			150	4.19 ± 0.4	5.1 ± 4.3	20.7 ± 2.1	24.4 ± 9.7	2.2 ± 0.2	14.1 ± 5.0	0.5 ± 0.1	9.5 ± 3.7	7.4 ± 0.7	21.5 ± 9.9	1.2 ± 0.1	0.6	0.3
			250	3.07 ± 0.3	5.2 ± 1.8	61.6 ± 6.2	14.9 ± 8.4	6.9 ± 0.7	15.6 ± 5.5	1.6 ± 0.2	10.5 ± 3.2	5.5 ± 0.6	18.0 ± 6.7	1.3 ± 0.1	0.2	0.2

Bibliography

[1] 5 Fast Facts About Nuclear Energy, (2021). https://www.energy.gov/ne/articles/5-fast-facts-about-nuclear-energy.
[2] Nuclear Power in the World Today, (2022). https://world-nuclear.org/information-library/current-and-future-generation/nuclear-power-in-the-world-today.aspx.
[3] G.S. WAS, Fundamentals of Radiation Materials Science, Springer New York, New York, NY, 2017. https://doi.org/10.1007/978-1-4939-3438-6.
[4] L. Jiang, P. Xiu, Y. Yan, C. Lu, M. Huang, T. Liu, C. Ye, H. Sun, R. Shu, L. Wang, Effects of ion irradiation on chromium coatings of various thicknesses on a zirconium alloy, J. Nucl. Mater. 526 (2019) 151740. https://doi.org/10.1016/j.jnucmat.2019.151740.
[5] K. Jin, C. Lu, L.M. Wang, J. Qu, W.J. Weber, Y. Zhang, H. Bei, Effects of compositional complexity on the ion-irradiation induced swelling and hardening in Ni-containing equiatomic alloys, Scr. Mater. (2016). https://doi.org/10.1016/j.scriptamat.2016.03.030.
[6] E. Wakai, S. Jitsukawa, H. Tomita, K. Furuya, M. Sato, K. Oka, T. Tanaka, F. Takada, T. Yamamoto, Y. Kato, Y. Tayama, K. Shiba, S. Ohnuki, Radiation hardening and -embrittlement due to He production in F82H steel irradiated at 250 °c in JMTR, in: J. Nucl. Mater., North-Holland, 2005: pp. 285–296. https://doi.org/10.1016/j.jnucmat.2004.10.167.
[7] P. Xiu, Y.N. Osetsky, L. Jiang, G. Velisa, Y. Tong, H. Bei, W.J. Weber, Y. Zhang, L. Wang, Dislocation loop evolution and radiation hardening in nickel-based concentrated solid solution alloys, J. Nucl. Mater. 538 (2020) 152247. https://doi.org/10.1016/j.jnucmat.2020.152247.
[8] S.J. Zinkle, A. Möslang, T. Muroga, H. Tanigawa, Multimodal options for materials research to advance the basis for fusion energy in the ITER era, Nucl. Fusion. 53 (2013) 104024. https://doi.org/10.1088/0029-5515/53/10/104024.
[9] E. Getto, K. Sun, A.M. Monterrosa, Z. Jiao, M.J. Hackett, G.S. Was, Void swelling and microstructure evolution at very high damage level in self-ion irradiated ferritic-martensitic steels, J. Nucl. Mater. 480 (2016) 159–176. https://doi.org/10.1016/j.jnucmat.2016.08.015.
[10] A.M. Monterrosa, Z. Jiao, G.S. Was, The influence of helium on cavity evolution in ion-irradiated T91, J. Nucl. Mater. 509 (2018) 707–721. https://doi.org/10.1016/j.jnucmat.2018.06.033.
[11] D. Woodley, S. Taller, Z. Jiao, K. Sun, G.S. Was, The Role of Co-injected Helium on Swelling and Cavity Evolution at High Damage Levels in Ferritic-Martensitic Steels, J. Nucl. Mater. 550 (2021) 152912. https://doi.org/10.1016/j.jnucmat.2021.152912.
[12] X. Ren, K. Sridharan, T.R. Allen, Corrosion of ferritic–martensitic steel HT9 in supercritical water, J. Nucl. Mater. 358 (2006) 227–234. https://doi.org/10.1016/j.jnucmat.2006.07.010.
[13] P. Ampornrat, G.S. Was, Oxidation of ferritic–martensitic alloys T91, HCM12A and HT-9 in supercritical water, J. Nucl. Mater. 371 (2007) 1–17. https://doi.org/10.1016/j.jnucmat.2007.05.023.
[14] M. Toloczko, F. Garner, Variability of Irradiation Creep and Swelling of HT9 Irradiated to High Neutron Fluence at 400–600°C, in: Eff. Radiat. Mater. 18th Int. Symp., ASTM International, 100 Barr Harbor Drive, PO Box C700, West Conshohocken, PA 19428-2959, n.d.: pp. 765-765–15. https://doi.org/10.1520/STP13902S.
[15] M.B. Toloczko, F.A. Garner, C.R. Eiholzer, Irradiation creep of various ferritic alloys irradiated at ~400°C in the PFR and FFTF reactors, J. Nucl. Mater. 258–263 (1998)

1163–1166. https://doi.org/10.1016/S0022-3115(98)00165-2.
[16] R.E. Clausing, L. Heatherly, R.G. Faulkner, A.F. Rowcliffe, K. Farrell, Radiation-induced segregation in HT-9 martensitic steel, J. Nucl. Mater. 141–143 (1986) 978–981. https://doi.org/10.1016/0022-3115(86)90128-5.
[17] B.H. Sencer, J.R. Kennedy, J.I. Cole, S.A. Maloy, F.A. Garner, Microstructural analysis of an HT9 fuel assembly duct irradiated in FFTF to 155 dpa at 443 °C, J. Nucl. Mater. 393 (2009) 235–241. https://doi.org/10.1016/j.jnucmat.2009.06.010.
[18] C. Zheng, M.A. Auger, M.P. Moody, D. Kaoumi, Radiation induced segregation and precipitation behavior in self-ion irradiated Ferritic/Martensitic HT9 steel, J. Nucl. Mater. 491 (2017) 162–176. https://doi.org/10.1016/j.jnucmat.2017.04.040.
[19] J.G. Gigax, T. Chen, H. Kim, J. Wang, L.M. Price, E. Aydogan, S.A. Maloy, D.K. Schreiber, M.B. Toloczko, F.A. Garner, L. Shao, Radiation response of alloy T91 at damage levels up to 1000 peak dpa, J. Nucl. Mater. 482 (2016) 257–265. https://doi.org/10.1016/j.jnucmat.2016.10.003.
[20] L. Tan, B.K. Kim, Y. Yang, K.G. Field, S. Gray, M. Li, Microstructural evolution of neutron-irradiated T91 and NF616 to ~4.3 dpa at 469 °C, J. Nucl. Mater. 493 (2017) 12–20. https://doi.org/10.1016/j.jnucmat.2017.05.041.
[21] Z. Shang, J. Ding, C. Fan, D. Chen, J. Li, Y. Zhang, Y. Wang, H. Wang, X. Zhang, He ion irradiation response of a gradient T91 steel, Acta Mater. 196 (2020) 175–190. https://doi.org/10.1016/j.actamat.2020.06.019.
[22] S. Taller, G.S. Was, Understanding bubble and void nucleation in dual ion irradiated T91 steel using single parameter experiments, Acta Mater. 198 (2020) 47–60. https://doi.org/10.1016/j.actamat.2020.07.060.
[23] Y. Dai, S.A. Maloy, G.S. Bauer, W.F. Sommer, Mechanical properties and microstructure in low-activation martensitic steels F82H and Optimax after 800-MeV proton irradiation, J. Nucl. Mater. 283 (2000) 513–517. https://doi.org/10.1016/S0022-3115(00)00267-1.
[24] M. Ando, E. Wakai, T. Sawai, H. Tanigawa, K. Furuya, S. Jitsukawa, H. Takeuchi, K. Oka, S. Ohnuki, A. Kohyama, Synergistic effect of displacement damage and helium atoms on radiation hardening in F82H at TIARA facility, in: J. Nucl. Mater., North-Holland, 2004: pp. 1137–1141. https://doi.org/10.1016/j.jnucmat.2004.04.290.
[25] C.A. Williams, E.A. Marquis, A. Cerezo, G.D.W. Smith, Nanoscale characterisation of ODS-Eurofer 97 steel: An atom-probe tomography study, J. Nucl. Mater. 400 (2010) 37–45. https://doi.org/10.1016/j.jnucmat.2010.02.007.
[26] M. Klimenkov, E. Materna-Morris, A. Möslang, Characterization of radiation induced defects in EUROFER 97 after neutron irradiation, in: J. Nucl. Mater., North-Holland, 2011: pp. 124–126. https://doi.org/10.1016/j.jnucmat.2010.12.261.
[27] O. V. Ogorodnikova, K. Sugiyama, Effect of radiation-induced damage on deuterium retention in tungsten, tungsten coatings and Eurofer, J. Nucl. Mater. 442 (2013) 518–527. https://doi.org/10.1016/j.jnucmat.2013.07.024.
[28] T.R. Allen, L. Tan, J. Gan, G. Gupta, G.S. Was, E.A. Kenik, S. Shutthanandan, S. Thevuthasan, Microstructural development in advanced ferritic-martensitic steel HCM12A, J. Nucl. Mater. 351 (2006) 174–186. https://doi.org/10.1016/j.jnucmat.2006.02.014.
[29] P. Ampornrat, G.S. Was, Oxidation of ferritic-martensitic alloys T91, HCM12A and HT-9 in supercritical water, J. Nucl. Mater. 371 (2007) 1–17. https://doi.org/10.1016/j.jnucmat.2007.05.023.

[30] J.S. Cheon, C.B. Lee, B.O. Lee, J.P. Raison, T. Mizuno, F. Delage, J. Carmack, Sodium fast reactor evaluation: Core materials, J. Nucl. Mater. 392 (2009) 324–330. https://doi.org/10.1016/j.jnucmat.2009.03.021.
[31] W.-Y. Lo, Y. Yang, Vanadium diffusion coating on HT-9 cladding for mitigating the fuel cladding chemical interactions, J. Nucl. Mater. 451 (2014) 137–142. https://doi.org/10.1016/j.jnucmat.2014.03.052.
[32] T.R. Allen, J.T. Busby, R.L. Klueh, S.A. Maloy, M.B. Toloczko, Cladding and duct materials for advanced nuclear recycle reactors, JOM. 60 (2008) 15–23. https://doi.org/10.1007/s11837-008-0002-6.
[33] B.H.H. Sencer, J.R.R. Kennedy, J.I.I. Cole, S.A.A. Maloy, F.A.A. Garner, Microstructural stability of an HT-9 fuel assembly duct irradiated in FFTF, J. Nucl. Mater. 414 (2011) 237–242. https://doi.org/10.1016/j.jnucmat.2011.03.050.
[34] O. Anderoglu, J. Van den Bosch, P. Hosemann, E. Stergar, B.H. Sencer, D. Bhattacharyya, R. Dickerson, P. Dickerson, M. Hartl, S.A. Maloy, Phase stability of an HT-9 duct irradiated in FFTF, J. Nucl. Mater. 430 (2012) 194–204. https://doi.org/10.1016/j.jnucmat.2012.06.038.
[35] S.N. Rosenwasser, P. Miller, J.A. Dalessandro, J.M. Rawls, W.E. Toffolo, W. Chen, The application of martensitic stainless steels in long lifetime fusion first wall/blankets, J. Nucl. Mater. 85–86 (1979) 177–182. https://doi.org/10.1016/0022-3115(79)90487-2.
[36] D. Gilbon, C. Rivera, Behaviour of different ferritic steels under ion, electron and fast neutron irradiation, J. Nucl. Mater. 155–157 (1988) 1268–1273. https://doi.org/10.1016/0022-3115(88)90509-0.
[37] P. Xiu, C.P. Massey, T.M.K. Green, S. Taller, D. Isheim, N. Sridharan, K.G. Field, Microchemical evolution of irradiated additive-manufactured HT9, J. Nucl. Mater. 559 (2022) 153410. https://doi.org/10.1016/j.jnucmat.2021.153410.
[38] Y. Chen, Irradiation effects of HT-9 martensitic steel, Nucl. Eng. Technol. (2013). https://doi.org/10.5516/NET.07.2013.706.
[39] N. Haghdadi, M. Laleh, M. Moyle, S. Primig, Additive manufacturing of steels: a review of achievements and challenges, J. Mater. Sci. 56 (2021) 64–107. https://doi.org/10.1007/s10853-020-05109-0.
[40] H.L. Ming, Z.M. Zhang, P.Y. Xiu, J.Q. Wang, E.H. Han, W. Ke, M.X. Su, Microstructure, residual strain and stress corrosion cracking behavior in 316L heat-affected zone, Acta Metall. Sin. (English Lett. (2016). https://doi.org/10.1007/s40195-016-0461-7.
[41] J. Hou, T. Shoji, Z.P. Lu, Q.J. Peng, J.Q. Wang, E.H. Han, W. Ke, Residual strain measurement and grain boundary characterization in the heat-affected zone of a weld joint between Alloy 690TT and Alloy 52, J. Nucl. Mater. (2010). https://doi.org/10.1016/j.jnucmat.2009.12.016.
[42] Z. Lu, T. Shoji, S. Yamazaki, K. Ogawa, Characterization of microstructure, local deformation and microchemistry in Alloy 600 heat-affected zone and stress corrosion cracking in high temperature water, Corros. Sci. (2012). https://doi.org/10.1016/j.corsci.2012.01.029.
[43] D. Zhang, S.A. Briggs, P.D. Edmondson, M.N. Gussev, R.H. Howard, K.G. Field, Influence of welding and neutron irradiation on dislocation loop formation and α′ precipitation in a FeCrAl alloy, J. Nucl. Mater. 527 (2019) 151784. https://doi.org/10.1016/j.jnucmat.2019.151784.
[44] S.. Fabritsiev, A.. Pokrovsky, Radiation resistance of weld joints of type 316 stainless

steel containing about 10 appm He, J. Nucl. Mater. 283–287 (2000) 1215–1219. https://doi.org/10.1016/S0022-3115(00)00095-7.
[45] B. Gurovich, E. Kuleshova, Y. Shtrombakh, S. Fedotova, O. Zabusov, K. Prikhodko, D. Zhurko, Evolution of weld metals nanostructure and properties under irradiation and recovery annealing of VVER-type reactors, J. Nucl. Mater. 434 (2013) 72–84. https://doi.org/10.1016/j.jnucmat.2012.11.026.
[46] Thermo-Mechanical Modeling of Additive Manufacturing, Elsevier, 2018. https://doi.org/10.1016/C2016-0-00317-0.
[47] J. Williams, B. Post, L.J. Love, C. Blue, Opportunities for Lighter Weight and Lower Total Cost Component Manufacturing, in: 2019: pp. 1–26. https://doi.org/10.1007/978-981-15-1263-6_1.
[48] N. Sridharan, K. Field, A Road Map for the Advanced Manufacturing of Ferritic-Martensitic Steels, Fusion Sci. Technol. 75 (2019) 264–274. https://doi.org/10.1080/15361055.2019.1577124.
[49] N. Sridharan, M.N. Gussev, K.G. Field, Performance of a ferritic/martensitic steel for nuclear reactor applications fabricated using additive manufacturing, J. Nucl. Mater. 521 (2019) 45–55. https://doi.org/10.1016/j.jnucmat.2019.04.020.
[50] Y. CHEN, IRRADIATION EFFECTS OF HT-9 MARTENSITIC STEEL, Nucl. Eng. Technol. 45 (2013) 311–322. https://doi.org/10.5516/NET.07.2013.706.
[51] N. Sridharan, K.G. Field, Preliminary Characterization and Mechanical Performance of Additively Manufactured HT9, 2018. https://info.ornl.gov/sites/publications/Files/Pub108260.pdf.
[52] R.L. Klueh, Elevated temperature ferritic and martensitic steels and their application to future nuclear reactors, Int. Mater. Rev. 50 (2005) 287–310. https://doi.org/10.1179/174328005X41140.
[53] R.L. Klueh, A.T. Nelson, Ferritic/martensitic steels for next-generation reactors, J. Nucl. Mater. 371 (2007) 37–52. https://doi.org/10.1016/j.jnucmat.2007.05.005.
[54] R. Klueh, D. Harries, eds., High-Chromium Ferritic and Martensitic Steels for Nuclear Applications, ASTM International, 100 Barr Harbor Drive, PO Box C700, West Conshohocken, PA 19428-2959, 2001. https://doi.org/10.1520/MONO3-EB.
[55] M. Molitch-Hou, Overview of additive manufacturing process, in: Addit. Manuf., Elsevier, 2018: pp. 1–38. https://doi.org/10.1016/B978-0-12-812155-9.00001-3.
[56] R.L. Klueh, D.S. Gelles, M. Okada, N.H. Packan, Reduced activation materials for fusion reactors (ASTM STP 1047), Mater. Des. 12 (1991) 60. https://doi.org/10.1016/0261-3069(91)90102-A.
[57] The Super 12% Cr Steels. J. Z. Briggs und T. D. Parker. 1965 Climax Molybdenum Company, 1270 Avenue of the Americas, New York, N.Y. 10020. 220 S., zahlr. Tabellen, Mater. Corros. Und Korrosion. 17 (1966) 642–642. https://doi.org/10.1002/maco.19660170738.
[58] F.B.P. PICKERING, Physical Metallurgy and the Design of Steels, Appl. Sci. Publ. (1978) 90–100.
[59] D. Woodley, The Role of Helium on Cavity Growth and Swelling at High Damage Levels in Ferritic-Martensitic Steels, University of Michigan, 2020. https://hdl.handle.net/2027.42/162904.
[60] S. Taller, The Role of Damage Rate on Cavity Nucleation with Co-Injected Helium in Dual Ion Irradiated T91 Steel, University of Michigan, 2020.

https://hdl.handle.net/2027.42/155217.
[61] R.C. Thomson, H.K.D.H. Bhadeshia, Carbide precipitation in 12Cr1MoV power plant steel, Metall. Trans. A. 23 (1992) 1171–1179. https://doi.org/10.1007/BF02665048.
[62] T.K. Kim, S.H. Kim, Study on the cold working process for FM steel cladding tubes, J. Nucl. Mater. 411 (2011) 208–212. https://doi.org/10.1016/j.jnucmat.2011.02.017.
[63] Z. Zhang, Z. Hu, S. Schmauder, M. Mlikota, K. Fan, Low-Cycle Fatigue Properties of P92 Ferritic-Martensitic Steel at Elevated Temperature, J. Mater. Eng. Perform. 25 (2016) 1650–1662. https://doi.org/10.1007/s11665-016-1977-8.
[64] PROCEEDINGS OF TOPICAL CONFERENCE ON FERRITIC ALLOYS FOR USE IN NUCLEAR ENERGY TECHNOLOGIES., (1984).
[65] R. Fenn, M.F. Jordan, Microstructure of weld heat-affected zone of 12Cr–Mo steel, Met. Technol. 9 (1982) 327–337. https://doi.org/10.1179/030716982803285701.
[66] Ferritic Steels for Fast Reactor Steam Generators, Br. Corros. J. 13 (1978) 103–103. https://doi.org/10.1179/000705978798276311.
[67] L. Schäfer, Influence of delta ferrite and dendritic carbides on the impact and tensile properties of a martensitic chromium steel, J. Nucl. Mater. 258–263 (1998) 1336–1339. https://doi.org/10.1016/S0022-3115(98)00200-1.
[68] J.F. King, V.K. Sikka, M.L. Santella, J.F. Turner, E.W. Pickering, Weldability of modified 9Cr-1Mo steel, Oak Ridge, TN (United States), 1986. https://doi.org/10.2172/712814.
[69] J. Hald, in: Rupture Ductility of Creep Resistant Steels, Ed. A. Strang (The Inst. of Metals, London, Book No. 522, 1991) 268., (n.d.).
[70] S.L. Sing, C.F. Tey, J.H.K. Tan, S. Huang, W.Y. Yeong, 3D printing of metals in rapid prototyping of biomaterials: Techniques in additive manufacturing, in: Rapid Prototyp. Biomater., Elsevier, 2020: pp. 17–40. https://doi.org/10.1016/B978-0-08-102663-2.00002-2.
[71] A.J. Pontes, Designing for additive manufacturing, in: Des. Manuf. Plast. Prod., Elsevier, 2021: pp. 249–292. https://doi.org/10.1016/B978-0-12-819775-2.00009-7.
[72] J.C. Lippold, Welding Metallurgy and Weldability, John Wiley & Sons, Inc, Hoboken, NJ, 2015. https://doi.org/10.1002/9781118960332.
[73] A. Gabriel, L. Hawkins, A. French, Y. Li, Z. Hu, L. He, P. Xiu, M. Nastasi, F.A. Garner, L. Shao, Effect of dpa rate on the temperature regime of void swelling in ion-irradiated pure chromium, J. Nucl. Mater. 561 (2022) 153519. https://doi.org/10.1016/j.jnucmat.2022.153519.
[74] N. Gao, Z.W. Yao, G.H. Lu, H.Q. Deng, F. Gao, Mechanisms for <100> interstitial dislocation loops to diffuse in BCC iron, Nat. Commun. 12 (2021) 225. https://doi.org/10.1038/s41467-020-20574-6.
[75] A.. Dvoriashin, S.. Porollo, Y.. Konobeev, F.. Garner, Influence of high dose neutron irradiation on microstructure of EP-450 ferritic–martensitic steel irradiated in three Russian fast reactors, J. Nucl. Mater. 329–333 (2004) 319–323. https://doi.org/10.1016/j.jnucmat.2004.04.309.
[76] G. Ayrault, Cavity formation during single- and dual-ion irradiation in a 9Cr-1Mo ferritic alloy, J. Nucl. Mater. 114 (1983) 34–40. https://doi.org/10.1016/0022-3115(83)90070-3.
[77] R. Hide, K. Kusanagi, M. Taguchi, Microstructural Change in Ferritic Steels Under Heavy Ion Irradiation, Eff. Radiat. Mater. 14th Int. (1989) 61–72.
[78] L.K. Mansur, Theory of transitions in dose dependence of radiation effects in structural

alloys, J. Nucl. Mater. 206 (1993) 306–323. https://doi.org/10.1016/0022-3115(93)90130-Q.
[79] G.S. Was, Fundamentals of radiation materials science: Metals and alloys, second edition, 2016. https://doi.org/10.1007/978-1-4939-3438-6.
[80] J.J. Kai, G.L. Kulcinski, 14 MeV nickel-ion irradiated HT-9 ferritic steel with and without helium pre-implantation, J. Nucl. Mater. 175 (1990) 227–236. https://doi.org/10.1016/0022-3115(90)90211-5.
[81] F. Smidt, P. Malmberg, J. Sprague, J. Westmoreland, Swelling Behavior of Commercial Ferritic Alloys, EM-12 and HT-9, as Assessed by Heavy Ion Bombardment, in: Irradiat. Eff. Microstruct. Prop. Met., ASTM International, 100 Barr Harbor Drive, PO Box C700, West Conshohocken, PA 19428-2959, n.d.: pp. 227-227–15. https://doi.org/10.1520/STP38051S.
[82] E. Wakai, T. Sawai, K. Furuya, A. Naito, T. Aruga, K. Kikuchi, S. Yamashita, S. Ohnuki, S. Yamamoto, H. Naramoto, S. Jistukawa, Effect of triple ion beams in ferritic/martensitic steel on swelling behavior, J. Nucl. Mater. 307–311 (2002) 278–282. https://doi.org/10.1016/S0022-3115(02)01076-0.
[83] E. Getto, Z. Jiao, A.M. Monterrosa, K. Sun, G.S. Was, Effect of pre-implanted helium on void swelling evolution in self-ion irradiated HT9, J. Nucl. Mater. (2015). https://doi.org/10.1016/j.jnucmat.2015.01.045.
[84] A.D. Brailsford, L.K. Mansur, The effect of precipitate-matrix interface sinks on the growth of voids in the matrix, J. Nucl. Mater. 104 (1981) 1403–1408. https://doi.org/10.1016/0022-3115(82)90796-6.
[85] A.D. Brailsford, R. Bullough, The rate theory of swelling due to void growth in irradiated metals, J. Nucl. Mater. 44 (1972) 121–135. https://doi.org/10.1016/0022-3115(72)90091-8.
[86] D. Carpentier, T. Jourdan, Y. Le Bouar, M.-C. Marinica, Effect of saddle point anisotropy of point defects on their absorption by dislocations and cavities, Acta Mater. 136 (2017) 323–334. https://doi.org/10.1016/j.actamat.2017.07.013.
[87] A.A. Kohnert, M.A. Cusentino, B.D. Wirth, Molecular statics calculations of the biases and point defect capture volumes of small cavities, J. Nucl. Mater. 499 (2018) 480–489. https://doi.org/10.1016/j.jnucmat.2017.12.005.
[88] J. Marian, B.D. Wirth, J.M. Perlado, Mechanism of Formation and Growth of <math display="inline"> <mi> 〈</mi> <mn>100</mn> <mi>〉 </mi> </math> Interstitial Loops in Ferritic Materials, Phys. Rev. Lett. 88 (2002) 255507. https://doi.org/10.1103/PhysRevLett.88.255507.
[89] Q. Peng, F. Meng, Y. Yang, C. Lu, H. Deng, L. Wang, S. De, F. Gao, Shockwave generates < 100 > dislocation loops in bcc iron, Nat. Commun. 9 (2018) 4880. https://doi.org/10.1038/s41467-018-07102-3.
[90] J.J. Kai, R.L. Klueh, Microstructural analysis of neutron-irradiated martensitic steels, J. Nucl. Mater. 230 (1996) 116–123. https://doi.org/10.1016/0022-3115(96)00165-1.
[91] P. Dubuisson, D. Gilbon, J.L. Séran, Microstructural evolution of ferritic-martensitic steels irradiated in the fast breeder reactor Phénix, J. Nucl. Mater. 205 (1993) 178–189. https://doi.org/10.1016/0022-3115(93)90080-I.
[92] B.H.H. Sencer, J.R.R. Kennedy, J.I.I. Cole, S.A.A. Maloy, F.A.A. Garner, Microstructural analysis of an HT9 fuel assembly duct irradiated in FFTF to 155dpa at 443°C, J. Nucl. Mater. 393 (2009) 235–241. https://doi.org/10.1016/j.jnucmat.2009.06.010.

[93] C. Zheng, D. Kaoumi, Dislocation loop evolution in F/M steel T91 under in-situ ion irradiation: Influence of the presence of initial dislocations, J. Nucl. Mater. 540 (2020) 152363. https://doi.org/10.1016/j.jnucmat.2020.152363.
[94] C. Zheng, S. Maloy, D. Kaoumi, Effect of dose on irradiation-induced loop density and Burgers vector in ion-irradiated ferritic/martensitic steel HT9, Philos. Mag. 98 (2018) 2440–2456. https://doi.org/10.1080/14786435.2018.1490825.
[95] D.S. Gelles, L.E. Thomas, Effects of neutron irradiation on microstructure in experimental and commercial ferritic alloys, Ferritic Alloy. Use Nucl. Energy Tech- Nol. (1984).
[96] P.J. Maziasz, Materials for Nuclear Reactor Core Applications, Br. Nucl. Energy Soc. 2 (1988).
[97] O. Anderoglu, J. Van Den Bosch, P. Hosemann, E. Stergar, B.H. Sencer, D. Bhattacharyya, R. Dickerson, P. Dickerson, M. Hartl, S.A. Maloy, Phase stability of an HT-9 duct irradiated in FFTF, J. Nucl. Mater. (2012). https://doi.org/10.1016/j.jnucmat.2012.06.038.
[98] N. Hashimoto, J.P. Robertson, K. Shiba, Microstructure of Isotopically-tailored Martensitic steel HT9 Irradiated at 400C to 7 dpa in HFIR, DOE/ER-0313/26. 26 (1999) 96–101.
[99] Z. Jiao, G.S. Was, Segregation behavior in proton- and heavy-ion-irradiated ferritic-martensitic alloys, Acta Mater. (2011). https://doi.org/10.1016/j.actamat.2011.03.070.
[100] K.G. Field, Y. Yang, T.R. Allen, J.T. Busby, Defect sink characteristics of specific grain boundary types in 304 stainless steels under high dose neutron environments, Acta Mater. 89 (2015) 438–449. https://doi.org/10.1016/j.actamat.2015.01.064.
[101] J.P. Wharry, G.S. Was, A systematic study of radiation-induced segregation in ferritic–martensitic alloys, J. Nucl. Mater. 442 (2013) 7–16. https://doi.org/10.1016/j.jnucmat.2013.07.071.
[102] C. Lu, T. Yang, K. Jin, N. Gao, P. Xiu, Y. Zhang, F. Gao, H. Bei, W.J. Weber, K. Sun, Y. Dong, L. Wang, Radiation-induced segregation on defect clusters in single-phase concentrated solid-solution alloys, Acta Mater. 127 (2017) 98–107. https://doi.org/10.1016/j.actamat.2017.01.019.
[103] J.M. Vitek, R.L. Klueh, Microstructure of 9 Cr-1 MoVNb steel irradiated to 36 dpa at elevated temperatures in HFIR, J. Nucl. Mater. 122 (1984) 254–259. https://doi.org/10.1016/0022-3115(84)90606-8.
[104] M.B. Toloczko, F.A. Garner, C.R. Eiholzer, Irradiation creep and swelling of the US fusion heats of HT9 and 9Cr-1Mo to 208 dpa at ~ 400°C, J. Nucl. Mater. 212–215 (1994) 604–607. https://doi.org/10.1016/0022-3115(94)90131-7.
[105] M.B. Toloczko, F.A. Garner, Irradiation creep and void swelling of two LMR heats of HT9 at ~ 400°C and 165 dpa, J. Nucl. Mater. 233–237 (1996) 289–292. https://doi.org/10.1016/S0022-3115(96)00413-8.
[106] D.S. Gelles, Microstructural examination of commercial ferritic alloys at 200 dpa, J. Nucl. Mater. 233–237 (1996) 293–298. https://doi.org/10.1016/S0022-3115(96)00222-X.
[107] J. Van den Bosch, O. Anderoglu, R. Dickerson, M. Hartl, P. Dickerson, J.A. Aguiar, P. Hosemann, M.B. Toloczko, S.A. Maloy, SANS and TEM of ferritic–martensitic steel T91 irradiated in FFTF up to 184dpa at 413°C, J. Nucl. Mater. 440 (2013) 91–97. https://doi.org/10.1016/j.jnucmat.2013.04.025.
[108] R.L. Klueh, D.J. Alexander, Embrittlement of 9Cr-1MoVNb and 12Cr-1MoVW steels irradiated in HFIR, J. Nucl. Mater. 187 (1992) 60–69. https://doi.org/10.1016/0022-

3115(92)90319-G.
[109] L.K. Mansur, Theory and experimental background on dimensional changes in irradiated alloys, J. Nucl. Mater. 216 (1994) 97–123. https://doi.org/10.1016/0022-3115(94)90009-4.
[110] J.G. Gigax, T. Chen, H. Kim, J. Wang, L.M. Price, E. Aydogan, S.A. Maloy, D.K. Schreiber, M.B. Toloczko, F.A. Garner, L. Shao, Radiation response of alloy T91 at damage levels up to 1000 peak dpa, J. Nucl. Mater. 482 (2016) 257–265. https://doi.org/10.1016/j.jnucmat.2016.10.003.
[111] L. Shao, C.-C. Wei, J. Gigax, A. Aitkaliyeva, D. Chen, B.H. Sencer, F.A. Garner, Effect of defect imbalance on void swelling distributions produced in pure iron irradiated with 3.5 MeV self-ions, J. Nucl. Mater. 453 (2014) 176–181. https://doi.org/10.1016/j.jnucmat.2014.06.002.
[112] ASTM A826 / A826M-95(2001), Standard Specification for Seamless Austenitic and Martensitic Stainless Steel Duct Tubes for Liquid Metal-Cooled Reactor Core Components (Withdrawn 2004), ASTM International, West Conshohocken, PA, 2001, www.astm.org, (n.d.).
[113] M.J. Hackett, G. Povirk, HT9 development for the traveling wave reactor, invited, in: Trans. Am. Nucl. Soc., 2012: pp. 1133–1135.
[114] C. Xu, M. Hackett, TerraPower HT9 Mechanical and Thermal Creep Properties, in: 2017: pp. 95–102. https://doi.org/10.1007/978-3-319-51097-2_8.
[115] G. Vetterick, C. Xu, HT9 material development for the TWR core, in: Trans. Am. Nucl. Soc., 2018.
[116] Manufacturing Demonstration Facility, (n.d.). https://www.ornl.gov/facility/mdf.
[117] S.A. Maloy, T.A. Saleh, O. Anderoglu, T.J. Romero, G.R. Odette, T. Yamamoto, S. Li, J.I. Cole, R. Fielding, Characterization and comparative analysis of the tensile properties of five tempered martensitic steels and an oxide dispersion strengthened ferritic alloy irradiated at ≈295 °C to ≈6.5 dpa, J. Nucl. Mater. 468 (2016) 232–239. https://doi.org/10.1016/j.jnucmat.2015.07.039.
[118] S. Taller, D. Woodley, E. Getto, A.M. Monterrosa, Z. Jiao, O. Toader, F. Naab, T. Kubley, S. Dwaraknath, G.S. Was, Multiple ion beam irradiation for the study of radiation damage in materials, Nucl. Instruments Methods Phys. Res. Sect. B Beam Interact. with Mater. Atoms. 412 (2017) 1–10. https://doi.org/10.1016/j.nimb.2017.08.035.
[119] ASTM E521-16, Standard Practice for Investigating the Effects of Neutron Radiation Damage Using Charged-Particle Irradiation, ASTM International, West Conshohocken, PA, (2016). www.astm.org.
[120] J.P. Wharry, The Mechanism of Radiation- Induced Segregation in Ferritic-Martensitic Steels - part 1, Thesis. (2012).
[121] S. Taller, F. Naab, G.S. Was, A methodology for customizing implantation profiles of light ions using a single thin foil energy degrader, Nucl. Instruments Methods Phys. Res. Sect. B Beam Interact. with Mater. Atoms. 478 (2020) 274–283. https://doi.org/10.1016/j.nimb.2020.07.017.
[122] L.A. Giannuzzi, J.L. Drown, S.R. Brown, R.B. Irwin, F.A. Stevie, Applications of the FIB lift-out technique for TEM specimen preparation, Microsc. Res. Tech. 41 (1998) 285–290. https://doi.org/10.1002/(SICI)1097-0029(19980515)41:4<285::AID-JEMT1>3.0.CO;2-Q.
[123] B. Yao, D.J.J. Edwards, R.J.J. Kurtz, TEM characterization of dislocation loops in irradiated bcc Fe-based steels, J. Nucl. Mater. 434 (2013) 402–410. https://doi.org/10.1016/j.jnucmat.2012.12.002.

[124] J. PIŇOS, Š. MIKMEKOVÁ, L. FRANK, About the information depth of backscattered electron imaging, J. Microsc. 266 (2017) 335–342. https://doi.org/10.1111/jmi.12542.
[125] T. Yang, The Effect of Principal Elements on Defect Evolution in Single-Phase Solid Solution Ni Alloys, University of Michigan, 2018. https://hdl.handle.net/2027.42/149968.
[126] C. Lu, L. Niu, N. Chen, K. Jin, T. Yang, P. Xiu, Y. Zhang, F. Gao, H. Bei, S. Shi, M.-R.R. He, I.M. Robertson, W.J. Weber, L. Wang, Enhancing radiation tolerance by controlling defect mobility and migration pathways in multicomponent single-phase alloys, Nat. Commun. 7 (2016) 13564. https://doi.org/10.1038/ncomms13564.
[127] P. Xiu, H. Bei, Y. Zhang, L. Wang, K.G. Field, STEM Characterization of Dislocation Loops in Irradiated FCC Alloys, J. Nucl. Mater. 544 (2021) 152658. https://doi.org/10.1016/j.jnucmat.2020.152658.
[128] C. Lu, K. Jin, L.K. Béland, F. Zhang, T. Yang, L. Qiao, Y. Zhang, H. Bei, H.M. Christen, R.E. Stoller, L. Wang, Direct Observation of Defect Range and Evolution in Ion-Irradiated Single Crystalline Ni and Ni Binary Alloys, Sci. Rep. 6 (2016) 19994. https://doi.org/10.1038/srep19994.
[129] C. Lu, T. Yang, L. Niu, Q. Peng, K. Jin, M.L. Crespillo, G. Velisa, H. Xue, F. Zhang, P. Xiu, Y. Zhang, F. Gao, H. Bei, W.J. Weber, L. Wang, Interstitial migration behavior and defect evolution in ion irradiated pure nickel and Ni-xFe binary alloys, J. Nucl. Mater. 509 (2018) 237–244. https://doi.org/10.1016/j.jnucmat.2018.07.006.
[130] T. Yang, C. Lu, G. Velisa, K. Jin, P. Xiu, M.L. Crespillo, Y. Zhang, H. Bei, L. Wang, Effect of alloying elements on defect evolution in Ni-20X binary alloys, Acta Mater. 151 (2018) 159–168. https://doi.org/10.1016/j.actamat.2018.03.054.
[131] Y. Zhang, X. Wang, Y.N. Osetsky, Y. Tong, R. Harrison, S.E. Donnelly, D. Chen, Y. Wang, H. Bei, B.C. Sales, K.L. More, P. Xiu, L. Wang, W.J. Weber, Effects of 3d electron configurations on helium bubble formation and void swelling in concentrated solid-solution alloys, Acta Mater. 181 (2019) 519–529. https://doi.org/10.1016/j.actamat.2019.10.013.
[132] C. Lu, T.-N. Yang, K. Jin, G. Velisa, P. Xiu, Q. Peng, F. Gao, Y. Zhang, H. Bei, W.J. Weber, L. Wang, Irradiation effects of medium-entropy alloy NiCoCr with and without pre-indentation, J. Nucl. Mater. 524 (2019) 60–66. https://doi.org/10.1016/j.jnucmat.2019.06.020.
[133] T. ni Yang, C. Lu, G. Velisa, K. Jin, P. Xiu, Y. Zhang, H. Bei, L. Wang, Influence of irradiation temperature on void swelling in NiCoFeCrMn and NiCoFeCrPd, Scr. Mater. 158 (2019) 57–61. https://doi.org/10.1016/j.scriptamat.2018.08.021.
[134] A. Schemer-Kohrn, M.B. Toloczko, Y. Zhu, J. Wang, D.J. Edwards, Removal of FIB Damage using Flash Electropolishing for Artifact-free TEM Foils, Microsc. Microanal. 25 (2019) 1606–1607. https://doi.org/10.1017/S1431927619008766.
[135] L. Jiang, Y. Hu, K. Sun, P. Xiu, M. Song, Y. Zhang, W.L. Boldman, M.L. Crespillo, P.D. Rack, L. Qi, W.J. Weber, L. Wang, Irradiation-Induced Extremes Create Hierarchical Face-/Body-Centered-Cubic Phases in Nanostructured High Entropy Alloys, Adv. Mater. 32 (2020) 2002652. https://doi.org/10.1002/adma.202002652.
[136] C.M. Parish, K.G. Field, A.G. Certain, J.P. Wharry, Application of STEM characterization for investigating radiation effects in BCC Fe-based alloys, J. Mater. Res. 30 (2015) 1275–1289. https://doi.org/10.1557/jmr.2015.32.
[137] K.G. Field, S.A. Briggs, K. Sridharan, Y. Yamamoto, R.H. Howard, Dislocation loop formation in model FeCrAl alloys after neutron irradiation below 1 dpa, J. Nucl. Mater.

495 (2017) 20–26. https://doi.org/10.1016/j.jnucmat.2017.07.061.
[138] C. Lu, M. Li, P. Xiu, X. Wang, G. Velişa, L. Jiang, K.L. More, J.D. Poplawsky, Y. Chang, Y. Zhang, L. Wang, High radiation tolerance of an ultrastrong nanostructured NiCoCr alloy with stable dispersed nanooxides and fine grain structure, J. Nucl. Mater. 557 (2021) 153316. https://doi.org/10.1016/j.jnucmat.2021.153316.
[139] P. Xiu, M. Jin, K. Bawane, B. Tyburska-Püschel, B.J. Jaques, K.G. Field, J.J. Giglio, L. He, Dislocation Loops in Proton Irradiated Uranium-Nitrogen-Oxygen System, J. Nucl. Mater. 557 (2021) 153244. https://doi.org/10.1016/j.jnucmat.2021.153244.
[140] C. Lu, T. Yang, K. Jin, G. Velisa, P. Xiu, M. Song, Q. Peng, F. Gao, Y. Zhang, H. Bei, W.J. Weber, L. Wang, Enhanced void swelling in NiCoFeCrPd high-entropy alloy by indentation-induced dislocations, Mater. Res. Lett. 6 (2018) 584–591. https://doi.org/10.1080/21663831.2018.1504136.
[141] L. He, M. Khafizov, C. Jiang, B. Tyburska-Püschel, B.J. Jaques, P. Xiu, P. Xu, M.K. Meyer, K. Sridharan, D.P. Butt, J. Gan, Phase and defect evolution in uranium-nitrogen-oxygen system under irradiation, Acta Mater. 208 (2021) 116778. https://doi.org/10.1016/j.actamat.2021.116778.
[142] Y. Zhu, C. Ophus, M.B. Toloczko, D.J. Edwards, Towards bend-contour-free dislocation imaging via diffraction contrast STEM, Ultramicroscopy. 193 (2018) 12–23. https://doi.org/10.1016/j.ultramic.2018.06.001.
[143] Y. Miyajima, M. Mitsuhara, S. Hata, H. Nakashima, N. Tsuji, Quantification of internal dislocation density using scanning transmission electron microscopy in ultrafine grained pure aluminium fabricated by severe plastic deformation, Mater. Sci. Eng. A. 528 (2010) 776–779. https://doi.org/10.1016/j.msea.2010.09.058.
[144] Y. Zhou, G. Velişa, S. San, M.L. Crespillo, Z. Fan, H. Bei, W.J. Weber, P. Xiu, L. Wang, F. Tuomisto, W.-Y. Ching, Y. Zhang, Role of Chemical Disorder on Radiation-Induced Defect Production and Damage Evolution in NiFeCoCr, J. Nucl. Mater. (2022) 153689. https://doi.org/10.1016/j.jnucmat.2022.153689.
[145] K.G. Field, X. Pengyuan, Python code for generating EDX overlay images from the Bruker software, (2021). https://github.com/nomelab/nome-software/blob/master/EDX_overlay_image_from_Bruker_Esprit_output_files.ipynb.
[146] SciKit-image, 0.18.0. (2020). https://scikit-image.org/.
[147] C. Ye, J. Xue, T. Liu, R. Shu, Y. Yan, Y. Liao, Q. Ren, G. Ran, K. Sun, L. Jiang, P. Xiu, L. Wang, The microstructure evolution in a SiCf/SiC composite under triple ion beam irradiation, Ceram. Int. 46 (2020) 9901–9906. https://doi.org/10.1016/j.ceramint.2019.12.266.
[148] C.A. Parkin, M. Moorehead, M. Elbakhshwan, X. Zhang, P. Xiu, L. He, M. Bachhav, K. Sridharan, A. Couet, Phase stability, mechanical properties, and ion irradiation effects in face-centered cubic CrFeMnNi compositionally complex solid-solution alloys at high temperatures, J. Nucl. Mater. (n.d.) under review.
[149] L. Jiang, Q. Peng, P. Xiu, Y. Yan, Z. Jiao, C. Lu, T. Liu, C. Ye, R. Shu, Y. Liao, Q. Ren, F. Gao, L. Wang, Elucidating He-H assisted cavity evolution in alpha Cr under multiple ion beam irradiation, Scr. Mater. 187 (2020) 291–295. https://doi.org/10.1016/j.scriptamat.2020.06.031.
[150] A. Gabriel, L. Hawkins, A. French, Y. Li, Z. Hu, L. He, P. Xiu, M. Nastasi, F.A. Garner, L. Shao, Effect of dpa rate on the temperature regime of void swelling in ion-irradiated pure chromium, J. Nucl. Mater. (2022) 153519.

https://doi.org/10.1016/j.jnucmat.2022.153519.
[151] W.G. Wolfer, The Dislocation Bias, J. Comput. Mater. Des. 14 (2007) 403–417. https://doi.org/10.1007/s10820-007-9051-3.
[152] T. Jourdan, Influence of dislocation and dislocation loop biases on microstructures simulated by rate equation cluster dynamics, J. Nucl. Mater. 467 (2015) 286–301. https://doi.org/10.1016/j.jnucmat.2015.09.046.
[153] Z. Chang, D. Terentyev, N. Sandberg, K. Samuelsson, P. Olsson, Anomalous bias factors of dislocations in bcc iron, J. Nucl. Mater. 461 (2015) 221–229. https://doi.org/10.1016/j.jnucmat.2015.03.025.
[154] K.G. Field, L.M. Barnard, C.M. Parish, J.T. Busby, D. Morgan, T.R. Allen, Dependence on grain boundary structure of radiation induced segregation in a 9wt.% Cr model ferritic/martensitic steel, J. Nucl. Mater. 435 (2013) 172–180. https://doi.org/10.1016/j.jnucmat.2012.12.026.
[155] J.P. Wharry, G.S. Was, The mechanism of radiation-induced segregation in ferritic–martensitic alloys, Acta Mater. 65 (2014) 42–55. https://doi.org/10.1016/j.actamat.2013.09.049.
[156] O.C. Hellman, J.A. Vandenbroucke, J. Rüsing, D. Isheim, D.N. Seidman, Analysis of three-dimensional atom-probe data by the proximity histogram, Microsc. Microanal. (2000). https://doi.org/10.1007/s100050010051.
[157] K. Wang, C.M. Parish, K.G. Field, L. Tan, Y. Katoh, Segregation behavior and phase instability of Eurofer97 after neutron irradiation to 72 dpa, J. Nucl. Mater. 547 (2021). https://doi.org/10.1016/j.jnucmat.2021.152834.
[158] Z. Jiao, S. Taller, K. Field, G. Yeli, M.P.P. Moody, G.S.S. Was, Microstructure evolution of T91 irradiated in the BOR60 fast reactor, J. Nucl. Mater. 504 (2018) 122–134. https://doi.org/10.1016/j.jnucmat.2018.03.024.
[159] P. Auger, P. Pareige, S. Welzel, J.C. Van Duysen, Synthesis of atom probe experiments on irradiation-induced solute segregation in French ferritic pressure vessel steels, J. Nucl. Mater. 280 (2000). https://doi.org/10.1016/S0022-3115(00)00056-8.
[160] C. Zheng, E.R. Reese, K.G. Field, E. Marquis, S.A. Maloy, D. Kaoumi, Microstructure response of ferritic/martensitic steel HT9 after neutron irradiation: effect of dose, J. Nucl. Mater. 523 (2019) 421–433. https://doi.org/10.1016/j.jnucmat.2019.06.019.
[161] Y. Nagai, Z. Tang, M. Hassegawa, T. Kanai, M. Saneyasu, Irradiation-induced Cu aggregations in Fe: An origin of embrittlement of reactor pressure vessel steels, Phys. Rev. B. 63 (2001) 134110. https://doi.org/10.1103/PhysRevB.63.134110.
[162] G.R. Odette *, T. Yamamoto, D. Klingensmith, G.R. Odette, T. Yamamoto, D. Klingensmith, On the effect of dose rate on irradiation hardening of RPV steels, Philos. Mag. 85 (2005) 779–797. https://doi.org/10.1080/14786430412331319910.
[163] M.K. Miller, K.F. Russell, Embrittlement of RPV steels: An atom probe tomography perspective, J. Nucl. Mater. 371 (2007) 145–160. https://doi.org/10.1016/j.jnucmat.2007.05.003.
[164] E.D. Eason, G.R. Odette, R.K. Nanstad, T. Yamamoto, A physically-based correlation of irradiation-induced transition temperature shifts for RPV steels, J. Nucl. Mater. 433 (2013) 240–254. https://doi.org/10.1016/j.jnucmat.2012.09.012.
[165] S. Kotrechko, V. Dubinko, N. Stetsenko, D. Terentyev, X. He, M. Sorokin, Temperature dependence of irradiation hardening due to dislocation loops and precipitates in RPV steels and model alloys, J. Nucl. Mater. 464 (2015) 6–15.

https://doi.org/10.1016/j.jnucmat.2015.04.014.
[166] M. Mamivand, P. Wells, H. Ke, S. Shu, G.R. Odette, D. Morgan, CuMnNiSi precipitate evolution in irradiated reactor pressure vessel steels: Integrated Cluster Dynamics and experiments, Acta Mater. 180 (2019) 199–217. https://doi.org/10.1016/j.actamat.2019.09.016.
[167] G.R. Odette, T. Yamamoto, T.J. Williams, R.K. Nanstad, C.A. English, On the history and status of reactor pressure vessel steel ductile to brittle transition temperature shift prediction models, J. Nucl. Mater. 526 (2019) 151863. https://doi.org/10.1016/j.jnucmat.2019.151863.
[168] Z. Jiao, V. Shankar, G.S. Was, Phase stability in proton and heavy ion irradiated ferritic–martensitic alloys, J. Nucl. Mater. 419 (2011) 52–62. https://doi.org/10.1016/j.jnucmat.2011.08.020.
[169] Z. Jiao, G.S.S. Was, Precipitate evolution in ion-irradiated HCM12A, J. Nucl. Mater. 425 (2012) 105–111. https://doi.org/10.1016/j.jnucmat.2011.12.017.
[170] T.P. Davis, M.A. Auger, N. Almirall, P. Hosemann, G.R. Odette, P.A.J. Bagot, M.P. Moody, D.E.J. Armstrong, Atom probe characterisation of segregation driven Cu and Mn–Ni–Si co-precipitation in neutron irradiated T91 tempered-martensitic steel, Materialia. 14 (2020) 100946. https://doi.org/10.1016/j.mtla.2020.100946.
[171] M.K. Miller, K.F. Russell, M.A. Sokolov, R.K. Nanstad, APT characterization of irradiated high nickel RPV steels, J. Nucl. Mater. 361 (2007) 248–261. https://doi.org/10.1016/j.jnucmat.2006.12.015.
[172] M. Perez, F. Perrard, V. Massardier, X. Kleber, A. Deschamps, H. de Monestrol, P. Pareige, G. Covarel, Low-temperature solubility of copper in iron: experimental study using thermoelectric power, small angle X-ray scattering and tomographic atom probe, Philos. Mag. 85 (2005) 2197–2210. https://doi.org/10.1080/14786430500079645.
[173] R.L. Klueh, E.T. Cheng, M.L. Grossbeck, E.E. Bloom, Impurity effects on reduced-activation ferritic steels developed for fusion applications, J. Nucl. Mater. 280 (2000) 353–359. https://doi.org/10.1016/S0022-3115(00)00060-X.
[174] A.P. Druzhkov, D.A. Perminov, Characterization of nanostructural features in reactor materials using positron annihilation spectroscopy, in: Focus Mater. Sci. Res., 2007.
[175] O.I. Gorbatov, P.A. Korzhavyi, A.V. Ruban, B. Johansson, Y.N. Gornostyrev, Vacancy–solute interactions in ferromagnetic and paramagnetic bcc iron: Ab initio calculations, J. Nucl. Mater. 419 (2011) 248–255. https://doi.org/10.1016/j.jnucmat.2011.09.002.
[176] A. Wagner, A. Ulbricht, F. Bergner, E. Altstadt, Influence of the copper impurity level on the irradiation response of reactor pressure vessel steels investigated by SANS, Nucl. Instruments Methods Phys. Res. Sect. B Beam Interact. with Mater. Atoms. 280 (2012) 98–102. https://doi.org/10.1016/j.nimb.2012.03.008.
[177] P.D. Edmondson, C.P. Massey, M.A. Sokolov, T.M. Rosseel, An Atom Probe Tomography Study of the Through Wall Attenuation Effect on Cu-rich Precipitate Formation in a Reactor Pressure Vessel Steel, J. Nucl. Mater. 545 (2021) 152740. https://doi.org/10.1016/j.jnucmat.2020.152740.
[178] R. Chaouadi, R. Gérard, Copper precipitate hardening of irradiated RPV materials and implications on the superposition law and re-irradiation kinetics, J. Nucl. Mater. 345 (2005) 65–74. https://doi.org/10.1016/j.jnucmat.2005.05.001.
[179] P. Pareige, B. Radiguet, A. Barbu, Heterogeneous irradiation-induced copper precipitation in ferritic iron–copper model alloys, J. Nucl. Mater. 352 (2006) 75–79.

https://doi.org/10.1016/j.jnucmat.2006.02.073.
[180] H. Ke, P. Wells, P.D. Edmondson, N. Almirall, L. Barnard, G.R. Odette, D. Morgan, Thermodynamic and kinetic modeling of Mn-Ni-Si precipitates in low-Cu reactor pressure vessel steels, Acta Mater. 138 (2017) 10–26. https://doi.org/10.1016/j.actamat.2017.07.021.
[181] F. Li, Y. Wei, F. Luo, W. Zhang, X. Zhou, Y. Chen, C. Chen, L. Guo, J. Xin, S. Mo, Behaviors of bubble-loop complexes in He-irradiated CLAM steels at elevated temperatures, J. Nucl. Mater. 529 (2020) 151954. https://doi.org/10.1016/j.jnucmat.2019.151954.
[182] K.G. Field, L.M. Barnard, C.M. Parish, J.T. Busby, D. Morgan, T.R. Allen, Dependence on grain boundary structure of radiation induced segregation in a 9wt.% Cr model ferritic/martensitic steel, J. Nucl. Mater. 435 (2013) 172–180. https://doi.org/10.1016/j.jnucmat.2012.12.026.
[183] K.G. Field, B.D. Miller, H.J.M. Chichester, K. Sridharan, T.R. Allen, Relationship between lath boundary structure and radiation induced segregation in a neutron irradiated 9wt.% Cr model ferritic/martensitic steel, J. Nucl. Mater. 445 (2014) 143–148. https://doi.org/10.1016/j.jnucmat.2013.10.056.
[184] C. David, B.K. Panigrahi, S. Balaji, A.K. Balamurugan, K.G.M. Nair, G. Amarendra, C.S. Sundar, B. Raj, A study of the effect of titanium on the void swelling behavior of D9 steels by ion beam simulation, J. Nucl. Mater. 383 (2008) 132–136. https://doi.org/10.1016/j.jnucmat.2008.08.049.
[185] A. Kimura, M. Narui, H. Kayano, Effects of alloying elements on the post-irradiation microstructure of 9%Cr-2%W low activation martensitic steels, J. Nucl. Mater. 191–194 (1992) 879–884. https://doi.org/10.1016/0022-3115(92)90599-G.
[186] N. Igata, T. Irino, A. Kohyama, The role of minor alloying elements in swelling of 316 steel, J. Nucl. Mater. 191–194 (1992) 1323–1326. https://doi.org/10.1016/0022-3115(92)90689-I.
[187] M.J. Makin, G.P. Walters, A.J.E. Foreman, The void swelling behaviour of electron irradiated type 316 austenitic steel, J. Nucl. Mater. 95 (1980) 155–170. https://doi.org/10.1016/0022-3115(80)90090-2.